High-Resolution Studies of Charge Exchange in Supernova Remnants with *Magellan*, *XMM-Newton*, and *Micro-X*

by

Sarah Nicole Trowbridge Heine

Submitted to the Department of Physics
in partial fulfillment of the requirements for the degree of

Doctor of Philosophy in Physics

at the

MASSACHUSETTS INSTITUTE OF TECHNOLOGY

June 2014

Author . . . .
Department of Physics
May 13, 2014

Certified by . . . .
Enectali Figueroa-Feliciano
Associate Professor of Physics
Thesis Supervisor

Accepted by . . . .
Krishna Rajagopal
Professor of Physics
Associate Department Head for Education

High-Resolution Studies of Charge Exchange in Supernova Remnants with *Magellan*, *XMM-Newton*, and *Micro-X*

by

Sarah Nicole Trowbridge Heine

Submitted to the Department of Physics
on May 13, 2014, in partial fulfillment of the
requirements for the degree of
Doctor of Philosophy in Physics

Abstract

Charge exchange, the semi-resonant transfer of an electron from a neutral atom to an excited state in an energetic ion, can occur in plasmas where energetic ions are incident on a cold, at least partially neutral gas. Supernova remnants, especially in the immediate shock region, provide conditions conducive to charge exchange. The emission from post charge-exchange ions as the captured electron cascades down to the ground state, can shed light on the physical conditions of the shock and the immediate post-shock material, providing an important tool for understanding supernova explosions and their aftermath.

In the first half of this thesis, I study charge exchange in the galactic supernova remnant G296.1-0.5 in two energy bands: the optical and the X-ray. The optical study, performed using both imaging and high resolution spectroscopy from the IMACS instrument on the *Magellan Baade Telescope* at Las Campanas Observatory, seeks to identify 'Balmer-dominated shocks' in the remnant, which signal the occurrence of charge exchange between hot, post-shock protons and colder neutral hydrogen in the environment. The X-ray study probes line ratios in dispersed spectral data obtained with *XMM-Newton* RGS from an X-ray lobe in the NW of the remnant to hunt for signatures of charge exchange. The dispersed data are degraded by the extended nature of the source, blurring emission lines and making precise measurements difficult.

The focus of the second half of this thesis is *Micro-X*: a sounding rocket-borne X-ray telescope, utilizing an array of microcalorimeters to achieve high energy resolution for even extended sources. I describe the design and commissioning of the payload and the steps toward launch, which is anticipated in the spring of 2015.

Thesis Supervisor: Enectali Figueroa-Feliciano
Title: Associate Professor of Physics

Acknowledgments

It truly takes a village to raise an astrophysicist and I'm grateful to everyone who has helped me get to this point. I feel I would be remiss if I failed to acknowledge the people who helped mold me before I started my grad school journey six years ago. I would never have even imagined being here without some truly incredible teachers, especially Kim Greene who taught my sixth grade astronomy class and inspired me to become an astrophysicist, my high school physics teachers Dan Albritten and Roger Briggs, and my high school calculus teacher Carla Burley. You all truly make a difference to every student you teach. I also must thank the great many wonderful professors who contributed to my undergraduate education at MIT, especially Dave Pritchard, John Belcher, Marin Soljacic, and Peter Fisher. My great thanks to Leo Hollberg, Scott Diddams, and Svenja Knappe at NIST for introducing me to research. Mike Nowak introduced me to ISIS, programming, scientific writing, and Project Runway, and can always be counted on to help me with my latest computer issues, for which I am truly grateful. Many thanks to Joe Formaggio and Scott Sewell for their support and tutelage in experimental physics. I propagated my errors carefully in this thesis for you.

Tali, thank you for getting me involved in *Micro-X*, and for all your help and guidance. Your seemingly boundless energy, optimism, and creativity have been inspirational and it has been a blast. John, my partner in crime and lab big brother, thank you for being super smart, thoughtful, having awesome taste in music, putting up with and occasionally joining in my giggle fits, and for commenting your code so thoroughly. Patrick, I learned so much from you over our time working together. Thank you for all your amazingly hard work designing the payload, your friendship, and for putting up with us less efficient human beings. Thank you to Phil Oakley and Rick Foster for all of the guidance, help, and encouragement. Meredith, thank you for saving me from carrying the rocket alone and for caring so much for this project from day one. Jean Papagianopoulos and Teresa Santiago are angels who keep us mere physicists from fainting at the sight of a budget or a purchase order. I am forever indebted to Andy Gallant and Scott Spence in the MIT Central Machine Shop for meeting me with a smile and a laugh no matter what crazy project I bring in at closing time to be done as quickly as possible, and for giving me cake when my salt pill rusted through. Our collaborators at GSFC, WFF, and NIST are incredibly smart and willing to share their vast knowledge of cryogenics, electronics, rocket systems, and detectors. Great thanks to Daniel Castro for including me on the Magellan observation in Chile, which was one of the highlights of my graduate school career, and for providing the RGS data for my X-ray analysis. Becky Levinson, Dan Milisavljevic, and Michael McDonald helped me immensely with the optical analysis when I would otherwise have been a fish out of water.

Last but most certainly not least, thank you to the MIT gymnastics team, past and present, for bringing me to MIT in the first place, giving me another reason to stay here, and being my friends, refuge, teammates, and overall inspiring people. I'd also like to thank my best friend of 25 years (and forever) Catherine Hammond. Somehow even though you're 2000 miles away, whenever I need you most my phone rings and there you are to help me get through anything. You're the best. I have the best parents in the world. Thank you for giving me the courage and confidence to go for anything and everything, for teaching me how to make a to do list, even at three years old, and for being okay with all of this just being a backup plan to my real dream of becoming the Cadbury bunny. I also want to thank the rest of my family, both by blood and by marriage, for being the most supportive, caring, sweet people in the whole world. Finally, to my husband Matt, you make me a better version of myself in every way. Thank you so much for your love and support, and for always knowing when to come home with ice cream. I love you more than I can say.

Contents

Chapter 1

Astrophysical Charge Exchange

1.1 Physics of Charge Exchange in Plasmas

Charge exchange (CX) is the semi-resonant transfer of one or more electrons from a neutral atom or molecule to an excited state of an ion [110]. It occurs when an energetic ion collides with a neutral, cold atom and strips it of an electron, which is subsequently captured into an excited state of the ion. This interaction is described in Equation 1.1, where A is the ion, q+ is its original charge, N is the originally neutral atom, and the star superscript denotes an excited state. CX can occur when a hot stream of ions hits a cloud of neutral gas (usually hydrogen in astrophysical situations), and can be detected via the signature of photons released when a captured electron cascades down into the ground state of the capturing ion. Thus, the energies of the photons emitted as the result of a CX event are simply the transition energies out of the electron's post-capture energy level in the newly formed ion. Any measurement of these photons will also be affected by Doppler shifts resulting from the relative motion between the emitting atom and the observer.

Astrophysical systems exhibiting strong CX are those containing ionized metals, neutral hydrogen and a rapid transition region between the two [94]. Examples of this are regions where the solar wind hits the interstellar medium, shocked, outflowing ejecta in supernova remnants hitting unshocked, cold gas blown off by the progenitor, and regions of gas mixing in galaxies. CX can occur between two ions but the cross sections for this type of interaction are very small due to Coulomb repulsion between the ions, so I will henceforth focus on CX between an ion and a neutral atom[110].

$$A^{q+} + N \rightarrow A^{(q-1)+*} + N^{+} \tag{1.1}$$

As an ion and a neutral atom come in close contact during a CX interaction, their energy levels are distorted as their internal electric fields are superposed. At certain internuclear distances, these distorted energy levels will overlap, allowing the radiationless transfer of an electron from the neutral to an excited state of the ion. The locations of these overlaps are called curve crossings, and occur at several discrete internuclear distances, each resulting in an electron transfer into a distinct energy level of the ion. For an ion with charge q, the most probable destination energy level for transfer of an electron from neutral hydrogen is given by Equation 1.2. For a single electron transfer from a neutral atom other than hydrogen, n_{max} scales by the square root of the ratio of the ionization potential of hydrogen to that of the neutral target. The larger the charge of the ion, the higher the destination energy levels of the captured electron, thus electrons are captured into high n levels in highly charged ions. If the neutral is not hydrogen (i.e. has multiple electrons) multiple electrons can be transferred, leading to a multiply excited ion, however the cross section for multiple transfer is much smaller than that for a single transfer [110].

$$n_{max} \approx q(1 + \frac{q-1}{\sqrt{2q}}) \approx q^{3/4} \tag{1.2}$$

The cross section for charge exchange is only weakly dependent on the collision energy and the specific target. For energies less than a critical energy, which scales as the square root of q, the cross section is roughly $\sigma_{CX} \approx q \times 10^{-15} cm^2$. For energies higher than the critical energy, the CX cross section decreases as the cross section for ionization of the neutral without capture by the ion (charge stripping) increases [110]. However, in most astrophysical situations, the CX cross section is high enough that when ions and neutrals are able to CX they will be very likely to do so [94].

1.2 Simulations and Calculations

Modeling the expected emission from plasma is important since CX line emission must be disentangled from thermal emission from any astrophysical source. A popular package for modeling plasma emission in the X-ray regime is the Astrophysical Plasma Emission Code or APEC along with the Astrophysical Plasma Emission Database or APED [94], [97]. This package calculates spectral models for hot plasmas taking into account collisional radiative rates, recombination cross sections, dielectronic recombination rates, and satellite line wavelengths. Other similar models (SPEX, CHIANTI, MEKAL) perform similar tasks with slight differences. The electron beam ion trap (EBIT) [110] is a laboratory astrophysics experiment that uses high resolution spectroscopy to measure emission from controlled plasmas. APEC results were compared with EBIT results [97] with good agreement, however many of the plasma states encountered in astrophysical systems are not achievable in laboratories. While these models are a good start, it is difficult to predict the emission without detailed knowledge of the plasma state. For example, the cross-section for charge exchange depends upon the detailed distribution of ion and neutral components and their velocities, but must be estimated as some average in lieu of this information [94].

Several other researchers have produced models or performed calculations to predict signatures of charge exchange to compare to data. Lallement [64] predicts systems in which CX emission is significant, by making approximate calculations of the CX flux of an object in the X-ray regime given electron and ion densities, shock velocity, and charge exchange cross-section, and comparing it to the thermal X-ray emission flux. In order to understand the dynamics of charge exchange, Schultz et al. [87] analyzes cross sections of elastic scattering and charge exchange in various shock velocity regimes using measurements and solutions to the Schrödinger equation. Ghavamian et al. [38], Smith et al. [96], Helder et al. [44], and several others perform calculations and simulations to compare expectations of Hα line profiles with and without cosmic ray acceleration in the shock.

High resolution data from astrophysical sources will be invaluable to test and refine many of these models in regimes not achievable in the laboratory. This type of data is currently only available from a very small sample of sources in the optical band and almost no sources in the X-ray band. The launch of *Micro-X* and the Japanese satellite *Astro-H* will jump-start a new wave of modeling efforts to understand the effects of, and emission from, charge exchange processes in astrophysical plasmas.

1.3 Experimental Measurements of Charge Exchange

Since the detailed physics in systems where CX occurs can be complicated, experimental measurements are a necessity. There are several different approaches currently in use for measuring CX in the laboratory. Cross beam experiments utilize a beam of highly charged ions crossing a supersonic gas jet of neutral atoms. In another type of experiment, ions are held in a storage ring and repeatedly enter a gas cell to undergo CX. Most of these types of experiments focus on measuring the relation between ion charge and cross section. Few of these study the photon emission due to charge exchange but it is becoming more popular to do so. It is also possible to study charge exchange in Tokamaks by injecting neutral hydrogen into the plasma held in the experiment [110].

Currently the most popular mechanism for studying charge exchange is the electron beam ion trap (EBIT). In these experiments electrons are focused by a magnetic field and passed through a trap region in a beam with diameter of about 60 μm. Neutral atoms or low charge ions from a vacuum arc source are injected into the trap and are then collisionally ionized or excited by the electron beam, or undergo charge exchange between the ions and neutrals in the trap. Emission is measured in a direction perpendicular to the beam direction, ensuring measurements of the emission with minimal complication from Doppler shifts, however absolute cross sections cannot be measured because the neutral gas density is not precisely known. The collision energy in any CX reaction is given by the energy of the incident ion, which is determined by the ion charge and trap depth in an EBIT experiment. The energy of the neutral target is negligible in the physics of the interaction. Most EBIT experiments run with a characteristic ion energy around 20 eV/amu. Another possible use of the EBIT apparatus is to measure charge exchange lifetimes by turning off the electron beam and measuring the emission from the trap over time [110].

1.4 Examples of Astrophysical Charge Exchange

Charge exchange is possible in any system where hot ionized gas is incident on a neutral gas population. There are many astrophysical systems where this occurs. Supernova remnants, the focus of this thesis, are prime candidates for charge exchange as hot, ionized gas (shocked gas and hot ejecta) streams into cooler neutral gas (either the interstellar medium (ISM) or gas thrown off by the precursor). I will discuss several examples of this in the coming chapters. Other systems in which charge exchange has been identified are comet comas in the solar wind, star forming regions in galaxies, solar wind interactions at the heliopause, pulsar wind nebulae, binary star systems (most often when the system is made up of a white dwarf and a cool giant), T Tauri stars, and supernovae [46]. I will discuss several of these systems in detail to give a scope of the type of measurements currently possible.

X-ray signatures from charge exchange in an astrophysical system was first observed in the detection of bright X-ray emission from the coma of the comet Hyakutake with *ROSAT* in 1996 [65], which arises from the interaction between ions in the solar wind and neutrals in the comet's cold coma [76]. Since then, similar bright, X-ray emission has been detected in several other comets. X-ray CX emission is also detected in the geocorona (solar wind ions charge exchanging with neutrals in the atmosphere), in the atmospheres of all the planets in our solar system from Venus to Jupiter, and in the heliosphere between solar wind ions and neutral hydrogen and helium in the interstellar medium at the boundary of the solar system. This solar wind charge exchange in the heliosphere is thought to make up a significant fraction of the diffuse X-ray background we observe in the quarter-keV region [76]. All of the most common heavy elements (O, C, Ne, Fe, N, Si, Mg, S) produce astrophysical X-ray CX emission, usually with hydrogen and helium as neutral targets. The hydrogen-, helium- and lithium-like states of these heavy ions are the most prolific as far as production of CX emission [76].

There is also evidence of CX emission in the X-ray band from star forming regions in galaxies. The origin of soft X-ray line emission in these sources is very important to understand galactic feedback mechanisms, which inform on the evolution of galaxies [109]. Charge exchange, unlike thermal emission, contributes only line emission with no continuum component. Modeling an X-ray spectrum that includes charge exchange photons with a thermal-only model can skew derived plasma properties. Wang and Liu [109] find the resonance line of the Kα triplet of O VII is often weaker than the forbidden line of the same triplet in star forming regions, suggesting that X-ray emission may be a result of CX at the interface of plasma and neutral gas, rather than solely thermal emission from the heated plasma. They also observe a spatial correlation of the soft X-ray line emission with various tracers of cool gas in some galaxies, supporting CX as a possible emission mechanism.

Wang and Liu [109] utilize the $\mathcal{G}$ ratio discussed in Section 1.6.1 and shown in Equation 1.8, as a spectroscopic diagnostic of significant contribution from CX. For several active star forming galaxies (NGC 253, M51, M83, M61, NGC 4631, and the antennae galaxies) they measure $\mathcal{G}$ ratios of about 2.2 in the Kα triplet of O VII using the RGS on *XMM*, which is consistent with lab-measured values for charge exchange. $\mathcal{G}$ ratios for other He-like ions with higher ionization thresholds (e.g., Ne IX) were typically much smaller and more consistent with thermal origins. For the analysis of emission from the center of the starburst galaxy M82, the authors found 90% CX contribution to the flux in the O VII Kα triplet, 50% in the Ne IX Kα triplet, and 30% in the Mg XI Kα triplet, giving an average CX contribution of around 50%. Also, for multiple galaxies, fits to the soft X-ray spectrum including both thermal and change exchange components give statistically better fits to the spectrum than a purely thermal model. This is strong evidence for the presence of CX in galaxies, however several other emission mechanisms capable of producing shifted line ratios, including recombination of H-like ions and electrons and innner-shell ionization of Li-like ions, have not been ruled out. Ideally a fit to the entire spectrum of one region, rather than isolated triplets, would help to decompose the thermal and CX contributions, as would improved spatially resolved spectroscopy [109].

There are very few radio signatures known to result from astrophysical charge exchange. In fact, those that have been posited in the literature are not direct signatures of CX (i.e. photons released in the initial electron cascade to the ground state of the incident ion after CX), but are produced by processes that involve the products of CX. In these cases CX acts as a mechanism to distribute ions and neutrals such that their interactions with the magnetic fields and free electrons in certain areas produce radio emission. For example, radio emission that is thought to be generated at the heliopause (the interface between the local ISM and the solar wind) has been detected by Voyager between 1.8 kHz and 3.6 kHz [103].

At the heliopause, there is an 'ion wall': one of the only areas with a density high enough to account for the strength of this radiation [102]. Interstellar neutral gas undergoes charge exchange with solar wind ions, ionizing interstellar neutrals at the heliosphere. These new ions are then picked up and heated by the solar wind. In some cases the original incident solar wind ion is neutralized in the CX, creating a fast-moving hot neutral. When this fast, hot neutral reaches the ion wall, it may CX with one of the ions there and be reionized [102]. The interaction of the ions produced in both of these CX events with the magnetic fields from the solar winds generates lower hybrid waves, which nonlinearly accelerate electrons into beams along the heliosheath spiral magnetic field. This spiraling of electrons could be a mechanism to produce the observed heliopause radio emission [103].

Komossa et al. [62] perform a multi-wavelength follow up to an extremely bright flaring event in SDSS J095209.56 +214313.3, to determine the nature of the event: a Type IIn supernova or an extreme accretion event in an AGN, like a stellar tidal disruption. In the optical band, they detect an Hα line with four components: an asymmetric broad base, a narrow core, and two strong but unresolved horns on either side of the line, which also appear in the Hβ line. In Section 1.5, I discuss the significance of the broad hydrogen line profile in the context of charge exchange. Over a three year baseline the broad line width changes from 2100 to 1500 km/s and its centroid shifts from 560 to 270 km/s. The narrow component shows nearly no change over the three year baseline while the peculiar horns fade significantly. N II and S II lines are present in several locations, but are spatially variable. Whatever the event, the Hα profile seems to imply some amount of resultant charge exchange. The event is quite interesting, since its resultant emission is not completely consistent with models for any of the proposed mechanisms.

1.5 Charge Exchange Signatures in the Optical Band: Balmer Dominated Shocks

One of the most established examples of astrophysical charge exchange emission is optical emission from CX in the thin post-shock region in supernova remnants. This is a result of charge exchange between hot protons flowing outward with the shock, and neutral gas (mostly hydrogen) in the pre-shock region [18]. The optical signature of this CX is a spectrum dominated by a distinctive Hα emission line. The characteristic Hα line is made up of two components: a narrow component, the result of the cold, neutral hydrogen gas being heated by the shock, and a broad component, the result of the decay of the hot neutral hydrogen atom produced after the charge exchange event. Their ratio can provide shock velocity and constrain the degree of electron-ion equilibration behind the shock, while their widths can shed light on the temperature profiles of the pre-shock material and the proton temperature of the plasma flowing out with the shock [93]. An example of this spectral feature can be seen in Figure 1-3. This signature has been successfully observed in SNRs for the last 30 years and is considered conclusive proof of CX in SNRs [18].

Supernova remnant shocks are considered to have roughly three evolutionary stages. Initially the shock moves collisionlessly at a high constant velocity. It heats material in the post-shock region to very high temperatures and begins to sweep up material as it propagates. Balmer dominated shocks are created in these early, fast shocks. When the shock has swept up material with mass about equal to the mass of the supernova ejecta, it enters the second phase, which is known as the Sedov, or adiabatic, phase. In this phase the shock begins to slow. Post-shock temperatures are still high and strong X-ray emission is expected. This stage is expected to last 10,000 to 30,000 years. In the final stage, known as the 'snow-plow' phase, the shock slows even further after sweeping up large masses of circumstellar material. Temperatures behind the shock fall, allowing recombination and radiative cooling. The post-shock radiation in this phase becomes dynamically important, so shocks in this phase are also called radiative shocks. Strong optical emission, especially the forbidden lines from N II, S II, and O III are expected in this phase.

1.5.1 The Broad Hα Line Component Problem

In 1959, Minkowski [75] detected bright Hα filaments around the Kepler, Tycho, and Cygnus loop supernova remnants in an optical study of previously observed radio sources. In 1976, van den Bergh [105] observed filamentary Hα emission from SN 1006. In 1978, two groups measured 'peculiar' optical spectra from supernova remnants. Schweizer and Lasker [88] studied the remnant of SN 1006 and Kirshner and Chevalier [60] studied Tycho's supernova remnant. Both remnants showed spectra with nearly pure Balmer emission, exhibiting strong Hα and Hβ lines but none of the O III, N II and S II emission generally used to characterize the optical spectra of SNRs [32].

In addition, the profiles of the Hα lines were very unusual. Rather than a single, narrow thermal component expected due to heating of the neutral hydrogen around the remnant as the shock moves outwards, a narrow component with faint broad wings was observed. The width of the broad component was so large that the inferred temperature of the hydrogen producing that line was higher than expected for any neutral hydrogen population.

The cause of this unusual emission was suggested by Chevalier and Raymond [18], and later expanded upon by Chevalier and Kirshner [19]. They suggested a model of a 'Balmer-dominated shock' (BDS), where a fast shock wave overtakes a population of neutral hydrogen. The collisionless shock heats the charged particles in its path (electrons and ions), but does not affect the neutrals. A fraction of the cold neutrals is excited or ionized by collisions with hot, post-shock electrons. The emission from the excited, cold neutrals comprises the observed narrow Hα line, which has a thermal width corresponding to the temperature profile of the cold, pre-shock, neutral population. However, some fraction of the cold neutral atoms in the post-shock region undergo charge exchange with high-velocity, post-shock protons, producing a population of hot, fast neutrals. The emission from this population produces the observed broad Hα line, which has a width corresponding to the thermal profile of the hot, post-shock protons. The Hβ line should also show a similar structure, however Hβ emission comes from a higher excited state than Hα emission and charge exchange will preferentially populate the lower excited state so the broad component may be weaker in the Hβ line.

The existence of a population of neutrals in the shock-front region implies a limit on the ionizing radiation emitted by the supernova (since large amounts of ionizing radiation would completely ionize the surrounding ISM). The widths of the emission lines can provide valuable information on the plasma states at various locations near the shock, and the ratio between the emission from the two lines is related to shock velocity and electron/ion temperature equilibrium, as described in Section 1.5.2. The lack of forbidden metal lines (N II, S II, and O III in particular) is expected in these shocks because of the high temperatures involved in the fast shocks cause thorough ionization behind the shock, and the radiative cooling and recombination necessary to produce these ions is not important in the immediate post-shock region (the timescales for cooling processes are much longer than the excitation and charge exchange processes that produce characteristic BDS emission) [46]. We do not expect to see these lines until the shock has reached its low-velocity ‘snow-plow’ (or radiative) phase [11].

1.5.2 Theory and Calculations

In order to understand the plasma properties of BDS systems, Chevalier and Raymond [19] performed simple analytic calculations, which I follow in this section. For neutrals to be present and undergo charge exchange in the post-shock region, they must survive any ionization processes in the region. The possible processes for ionization of a neutral particle in the post-shock region are ionization by proton or electron collision or ionization by a collision with another neutral. Photo-ionization is also possible, however it is less important in these plasmas than collisional ionization, and will thus be neglected in the following calculations. In this case we assume ionization by neutrals is insignificant. We introduce σ_i, which is defined as the cross section for ionization by protons or electrons, which are assumed to have similar densities $n_e \approx n_p$. We also introduce σ_x, which is the charge exchange cross section. σ_x is highly dependent on the relative velocity between the cold neutral and hot proton [72]. The lifetime of a slow neutral particle in the post-shock region will be given by Equation 1.3, where the subscript s denotes the average over the relative velocity between a slow neutral and a fast charged particle.

$$\tau_s \approx \frac{1}{n_p\left(\langle\sigma_i v\rangle_s + \langle\sigma_x v\rangle_s\right)} \tag{1.3}$$

From this we can obtain the fraction of incoming cold neutrals that undergo charge exchange in Equation 1.4.

$$f_{cx} \approx \frac{\langle\sigma_x v\rangle_s}{\left(\langle\sigma_i v\rangle_s + \langle\sigma_x v\rangle_s\right)} \tag{1.4}$$

A fast neutral produced by CX will have a lifetime $\sim (n_p\langle\sigma_i v\rangle_f)^{-1}$ before it is ionized, where the subscript f designates an average over the relative velocity between a fast neutral and a fast charged particle. From this we can obtain the ratio between the fraction of fast neutrals and the fraction of slow neutrals in the CX region, which is given in Equation 1.5.

$$\frac{f_f}{f_s} = \left(\frac{\langle\sigma_x v\rangle_s}{\left(\langle\sigma_i v\rangle_s + \langle\sigma_x v\rangle_s\right)}\frac{1}{n_p\langle\sigma_i v\rangle_f}\right)\left(\frac{1}{n_p\left(\langle\sigma_i v\rangle_s + \langle\sigma_x v\rangle_s\right)}\right)^{-1} = \frac{\langle\sigma_x v\rangle_s}{\langle\sigma_i v\rangle_f} \tag{1.5}$$

To obtain $\langle\sigma_x v\rangle_s$ we work in a cartesian coordinate system where z is perpendicular to the shock front, and take v_0 to be the bulk velocity of the shocked gas. We require the neutral population to be stationary such that the relative velocity between the neutrals and the hot protons is simply the velocity of the hot protons. We also assume a small incoming neutral fraction so that only a small fraction of hot protons will be lost to charge exchange and we can assume a Maxwellian velocity distribution for the protons. If there were a high neutral fraction, the velocity distribution of the hot protons would be skewed because the charge exchange cross-section strongly favors charge exchange with low relative velocities as shown in Figure 1-1. The resulting integral for $\langle\sigma_x v\rangle_s$ is given in Equation 1.6 where $l \equiv \left(\frac{m_p}{2kT}\right)^{1/2}$.

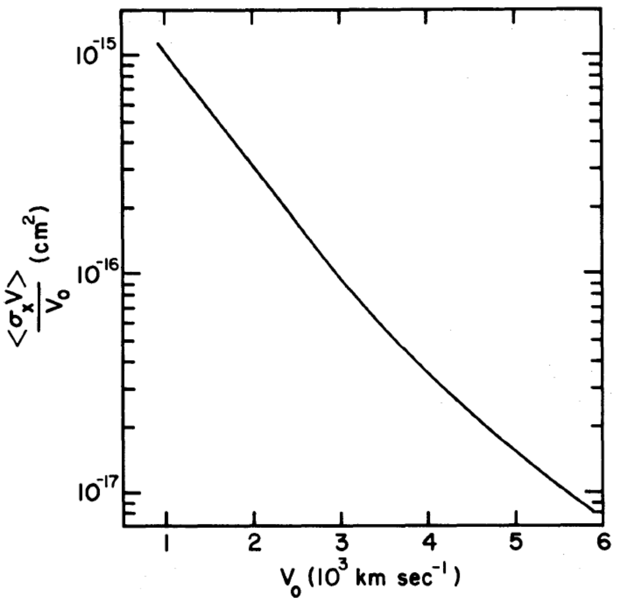

Figure 1-1: The charge exchange cross section average $\langle \sigma_x v \rangle / v_0$ as a function of v_0, the mean velocity of gas behind the shock wave. The charge exchange cross section is much larger for interactions between ions and neutrals with lower relative velocities. Reprinted from [19].

$$\langle \sigma_x v \rangle_s = \frac{l^{3/2}}{\pi^{3/2}} \int_{-\infty}^{\infty} \int_{-\infty}^{\infty} \int_{-\infty}^{\infty} v \sigma_x(v) \exp\left(-l^2[v_x^2 + v_y^2 + (v_z - v_0)^2]\right) dv_x dv_y dv_z \tag{1.6}$$

The relationship between v_0 and the post-shock proton temperature is determined by assumptions about the extent of proton-electron temperature equilibration. Chevalier and Raymond [19] derive these relations in detail in several cases. All models discussed here assume a strong adiabatic shock wave with the ratio of specific heats $\gamma = \frac{C_P}{C_V} = 5/3$, the value for a monatomic gas with three degrees of freedom. For a fast shock where only the protons are thermalized behind the shock (no equilibration of electrons) and the gas composition is 100% hydrogen behind the shock, the post-shock temperature will be given by $T = \frac{1}{3}\frac{m_p}{k} v_0$. If we instead assume complete thermalization behind the shock and 10% He by number relative to H, $T = \frac{1}{5}\frac{m_p}{k} v_0$.

Chevalier and Raymond [19] calculate the integral in 1.6 for a range of values of v_0 between 1000-6000 km/s using $\sigma_x(v)$ from McClure et al. [72]. They obtain a range of $\langle \sigma_x v \rangle_s / v_0$ between $\sim 10^{-15}$ cm^2 at $v_0 = 1000$ km/s to below $\sim 10^{-17}$cm^2 at $v_0 = 6000$ km/s.

The calculation for $\langle \sigma_i v \rangle_f$ is more complicated because it requires knowledge of the non-Maxwellian velocity distribution of fast neutrals. However, it can be approximated because σ_i is not a strong function of the relative velocity, so $\langle \sigma_i v \rangle_f \approx \sigma_i v_{th}$ where v_{th} is the mean velocity of fast particles. A typical value for σ_i is 2.2×10^{-16}cm^2.

To obtain the predicted ratio between the intensity of the broad and neutral components, some of the conditions of the remnant need to be taken into account. For instance, the optical depth of the emission for fast and slow components can be fairly different due to the effects of velocity and location in the shock, enhancing one of the components over the other (in Tycho, Chevalier and Kirshner [19] approximate that the emission from the slow component is enhanced by a factor of six due to optical depth considerations). The probability of a fast neutral charge exchanging with a fast proton must also be taken into account to understand the plasma state. Finally, a value for the fraction of CX interactions resulting in Hα emission g_α is required. Chevalier and Raymond [19] take this value to be 0.02-0.04. They thus arrive at Equation 1.7 for the intensity ratio between the broad and neutral components in Tycho. Since the extent of electron-ion temperature equilibration must be assumed to calculate the expected broad to narrow line ratio, the measured ratio can be used to constrain the extent of equilibration. The dependence of the broad line width and broad to narrow line ratio for various shock velocities and temperature equilibration levels is shown in Figure 1-2.

$$\frac{I(broad)}{I(narrow)} \approx \frac{e_s^{-\tau} \langle \sigma_x v \rangle_s}{e_f^{-\tau} \langle \sigma_i v \rangle_f} \left[1 + g_\alpha \left(1 + \frac{\langle \sigma_x v \rangle_f}{\langle \sigma_i v \rangle_f} \right) \right] \tag{1.7}$$

Schultz et al. [87] study momentum transfer and viscosity due to interactions between cold neutrals and hot ions to understand the contribution of both elastic scattering and charge exchange to the dynamics of a plasma. By computing viscosity and momentum transfer cross sections from differential cross section integrals in the range v ~200-2000 km/s, they confirm that the ratio of narrow and broad Hα emission should depend on the

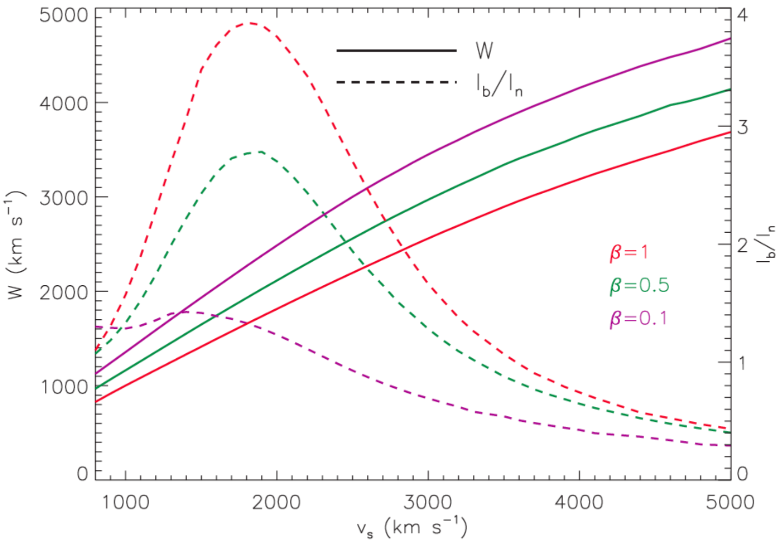

Figure 1-2: Broad line width W and broad to narrow line ratio I_b/I_n versus shock velocity for an edge-on shock with electron to proton temperature ratio β. Reprinted from [46], based on calculations from [104].

ratio of ionization and charge exchange rates, which depend on the thermal equilibrium state of electrons and ions. In order to understand scattering processes at higher velocities, the authors solve the Schrödinger equation for colliding particles using the best possible approximations (or feasible approximations where the best are not known), since there is not yet experimental data (i.e. laboratory experiments) at these high velocities to compare with theoretically calculated cross-sections.

The thermal width of an emission line is derived in Section 2.5, assuming a Maxwellian velocity distribution of the emitting atoms. This relates the full width at half maximum of the line to the temperature of the emitting plasma. Using this relation, we can measure the temperature of the pre- and post-shock protons using the widths of the emission lines. The extent of electron-ion equilibration behind the shock can also be probed both by the broad to narrow line emission ratio, and by comparing the measured hot proton temperature to an electron temperature derived through X-ray observations of the post-shock material.

BDSs are 'non-radiative' shocks, meaning that strong radiative cooling is not yet occurring in the plasma. This cooling is needed to create the N II and S II ions that produce the lines characteristic of radiative shocks. The age of non-radiative shocks is shorter than the cooling and recombination timescales, meaning that radiation from the shock is not dynamically important. Heng [46] describes non-radiative shocks as those that are ~100-1000 years old, with shock velocity $v_s \sim 1000$ km/s, propagating through ISM with a density $n \sim 0.1 - 1\text{cm}^{-3}$. The shock is fast and collisionless, and temperatures behind the shock are high. This also implies that the equilibrium state of the electrons and ions is determined primarily by electromagnetic interactions rather than physical collisions.

Radiative shocks are more often observed in evolved SNRs. Shull and McKee [92] present a numerical model of emission from radiative shocks. Fesen, Blair, and Kirshner [32] describe the general characteristics of radiative filaments in evolved SNRs. The optical spectra of radiative shocks are generally characterized by strong emission lines from O II, O III, S II, N II, and H, along with fainter emission lines from He I, He II, O I, N I, Ne III, Fe II, Fe III, Ca II, and Ar III. S II is an especially strong indicator of a radiative shock. The high collisional cross section of S II transitions in regions with electron temperatures around 10,000 K generally leads to strong S II emission. For radiative shocks in SNRs, the ratio of Hα emission to S II emission is generally less than 2.0. Typically, N II lines will have a strength about 25-50% that of Hα emission and S II lines will have strengths of 40-100% that of Hα (though the N II strength is sensitive to the local N distribution). This is in contrast to non-radiative shocks, where line strengths of N II and S II of even 5% that of Hα are considered unusually strong. There may be a combination of radiative and non-radiative shocks in a single remnant [46]. In fact, Blair, Long, and Vancura [10] observe radiative, transitional, and non-radiative filaments in Kepler, using a classification based on S II emission.

1.5.3 Shocks as Cosmic Ray Precursors

Cosmic rays (CR) are widely believed to originate in SNR shocks. The measured cosmic ray energy spectrum agrees with SNR model predictions and the power required to maintain the observed cosmic ray population could be supplied by about 10% of the kinetic energy in galactic supernovae at their observed rate of about three per century. Since Hα emission from non-radiative shocks originates very close to the shock front, it could contain signatures of particle acceleration occurring in a cosmic ray precursor. Since BDS emission contains information about both the pre- and post-shock populations, and the shock itself, it is an ideal dataset in which to search out signatures of CR acceleration. Neutrals can impede the particle acceleration process by damping plasma waves, however as long as the density and neutral fraction near the shock are not too high, the acceleration efficiency can be high enough in SNR shocks to produce the observed CR spectrum [82].

Raymond et al. [82] create a model for a cosmic ray precursor in a SNR shock, and study the effects of that precursor on the emission from the shock. In the precursor, gas is compressed and accelerated to a fraction of the shock speed. Neutrals only interact with the cosmic ray precursor through collisions with charged particles, since the electromagnetic fields responsible for charge acceleration do not affect them. For high densities in the precursor, neutrals and protons are tightly coupled through charge exchange, such that the neutral population will be compressed and heated along with the protons. This could lead to an abnormally broad ‘narrow’ Hα line (meaning one that is non-thermally broadened) in BDS emission, however for particularly high shock velocities and low densities, neutrals will interact seldomly with the precursor and the narrow line will be unaffected by the particle acceleration so measurement of a thermally-broadened narrow line does not rule out CR acceleration. The model also predicts that while protons and electrons are both strongly heated in models of effective charged particle acceleration, the proton heating will be much stronger than the electron heating. This skewing of the thermal equilibrium state would be noted in broad to narrow line ratios in BDSs. The model also predicts that emission from neutrals interacting with the precursor could lead to non-Maxwellian temperature profiles of the broad line. It may also lead to narrow line velocity offsets with respect to the local ISM.

Helder et al. [44] observe a BDS in the northeastern rim of the remnant RCW 86, which is believed to be a core-collapse supernova remnant evolving into a stellar-wind-blown cavity. In this region, where the shock is believed to be expanding freely into the cavity, X-ray spectra are dominated by synchrotron emission, which indicates efficient particle acceleration. The broad Hα line width measurement gives a post-shock proton temperature of 2.3±0.3 keV.

Using *Chandra* X-ray observations from 2004 and 2007 to measure the proper motion of the shock, and assuming a distance based on previous measurements of 2.5 kpc, the shock velocity is measured to be $(6.0\pm2.0)\times10^3$ km/s. The shock velocity and post-shock temperature are highly correlated, and the measured shock velocity implies a post-shock temperature of between 42-70 keV depending on the extent of thermal electron-ion equilibrium. This is larger than the BDS-determined proton temperature by a factor of at least 18. Helder et al. [44] interpret this factor of 18 discrepancy as an indication that a fraction of the energy behind the shock is devoted to acceleration of cosmic rays rather than heating of the post-shock plasma. Using these measurements they predict that greater than half of the post-shock pressure is due to cosmic rays.

Ghavamian et al. [38] use the broad and narrow Hα lines from four remnants to determine proton temperature to electron temperature ratios and shock velocities. The broad component width is used to constrain the range of shock speeds for each filament, then the ($\mathrm{T}_e/\mathrm{T}_p$) and shock velocity values are fine-tuned to match the observed broad-to-narrow flux ratio. When plotting the electron to proton temperature ratio versus shock velocity, the authors note that for shock speeds below ∼400 km/s electrons and protons are quickly equilibrated at the shock front, but that for shock speeds above ∼400 km/s ($\mathrm{T}_e/\mathrm{T}_p$) declines rapidly to values consistent with mass-proportional heating (minimal equilibrium) following $(T_e/T_p) \propto v_s^{-2}$. They present a model of Bohm-like CR diffusion with CRs generating waves upstream of the shock that reproduces the observed trend.

Other observations have shown hints of cosmic ray indicators. Tycho has shown non-Maxwellian broad line shapes and offset narrow Hα lines [82], and SN 1006 has shown varying levels of indication of particle acceleration at BDSs in various locations throughout the remnant [46].

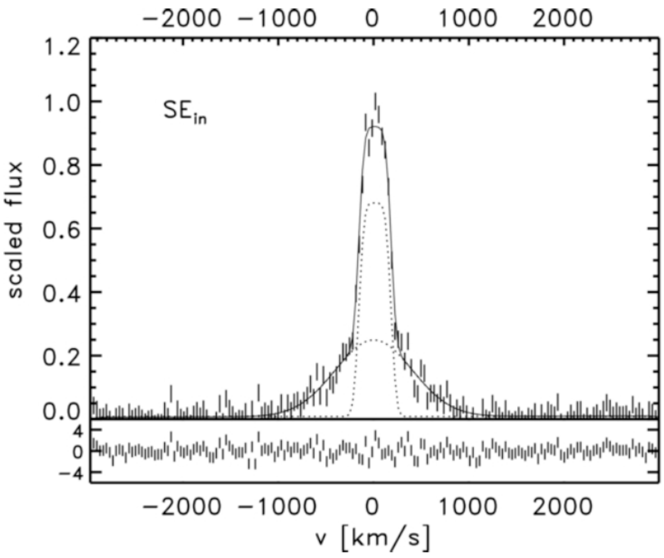

Figure 1-3: Spectrum extracted from an observation of the Southeast Hα filament of SNR RCW 86 observed with the VLT/FORS2 showing the narrow and broad line components of Hα emission. Reprinted from [44].

1.5.4 Observations of Balmer-Dominated Shocks in SNRs

I described some of the first observations of BDSs in Supernova Remnants (SNRs) in Section 1.5.1. Since the explanation of their origins in 1980 [19], a field of study has blossomed from observations of faint optical filaments around predominantly Type Ia SNRs (though BDSs have been identified in core collapse SNRs like RCW 86). BDSs, traditionally found around historical SNRs (those recent enough to have been recorded), tend to have ∼200-9000 km/s shocks (the high velocity shock produces nonradiative plasma conditions just behind the shock front), and occur where the shock is overtaking ISM with a density ∼0.1-1 cm^{-3} [46]. The Hα line from RCW 86 as measured by Helder et al. [44], and is shown in Figure 1-3, along with their gaussian broad and narrow line fits. I have compiled the results of broad line width and broad to narrow line ratios measured in several SNRs in Table 1.1, where I have attempted to include the most recent measurements available. Multiple entries for the same SNR in the table indicate measurements at different locations in the same remnant. Lines indicate information that was not given in the respective references.

Table 1.1: A compilation of measurements of BDSs in various supernova remnants. Measurements shown are the most recent published. Multiple entries for a single remnant denote measurements of several shocks throughout the remnant.

Remnant	W_{broad} (km/s)	I_b/I_n	Citation
SN 1006	2310 ± 210	0.73 ± 0.06	[61]
Tycho	1800 ± 100	1.08 ± 0.16	[61]
Kepler	1750 ± 200	1.1 ± 0.25	[33]
Cygnus	262 ± 32	0.59 ± 0.3	[37]
RCW 86	660 ± 90	1.0 ± 0.2	[66]
RCW 86	562 ± 18	1.18 ± 0.03	[37]
RCW 86	1100 ± 63	–	[44]
SN 0519-69.0	2800 ± 300	0.4-0.8	[101]
SN 0519-69.0	1300 ± 200	–	[96]
SN 0505-67.9	580 ± 70	≥ 0.7	[96]
SN 0548-70.4	760 ± 140	1.1 ± 0.2	[96]

The pertinent details and interesting features of these remnants are described below:

SN 1006: Along with Tycho, SN 1006 touched off the search for an explanation for the lack of forbidden lines and the presence of the narrow and broad Hα lines in supernova remnant spectra after Schweizer and Lasker[88] observed it in 1978. It is the only instance of a spatially resolved SNR where both efficient and inefficient sites for particle acceleration have been identified.

Tycho: Also known as the remnant of SN 1572, Tycho was observed by Kirshner and Chevalier [60] in 1978, leading to the formation of the theory of BDSs by Chevalier and Kirshner [18] and Chevalier and Raymond [19]. Smith et al. [96] studied several locations throughout the remnant and found significant variations between various Hα filaments.

Kepler: BDSs were originally discovered along the northern rim of the Kepler SNR by Fesen et al. [33] in 1989. Additional observations by Blair et al. [10] in 1991 identified radiative, transitional, and non-radiative filaments in different locations throughout the remnant.

Cygnus Loop: BDSs in the Cygnus loop were first identified by Raymond et al. [81] in 1983. In 1985, Fesen and Itoh [31] studied the remnant and found that the N II and S II lines were weak, but present ($\sim$ 2-5% of the Hβ flux). They noted that the N II and S II intensities were an order of magnitude larger than the nonradiative model predictions, and hypothesized that the N II and S II emission was a result of some radiative component within the filament, or reflected light from nearby filaments of NGC 6992. In 2001, Ghavamian et al. [37] studied the remnant and noted that their measurements required nearly complete electron-ion equilibration in the post-shock plasma.

RCW 86: This remnant has been extensively studied and is one of the only core collapse SNRs found to exhibit BDSs. It was originally studied by Long and Blair [66] in 1990, then later by Smith [95], who mapped the Balmer-dominated filaments and argued that they provide a more accurate picture of the blast wave than radiative filaments. Ghavamian et al. [37] observed a different region than Long and Blair[66] and Smith [95] in 2001, and in 2009 Helder et al. [44] observed yet a different region, and suggested that a significant portion of the blast wave energy leads to acceleration of cosmic rays.

SNR 0519-69.0: Touhy et al. [101] observed SNR 0519-69.0 in the LMC in 1982, identifying it as the first SNR hosting BDSs to be discovered outside of the galaxy. Smith et al. [96] followed up in 1991, observing a different BDS in the same remnant.

SNR 0505-67.9 and *SNR 0548-70.4* were observed by Smith et al. [96] as part of a survey of several SNRs hosting BDSs in 1991. The authors were only able to identify one location with a broad Hα line in each. All other locations in the SNRs exhibited radiative emission.

SNR 0509-67.5 was identified by Touhy et al. [101] in 1982, as hosting a BDS on the basis of strong Hα emission and a lack of O III emission, however a broad line has not been observed.

SNR 1987A: Observations of SNR 1987A by Michael et al. [74] make a controversial identification of a BDS moving at nearly 12,000 km/s. The source of the neutrals appears to be from the ejecta rather than from ISM.

In Chapter 2, I describe imaging and spectroscopy measurements of the galactic, core-collapse SNR G296.1-0.5 in search of BDSs.

1.6 Charge Exchange Signatures in the X-ray Band

Since supernova remnants provide an environment where hot, shocked material runs into cold, unshocked, neutral material, some amount of charge exchange is expected to occur. Supernova remnants are often bright in the X-ray because of the high temperatures caused by strong shock heating. X-ray emission from charge exchange in SNRs is expected because of the H-, He- and Li-like ions commonly observed in SNR shocks. Charge exchange emission is line emission with no continuum component. This emission, combined with the continuum and line emission from other processes makes up the spectra we observe from these objects. While much work has attempted to observe charge exchange emission in the X-ray regime in SNRs, it is difficult to prove conclusively without access to higher energy resolution observations of these sources. The current standard technology for observations and spectroscopy of extended sources like SNRs are Charge Coupled Device (CCD) detectors like the ACIS on *Chandra*, EPIC on *XMM-Newton*, and XIS on *Suzaku*. However, these only provide moderate spectral resolution. Dispersive optics can provide high energy resolution spectra of point sources, however are not well-suited to observations of extended objects. The Reflection Grating Spectrometer (RGS) on *XMM* is better suited to observations of extended sources than the High Energy Transmission Grating (HETG) on *Chandra* so for sources for which dispersed spectra can offer some improvement over CCD spectra, the RGS is often used to provide moderate resolution spectroscopy.

There are several classifications of plasma states based on the dominant processes occurring in the plasma and its equilibrium state. Porquet et al. [80] reviews details of several types of plasmas expected to be found in astrophysical systems. I will give a brief overview of each of them, then focus on the charge exchange in the non-equilibrium plasmas common in supernova remnants.

Collisional Ionization Equilibrium (CIE) plasmas are those where ionization is mostly due to electron-ion collisions and atomic levels are populated by electron impact. They are generally (though not always) optically thin to their own radiation and assumed to have no external radiation field affecting their ionization balance. This plasma state is often observed in stellar coronae, galaxy clusters, the hot intra-cluster medium, in the Galactic ridge, and in the Galactic center.

Recombination Dominated/Photo-Ionization Equilibrium (PIE) plasmas are those where ionization is due to photons and atomic levels are populated by radiative recombination. These are generally overionized with respect to the local electron temperature and have much lower electron temperatures than similar CIE plasmas. This plasma state is often observed in active galactic nuclei and X-ray binaries.

Non-equilibrium Ionization (NEI) plasmas are those that depart from ionization equilibrium because of a sudden change in physical conditions like temperature, density, or incident radiation. This plasma state is often found in rapidly changing physical systems like supernova remnants, solar flares, colliding winds in star clusters, X-ray binaries, galaxy clusters, and merging galaxy clusters, especially where shocks have occurred. A plasma will remain in NIE as long as the timescale of changes in temperature or other plasma parameters is shorter than the equilibrium timescale. There will likely be many active processes occurring in a non-equilibrium plasma driving it towards equilibrium (CIE), each of which has a different timescale. For instance, the timescale for high temperature electron excitation is shorter than the timescale for electron collisional ionization, which is shorter than the timescale for recombination. The timescales for ionization and recombination depend on the density of the plasma, so the time to equilibrium will depend on the plasma density. The evolution of the NEI plasma towards CIE can be characterized by the ionization age (the plasma density multiplied by the time since the plasma has been shocked). Typically hot NEI plasmas have ionization ages $n_e t \lesssim 10^{10} - 10^{13}\text{cm}^{-3}\text{s}$, after which the plasma will reach a state of CIE.

1.6.1 Line Ratio Diagnostics

In order to identify charge exchange emission, we require some characterization by which to distinguish it from other sources of emission. Porquet et. al [80], review the use of He-like emission line triplets as plasma diagnostics. H-like (containing only one electron) and He-like (containing only two electrons) emission lines are some of the more prominent spectral features in the X-ray band. This is partially due to the closed-shell ground state of He-like ions, which makes them abundant over the widest range of temperature of any ionization state in collisional plasmas.

Transitions between the n=2 state and n=1 state are typically the most intense He-like lines observed in X-ray emitting plasmas. A triplet of emission lines can result from various n=2 to n=1 transitions. The resonance line (denoted R or w) is an electric dipole transition: $1s2p^1P_1$–$1s^{21}S_0$. The forbidden line (denoted F or z) is a relativistic magnetic dipole transition: $1s2s^3S_1$–$1s^{21}S_0$. The intercombination line (denoted I or x and y) is made up of two lines: a magnetic quadrupole transition (x) that is only significant for He-like ions heavier than S XV $1s2p^3P_2$–$1s^{21}S_0$ and an electric dipole transition (y) $1s2p^3P_1$–$1s^{21}S_0$, which is achieved through a spin-orbit coupling from the ${}^3P_1$ state to the ${}^1P_1$ state followed by an electric dipole transition from the ${}^1P_1$ state to the ground state. The weakness of the spin-orbit coupling between the triplet P state and the singlet P state that precipitates the otherwise forbidden spin-flip transition required to produce the intercombination line accounts for the relative weakness of the observed y line with respect to the observed w and z lines. An atomic level diagram with these transitions labelled is shown in Figure 1-4.

Ratios of these line intensities can be used to determine the electron temperature and density in the plasma. The use of these line intensity ratios was introduced by Gabriel and Jordan in 1969 [35] for the study of the stellar corona and have been used in C V- S XIII ions in stellar coronae, solar system objects, X-ray binaries, supernova remnants and active galactic nuclei (Fe lines would provide very useful diagnostics for plasmas with higher temperatures and densities, however they cannot be resolved with current spectroscopy). The two diagnostic ratios suggested by Gabriel and Jordan [35] are given in Equations 1.8

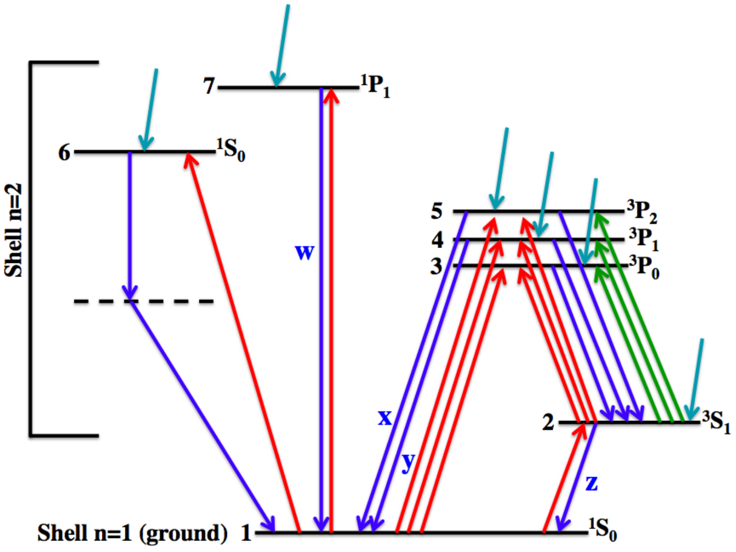

Figure 1-4: A level diagram for He-like ions reproduced from a similar figure in [80]. Radiative transitions (resulting in the release of a photon) are shown in blue, recombination and cascade processes are shown in teal, electron collisional excitations are shown in red, and photo-excitations are shown in green. The transition from the n=2 $^1S_0$ state to the n=1 $^1S_0$ state is a two-photon transition.

and 1.9. As implied in the equations, $\mathcal{G}$ is more sensitive to the electron temperature of the plasma and $\mathcal{R}$ is more sensitive to the electron density in the plasma.

$$\mathcal{G}(T_e) \equiv \frac{F+I}{R} \tag{1.8}$$

$$\mathcal{R}(n_e) \equiv \frac{F}{I} \tag{1.9}$$

In order to distinguish CX line emission from various atomic processes that populate and depopulate the atomic levels of He-like ions, we must first understand those processes, and the conditions that determine their relative strengths.

Collisional excitation inside He-like ions occurs when a projectile electron hits a He-like ion, causing either direct excitation of an electron in the ion or exchange of an electron from the ion with the projectile electron into an excited state of the ion. This process is more efficient at higher temperatures and can also result from the impact of a projectile proton or alpha particle for high Z ions at very high temperatures.

Recombination from H-like to He-like ions occurs when an electron is captured by a H-like ion through either radiative recombination (efficient at low temperatures) or dialectric recombination (efficient at high temperatures). This process favors population of the $^3P_1$, $^3P_2$, and $^3S_1$ states, leading to higher intensity F or I lines depending on the density of the plasma, increasing $\mathcal{G}$.

Inner-shell ionization of Li-like ions (those with three electrons) occurs when an electron from an inner shell of a Li-like ion escapes due to excitation. This process can significantly enhance the strength of the F line, which will increase both the $\mathcal{G}$ and $\mathcal{R}$ ratios. For inner-shell ionization to occur in Li-like ions, the ionization rate must be large (requiring a high temperature plasma) and there must be a high ratio of Li-like to He-like ions, which would be indicated by strong Li-like satellite lines. This is not satisfied in CIE plasmas but can be satisfied in NEI plasmas. This process can be especially significant in high-Z ions.

Photo-excitation is excitation of an electron due to an incident UV photon. This process is important at moderate radiation field temperatures for low Z ions like C V, N VI, and O VII, and for higher temperature radiation fields for high-Z ions. Atomic levels will be populated preferentially by different temperature radiation fields. As the temperature of the radiation field increases, the intercombination line will become stronger, leading to a decrease in the $\mathcal{R}$ value and an increase in the $\mathcal{G}$ value.

Charge Exchange, as discussed earlier, occurs when a highly charged ion collides with a neutral atom, transferring one or more electrons to the ion in an excited state. Though neutral fractions are fairly small in high temperature plasmas, the charge exchange cross section is quite high (a factor of 10^5 higher than the cross section for collisional excitation by an electron) such that charge exchange can be significant in certain situations. The level into which the electron is captured depends on the nature of the incident hot ion (Z and ionization state), the neutral target, and the velocity of the collision. However roughly three quarters of the captures of electrons by H-like ions producing He-like ions are made into

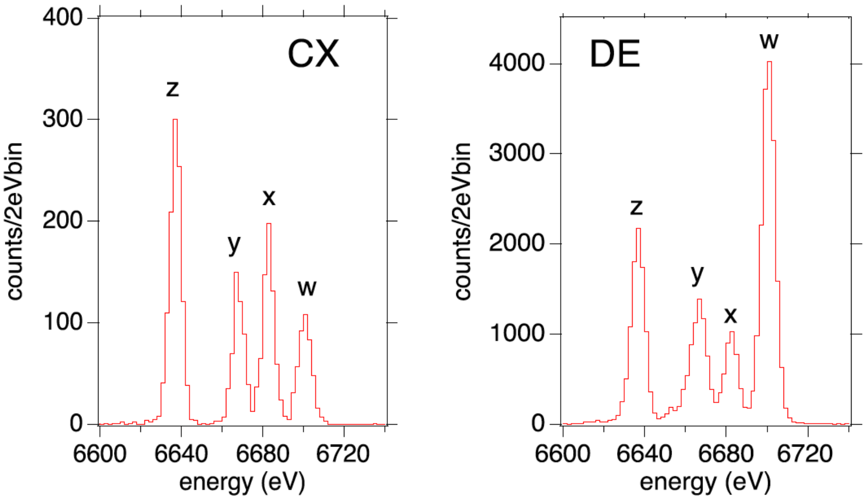

Figure 1-5: EBIT measurements of the spectra of Fe XXV for charge exchange between Fe XXVI and N_2 (left) and for direct electron collisional excitation (right) demonstrating the different line ratios produced by different atomic processes. Reprinted from [14].

the triplet states, leading to a significantly enhanced F line, enhancing the $\mathcal{G}$ ratio. Figure 1-5 shows EBIT spectra from plasmas undergoing electron impact excitation and charge exchange, demonstrating the shift in line ratios. Porquet et al. [80] note that even with low resolution spectral data, a shift in the centroid of a He-like ion triplet that has been blurred into a single line by the instrument resolution towards the F line centroid could be indicative of charge exchange.

Photon propagation effects can also affect observed line ratios. Resonance line scattering, in which the resonance line is preferentially scattered out of the line of sight when propagating through a plasma of high enough optical depth, can lead to enhanced $\mathcal{G}$ ratios.

In a non-equilibrium plasma, the line intensities of He-like ions will vary with time, indicating the impact of different atomic processes as the plasma evolves through various ionization states.

In order to predict line ratios in various plasma states, it is important to build a good atomic model with accurate atomic data for a wide range of ionization states. Smith et al. [97] find that the He-like lines from the n=2 state are affected by the presence of H-like ions in excited states up to n=10. A plot of the $\mathcal{G}$ ratio versus temperature calculated with

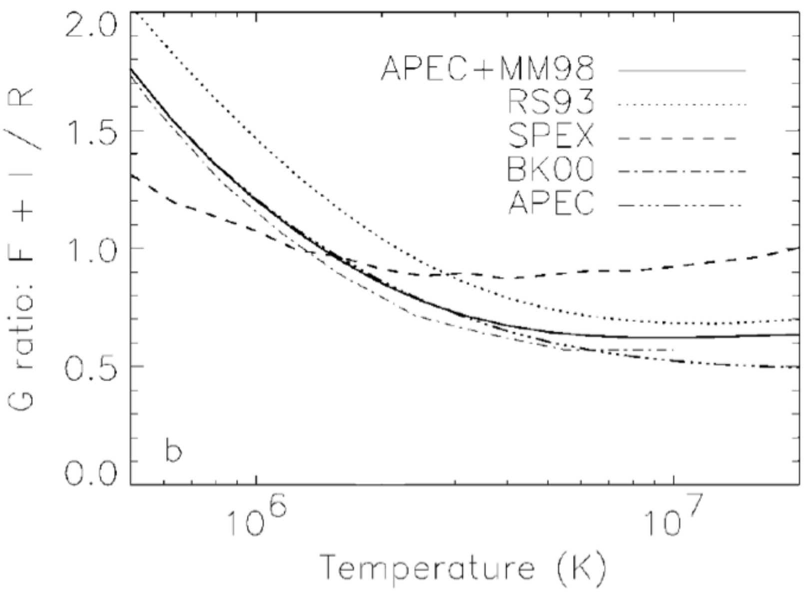

Figure 1-6: The calculated $\mathcal{G}$ ratio vs. electron temperature calculated with various atomic packages. Reprinted from [97].

various atomic packages is shown in Figure 1-6. These models should be (and are in most cases) checked against Tokamak and EBIT data in accessible regions to verify their efficacy.

Spectral resolution in the X-ray regime is a huge hurdle in performing line ratio diagnostics on extended sources. I will describe several studies fitting line ratios to lower resolution data combined with other diagnostics to attempt to diagnose the plasma state, however these types of diagnostics have large uncertainties. Not only would increased spectral resolution improve the measurements of the F, I, and R lines and their strengths, but it would also allow resolution of satellite lines. These are lines that appear very close to or blended with lines of He-like ions. They are formed by dielectronic recombination and inner-shell excitations by electrons or photons. Most importantly, the intensity ratios of satellite lines to the resonance line provides a very sensitive measure of electron temperature and ionic fractions. Ideally, line ratio calculations for lower resolution data should take into account the blending of these lines into the triplet lines. This will have a larger effect at high Z values. Once microcalorimeter data are available for extended sources, line ratio diagnostics will become an even more powerful tool for diagnosing plasma states in SNRs.

1.6.2 Calculating Expected Charge Exchange Flux

There are several spectral features that imply significant charge exchange contribution to the emission from a particular system. These include anomalies in derived abundances of elements when using a thermal model that does not include charge exchange (expected because charge exchange produces only line emission so a thermal model will need enhanced abundances to provide the additional line emission) and the line ratio anomalies discussed in the Section 1.6.1. Other evidence of active charge exchange includes tight spatial correlation between Hα emission and X-ray emission. Excluding charge exchange, this is not generally expected because plasma temperatures leading to X-ray emission generally also lead to completely ionized hydrogen populations and the particle acceleration that leads to X-ray synchrotron emission is damped by the presence of neutral hydrogen.

Data from the *Chandra* and *XMM* satellites have allowed several sources to be investigated for these signs. It is also useful to make some approximation of the expected CX flux to compare with measurements and plan future observations with higher resolution instruments. Lallement [64] performs these types of calculations for several different systems. I will follow those calculations here to provide additional insight as to the physical picture and requirements of charge exchange systems, and the variables that affect the emission we measure.

As I have discussed, charge exchange can take place in any location where hot plasma impacts on partially neutral gas. This requires that the impacted gas has not been completely ionized by the shock precursor, associated cosmic rays, or other photo-ionizing sources. More specifically, charge exchange will take place where neutrals can diffuse into the hot gas layer deep enough to encounter hot ions. Figure 1-7 is a diagram of a shock front with a charge exchange region where neutrals can penetrate the hot shocked gas far enough to encounter a hot ion. The length scale of this diffusion is set by the relative velocity of the components and the timescale for destruction of the neutral. This timescale is set by either the time before the neutral is destroyed through charge exchange with hot protons/ions or the time for the neutral to become ionized by electron impact, whichever happens more quickly. Thus,

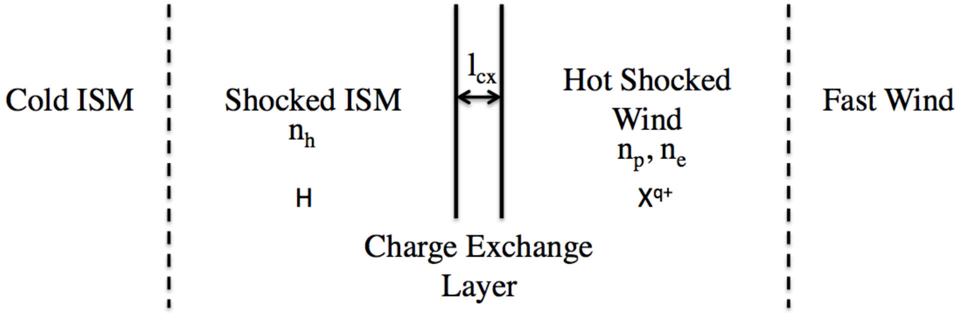

Figure 1-7: A diagram of the conduction front where cold neutrals mix with hot ions. Charge exchange will only occur in a thin layer at the interface of hot ions and cold neutrals.

the estimated thickness of the charge exchange layer is given by the smaller of the mean free paths for charge exchange and collisional ionization.

We define ϵ as the ratio of the probability of charge exchange to the probability of collisional ionization for any given neutral in the charge exchange layer. An expression for ϵ in terms of plasma and shock parameters is given in Equation 1.10 where σ is the proton-Hydrogen charge exchange cross section, n_p is the proton density in the hot plasma, V_r is the relative velocity between the hot plasma and cold neutrals, q is the charge of the ions in the hot plasma, and n_e is the electron density in the plasma.

$$\epsilon = \frac{\sigma n_p V_r}{q n_e} \tag{1.10}$$

For a neutral hydrogen atom, ϵ can range between 0.1-50 for relative velocities of 100-1000 km/s and plasma temperatures of $10^5 - 10^7$ K. This corresponds to a charge exchange layer with thickness between 0.001-5 pc. In these calculations, the neutral and plasma density profiles across the interface are not modeled, rather it is assumed that ion relative abundances are the same everywhere in the hot gas in the interaction region. For simplicity of calculations Lallement [64] defines the thickness of the charge exchange layer to be the mean free path for charge exchange l_{cx}, then scales the neutral density in the region by ϵ to effect the change due to the interaction rates such that the neutral density in the charge exchange layer is given by ϵn_h.

For fast shocks like those in SNRs, nearly all of the neutrals streaming into the charge exchange region will CX before being ionized because epsilon is high. It should be noted that the estimation of the thickness of the charge exchange layer as the mean free path of an initial charge exchange event may underestimate the amount of charge exchange occurring since hot neutrals produced due to an initial charge exchange event may undergo additional charge exchange, and their mean free path is much larger than a cold neutral.

We now consider a cold neutral gas of density n_h and thickness l_{cx}, with a hot gas flow of flux $\phi_w = n_p V_r$ streaming through it (n_p is the hot gas density and V_r is the relative velocity between the neutral gas and the hot gas). To estimate the X-ray emission due to charge exchange in this layer, we will calculate its volume emissivity P_{cx}. By comparing this with the volume emissivity of the thermal emission from the hot plasma, taking into account our line of sight through the emission regions for both, we can estimate the importance of CX emission in the overall spectrum. The charge exchange volume emissivity will be proportional to the neutral density n_H, the amount of hot gas streaming through the neutrals, and Σ_x, the global emissivity cross section for charge exchange between neutral hydrogen or helium and any hot ions capable of producing X-rays in hot plasma.

Σ_x encapsulates the physics of cascades and the relative abundances of various ions, and is equal to the average X-ray emission per neutral H atom for a hot gas proton flux of unity. Σ_x has been measured for the hot gas in the solar wind yielding $\Sigma_0 = 6 \times 10^{-19}$ keV cm^2. Since the ion content, temperature, and metallicity will be different in an SNR hot plasma than in the solar wind, we take $\Sigma_x = \alpha\Sigma_0$. In this way we get the total CX volume emissivity, given in Equation 1.11.

$$P_{cx} = \Sigma_0 \epsilon \alpha n_h \phi_w = 6 \times 10^{-19} \epsilon \alpha n_h \phi_w \, \mathrm{keV cm^{-3} s^{-1}} \tag{1.11}$$

Lallement [64] gives the hot gas volume emissivity as the expression in Equation 1.12 in units of keV cm^{-3}s^{-1}, where $\chi(T, a)$ accounts for the ratio between the hot gas volume emissivity at temperature T and metallicity a (where a is in units of solar abundance) and the hot gas volume emissivity at T=10^6 K and a=1.

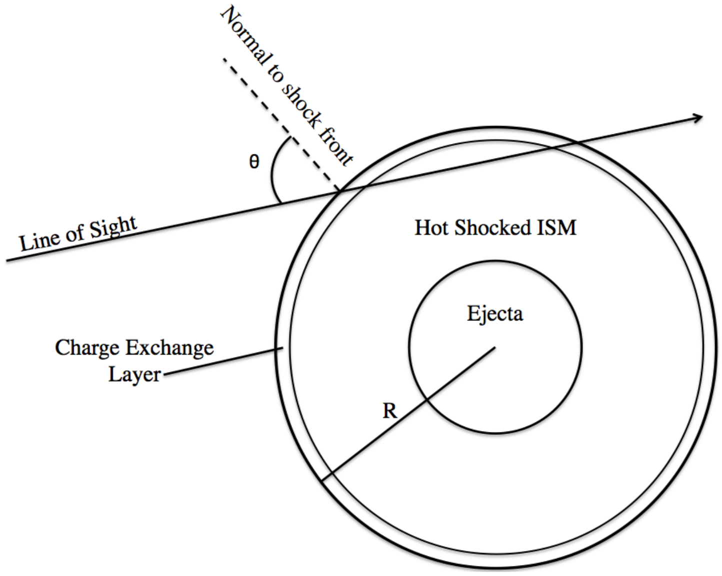

Figure 1-8: A diagram of the SNR with the charge exchange layer of thickness l_{cx}, blast radius R, line of sight, and θ (the angle between the line of sight and the normal to the blast wave) labelled. The thickness of the charge exchange layer has been exaggerated for effect. In most SNRs the charge exchange layer is only a small fraction of a percent of the blast wave radius.

$$P_h = 5.8 \times 10^{-14}(n_e^2)\chi(T,a)\,\mathrm{keV cm^{-3} s^{-1}} \tag{1.12}$$

So, the ratio between the charge exchange and hot gas volume emissivities is given in Equation 1.13.

$$\frac{P_{cx}}{P_h} = 10^{-5}(\epsilon\alpha\chi^{-1})\frac{n_h}{n_e}V_r \tag{1.13}$$

In order to obtain the ratio of emission from the charge exchange and thermal components, we have to take into account our line of sight through the emitting material. Figure 1-8 defines θ, the angle between the line of sight and the normal to the (assumed) circular shock front. For lines of sight that are not edge-on to the shock front, the line of sight crosses the charge exchange region twice, giving a line of sight distance through the charge exchange layer of $L_{cx} = 2l_{cx}\cos(\theta)^{-1}$. For an edge-on line of sight, the distance through the charge exchange layer will be $L_{cx} = 2\sqrt{2Rl_{cx} - l_{cx}^2}$. The thickness of the charge exchange layer is given by the mean free path for charge exchange, which is approximately $l_{cx} \approx \frac{1}{\sigma n_h}$. For a blast wave of radius R, the line of sight distance through the hot gas will be $L_h = 2R\cos(\theta)$. This gives us the ratio of line-of-sight-integrated emissivities given in Equation 1.14, in the case of a non-edge-on line of sight.

$$\frac{P_{cx}L_{cx}}{P_hL_h} \approx \frac{10^{-5}\epsilon\alpha V_r}{R\cos^2(\theta)\chi\sigma n_e} \tag{1.14}$$

Finally, to assess the contribution of charge exchange with respect to the contribution of thermal emission, Lallement plugs in approximate numbers from a representative system: DEM L71, a type I SNR $\sim$ 4000 years old, with a shock velocity of about 1000 km/s leading to V_r $\approx$750 km/s, an outer blast wave radius $\approx$ 8pc, a hot gas density of n_e=2 cm^{-3} and temperature of T=4×10^6K, expanding into a partially neutral medium with $n_h \sim 0.5$cm^{-3}. α and ϵ are taken to be 1 and χ^{-1}=2.5. A good value for σ for relative velocities between 100-1000 km/s is 1×10^{-15}cm^2. For a line of sight angle of 72°, there is a factor of 10 more thermal emission than CX emission. In fact, for the levels of emission to be comparable requires $\theta \geq 82°$. For a completely edge-on line of sight charge exchange emission is roughly 400 times the strength of thermal emission. So charge exchange emission can be significant, however the line of sight must be nearly edge-on to the shock and the majority of lines of sight do not result in CX emission that is significant with respect to the strength of thermal emission.

It is important to note that this calculation is an upper limit, applying to light elements and low charge states. The assumption is also implicitly made that the gas behind the shock is immediately heated to the post-shock temperature, along with assuming electron-ion equilibration behind the shock, which is not the case in detailed models. Taking these parameters into account tends to lower the CX contribution, resulting in a maximum charge exchange emission of about a factor of ten below the amount of thermal emission, which could still measurably affect measured spectra.

1.6.3 Charge Exchange Measurements in SNRs

Several SNRs have been studied with the goal of identifying charge exchange emission in the X-ray band. Because of the limitations of the data as far as energy resolution, none of these studies provides conclusive evidence of CX emission, but rather point to its feasibility. Katsuda et al. [58] use *XMM*-RGS spectral observations of the bright eastern knot in Puppis A. With the enhanced resolution of the Reflection Gratings Spectrometer (RGS), the forbidden and resonance lines can be somewhat resolved. The authors perform a fit of a Bremsstrahlung continuum model plus several gaussians to measure the line strengths and derive F/R ratios for each of the He-like ion lines from the data. They derive F/R ratios for thermal model values by measuring the line ratios of plausible plane parallel shock (`vpshock`) models with plausible values derived from plasma model fits to CCD spectra throughout the remnant. They find several of the He-like ion F/R ratios are anomalously enhanced when compared to the plasma model F/R ratios for O, N, and Ne. The authors rule out resonance-line scattering, inner shell ionization of Li-like ions, and H-like to He-like recombination as causes of the anomalous F/R ratios, and perform a calculation similar to that in the previous Section, to obtain an order of magnitude estimation of the CX flux showing that CX is a plausible cause for the anomalous line ratios.

Van der Heyden et al. [107] study spectra of DEM L71, a type Ia SNR in the LMC, with the *XMM*-RGS. They find that the temperature and ionization age predictions based on O VII F/R line ratios vary significantly in the outer shell of the remnant. The ratio in the shell is found to be anomalously higher than a thermal NEI plasma F/R ratio for plausible plasma parameters. They hypothesize that the anomalous ratios are caused by either recombination, resonance-line scattering, or some combination of the two. They do not consider charge exchange as a possible cause, but considering the location of the anomalous ratios in the outer blast shell, CX could also provide a plausible explanation for these observations.

Broersen et al. [13] study the core collapse SNR 0506-68 using the *XMM*-RGS. They find the O VII F line to be stronger than predicted by an NEI plasma model that describes the R line well. Utilizing observations from 2000 and 2002, they find that the F/R ratio is larger in the 2002 observation than in the 2000 observation, though the total triplet flux is similar between the two. They derive a $\mathcal{G}$ ratio of 0.87 ± 0.09 for the observation in 2000 and a $\mathcal{G}$ ratio of 1.19 ± 0.09 for the observation in 2002. The authors attribute the anomalously high F/R ratio as evidence of a recombining plasma moving toward equilibrium, however do not find evidence of a recombination edge that would be a smoking gun to prove that hypothesis. They state that resonance line scattering cannot be ruled out, but do not consider charge exchange as a possible mechanism to produce the anomalous ratio.

Katsuda et al. [57] describe analysis using a *Suzaku* XIS CCD observation of the Cygnus Loop SNR. The authors argue for the presence of CX emission in the X-ray band. Fitting pure thermal models to the CCD spectra of several locations in the rim of the remnant yields depleted abundances around 0.2 of solar, however some narrow regions along the outermost region of the rim show 'enhanced' abundances near 1 solar. The authors suggest that these enhanced abundances may be the result of the plasma fit not including CX emission and therefore misdiagnosing the plasma state. This assertion is supported by the fact that the 'enhanced' regions show much stronger emission in the K-shell lines from O and Ne, whereas the complex of Fe-L shell lines are of comparable magnitude to the thermal model. The original, thermal-only fits for the 'enhanced' regions were much worse than those for normal regions. By ignoring the K-shell region for O (0.68-.76 keV) a significantly better fit is found, with abundances agreeing with the 'normal' regions in the surrounding area. This implies that the difference between the two types of regions is due to line emission that could be attributed to charge exchange rather than thermal emission, which contains both line emission and a continuum component. Being able to resolve other triplets in the spectrum, which requires a higher energy resolution detector like a microcalorimeter, will be essential to prove CX emission in Cygnus, [57].

Chapter 2

Magellan Observations of G296.1-0.5

2.1 Supernova Remnant G296.1-0.5

2.1.1 Initial Detections

G296.1-0.5 is a bright galactic supernova remnant located in the Carina Spiral arm (which extends over a distance of about 2-10 kpc along our line of sight). G296.1-0.5 has been detected and studied in the radio, optical, and X-ray bands. It was initially observed in the radio band by Clark et al. [21], [22], who made surveys of the Southern sky at 408 MHz with the *Molonglo Cross telescope* and at 5000 MHz with the *Parkes 64 meter telescope*, both of which produced high resolution contour maps of surface brightness with approximately 0.5' positional accuracy. The remnant is designated G296.0-0.6 by [21] and G296.1-0.7 by [22]. In the survey, Clark et al. identified 28 previously unknown supernova remnants, characterizing sources as SNRs on the basis of non-thermal spectral indices α (defined by (flux density) $\propto$ (frequency)$^{\alpha}$), significant angular extent, proximity to the galactic plane, and a recognizable shell structure. In the case of G296.1-0.5, a well-defined shell of emission was detected at 408 MHz. Distance estimates from the measured surface brightness and size on the sky (using the Σ-D relation $\Sigma = AD^{\beta}$ posited by Clark and Caswell 1976 [20] to relate the measured surface brightness to the physical diameter of the remnant) give an estimate of about 8 kpc, though this type of distance estimate has been shown to be somewhat unreliable, producing estimates with errors up to a factor of 2-3 due to the large spread in possible diameters for a given surface brightness [42].

Optical nebulosity associated with the radio emission from G296.1-0.5 was first detected by Longmore et al. [67], during an optical survey searching of the sources in the Clark catalog. The survey used the *UK Schmidt telescope* IIIa-J plates for the ESO/SRC Southern Sky Survey. Filamentary emission was detected in the southwestern corner of the radio remnant while diffuse emission was detected along the northern and northwestern periphery of the radio remnant, including areas beyond the boundaries of the radio detection. While the optical and radio emission are clearly correlated, the locations of peak optical emission do not correspond exactly with the locations of peak radio brightness.

Longmore et al. also obtained optical spectra for three filaments in the southwest region of the remnant using the RGO Spectrograph and Image Photon Counting System mounted on the 3.9 meter *Anglo-Australian telescope* with a spectral resolution of about 0.8 Å. The spectra exhibit fairly strong collisionally excited S II lines ([S II]/Hα just over 1), indicating an SNR. The ratio of the two S II lines gives density estimates generally greater than 10^3 cm^{-3}, which vary on small scales. The S II, Hα, and N II lines have widths around 42 km/s FWHM, which are consistent with expectations for SNR emission, but far too high for an H II region. Longmore et al. make distance estimates using two different methods. Fitting the measured radial velocity to galactic rotation curves produces a distance estimate of 4 kpc, while comparing the expected reddening vs. distance to the observed Balmer decrement (Hα/Hβ=7.3$\pm$0.8) produces a distance estimate of 3$\pm$1 kpc, both of which imply a remnant diameter $\sim$17 kpc.

van den Bergh et al. [106] performed a similar optical survey of known radio SNRs using the red plates on the *Curtis Schmidt telescope* on Cerro Tololo to image a $\sim 12°$ wide strip along the southern Milky Way, complementing the blue-green spectral region studied by [67]. For remnants in particularly crowded fields, observations were made through Hα and S II filters on the 1.2 meter *Schmidt telescope* on Palomar mountain. Very faint filaments were detected in the red plate along the NW edge of the radio shell. Additional observations were made utilizing the blue plate, confirming the results of Longmore et al. [67] in identifying only bright portions of the remnant in the SW.

Hutchings et al. [49] observed faint diffuse X-rays to the NE of the observed optical and radio emission during a study of the nearby pulsars 2S 1145-619 and 1E 1145-6141 with the *Einstein*-HRI camera. They note the proximity of G296.1-0.5, but posit that it is not associated with the X-ray emission they detect.

Markert and Lamb [68] made the first definitive X-ray detection of G296.1-0.5 using the imaging X-ray IPC detectors on *Einstein* during a survey of a 1° square area with an angular resolution of about 1'. They detect diffuse emission of about 15' in diameter (about the same extent as the radio emission) roughly coincident with the peak surface brightness locations in the radio. They find no obvious correlation between the locations of the X-ray emission and previously detected optical emission, but note that the X-ray and optical emission are produced by different processes, and so would not necessarily be precisely correlated.

The authors also detect a nearly complete ring of diffuse X-ray emission with diameter 20'-25' to the north of the G296.1-0.5 emission, which does not correspond with emission detected in any other waveband. They classify this object as supernova remnant 1E 1149.4-6209 based on its morphology and the lack of time variation of its emission. Fits of spectra from the object to simple thermal models give temperatures $\sim 0.1 - 0.4$ keV and a column density around $1{\times}10^{21}\mathrm{cm}^{-2}$. The authors also find no evidence of interaction between this object and G296.1-0.5, leading them to conclude that they are simply superposed on the sky.

Brand et al. [12] detected CO emission in the direction of G296.1-0.5 during a 115 GHz survey of galactic emission and reflection nebulae on the 4 meter, mm-wave telescope at the Division of Radiophysics of CSIRO, Epping, NSW, Australia, which has a pointing accuracy better than 30" and a velocity coverage (due to the spectral capabilities of the survey) of about 230 km/s. The velocity centroid of CO emission in a particular location is calculated as the weighted average of velocities over the entire detection, weighting inversely with the noise of the component spectra. CO emission in the direction of G296.1-0.5 is found to have a radial velocity ~ -38 km/s, similar to Longmore's [67] measurement in the optical of ~ -35 km/s. The CO emission is interpreted as an H II region nearby the remnant.

Green et al. [41] search for maser emission from the satellite line of the hydroxyl radical OH at 1720.5 MHz using the *Parkes 64 meter telescope* in a survey of 75 SNRs. They find emission in 33 of those SNRs and argue that these features are masers, collisionally excited by the passage of the SNR shock through an adjacent molecular cloud. No detection of OH maser emission was made in or near G296.1-0.5.

2.1.2 A Unified Picture of G296.1-0.5

In response to the 1981 Markert and Lamb [68] detection of two overlapping SNRs, Caswell and Barnes [17] obtained a new map of the area in the radio at 408 MHz using the *Molonglo Cross telescope*, averaging the data from several days of observation. They detect an egg-shaped ring structure with an average diameter of 33', centered at 296.05°,-0.50°, whose overall appearance suggests a single object. This ring shows good correlation with all of the Markert X-ray emission, including the regions to the north.

Caswell and Barnes propose that the X-ray emission previously thought to be from two separate sources, G296.1-0.5 and 1E 1149.4-6209, is in fact from a single large diameter SNR, which they denote G296.05-0.5 (although the radio map cannot conclusively rule out two smaller overlapping objects). The brightest features in X-ray do not correspond with the brightest features in the radio, which is commonly observed in SNRs. A new distance estimate is calculated from the surface brightness of the larger radio emission, giving an estimate of 7.7 kpc.

In 1986, Bignami et al. [9] published an additional X-ray study of the region using *Einstein* and *EXOSAT* observations of the diffuse X-ray emission over a $\sim 1°$ region including both of the features identified by Markert and Lamb [68]. *EXOSAT* observations were made with the LE telescope using the CMA focal plane instrument and revealed a complex region including both point sources and diffuse emission. The *Einstein* observations were made with both the IPC and the HRI instruments, providing both a Gaussian-smoothed image and rough spectroscopy. Spectra from throughout the area are consistent with thermal emission of a source between 0.1-0.6 keV.

In order to evaluate the consistency of the spectrum throughout the large feature, Bignami et al. create an IPC pulse-height histogram for three image regions selected over the SNR. They find that all of the distributions were compatible with soft spectra with heavy interstellar absorption and that no significant differences in spectral shape existed across the region. This also implies that the distance to the emission regions is similar across the region. They also analyzed the 'hardness ratio,' defined as the ratio of 0.7-1.5 keV emission to 0.16-0.7 keV emission, across the image. The authors were unable to find significant variation on any size scale in the region. The authors also note that in the 1981 Markert et al. observation, a counter support rib in the *Einstein* Field of View (FOV) fell between the structures identified as separate SNRs, making it more difficult to see the connection between the two. They thus conclude that the combination of X-ray and radio data support the interpretation of the object as a single, large SNR with patchy surface emission rather than two separate, superposed SNRs. In the work since these papers, the emission across the entire area is considered to be a single, large remnant. Images of G296.1-0.5 in several bands are shown in Figure 2-1.

2.1.3 Characterization

Since the initial observations of G296.1-0.5, several studies have been performed in the X-ray band to characterize the remnant and its progenitor. Hwang and Markert [50] performed a detailed spatial and spectral analysis of the remnant with the *ROSAT*-PSPC, covering an energy band of 0.07-2.48 keV. The X-ray image is characterized by three bright lobes labelled N, S and SW by [50]. These correspond with the radio contours, however detailed features in the radio and X-ray bands are not well correlated. The strongest X-ray emission is in the northern lobe, which is very weak in the radio, while the brightest radio emission is in the southwestern lobe, where the X-ray is bright, but slightly offset from the radio emission.

Spectra from an elliptical region around each of the three lobes were extracted and fit

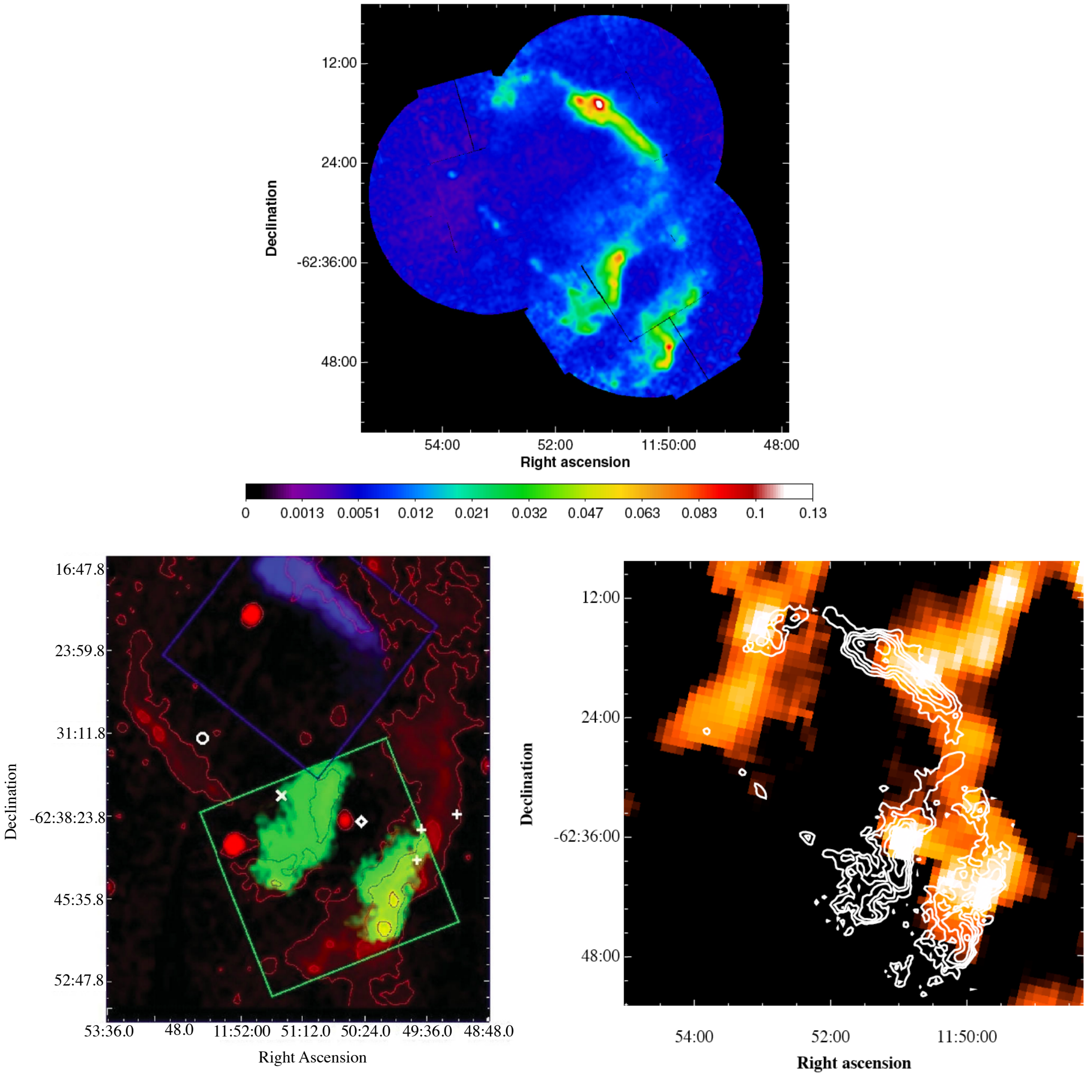

Figure 2-1: Top: The *XMM-Newton* EPIC MOS (X-ray) intensity map of G296.1-0.5 in the 0.3-3.0 keV band (Reprinted from [16]). The image (in units of photons $s^{-1}arcmin^{-2}$) is smoothed with a Gaussian of width 12". Pixel binning is 4". Bottom left: The radio image at 843 MHz (red) smoothed with a Gaussian with width 2" in units of counts s^{-1} with contours drawn at 0.02, 0.06, 0.10, 0.14, 0.18, and 0.22 counts/pixel. Blue and green squares show the two pointings of the XIS instrument on *Suzaku* used in [40]. The X-ray mosaic image from those pointings smoothed with a Gaussian with 2" width are shown in blue and green. Crosses show the location of the optical filaments identified by Longmore et al. [67], a diamond shows the location of the CO emission detected by Brand et al. [12], the x shows the location of thin filament Hα emission detected by Russeil and Parker [84], and the circle shows a location of diffuse Hα emission (Reprinted from [40]). Bottom right: Hα emission detected by the Gaustad et al. [36] Hα survey in field 033 in the intensity range 0-1000 Rayleigh, with *XMM* X-ray contours from [16] overlaid (Reprinted from [93]).

with models of an optically thin plasma in equilibrium ionization, absorbed by a column of interstellar hydrogen. Fits to all three lobes give high hydrogen column densities $\gtrsim 1.5 \times 10^{21}$, very low abundances ($\sim 3 - 8\%$ of solar) and low temperatures (kT$\sim$ 0.2 keV). Using the fit column density and estimated hydrogen density along the line of sight gives a distance estimate of 1.5-2 kpc, however the authors use the optically derived distance of 4 kpc for calculations since the measured X-ray and radio column densities are different by a factor of 10 and therefore not considered reliable. The fit is equally as good for a plasma with two components of different temperatures and solar abundances. This model is favored because the abundances required by the single-temperature fit are unrealistically low. The largest spectral differences between the regions was between the northern and southern lobes, where the temperatures and column densities were different by 10-15%. This is significant, however not large for variations across an SNR. For example, temperature is shown to vary by as much as a factor of four across the Puppis A SNR [120], [115].

The fit for the northern lobe is shown to be incompatible with fits for the southern and southwestern lobes to 99% confidence in kT and N_h. Using the Kolmogorov-Smirnov test, the authors determine that the spectra from the three regions are not derived from the same parent distribution to >99% confidence. Assuming the two temperature components are in pressure equilibrium, the authors calculate the estimated X-ray emitting mass in each of the three lobes: 13 $M_\odot$, 8 $M_\odot$, and 14 $M_\odot$ for the N, S, and SW lobes respectively. Density estimates for the high temperature plasma components are 1.5-2.5 cm^{-3}. Assuming that age is linearly proportional to size and taking into account the temperatures, the authors estimate an age of the remnant of about 20,000 years.

Castro et al. [16] use *XMM-Newton* EPIC and RGS observations of G296.1-0.5 in the X-ray to establish the evolutionary state of the SNR and derive properties of its progenitor. The EPIC image shows a partial elliptical shell with three distinct lobes of emission, similar to the morphology seen by [50] using *ROSAT* (the EPIC image is shown as the top image in Figure 2-1). They were only able to obtain RGS data for the northwest filament (the N filament from [50]) because of contamination from a flaring compact source near the southwest edge of the remnant. EPIC CCD spectra were extracted from several regions in the 0.3-2.0 keV range (above 2 keV the spectra are background-dominated). They apply an absorbed plasma model describing a non-equilibrium ionization plasma with variable abundances (`vnei`) to the EPIC data from several areas of the remnant. In the northwest, they fit a hydrogen column density $\sim 2\times10^{20}\mathrm{cm}^{-2}$ with a temperature around 0.6 keV, and ionization age $n_e t$ of 2-$4\times10^{10}\mathrm{cm}^{-3}$. The fits are similar in the southwest and eastern regions. The faintness of emission in the east makes significant conclusions about the plasma state difficult.

A high energy resolution RGS spectrum was obtained for a 2.8' wide strip on the NW limb, and was found to be suitably described by the fits to the EPIC CCD data in the region. These fits are significantly different than the equilibrium ionization fits made to the ROSAT data by [50] in both column density (which was high in [50] and is found to be quite low by [16]) and temperature (which is much higher in the [16] fits than in the [50] fits). There is very poor agreement between the [50] model and the [16] EPIC and RGS data. However, applying the [16] `vnei` model to the *ROSAT* data leads to a good fit with $\mathrm{N}_h \approx 8\times10^{20}\mathrm{cm}^{-2}$ and kT$\approx$ 0.35 keV. The low column density derived by the fits combined with the average hydrogen density along the line of sight of $\langle n_H\rangle \sim 0.03\ \mathrm{cm}^{-3}$, gives a distance estimate of $\sim$2 kpc, which is consistent with the optical measurement from [67] of 3±1kpc.

The fit abundances show that the X-ray emitting material is N-enriched and O-depleted. One possible cause of this is the CNO cycle in red supergiant (RSG) stars and the subclass WN of Wolf-Rayet stars. The CNO cycle is a process for the production of helium-4 from hydrogen, in which carbon, nitrogen and oxygen are used as catalysts being consumed and then regenerated [15]. During the Red Supergiant (RSG) phase, the mass loss rate is high and the terminal wind is slow ($<$ 100km/s). In the Wolf-Rayet (WR) phase, the stellar wind is several thousand km/s with a low mass loss rate. At the time of a SN, a low density wind bubble is expected to have formed with a shell of clumped wind at $\gtrsim$10 pc. If G296.1-0.5 were the result of a core-collapse SNR expanding into the late-stage wind of a $> 25\mathrm{M}_\odot$ star, the swept up shell material would be overabundant in N and underabundant in O. The circumstellar medium of stars in which the CNO cycle occurs is expected to have a nitrogen abundance in excess of 3 times solar values. This is not seen in the fits so the authors posit that some dilution of the CNO material must have occurred at some point.

Castro et al. propose an analytic model of the SNR expanding into an RSG wind to derive the swept-up mass, the diameter of the shell, the time of SN explosion, and the shock velocity. All of the derived values seem reasonable given the expectations of the model and the observations of the remnant. There is strong evidence for clumping in the winds of WR stars, and WR stars tend to be located in star forming regions, which is consistent with the environment of G296.1-0.5, so given this data, the abundances derived in the fits, and the success of the analytic model, the authors conclude that the remnant may be consistent with a WR progenitor.

Gök and Sezer [40] used the XIS instrument on *Suzaku*, a CCD detector, to observe G296.1-0.5 and perform spectral analyses. They extract spectra from four elliptical regions, each of the three X-ray lobes, which they label N, SE, and SW, and a region of weaker diffuse emission in the center of the remnant they label M. They note that the spectra of these regions are dominated by 0.3-2.0 keV emission (emission in the 2-10 keV range is too faint to be used in fits) and note that the K-shell lines from N, O, Ne, Mg, and Si are present in spectra from all four regions. The presence of silicon implies a contribution to the total emission by ejecta. They fit the regions with absorbed `vnei` models, and find that they require a two-component fit in the SW, but only a one-component fit for the other three regions.

In the N, SE, and M regions, fit temperatures are in the range 0.51-0.76 keV and ionization ages are in the range of $1.25 \times 10^{10} - 2.45 \times 10^{10} \mathrm{cm}^{-3}\mathrm{s}$, which are in agreement with the fits from [16]. The values obtained for ionization age imply a plasma far from equilibrium, as ionization equilibrium is expected to require $n_e t \gtrsim 10^{12} \mathrm{cm}^{-3}\mathrm{s}$. The fit abundances in the N and SE regions show O depletion and N, Ne, Mg, and Si overabundance (higher than solar values), implying that the plasma contains swept-up ISM with contamination from ejecta. In the M region both the abundance values and the errors on the values are higher than in the N and SE regions. In the SW, where a two-component `vnei` fit was applied, the lower temperature component required T$\sim$0.18 keV and $n_e t \sim 5.4 \times 10^{11}$cm^{-3}s with lower than solar O and N abundances, which the authors believe corresponds to ISM emission. The higher temperature component required T$\sim$ 0.84keV, with $n_e t \sim 1.7 \times 10^{10}$cm^{-3}s and an overabundance of Ne, Mg, and Si, which the authors believe corresponds to a clump of ejecta.

Given the age of the remnant (roughly middle-aged) the presence of ejecta is not expected, though the authors cite other recent studies of middle-aged remnants that have shown evidence of metal-rich ejecta. They posit that the presence of molecular material in the vicinity of the SE and SW regions (the CO emission detected by Brand et al.[12]) may cause the survival of ejecta, especially in the southern regions nearest the molecular material.

The hydrogen column densities N$_h$ derived by the fits are in the range $2 \times 10^{20} - 14.6 \times 10^{20}$ cm^{-2}, which are in between the values derived by Hwang and Markert [50] who measured a high column density, and Castro et al. [16] who measured a low column density. The authors therefore choose to take a distance of 3 kpc to the remnant, as it is in between the values derived by the two other papers and consistent with the optical observation estimates by [67]. They use the Sedov equations (assuming that the remnant is in its adiabatic expansion stage) to derive the age of the remnant ($\sim$28,000 years), shock velocity ($\sim$320 km/s), shock temperature ($\sim 1.2 \times 10^6$K), density ($\sim$0.45cm^{-3}), and total swept-up mass ($\sim$ 340M$_\odot$).

Comparing the derived fit abundances to ratios predicted in a core-collapse model, they find that the progenitor mass is roughly consistent with 30M$_\odot$, which is consistent with the [16] claim of a progenitor of mass $\gtrsim$ 25M$_\odot$. Since the measured amount of swept-up mass is about ten times larger than the derived progenitor mass, the authors believe the remnant is in a stage where the shock is slowing significantly causing mixing between post-shock material and outflowing ejecta such that the observed ejecta contamination is not surprising.

2.1.4 Other Observations

I have described several observations of G296.1-0.5 and the conclusions drawn from them. G296.1-0.5 is also described briefly in the Einstein SNR catalog [91] and the *Molonglo Observeratory Synthesis Telescope* (MOST) SNR catalog [111].

In addition to the initial optical observations, which showed Hα emission, G296.1-0.5 has also been detected in more recent Hα surveys. Russiel and Parker [83], [84], describe a photographic survey of the southern Galactic plane and Magellanic clouds using the 1.8 m *AAO/UK Schmidt Telescope* with a monolithic interference filter giving $\sim$ 2' resolution. Sources located using the AAO/UKST survey were followed up with pointings of the Marseille Hα survey, which used a scanning Fabry-Perot interferometer at the ESO (La Silla) observatory to obtain spectral information to determine velocities and widths. Many thin filaments were detected and clearly linked to G296.1-0.5. Diffuse Hα emission over a large portion of G296.1-0.5 was also detected by the Robotic Wide-Angle Hα Survey of the Southern Sky [36], which can be seen in Figure 2-1.

2.2 Observation Objectives

Our optical study of G296.1-0.5 focuses on detecting charge exchange in and around the SNR shock through the detection of Balmer Dominated Shocks. As a supernova expands, its shock wave heats the surrounding interstellar material, causing filamentary optical line emission. As described in Section 1.5, there are two general classifications of this emission: radiative and nonradiative. Radiative filaments are relatively bright, and their emission is the result of radiative cooling of shock-heated interstellar clouds whose pre-shock densities are much higher than the surrounding regions. These filaments are usually located downstream from the shock front. Their line emission is characterized by strong O III, N II, and S II lines.

Nonradiative filaments are produced in low density regions between clouds, where shocks have higher velocities and thus higher post-shock temperatures, often leading to X-ray emission. Optical emission is produced in these filaments when the high velocity shock encounters partially neutral gas. The collisionless shock heats charged particles, while the neutral atoms are unaffected. These neutrals can be collisionally excited or ionized by the shock-heated plasma around them, causing emission of Hα photons with a thermal width corresponding to the pre-shock temperature. The neutral hydrogen left behind can also undergo charge exchange with a hot, post-shock proton, producing a neutral hydrogen population emitting Hα with a thermal line with width and location corresponding to the post-shock temperature and velocity respectively (Section 1.5). These shocks are characterized by Balmer-dominated emission, with a lack of strong N II and S II lines. Their emission is expected to have low flux, and be located along the outer perimeter of the optical and X-ray emission from the remnant, close to the shock front [30].

Our optical observation focused on locating and studying Balmer-dominated shocks in G296.1-0.5, which I have discussed extensively in Section 2.1. It is a good candidate for this search because it is not highly absorbed ([16]) and has a strong Hα component ([36]). If present, Balmer-dominated shocks would show emission around the Hα line at 6562.8 Å, and not in bands associated with radiative shocks (like O III). For this reason we observed the remnant with three filters: an Hα filter with center 6565 Å and width 50 Å, a Rominovsky O III filter with center 5054 Å and width 75 Å, and a Sloan red filter with center 6250 Å and width 1500 Å. The transmission of these filters as measured at LCO[1] is shown in Figure 2-2 with the Hα filter shown in red, the O III shown in blue, and the Sloan red shown in green. Once we completed the imaging, we planned to take spectra of any promising filaments identified in the imaging campaign to search for the characteristic narrow and broad Hα lines, which, if detected, would allow measurement of the pre- and post-shock temperatures and the shock velocity.

Daniel Castro and I travelled to Chile in February, 2012 to complete the observation, which was limited to a single night. Our plan was to obtain three dithered images in each of six fields with all three filters, then to choose the best several locations for spectroscopy and make gratings observations of each of these. Because of two separate issues with the

---

[1] `http://www.lco.cl/telescopes-information/magellan/operations-homepage/instruments/IMACS/imacs-filters/imacs-filters-1`

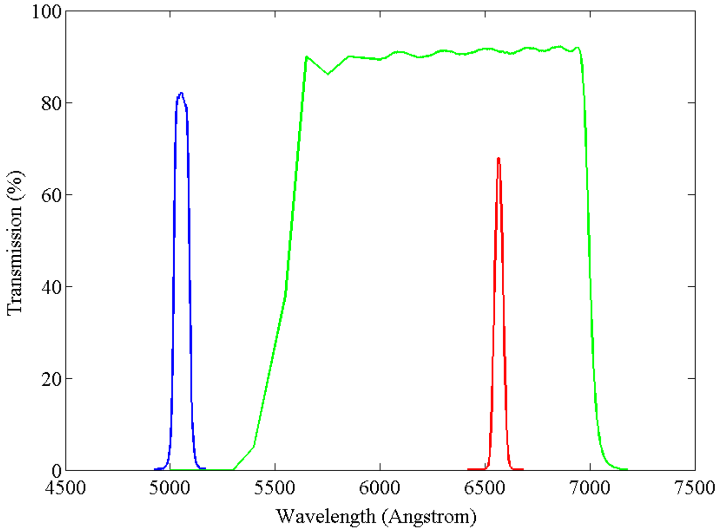

Figure 2-2: The filter transmission measured at Las Campanas Observatory for each of the three filters we utilized in our observation: Hα in red, O III in blue and Sloan red in green.

telescope during the night we only had time to make a spectroscopic observation in one location, which is discussed in Section 2.5. Other than the telescope issues, we had a fairly good night for observing, with very few clouds and fairly low winds.

2.3 The *Magellan* IMACS Instrument

The Inamori-Magellan Areal Camera and Spectrograph (IMACS) is a powerful imager and spectrometer on the *Magellan-Baade Telescope* at the Las Campanas Observatory (LCO), run by the Carnegie Institution. Its design and functionality are described in detail in [28], and more details about the specifics of observing with IMACS can be found in the user manual [27]. IMACS is an internally baffled imaging spectrograph with two basic operating modes. A single 150 mm beam reflective collimator feeds one of two cameras: the f/4 all-spherical refractive camera or the f/2 double-aspheric, oil-coupled multiplet refractive camera. The principle distinguishing features of these cameras are field of view and resolution. The f/2 covers an FOV of nearly 0.5° with a resolution of 0.2”/pixel while the f/4

Figure 2-3: The *Magellan* telescopes, *Clay* and *Baade*, at Las Campanas Observatory, taken the day of our observation in February, 2012. The *Baade* telescope, which hosts the IMACS instrument, is the closer of the two in the image.

camera covers a 0.25° × 0.25° FOV with a resolution of 0.1"/pixel. We utilized the f/4 camera for our observations so I will limit detailed discussion to its parameters and performance.

The *Baade telescope* is a 6.5 meter telescope with a borosilicate mirror produced by Steward Observatory Mirror Lab. Both of the *Magellan* telescopes (*Clay* and *Baade*) are shown with domes closed in Figure 2-3. Las Campanas Observatory is located about a two and a half hour drive from La Serena, Chile, which is an hour plane flight north of Santiago. IMACS was shipped to Chile from the Carnegie Institution in California and mounted on the IMACS telescope in 2003. The instrument became available for regular use in April of 2004. The IMACS instrument is utilized during $\sim$67% of the available observing time on *Baade*, and is designed to produce images with seeing-limited spatial resolution (Full Width at Half Maximum (FWHM)$\leq$0.30") and spectra with R=600-5000 depending on the slit, disperser, and camera.

The f/4 camera is an 8 kilopixel square array of 8 E2V CCDs, each with 2000 × 4000, 15μm pixels. Several filters are available and can easily be inserted into the beam during imaging observations. Likewise, several dispersers are available, and are inserted into the beam line, along with a 1.0 arcsecond-wide slit (or other single or multi-slit masks), to perform spectroscopic observations at high resolution. For the spectroscopic measurements described in this chapter, we utilized a grating with 600 lines/mm at a blaze angle of 13.0° along with the 1.0" width slit (called a 'long slit' in the instrument manuals). Taking into account the optics (but not the atmosphere) the typical throughput of the IMACS instrument is about 60% for direct imaging and 15%-35% in spectroscopic mode.

A schematic of the IMACS optical components is shown in Figure 2-4. The IMACS system is highly configurable, designed to provide as many observation options as possible without requiring labor-intensive reconfiguration. Several slit masks, filters, and dispersers can be changed out quickly, controlled by settings on a Graphical User Interface (GUI) in the control room.

Images of IMACS mounted on *Baade* with and without the instrument covers are shown in Figure 2-5. The main structure of the instrument is made up of 2, 2.5 meter stainless steel weldment wheels. The rims of these wheels act as the bearings on which the entire instrument rotates. The forward wheel (closer to the telescope) is the mounting surface for the guiders, the disperser server, and calibration sources. The aft wheel (further from the telescope) is the mounting surface for the optical bench with the collimator and both cameras. The filter server, the slit mask server, and disperser server are all 'jukebox style' wheels, which rotate to bring the selected optic into the beam line. The disperser server wheel can be seen on the image in Figure 2-5.

Several aspects of the IMACS design service stability. Three guiders monitor star images, and adjust the primary mirror support system, collimation, focus, and pointing to maintain zero telescope position during long exposures. The focus is also maintained by changing the temperature of IMACS components in response to ambient conditions (autofocus). The

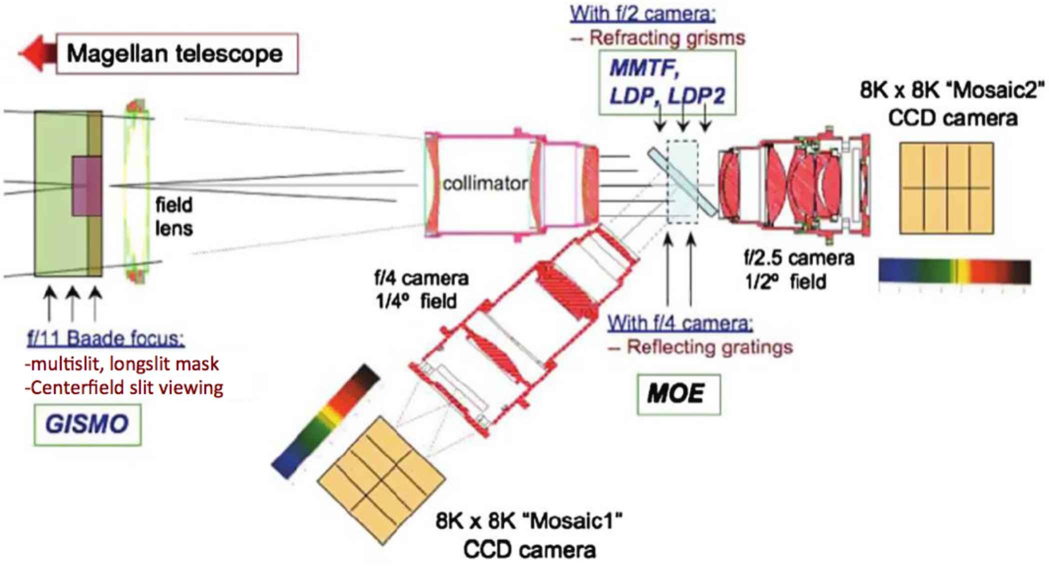

Figure 2-4: A schematic of the IMACS optical components and paths (reprinted from [28]). Light from the telescope enters the collimator, and is then either allowed to travel straight into the f/2 camera or is reflected into the f/4 camera depending on user settings. Various other optical components (filters, slits, dispersers, etc.) can be inserted into the beam line during observation.

Figure 2-5: Pictures of the IMACS instrument with (left) and without (right) the instrument covers, mounted on the *Baade* telescope (reprinted from [28].)

focus is manually reset by instrument engineers after each observation, but this autofocus is sufficient to maintain image quality over several nights.

For the stability of spectroscopic exposures, the slit holder is rigidly mounted to the guiders so that there will be negligible drift of objects with respect to the field during even several-hour exposures. Also, optical components are mounted as close to their center of gravity as possible and unavoidable cantilever lengths are minimized to prevent shifts of these components due to gravity as the telescope position changes. To correct for slight changes in the optical path due to change in position of the telescope components, the detectors are mounted on piezo-stages to allow adjustment to maintain focus.

The CCD arrays are each located in a vacuum vessel connected to a Cryotiger pump through copper straps. The cryogen-less pump keeps the array temperature around $-120°$C during operation. The pump was chosen above a cryogen system for ease of operation and maintenance.

2.4 Imaging

2.4.1 Data reduction in IRAF

I processed the science images produced by the IMACS instrument using the Image Reduction and Analysis Facility (IRAF) software package [99], [100]. As discussed in Section 2.3, the IMACS camera is made up of eight chips. Each of these chips has a unique response on both large and small scales, that affects the image measured by the chip. The goal of a large portion of the processing is to remove the artifacts of these responses in order to obtain the best image from the entire array. Unlike large satellite missions like *Chandra*, which employ staff to oversee data cleaning and reduction so that observers are handed a ready-made, clean observation file, smaller ground-based telescopes do not have the budget to accomplish this, so image processing falls to the observer. This processing requires several steps, which can all be accomplished in IRAF: overscan bias correction, zero bias correction, flat illumination correction, and flat correction.

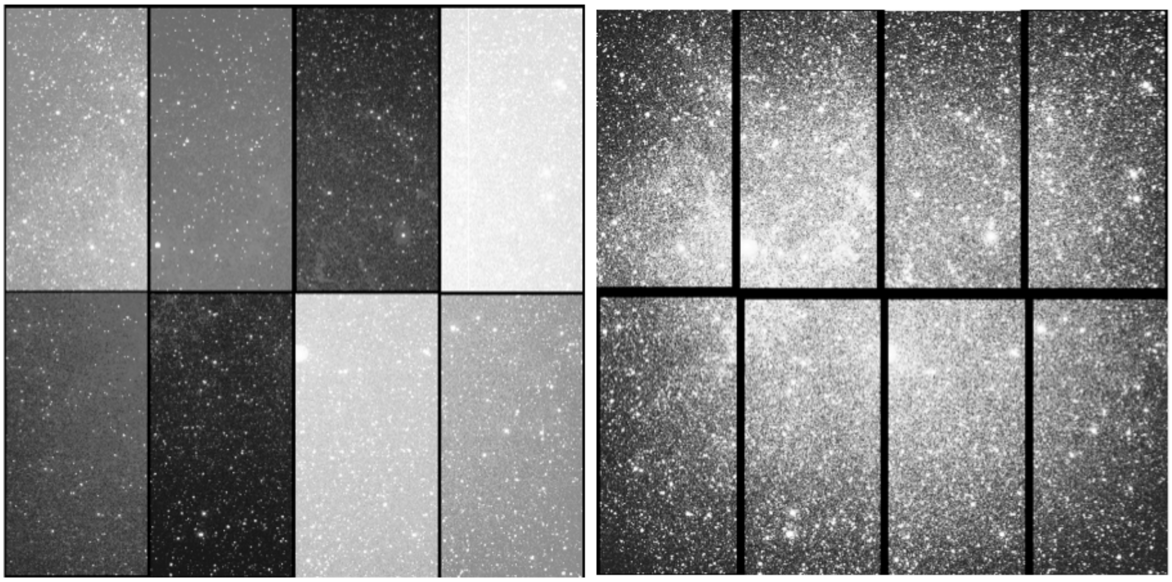

Figure 2-6: An image of the eight chips in field 1, dither position 1, using the Hα filter, stitched together using the `igapmos` tool in the imacs toolbox in IRAF without overscan correction (left) and with overscan correction (right). The chips have varying offsets, which must be removed from each of them so that they have comparable brightnesses. The chip gaps are larger in the overscan-corrected images because the overscan areas have been trimmed out of the image.

IRAF provides several sets of tasks to accomplish the necessary processing. The primary processing task is `ccdproc`, which encompasses several processing steps that can be run simultaneously, or one at a time in successive calls of `ccdproc`. The first processing step is overscan correction. Each chip has an overscan region (an extension of the chip beyond the 2048 by 4096 pixels used to produce the image). The values of the pixels in this region can be fit to give a first-order additive correction for the electronic pedestal level for each of the chips, which is then subtracted from science images. Figure 2-6 shows an 8-chip image before and after overscan processing. All of the images (including calibration images) are overscan-processed to remove offsets.

The next stage of processing is bias image, or zero processing, which helps to remove higher order effects in electronic pedestal level [70]. Bias images are zero second exposures. Several of these images are combined for each chip and subtracted from the science images.

`ccdproc` also includes a dark current correction option. Dark images are taken with the shutter closed to characterize the amount of dark current, which is then removed from the image. This correction was not recommended for IMACS images because the camera is cold enough that significant dark current is not expected, so I did not apply it to our data.

The final image correction step is flat correction. Flats are images of as uniformly illuminated a field as possible, taken through the full optical path of the telescope. Flat correction removes features from the optics that affect the measured images. There are two types of flats: dome flats and sky flats. Dome flats are taken with lamps illuminating an opaque screen in front of the secondary mirror of the telescope. Sky flats (or twilight flats) are taken as the Sun is setting or rising and the sky is a uniform color. Ideally one could also take a long exposure flat of a blank region of sky at night, however we did not have time during our observation to obtain this data. Separate flats must be taken for each filter, to correct small-scale transmission differences.

We obtained both dome and twilight flats during our observation. These can be corrected and combined together, or one can be chosen. After carefully inspecting the image quality for both, I chose to use only the twilight flats for correction. After overscan and zero processing the flats, I applied an illumination correction using the IRAF task `flatcor`. This performs a fit to large-scale changes in illumination over the flat, and divides the flat by the result to take out any effects from an unevenly illuminated array (this is necessary because it is difficult to take either a dome flat or a sky flat with a perfectly uniform input). After illumination-correcting the sky flats, I applied flat correction to the science images using `ccdproc`, which simply divides the processed science image by the processed flat to produce cleaned science images.

2.4.2 Star mapping, removing distortions, and co-addition

As mentioned previously, the IMACS camera is made up of eight chips with fairly sizable gaps (chip-gaps) between them. In order to produce a continuous image without chip-gaps, we took three images for each field, dithering the telescope by 30” in Right Ascension (RA)

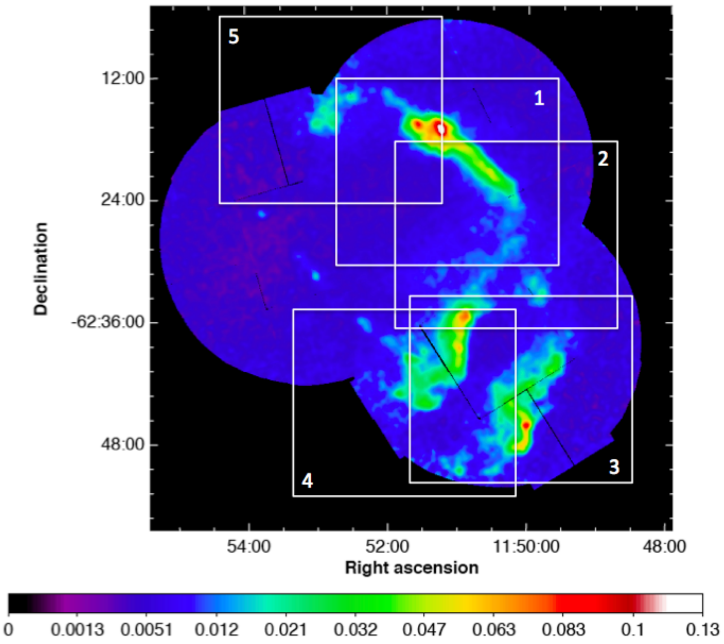

Figure 2-7: The EPIC MOS intensity map in the 0.3-3.0 keV energy band (reprinted from [16]), with the sizes and locations of our five optical fields overlaid and labelled.

and 30" in Declination (DEC) between each. These images must be aligned and co-added after processing to produce the complete continuous image.

To cover the entire remnant, we took images of six fields. The last of these (field 6) showed no filamentary emission from the remnant so we did not dither the telescope (we were running short on observing time). This field is not included in my imaging results. The locations of our five good fields are shown overlaid on the X-ray EPIC MOS intensity map from [16] in Figure 2-7.

I performed the processing described in Section 2.4.1 separately for each of the chip images for fields 1-5 (8 chips per image, 3 images per field, 3 filters per image). The next step is to reconstruct the entire continuous image. A set of IMACS-specific tools in IRAF can be used to stitch the chips together for each image (specifically the `igapmos` task). Another set of tasks can be used to align and co-add these images (`imalign` and `imcombine`).

However, these tasks do not take into account any warping of the chips. The `igapmos` tool assumes a linear plate scale across the entire chip, which is not a valid assumption due to

Figure 2-8: A section of field 3 in three colors with red corresponding to Hα, blue to OIII and green to Sloan red. Here stitching of the chips was done using a linear plate scale with `igapmos`, then using the iraf tasks `imalign` and `imcombine` to co-add the dithered images. The chip warps on the edges of the chip have caused misalignments in the constituent images, resulting in double images of stars where the chip-gaps originally fell even though alignment is good in the center of chips.

minor warping across the chip area. If a linear plate scale is assumed, the combined images will have slight misalignments where the linear plate scale breaks down. The chips tend to be more warped along the edges than in the center, so this manifests as double or triple images of stars in the co-added images where the chip gaps were located in the constituent images. This effect is shown in a poorly co-added image due to assumption of a linear plate scale in Figure 2-8.

In order to produce better co-added images, I used a suite of tools written by E. Bertin[2]: SExtractor [6], SCAMP [4], and SWarp [7]. SExtractor finds star-like sources in the input field, and outputs a binary file containing the pixel coordinates of the Gaussian-weighted centroids of the detected sources. SCAMP computes an astrometric solution based on a chi-squared minimization of differences in positions between sources from the SExtractor output and a selected survey catalog (I used the 2MASS catalog, since it covers the entire sky [24]). SCAMP is particularly convenient because it accesses the sky catalogs from a

---

[2] Similar functionality can be found in the IRAF `wcstools` and the IMACS-specific tool `iwcs`

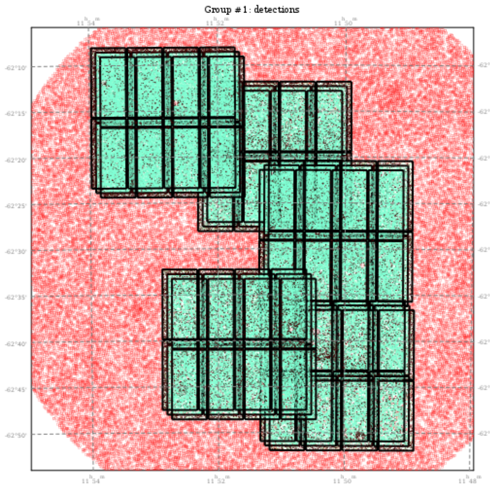

Figure 2-9: An output image from SCAMP showing the location of all of the individual chips in the full image with green dots denoting sources matched between the SExtractor output and a star catalog and red dots denoting unmatched sources (mostly where there are no chip images).

server, saving the user from the task of finding the proper file in the proper format. SCAMP assumes that the World Coordinate System (WCS) information in the FITS header for each image is accurate to the level of a few arc minutes, pixel scale accurate to a factor of about 2, and that image orientation may be off by up to 180°. It also allows for images that are flipped (reflected) from physical orientation. I included the known flips in orientation of the IMACS chips using negative plate scales rather than relying on SCAMP to detect flips.

For each image, I edited the header to include the pixel coordinates and WCS location of a reference star, as well as the pixel scale in both the X and Y directions (X roughly corresponding to RA and Y roughly corresponding to DEC). I ran SCAMP on all of the chips simultaneously. Figure 2-9 shows the layout of the chips with green dots corresponding to SExtractor sources that were successfully mapped to stars in the sky catalog. Red dots correspond to sky catalog sources that were unmatched. Nearly all of the sources on the chips were matched, implying a successful astrometric calibration. SCAMP computes the nonlinear plate scale, writes it to an external header, and outputs a map of the chip warping, an example of which is shown in Figure 2-10.

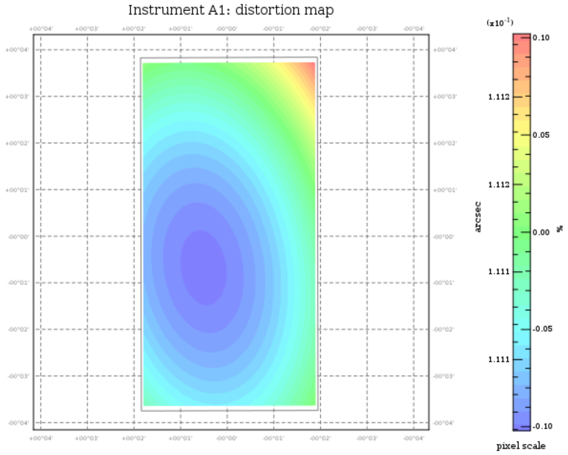

Figure 2-10: An output image from SCAMP showing the chip distortion over a single chip in the field. The distortion is worse towards the outer edges of the chip, explaining why misalignments due to an assumed linear plate scale are only noticeable where chip edges overlap.

SWarp resamples and co-adds the images using the information in the output SCAMP headers and the input FITS images. It uses an 'inverse mapping' technique in which the output frame is scanned across pixels and lines and each output pixel center is associated with an input image position at which the co-added image is interpolated [5]. For co-addition I set SWarp to average overlapping images. The complete, three color co-added image is shown in Section 2.4.3.

2.4.3 Imaging results

One of the major issues we encountered in our images was contamination from bright stars. Very bright stars cause both saturation of the detector and reflections within the telescope that lead to bright, donut-like artifacts in the image. Figure 2-11 shows one such artifact. It is nearly impossible to remove these artifacts without losing the image underneath them[3]. It would be best to choose pointings such that these bright stars are not in the field to avoid these artifacts.

---

[3] Private communication Rebecca Levinson

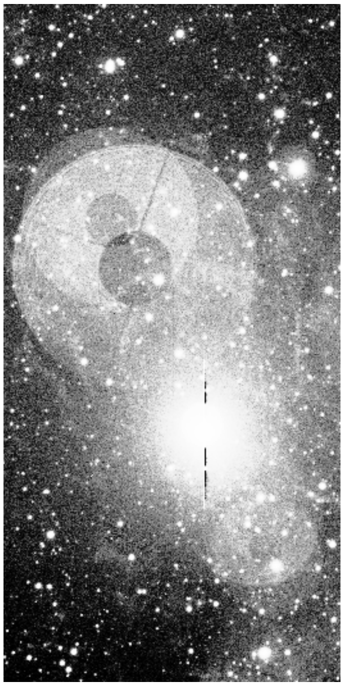

Figure 2-11: An image from a single chip in field 3 through the Hα filter. A single bright star has produced reflection artifacts that are extremely difficult to remove.

The complete, co-added, three-color image of all five fields of G296.1-0.5 is shown in Figure 2-12. I have overlaid black boxes where artifacts from bright stars occurred. In this image the emission through the Hα filter is shown in red, the emission through the O III filter is shown in blue, and the emission through the Sloan red filter is shown in green. Zoomed-in images of each of the filaments are shown in Figures 2-13, 2-14, 2-15, and 2-16.

The strongest candidates for Balmer-dominated shock filaments are those in fields 1 (Figure 2-13) and possibly 2 (Figure 2-14). The optical image is shown with X-ray contours overlaid in Figure 2-17. The Hα dominated filaments appear along the outer edges of the strong X-ray emission. This further supports the case that these may be Balmer-dominated shocks, as they appear on the outer edges of the shock front.

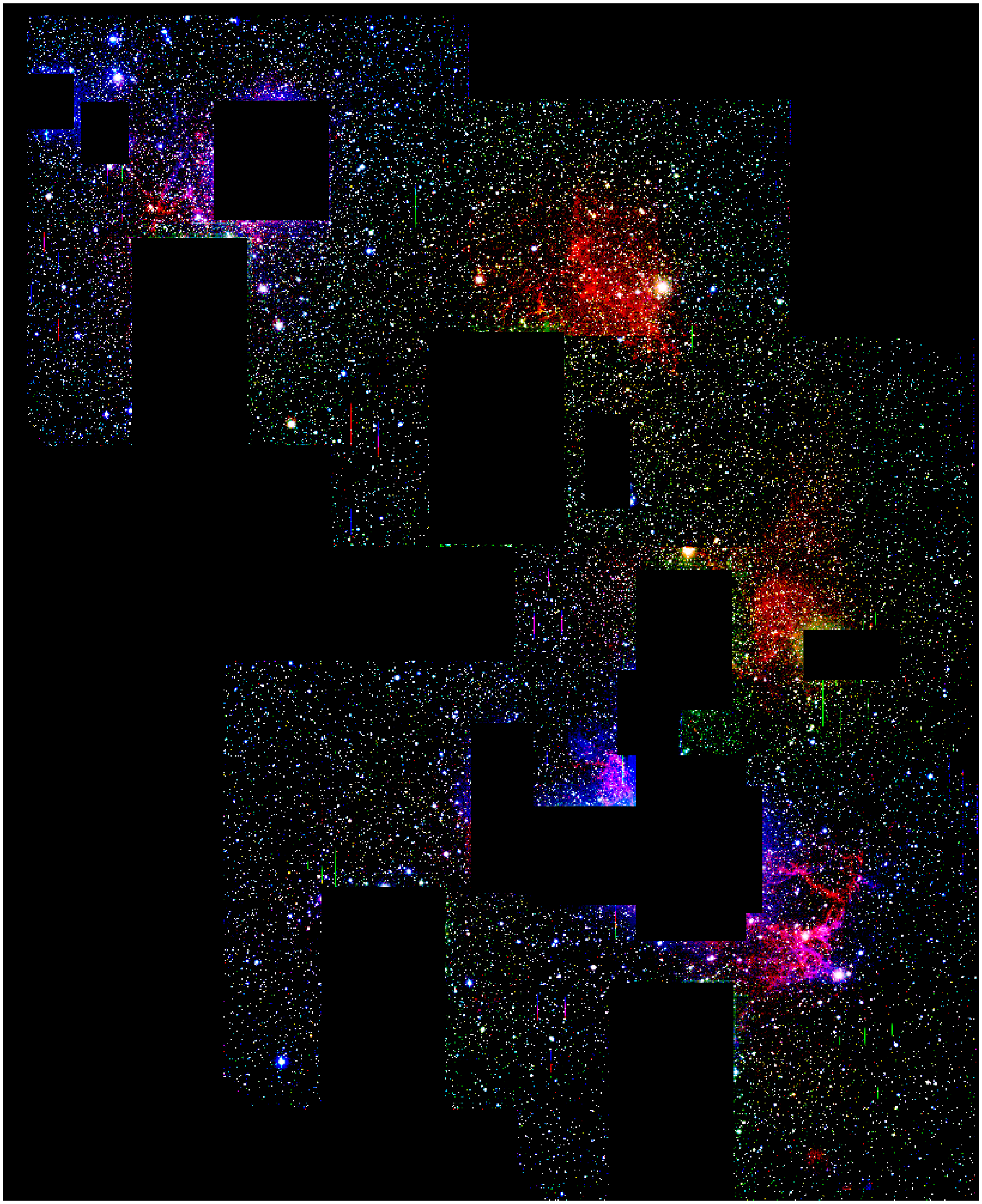

Figure 2-12: The full, co-added image of G296.1-0.5 with Hα emission shown in red, O III emission shown in blue, and Sloan red emission shown in green. Black boxes are overlaid over artifacts from bright stars. Some excess emission from the bright stars is still visible. Several regions of filamentary emission are visible.

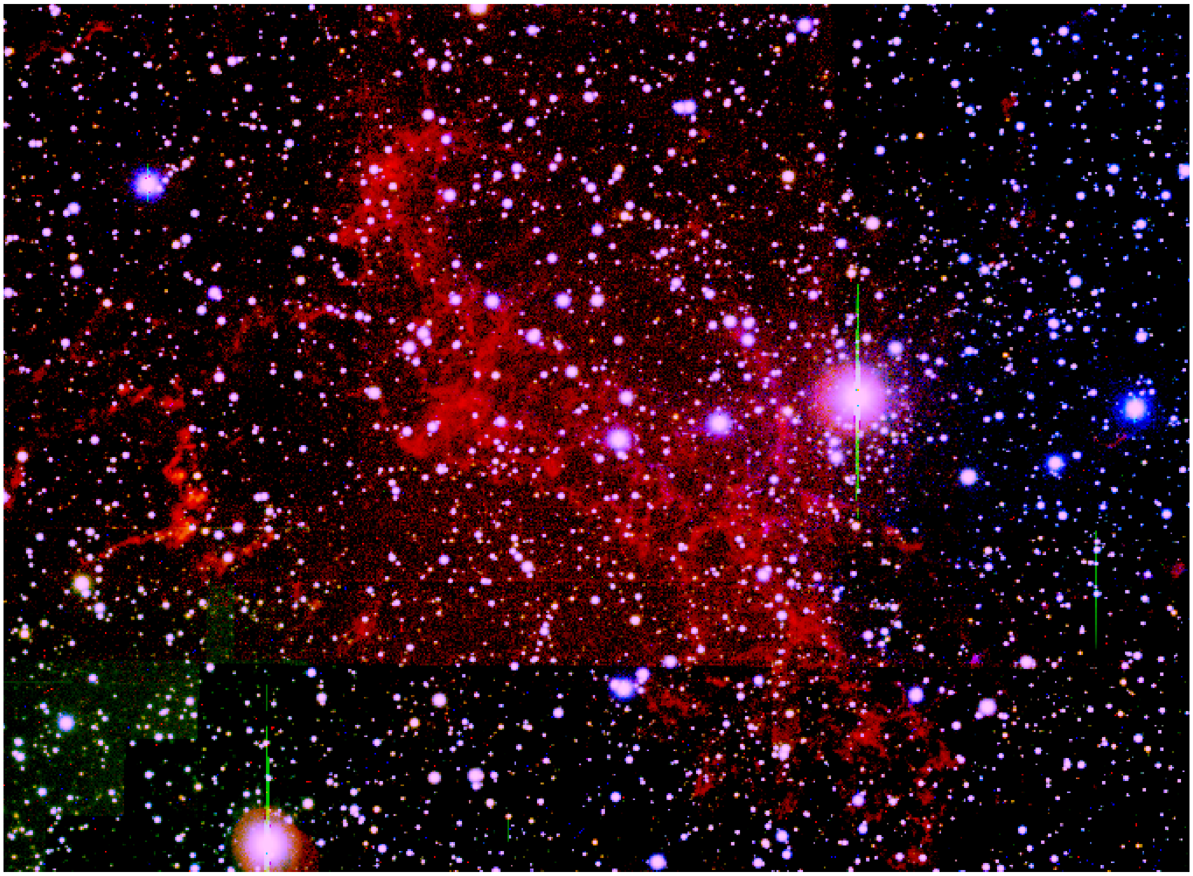

Figure 2-13: A zoomed-in view of the field 1 filament, which is located in the upper right hand corner of the image in Figure 2-12. This is the most promising filament, showing the characteristics of a Balmer-dominated shock, with very strong Hα emission and no noticeable O III emission. Hα emission shown in red, O III emission shown in blue, and Sloan red emission shown in green. This image is centered on 11:50:48.0, -62:18:57.3.

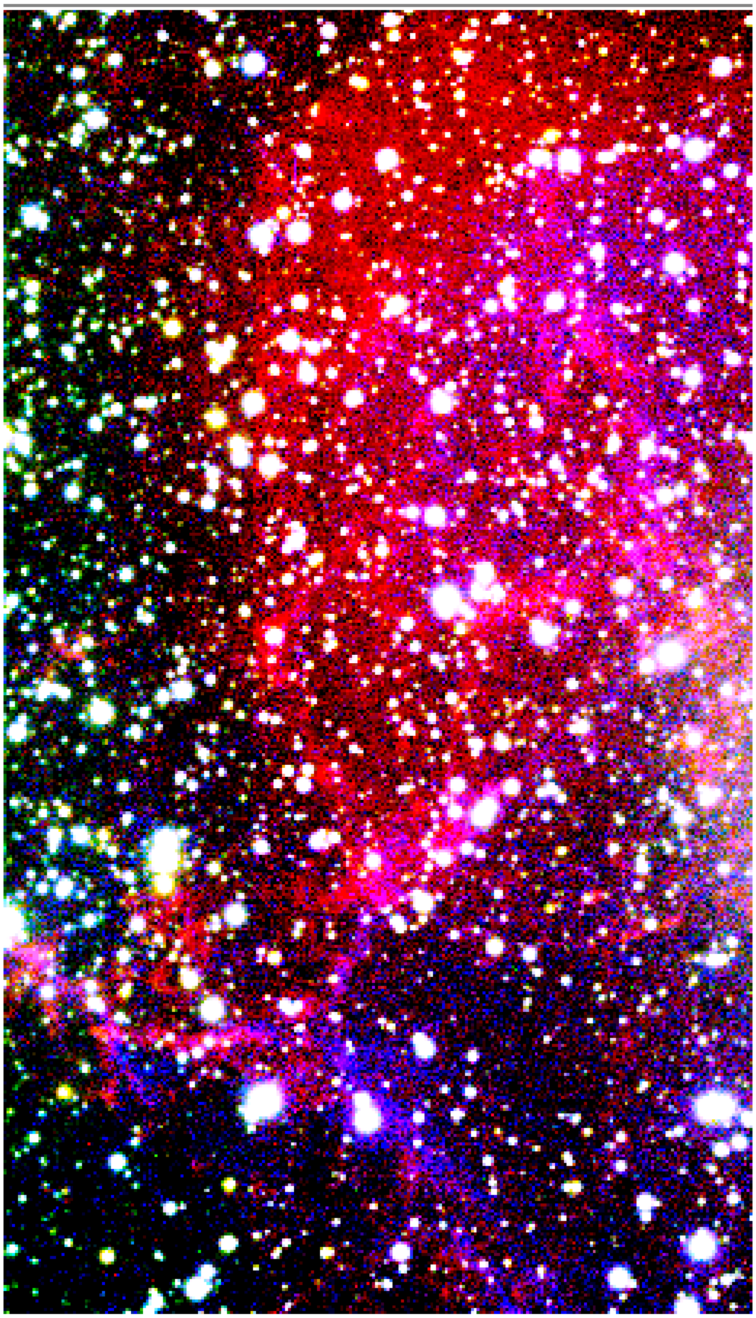

Figure 2-14: A zoomed-in view of the field 2 filament, located in the center right of the complete image in Figure 2-12. The non-filamentary Hα emission is contamination by an artifact from a bright star just out of the field on the right side of the image. Hα emission shown in red, O III emission shown in blue, and Sloan red emission shown in green. This image is centered on 11:49:56.3, -62:31:26.7.

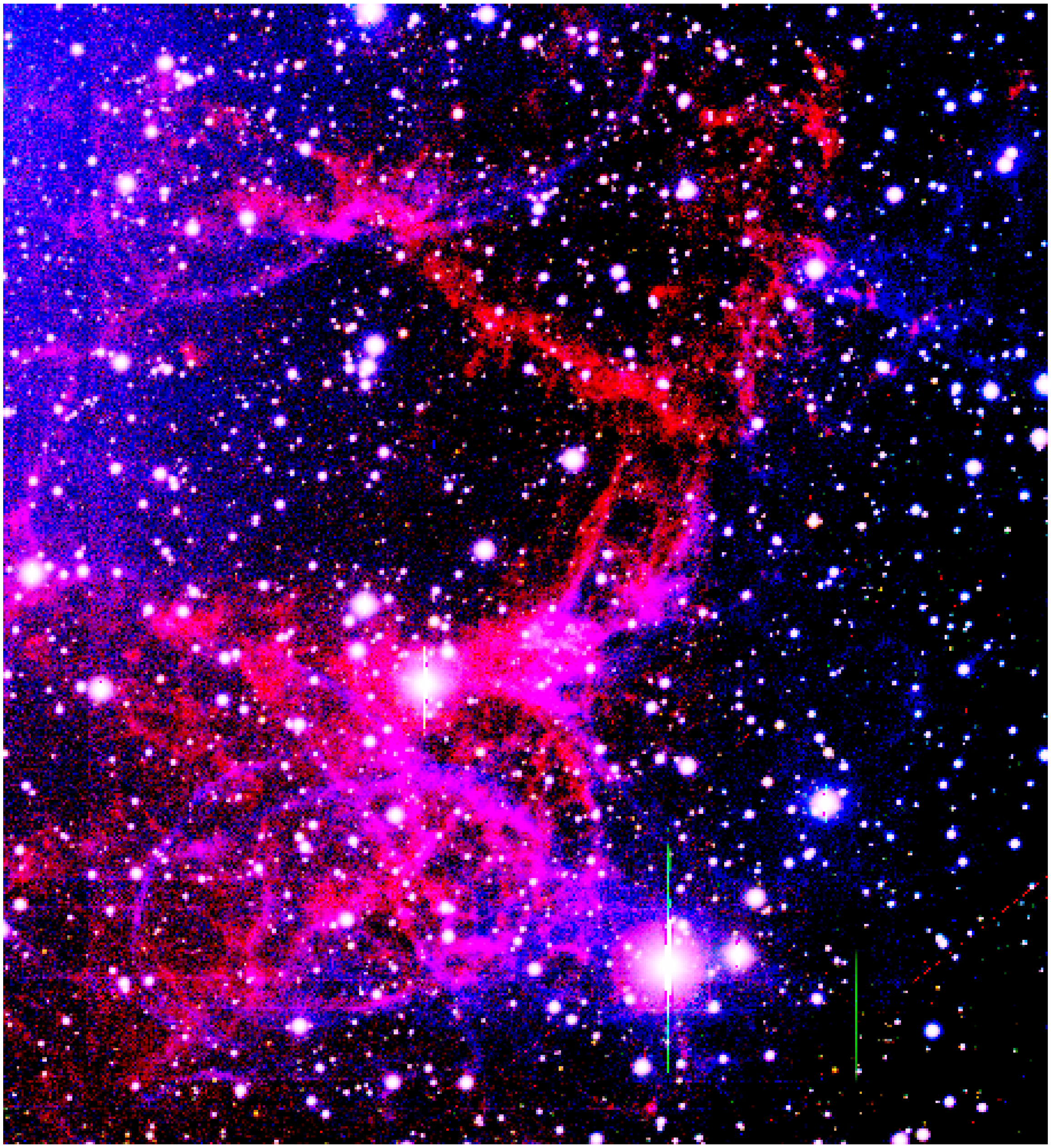

Figure 2-15: A zoomed-in view of the field 3 filament, located in the lower right of the complete image in Figure 2-12. This is by far the brightest filament, and is the location we chose for spectroscopy for this reason. There are some regions of the filament that do not exhibit O III emission, but the majority of the filament does exhibit radiative emission. There are three very bright stars to the left of the filament in the image, which cause strong contamination. Taking images of fields around but not including these stars may allow us to see even more of this filament, which is obscured in our image by the bright-star halos and artifacts. Hα emission shown in red, O III emission shown in blue, and Sloan red emission shown in green. This image is centered on 11:49:44.5, -62:41:34.1.

Figure 2-16: A zoomed-in view of the field 5 filament, which is located in the upper left of the complete image in Figure 2-12. This filament is fairly weak and is near a bright star, but shows some regions with Hα emission and no O III emission. Hα emission shown in red, O III emission shown in blue and Sloan red emission shown in green. This image is centered on 11:53:02.3, -62:14:12.5.

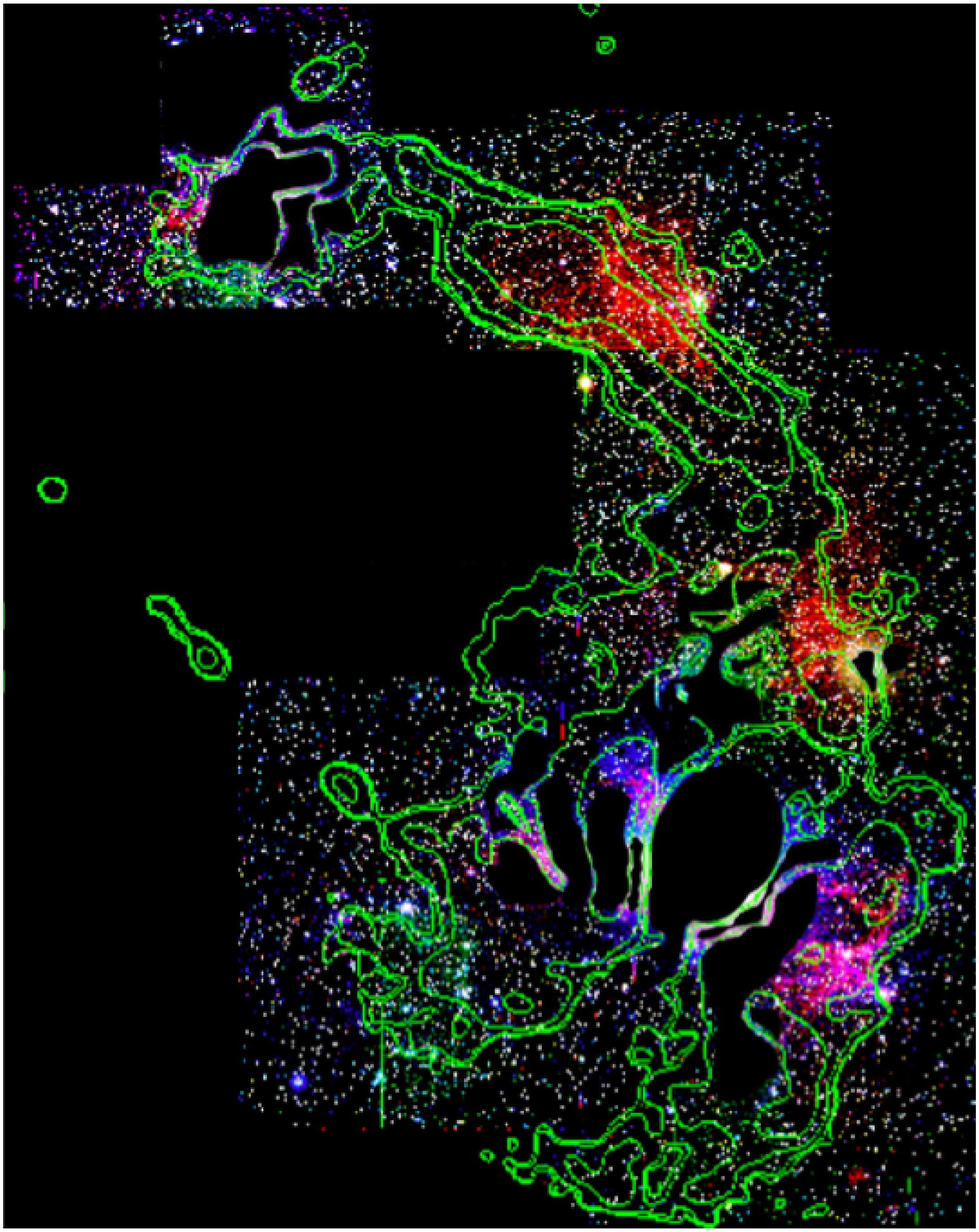

Figure 2-17: The optical three color image (Hα emission shown in red, O III emission shown in blue, and Sloan red emission shown in green) with *XMM* X-ray intensity contours overplotted in bright green. A black mask is overlaid where bright star contamination dominates in the image. The optical filaments follow the general structure of the X-ray emission but are not coincident with the brightest areas of the image. Filamentary structures dominated by Hα emission are located towards the outer edges of the X-ray emission.

2.5 Spectroscopy

2.5.1 Data reduction in IRAF

As with the imaging data, the spectroscopy images require a good deal of processing before arriving at a spectrum. First, all of the processing steps (overscan, zero, flat illumination correction, and flat correction of science images) described in Section 2.4.1 must be performed on the spectroscopy images. The flat illumination correction is somewhat different with spectroscopy flats and is performed using the IRAF task `response`. We do not combine chip images in the spectroscopy data, since each chip will yield a separate portion of the spectrum. These can be plotted together later with much less effort than combining the chip images before processing. In fact, in this analysis we are only interested in the portion of the spectrum on a single chip, negating the concern altogether.

In order to understand several of the additional processing steps, it is useful to understand the anatomy of a spectroscopic 'image' on a chip. As discussed in Section 2.3, a long slit is placed over the FOV, and the light coming through that slit is dispersed onto the imaging chips through a grating. One of the resulting images is shown in Figure 2-18. Objects on the slit are dispersed horizontally, so horizontal lines are dispersed light from slit objects (there are other, very clean horizontal lines that are artifacts of the structure of the slit/gratings and not part of the data). The vertical lines are 'sky lines': dispersed light from the sky background over the entire slit. These are curved because the slit is not perfectly aligned with the pixels, which must be corrected in post-processing.

Once we have obtained the individual chip images resulting from initial processing, there are several additional steps required to produce a spectrum. We took two identical 1800-second exposures of our spectroscopy field. These were much longer than the exposures for imaging (the longest of which was the Hα at 300 seconds) because of the low flux through the disperser. During this long exposure, a large number of cosmic rays hit the detectors causing thin, streak-like artifacts. While this type of artifact in the imaging only makes the

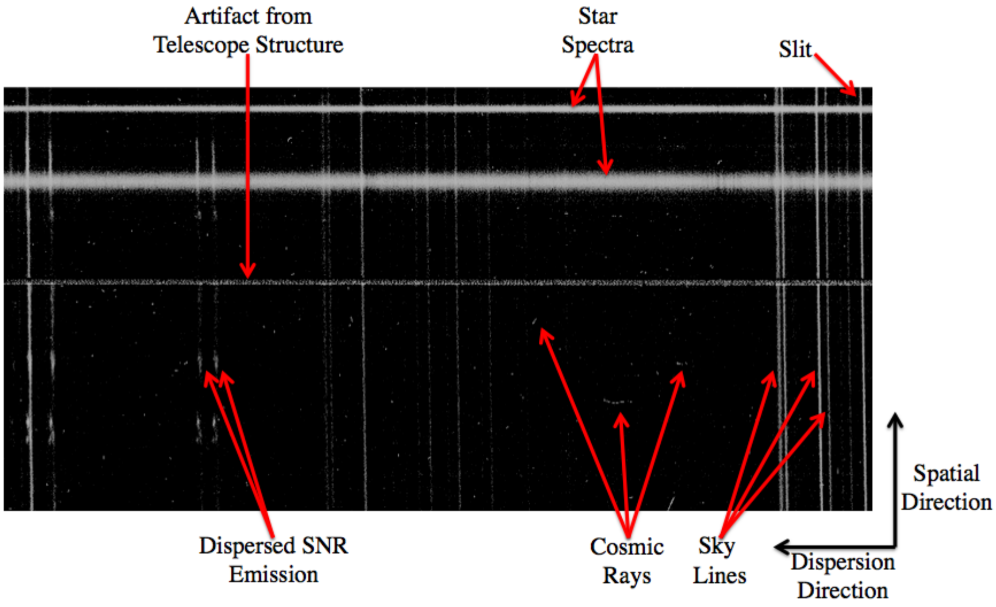

Figure 2-18: A portion of a cleaned spectroscopy image from a single chip with features labelled. Several additional processing steps are required to get from this image to an object spectrum.

images less attractive, it can cause much more trouble in the spectroscopic exposures, where excess counts on a particular region of the chip could skew the spectrum.

I used the program L.A.Cosmic [108], to clean the cosmic rays from my images. L.A.Cosmic uses an algorithm to detect sharp edges in the image, which identify cosmic ray strikes. Since light from astronomical sources travels through the atmosphere, it will not produce images with sharp edges, while the cosmic rays that are the result of particles hitting the CCDs will. L.A.Cosmic provides an IRAF task to perform the cleaning, that takes as input the gain and read noise of the detectors as well as a few parameters defining the statistical certainty required for removing a cosmic ray. A portion of a spectroscopic image before and after cosmic ray cleaning is shown in Figure 2-19, demonstrating the impressive effectiveness of the tool.

After completing the cosmic ray cleaning on each of the exposures, I averaged them using the IRAF task `imcombine`. The next step is to correct for the tilt of the slit with respect to the pixels and perform wavelength calibration. Though it is not visible in Figure 2-18,

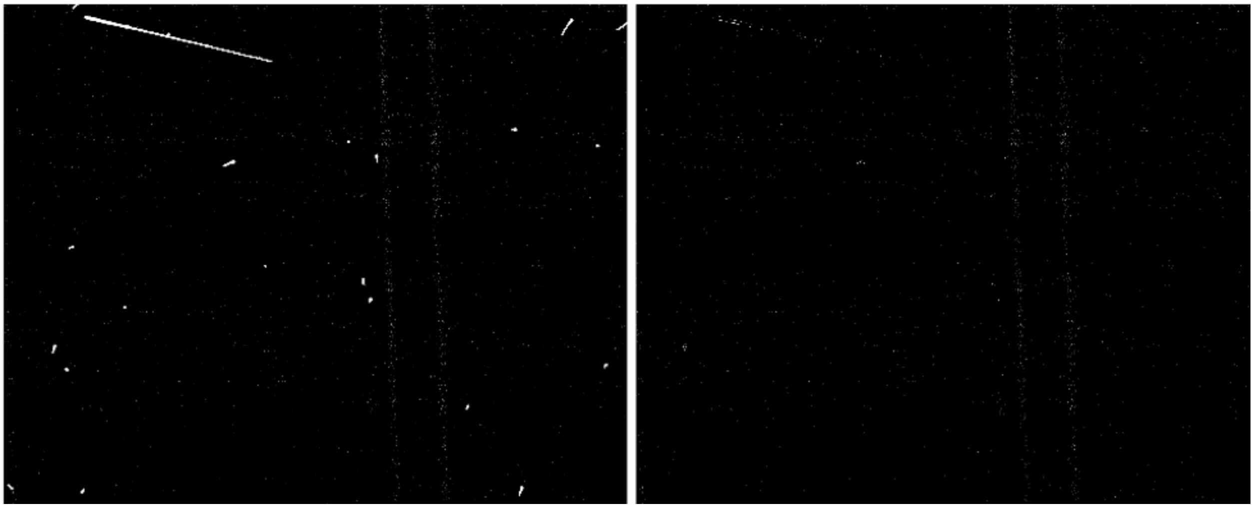

Figure 2-19: Portions of a spectroscopy image on a single chip before (left) and after (right) cosmic ray cleaning using L.A.Cosmic. The program is very effective in removing all of the cosmic rays from our images. The faint vertical lines on the right of the images are sky lines.

there is some curvature in the horizontal lines, which must be corrected. This is achieved by using a spectroscopy image of a standard star. The slit is laid over the star and the gratings disperse its spectrum horizontally. Since the star is a point source, we know that its spectrum should be dispersed as a straight, horizontal line and the distortion can be calibrated using the actual shape of the dispersed spectrum. The IRAF task `identify`, with variables set to specify calibration along the vertical direction, is used for this purpose. The user selects the location of the standard star spectrum using an interactive GUI, and IRAF completes a fit to characterize its shape and saves a file containing the transformation matrix describing the curvature correction.

A similar procedure is performed on a different calibration image to obtain the wavelength curvature. Since inserting the slit mask is a physical process, the eventual location of the slit with respect to the camera is slightly different each time it is inserted. Because of this, wavelength calibration images must be taken with the slit in just before or after science spectroscopy exposures are taken. The calibration image is obtained by turning on a He-Ne-Ar arc source inside the dome and taking an exposure. A section of this exposure is shown in Figure 2-20. This image contains only vertical lines since the arc source illuminates the slit

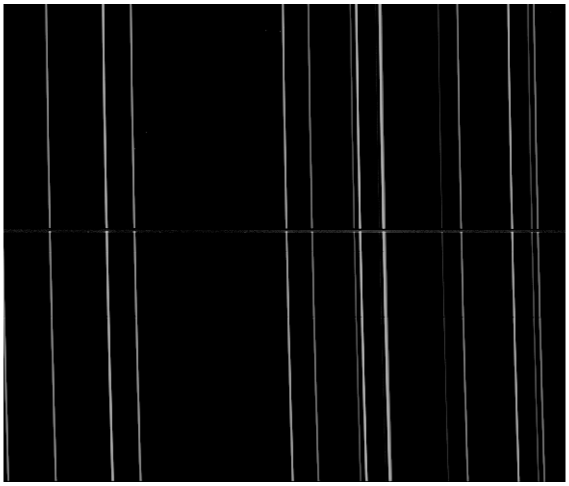

Figure 2-20: A portion of the spectroscopy image of the He-Ne-Ar arc source. Several clean emission lines from this source are dispersed onto each chip, allowing wavelength calibration.

uniformly. Again, the IRAF `identify` task is used, this time with variables set to specify calibration performed along the horizontal axis.

In this case, since we wish to perform calibration in the dispersion direction, IRAF requires a calibration file to describe the wavelengths of the lines in the exposure. A file containing all the optical He, Ne, and Ar lines is distributed with IRAF. The user inputs a starting wavelength and dispersion scale, and specifies the line corresponding to the starting wavelength interactively[4]. IRAF fits the observed line locations to known spacings of lines in the calibration spectrum list, and fits the shape of the line on the chip to create a file containing both the transformation matrix to remove the wavelength curvature and to apply the wavelength calibration[5].

Finally, the IRAF task `transform` is used to apply the x-curvature transformation from the standard star calibration image and the wavelength-curvature transformation from the spectroscopy arc calibration image to the science image. The untransformed and transformed images are shown in Figure 2-21.

---

[4] Despite the well-known characteristics of the gratings it is somewhat of a guessing game to find the proper wavelength to describe a selected line.

[5] The wavelength calibration is simply written as a linear pixel to wavelength conversion in the FITS header of the final, calibrated image

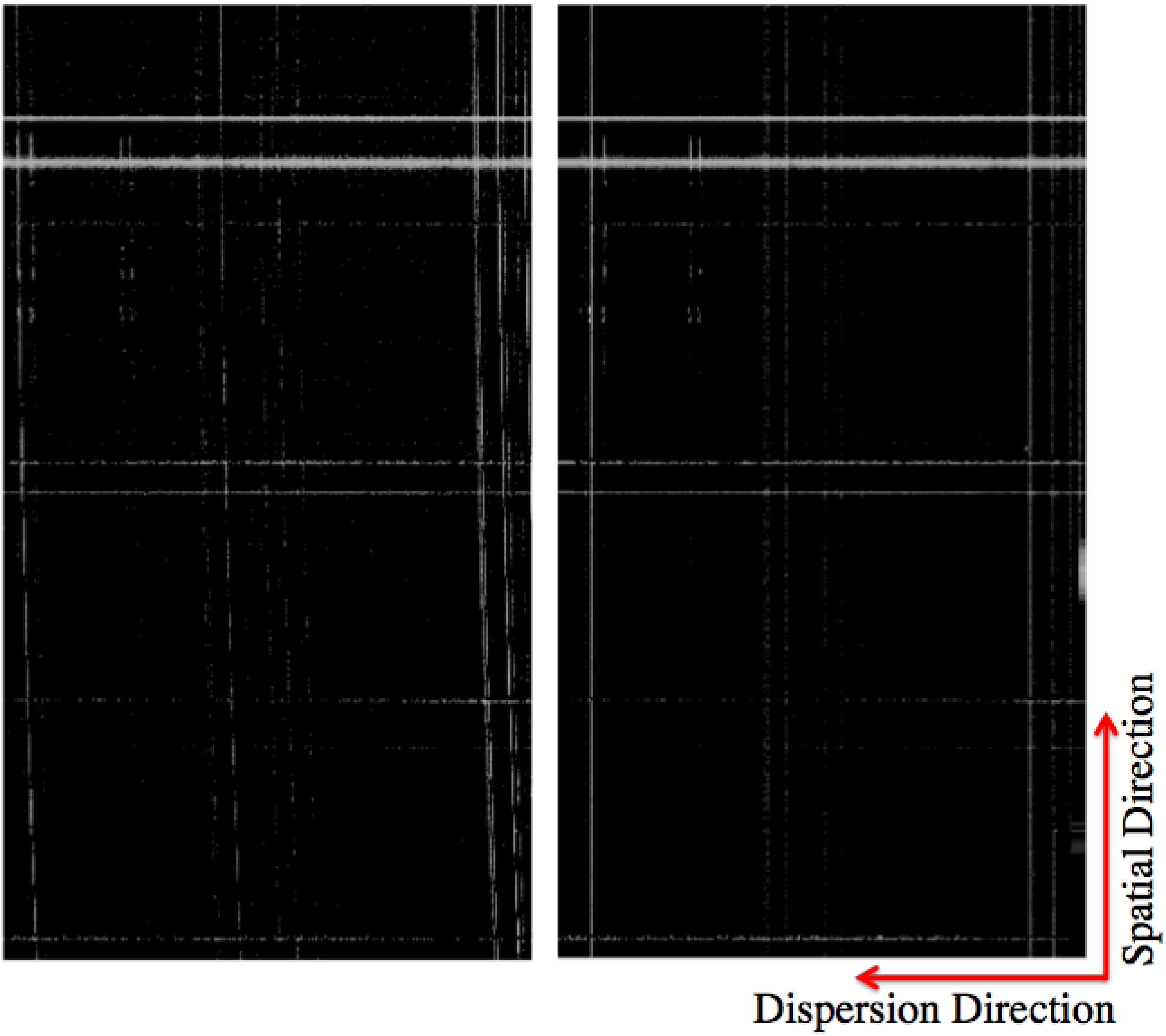

Figure 2-21: A spectroscopic image from a single chip before (left) and after (right) transforming to correct curvature in both the x and wavelength directions. The transformation maps the counts to a space where each column is made up of emission from a single wavelength and a single source on the slit is dispersed straight across rows. The transformation causes distortions along the edges of the chip.

The next step is to subtract the sky lines (background subtraction). I used MATLAB to perform the subtraction and to obtain spectra for flux calibration. First, I identified a region of blank sky in the slit image in SAOimage DS9[6], then I averaged the value of the columns in those regions to obtain an average sky value for each column and subtracted the average sky value from every pixel in the column.

I checked that the subtraction was successful by examining the images (Figure 2-22) and by using the iraf tool `implot` to check that spectra in several regions on the chip (including those without dispersed source data) did not contain any remaining sky lines or dips due to sky over- or under-subtraction. It is important to take great care in selecting good sky. What appears by visual inspection of the image to be blank sky often contains line emission that is not present in data regions, resulting in dips in the sky-corrected data spectrum. Selecting a bad sky region can even result in distortion of the line shapes in data spectra since lines like Hα are present in both the sky and the data, so proper background subtraction is extremely important.

Finally, I created the spectra. After defining data apertures by viewing the slit image in DS9 (see Figure 2-23), I used MATLAB to sum the sky-subtracted data from those apertures to create a one-dimensional spectrum. IRAF contains a set of tools (`standard`, `sensefunc`, and `calibrate`) to perform flux calibration on spectra. The program uses the known flux from the standard star as well as the standard star spectrum provided by the user to flux-calibrate the science object spectrum to erg/cm^2/s/Å. However, since we are only interested in the shapes of lines and the ratios between them and the flux calibration is only a scaling by a constant factor (which I confirmed by performing the flux calibration and comparing the calibrated spectra with the input spectra) I moved forward with analysis using the initial spectrum in counts/bin. The scaling factor ranged from 7.38×10^{18}-8.04×10^{18}(counts/bin)/(erg/cm^2/s/Å) for the four apertures.

When fitting the spectra, I used a slightly different method of background subtraction. Using the background sky region defined using the previous method, I produced a sky spec-

---

[6] DS9 is software obtained from NASA's High Energy Astrophysics Science Archive Research Center (HEASARC), a service of Goddard Space Flight Center and the Smithsonian Astrophysical Observatory.

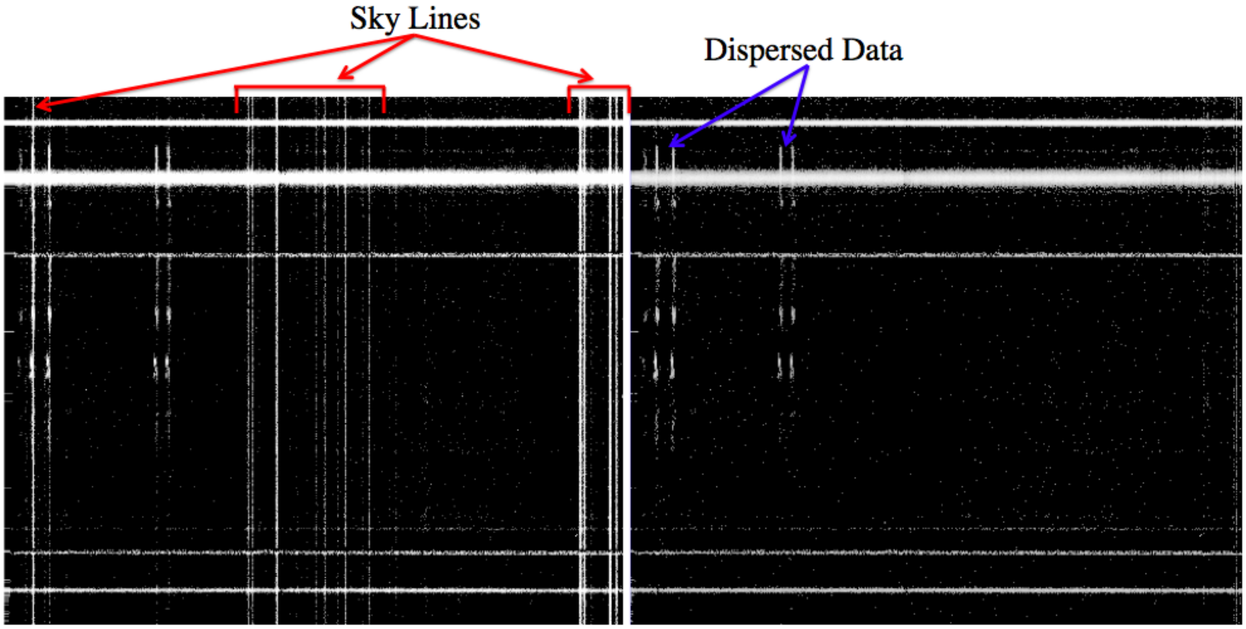

Figure 2-22: Portions of the spectroscopic image on a single chip before (left) and after (right) sky subtraction, showing that the sky lines were successfully removed.

trum file and a non-sky-subtracted data spectrum file using MATLAB. I read the data spectrum into the Interactive Spectral Interpretation System (ISIS) software [48], and loaded the sky spectrum as the background. ISIS adds the background spectrum to a model before it compares it to the data during fitting. While this is functionally equivalent to subtracting the sky from the data and comparing the sky-subtracted spectrum directly to the model, it avoids unphysical situations like occasional negative counts in the sky-subtracted data spectrum (these mostly occur in non-line regions because of noise in the measurements of small numbers of counts in both the data and sky regions), and works much better with the internal structure of ISIS.

2.5.2 Fitting and results

I chose four apertures from which to extract and fit spectra, corresponding to four different features of the remnant on the slit. These are shown in Figure 2-23. After examining the spectra, which are shown in Figure 2-25, I defined a fit model of a constant plus six gaussians

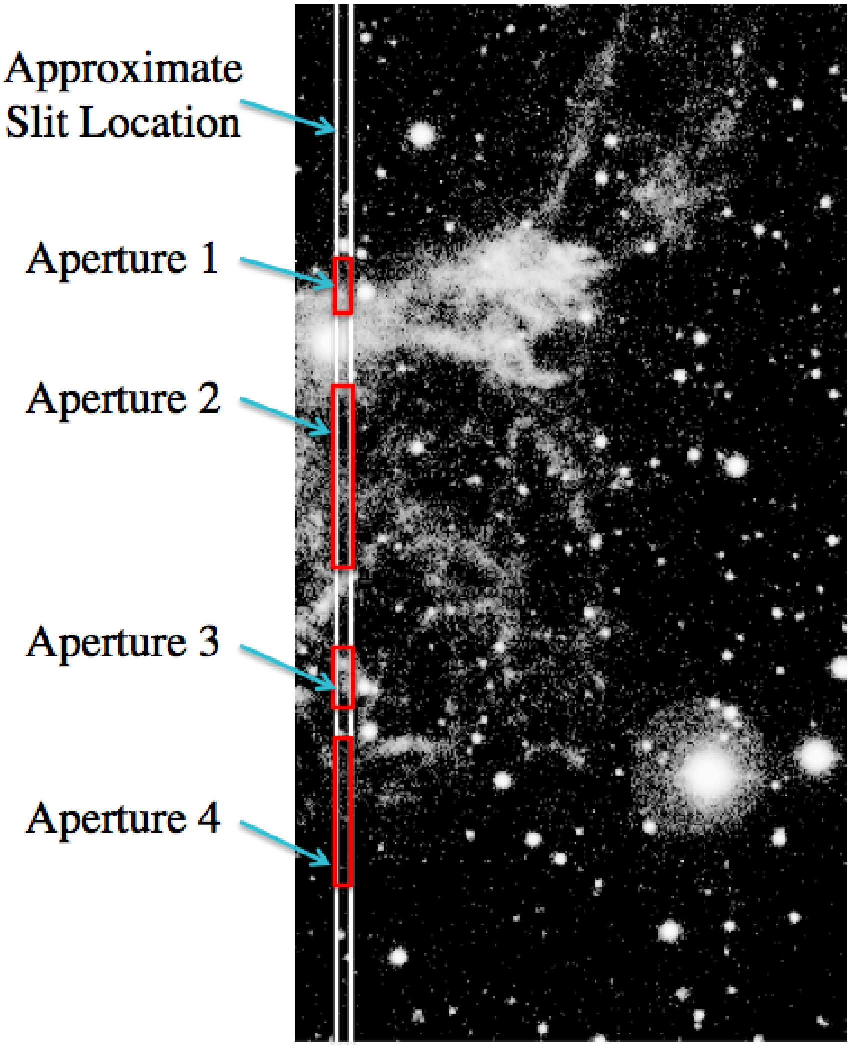

Figure 2-23: An image in the Hα filter of the region of the remnant used for spectroscopy with the approximate slit location marked in white (note that the width of the marked location of the slit is wider than the actual slit) and the apertures used for spectrum extraction highlighted in red.

(two for the N II a and b lines at 6549.9 and 6585.3 Å, two for the S II a and b lines at 6718.3 and 6732.7 Å, one for the narrow component of the Hα line, and one for a broad component of the Hα line, both at 6562.8 Å). For each line I used the rest wavelength as the starting value for its centroid, then allowed it to float within a range of 10-15 Å to allow for Doppler shifts. I fit the region between 6545 and 6750 Å (it would have been ideal to fit to lower wavelengths to better constrain the N IIa line shape and location, however the wavelength transformation used to remove distortions due to misalignment of the chip and the slit causes distortions along the edges of the chip, cutting off the usable data at 6545 Å). In future observations we may consider using a mask with the slit in a different position with respect to the chips to put our region of interest closer to the center of the chip than the edge.

The results of the fits are listed in Table 2.1. The background-subtracted spectrum with fit and residuals for aperture 1 is shown with the emission lines labelled in Figure 2-24. The spectra from all four apertures are shown in Figure 2-25. Zoomed-in views of the Hα line region in all four apertures are shown in Figure 2-26, with the total model and the fits for the broad and narrow lines overlaid.

We can derive the temperature of the emitting material from the width of its spectral line. The width of a line due to thermal motion is also known as Doppler-broadening because it arises from the Doppler shifts of the emitting atoms. The higher the temperature of the gas, the faster the constituent atoms move. Thermal velocities are non-relativistic, so only velocities along our line of sight are measurable and we can use the classical Doppler shift formulas. The frequency shift due to velocity is described by Equation 2.1, where I have defined positive velocity to be towards the observer.

$$f = f_0 \left(1 + \frac{v}{c}\right) \tag{2.1}$$

The distribution of velocities in a gas of temperature T is given by the Maxwell-Boltzmann distribution in Equation 2.2, where k_B is the Boltzmann constant and m_0 is the mass of the emitting atoms.

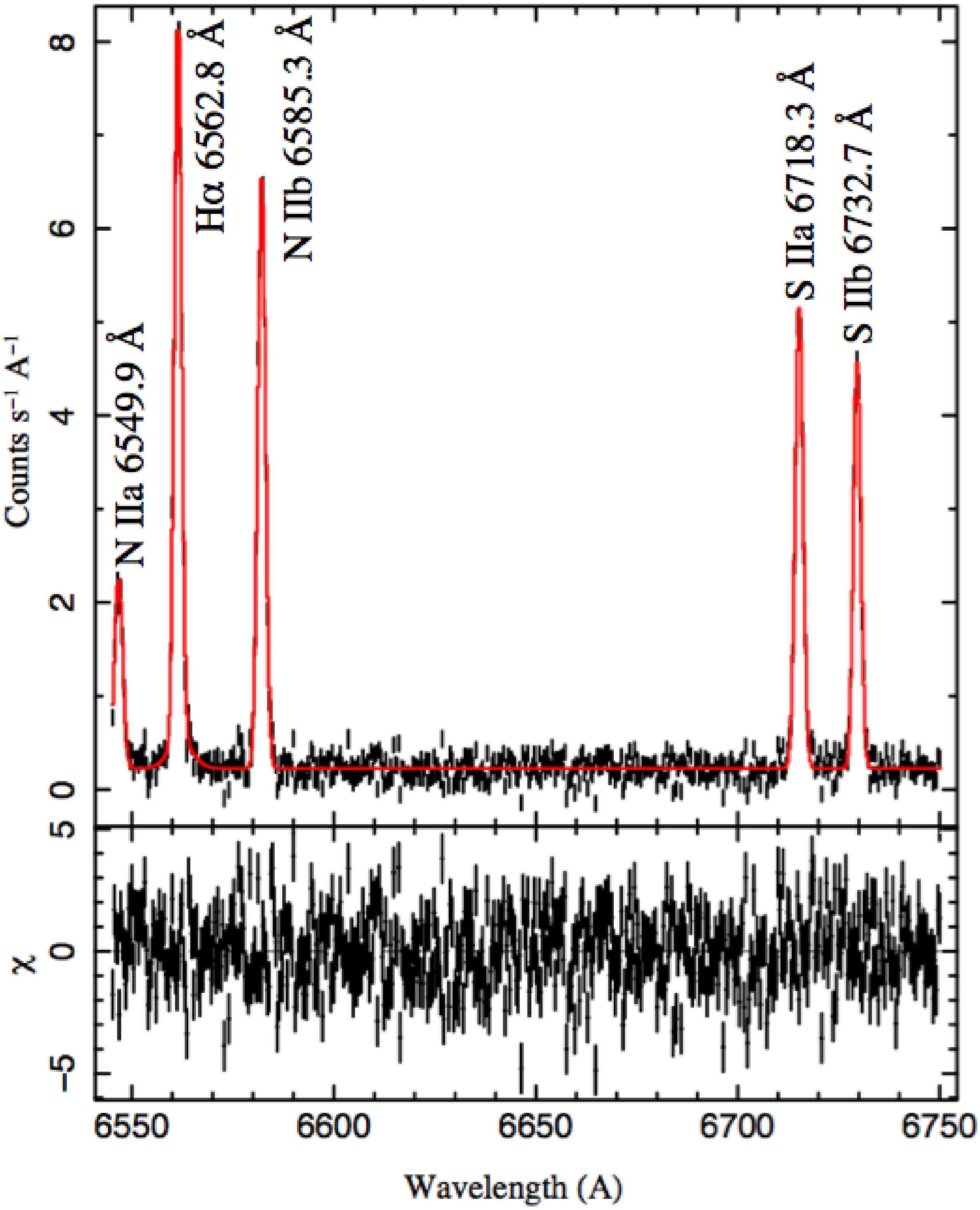

Figure 2-24: The background-subtracted spectrum extracted from aperture 1 (black) with fitted model (red) and residuals. The emission lines with their rest wavelengths are labelled.

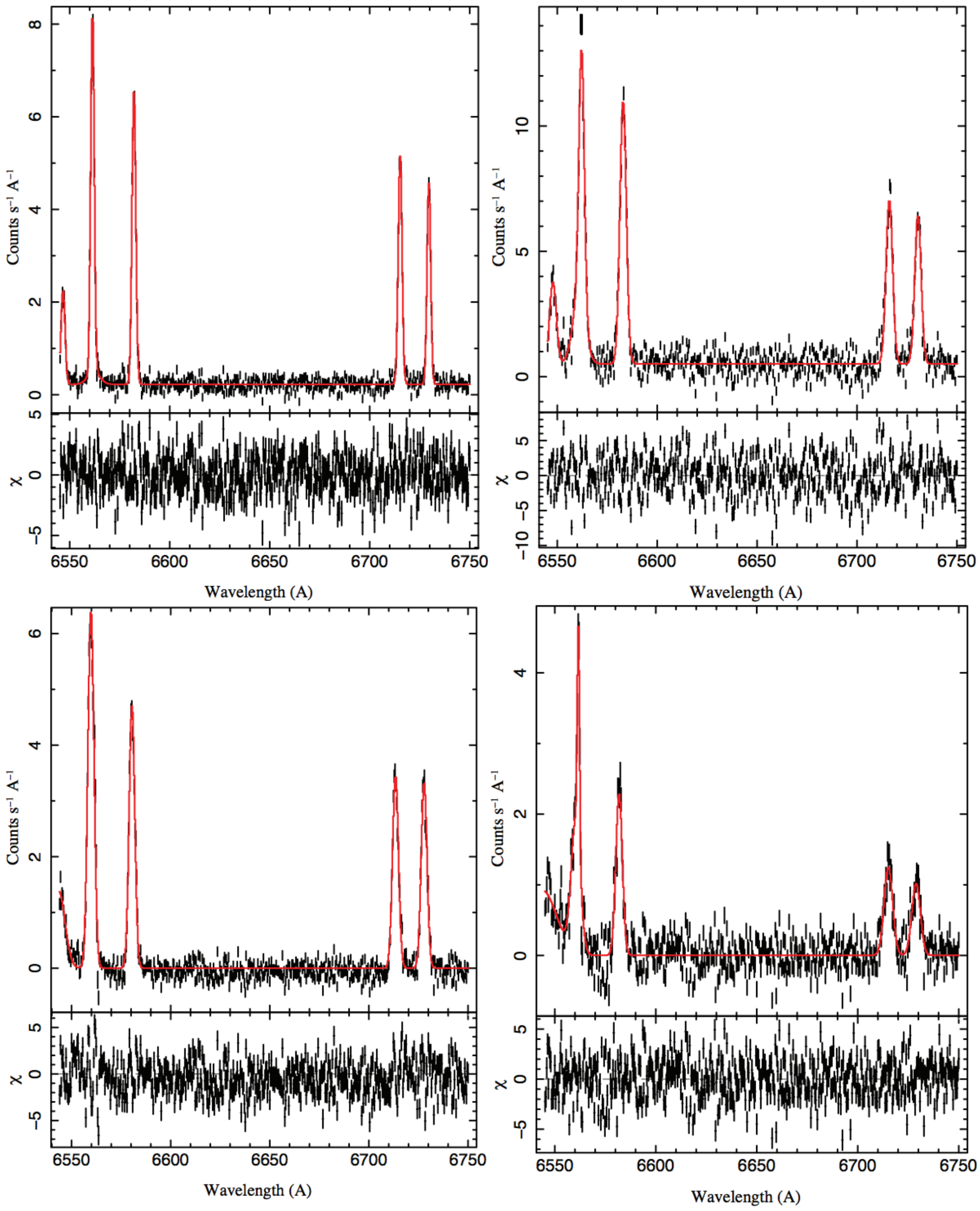

Figure 2-25: The background-subtracted spectra extracted from aperture 1 (upper left), aperture 2 (upper right), aperture 3 (lower left), and aperture 4 (lower right). Data points and residuals are plotted in black and models are plotted in red.

$$n(v)dv = N\sqrt{\frac{m_0}{2\pi k_B T}}e^{-m_0 v^2/2k_B T} \tag{2.2}$$

Using the Doppler equation in Equation 2.1, we can solve for the line of sight velocity in terms of the observed frequency f and the difference between the observed frequency and the rest frequency of the emitted light $\Delta f = f - f_0$, to get velocity $v = \frac{\Delta f}{f_0}c$. We can substitute this into the Maxwell-Boltzmann distribution to obtain the distribution of emission intensity as a function of frequency for a gas at temperature T in Equation 2.3.

$$I(f) = I_0 \exp\left[\frac{-m_0 c^2 (f - f_0)^2}{2k_B T f_0}\right] \tag{2.3}$$

This describes a Gaussian in frequency with a full width at half maximum (FWHM) given by Equation 2.4.

$$\Delta f_{FWHM} = \frac{2f_0}{c}\sqrt{2\ln(2)\frac{k_B T}{m_0}} \tag{2.4}$$

We can rearrange Equation 2.4 and transform from frequency to wavelength[7], to obtain the temperature of the gas as a function of known (m_0, c) and measured quantities $(\Delta\lambda, \lambda_0)$ in Equation 2.5.

$$k_B T = \left(\frac{\Delta\lambda}{\lambda_0}\right)^2 \frac{m_0 c^2}{8\ln(2)} \tag{2.5}$$

I calculated the temperatures associated with the measured Hα lines assuming pure Doppler broadening. These results are listed in Table 2.1, where errors are propagated using the simple Monte Carlo method described in Section 3.3. The temperatures corresponding to the broad Hα lines are fairly low compared with those measured in other observations of Balmer-dominated shocks, where temperatures are most often in the few-10 keV range [44], [45] (an interesting exception is a detection of a broad Hα component with temperature 0.13 keV in the Cygnus loop by [37], which is much more consistent with our measurements). The

---

[7] My change from frequency to wavelength here is not an exact equality since $\Delta f/f_0 = \Delta\lambda/\lambda$, however because the widths of the lines are small compared to the rest wavelength of the lines $\lambda \approx \lambda_0$, so Equation 2.5 is fairly robust in this situation

broad line in aperture 3 shows a much higher temperature than those in the other datasets, however its area is so low that it is not a convincing detection.

These results, coupled with the relative strength of the N II and S II lines, which are associated with radiative shocks [30], suggests that we are not observing Balmer-dominated emission in this observation, rather that the emission is due to radiative processes. Fesen, Blair, and Kirshner [30] predict that radiative shocks should have S II strengths 40-100% of the Hα strengths. Our measured S II strengths range from 81%-113% of the Hα strengths, consistent with a radiative shock. [30] also predicts the Hα/[N II] ratio should be less than three in radiative shocks. We measure Hα/[N II] ratios ranging from 0.59-1.20, again supporting the hypothesis that we are observing a radiative shock. In addition, the color image of the slit region shown in Figure 2-27 shows emission in the O III filter corresponding to radiative emission (shown in blue) over the entire slit region. The exact placement of the slit on the image was coincidental. At the time we did not have detailed information as to the exact locations of the Hα and O III emission and based our choice of location on the brightest, most identifiable Hα emission. Now that we have a full analysis chain built up for this type of data, we could easily perform better determination of promising locations at Magellan for future observations.

Seraph and Seaton [89] show a correlation between the ratio of the S II lines and the density of the plasma in radiative shocks. Using our measurements (giving a λ6731/λ6717 ratio between 0.805-0.94) and the information in [89], we obtain electron densities $n_e \leq 1000\text{cm}^{-3}$ at a temperature of T_e=10^4K. The values of the [N II]/Hα, [S II]/Hα, and λ6731/λ6717 ratios measured in our data are consistent with several of the values listed in Table 5 of [30] measured in examples of evolved, radiative shocks in SNRs.

Longmore et al. [67] studied three optical filaments in a similar area with radial velocities near -35 km/s. CO emission to the east of this region detected by Brand et al. [12] showed a radial velocity of -38 km/s. Measuring the line shifts and converting them to velocity using the Doppler formula, I measure an average radial velocity of ∼-112 km/s in aperture 1, ∼-85 km/s in aperture 2, ∼-202 km/s in aperture 3, and ∼-149 km/s in aperture 4.

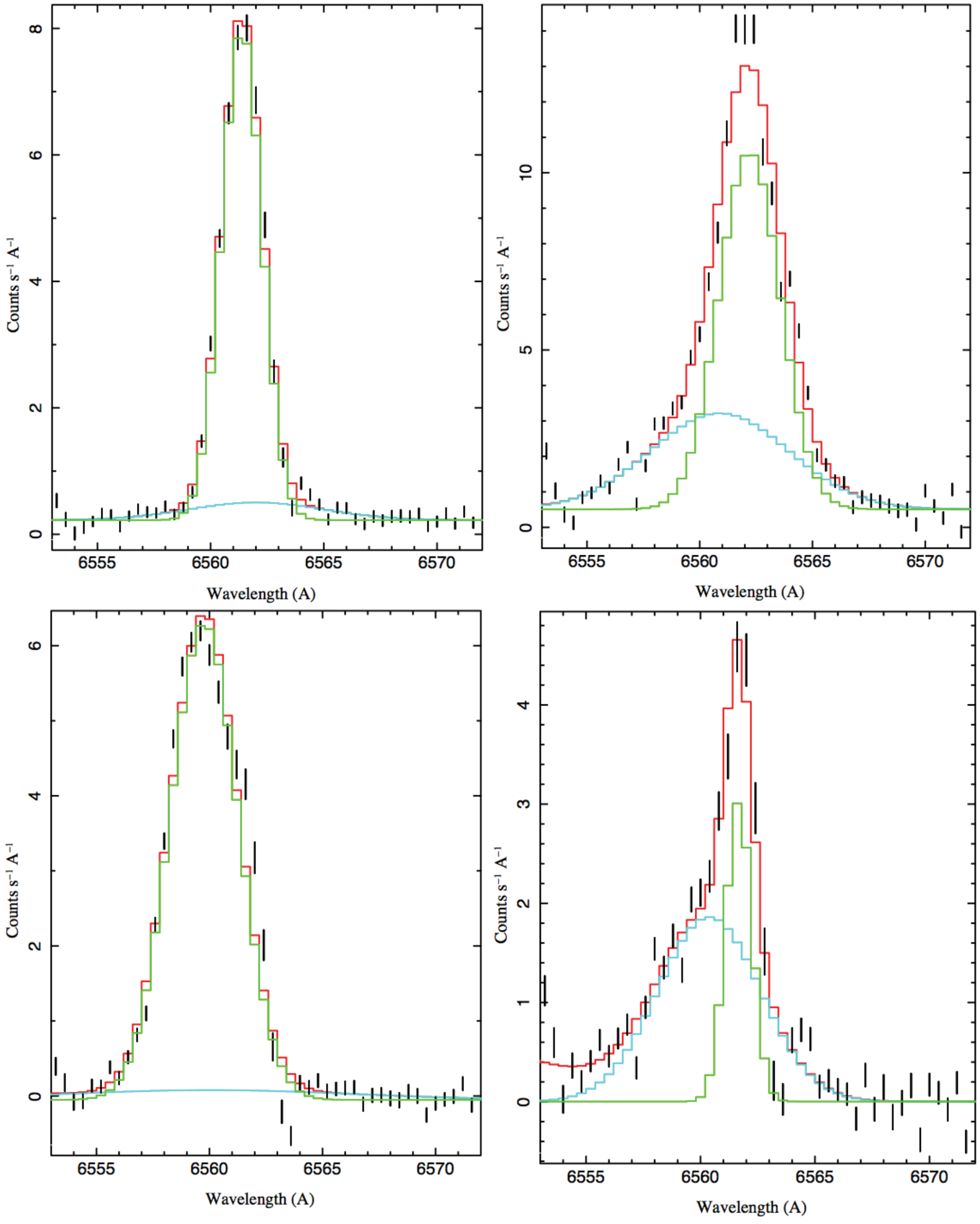

Figure 2-26: Zoomed-in plots of the Hα lines from each of the four apertures. Aperture 1 is shown in the upper left, aperture 2 is shown in the upper right, aperture 3 is shown in the lower left, and aperture 4 is shown in the lower right. Data points are shown in black, the overall fit is shown in red, the narrow component fit is plotted in green and the broad component fit is plotted in light blue.

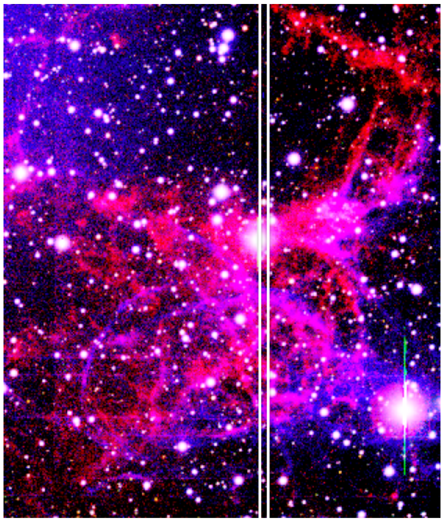

Figure 2-27: The three color image from field three with the approximate slit location shown in white. Unfortunately, the slit only covers regions with strong radiative emission (blue) in addition to the strong Hα emission (red) identified in initial imaging.

Interestingly, the Hα lines all showed lower radial velocities than the S II and N II lines in the same apertures. I measured the average radial velocity of the Hα lines in each aperture and obtained $\sim$-51 km/s in aperture 1, $\sim$-57 km/s in aperture 2, $\sim$-133 km/s in aperture 3 and $\sim$-79 km/s in aperture 4. These disparities imply that the Hα line emission may be coming from gas with a different velocity distribution than the emitting material for the N II and S II lines. However, the velocity widths measured for the narrow component of the Hα line and the N II and S II lines are consistent with each other (except in some cases in the N IIa line where the fit is not well-constrained by the data), implying that the distributions are similar. None of the emission I measured has radial velocities consistent with the filaments measured by Longmore and Brand.

In order to investigate further whether or not a broad Hα component is present, I also fit models without the broad line. The spectra in Figure 2-26 show a stronger broad component in apertures 2 and 4 than in apertures 1 and 3 so we would expect the fits of 2 and 4 to suffer more when removing the broad component and refitting. This is supported by the data in that the resulting $\Delta\chi^2_{reduced}$ is +0.1 and +0.03 for the fits of apertures 1 and 3, respectively, and +1.15 and +0.78 for apertures 2 and 4, respectively, when fitting a model with no broad component compared to the model discussed above. In apertures 2 and 4 there appears to be a clear, separate, warmer distribution of hydrogen atoms moving into our line of sight, in addition to the more stationary, cooler distribution responsible for the narrow line (though due to the temperature of the warmer distribution and the presence of N II and S II lines in the spectra, it is unlikely that this emission probes the temperature distribution of the post-shock protons through charge exchange). In apertures 1 and 3 there is not a convincing detection of a broad component.

Table 2.1: Measurements of line centroids, widths, areas, and derived temperatures of emitting material from each of the four apertures.

Aperture 1				
Line	Center (Å)	FWHM (km/s)	Area (photons/s/cm^2)	kT (eV)
N IIa	6546.69 ± 0.04	$560.06^{+6.46}_{-30.14}$	$1.004^{+0.001}_{-0.065}$	
Hα narrow	6561.38 ± 0.02	94.53 ± 2.15	17.3 ± 0.5	16.75 ± 0.72
Hα broad	$6562.01^{+0.55}_{-0.52}$	$322.3^{+107.4}_{-53.7}$	2.1 ± 0.5	$194.69^{+233.67}_{-45.14}$
N IIb	$6582.10^{+0.01}_{-0.02}$	$101.70^{+2.14}_{-1.07}$	15.2 ± 0.2	
S IIa	6715.22 ± 0.02	100.74 ± 2.10	12.0 ± 0.2	
S IIb	6729.58 ± 0.02	95.23 ± 2.09	9.9 ± 0.2	
Aperture 2				
Line	Center (Å)	FWHM (km/s)	Area (photons/s/cm^2)	kT (eV)
N IIa	6547.86 ± 0.05	179.81 ± 6.46	13.7 ± 0.4	
Hα narrow	6562.21 ± 0.03	145.02 ± 5.37	$34.3^{+2.3}_{-2.1}$	39.37 ± 2.83
Hα broad	$6560.88^{+0.20}_{-0.26}$	$330.87^{+19.34}_{-15.04}$	$20.9^{+2.0}_{-2.2}$	$205.28^{+25.95}_{-16.91}$
N IIb	6582.97 ± 0.02	171.29 ± 2.14	42.2 ± 0.5	
S IIa	6716.19 ± 0.03	174.20 ± 3.15	27.3 ± 0.4	
S IIb	6730.49 ± 0.03	167.54 ± 3.14	$23.7^{+0.4}_{-0.5}$	
Aperture 3				
Line	Center (Å)	FWHM (km/s)	Area (photons/s/cm^2)	kT (eV)
N IIa	$6543.5^{+0.2}_{-0.0}$	344.4 ± 21.5	$11.5^{+0.5}_{-0.9}$	

Hα narrow	$6559.76^{+0.02}_{0.03}$	160.06 ± 2.15	23.8 ± 0.5	48.08 ± 1.50
Hα broad	$6560.0^{+0.3}_{-0.0}$	$676.77^{+171.88}_{-118.17}$	2.1 ± 0.6	$859.11^{+554.52}_{-209.94}$
N IIb	$6580.48^{+0.02}_{-0.03}$	155.23 ± 2.14	17.3 ± 0.3	
S IIa	$6713.44^{+0.03}_{-0.05}$	160.55 ± 3.15	$13.4^{+0.2}_{-0.3}$	
S IIb	$6727.86^{+0.03}_{-0.04}$	157.07 ± 3.14	$12.6^{+0.2}_{-0.3}$	
Aperture 4				
Line	Center (Å)	FWHM (km/s)	Area (photons/s/cm^2)	kT (eV)
N IIa	$6544.0^{+1.9}_{-0.5}$	$753.4^{+129.2}_{-150.7}$	$16.1^{+2.4}_{-4.0}$	
Hα narrow	6561.75 ± 0.05	55.86 ± 5.37	$4.4^{+0.5}_{-0.6}$	$5.82^{+1.33}_{-0.94}$
Hα broad	6560.38 ± 0.13	$230.96^{+18.26}_{-11.82}$	$10.5^{+0.7}_{-0.8}$	$100.04^{+18.30}_{-9.04}$
N IIb	6581.86 ± 0.06	$173.43^{+5.35}_{-6.42}$	9.3 ± 0.3	
S IIa	$6715.15^{+0.11}_{-0.10}$	223.52 ± 10.49	6.7 ± 0.3	
S IIb	$6728.91^{+0.14}_{-0.13}$	$219.90^{+12.57}_{-11.52}$	5.4 ± 0.3	

2.6 Outlook

The images in Section 2.5 provide an interesting picture of G296.1-0.5 in terms of charge exchange. We have identified multiple filaments exhibiting Hα emission and one strong candidate for a Balmer-dominated shock. The spectroscopy does not show conclusive evidence of charge exchange, but this is possibly because the position of the slit was over a region where radiative processes are active (not over the best BDS candidate identified in the remnant).

The information from this observation shows some promising hints of what could be obtained from another observation. On the imaging side, now that we have imaged the entire area and know where filaments and bright stars are located, we could repeat the imaging with the fields located in such a way as to avoid the bright stars to make a much cleaner final image. On the spectroscopy end, we have identified better candidates for BDSs than our original spectroscopy location, so it would be useful to take spectra of the filaments in fields 1 and 2, at different locations on the field 3 filament, and possibly on the small filament in field 5. With the data from our initial observation we have a strong case for another proposal to obtain this data, which should yield illuminating results.

Chapter 3

XMM-RGS Observations of G296.1-0.5

While Balmer Dominated Shocks provide valuable information on charge exchange in supernova remnants, they are not visible in every SNR. BDSs will only occur in very young, fast shocks where hydrogen in the environment has not yet been ionized. We also require low hydrogen column densities in order to observe BDSs and measure their spectra. These requirements are not met in the majority of SNRs. Most SNRs are very bright in the X-ray band, so in order to measure charge exchange in a broader sample of remnants, we will need to study the X-ray signatures of CX described in Section 1.6.1. Measurement of the line ratios of He-like triplets requires high spectral resolution, which is not quite yet achievable in the X-ray band. In this chapter I will discuss a spectral study of charge exchange in G296.1-0.5 using the best X-ray spectroscopy currently available.

3.1 The *XMM*-RGS Instrument

The *XMM-Newton* satellite was launched by the European Space Agency (ESA) in December, 1999. The 10 meter long, 4000 kg spacecraft is made up of two payload modules connected by a long carbon fiber tube, which acts as the optical bench. Light enters the

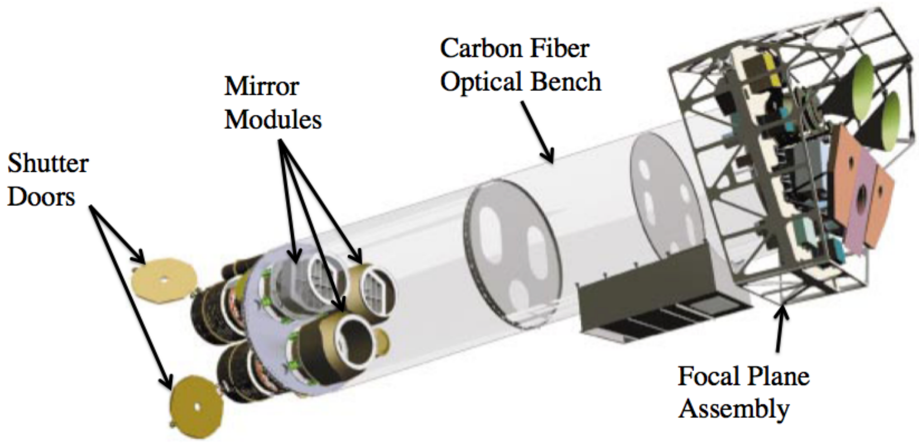

Figure 3-1: A CAD rendering of the *XMM* spacecraft (reprinted from [56]) with labels indicating several major features

spacecraft in the spacecraft service module, which houses many of the spacecraft subsystems, the optical monitor instrument, two redundant star trackers, and three X-ray mirrors. The light is focused by the mirrors through the carbon fiber tube into the second payload module: the focal plane assembly. This assembly holds two reflection grating spectrometer (RGS) readout cameras, one EPIC PN detector and two EPIC MOS detectors for imaging [56]. A labelled CAD rendering of the spacecraft is shown in Figure 3-1.

Each X-ray mirror module consists of 58 Wolter I optics (see Section 4.6), nested in a coaxial and confocal configuration with a focal length of 7.5 meters. Each of the optics is a superpolished, gold-coated mandrel, manufactured using a nickel electroforming technique. The 58 mirrors are bonded to 16 spokes. An electron deflector at the exit aperture acts as an electron broom (we use a similar technique in the *Micro-X* payload), and X-ray baffles act as collimators to block stray light from entering the optical path [56].

The specifics of the RGS system are described in detail in [25]. Two of the three nested mirror sets feed identical reflection grating spectrometers (RGS) while the third feeds an EPIC camera. Each grating stack is made up of 182 precisely aligned reflection gratings, which are optimized to detect K-shell transitions of C, N, O, Ne, Mg, and Si, and the L-shell

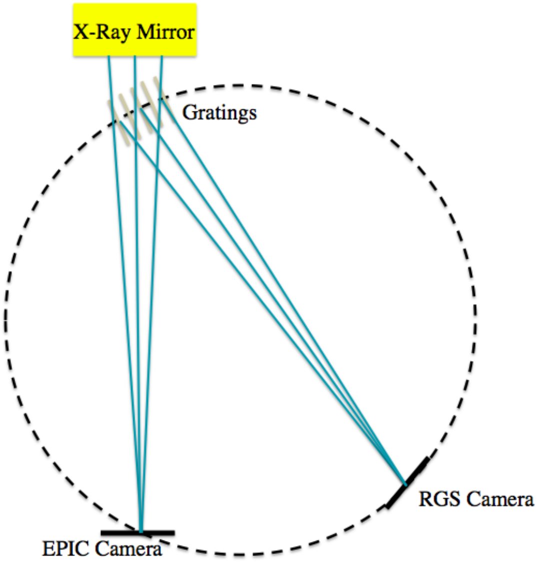

Figure 3-2: A diagram of the optical path through the RGS. The light is focused by the mirror onto the RGS. The diffracted light is focused onto the RGS camera while the light that passes through is focused onto the EPIC imaging camera. Both camera CCD arrays are located on the 'Rowland circle' containing the dispersion grating and focus points for the incoming X-rays.

transition of Fe with resolution $E/\Delta E$ of 100-500 in the 0.3-2.1 keV range, with a maximum effective area of 140 cm^2 at 827 eV.

The grating intercepts about half of the incoming light. The light that passes through is focused onto EPIC cameras for imaging as shown in Figure 3-2. The gratings are oriented such that the angle of the incident X-rays with respect to the surface of the grating, α, is the same for each of the gratings. Since the X-rays incident on the gratings are converging, the gratings are oriented in a trapezoidal shape.

The RGS gratings disperse the incoming light onto nine large format, back-illuminated CCDs. The first and second orders overlap on the detectors, but can be separated out using the energy resolution of the CCDs. The location a photon arrives on the CCD array depends on its dispersion angle β. This is related to the wavelength of the photon by Equation 3.1, where m is the dispersion order, d is the groove spacing of the grating, and α is the incident angle of the photon on the grating.

$$m\lambda = d(\cos\beta - \cos\alpha) \tag{3.1}$$

The CCDs in the array are cooled to −120°C to reduce possible radiation damage and dark current. This cooling is accomplished by a two-stage radiator along with three nested thermal shields around the CCD bench. The CCDs have an energy resolution of ∼160 eV at 2 keV, which allows distinction of overlapping orders.

Each reflection grating array has 182 identical gratings, each of which is 10×20 cm. The grating substrates need to be thin to minimize obscuration of the field. They are made of 1 mm thick SiC with stiffening rings in the back, covered in 2000 Å of gold on the reflection surface. The groove density is ∼ 646 grooves/mm in the center of the grating. The gratings are aligned to 1 μm tolerance for best energy resolution.

A dispersive optic is not ideal for observing extended sources, as the physical size of the source degrades the energy resolution. In the following analysis, we use a convolution to predict the degradation of the dispersed spectrum by the physical extent of the source.

3.2 Data reduction

High spectral resolution studies of supernova remnants in the X-ray band are currently limited by technology. SNRs are, in general, extended sources, so dispersive spectra are degraded by the extent of the source (light from a particular wavelength from one region of the remnant will be dispersed to the same location as light from a different wavelength in another region of the remnant). The only instances in which dispersive instruments can be used to study SNRs is when small, bright features can be targeted and distinguished from other emission in dispersed data. This has been done with fairly good success in projects like studying the bright knots in Cassiopeia A [85] and the Puppis A Bright Eastern Knot (BEK) [58], however not with the spectral resolution achieved in dispersed spectra of point sources.

For this analysis, I utilized *XMM-Newton*/RGS data reduced and studied by Castro et al. [16] from the RGS 1/2 in an observation of the G296.1-0.5 SNR during period A06 (ObsID 0503220101 observed July 7, 2007). They reduced the data with SAS[1] version 9.0.0, starting from the observational data files. Events creating charge on one to four pixels are included while those causing charge spreading across more than four pixels simultaneously are thrown out. In order to filter out high background level data, they create a count rate histogram and remove periods of data where the number of counts per second exceeds 0.35 counts/s (a standard limit). The exposure was 15.2 kiloseconds, with 6.4 kiloseconds of effective exposure after filtering. I binned the spectrum with a minimum 20 counts per bin before fitting.

The RGS pointing was in the NW corner of the remnant (corresponding to our optical field 1) and is shown in Figure 3-3. The extraction region is a 2.8' wide cut across the NW filament, centered at an RA and DEC of 11:50:56.748, -62:18:52.25. The background was obtained with the SAS task `rgsbkgmodel`, which derives a model of the background from linear combinations of background templates based on empty sky fields, along with details of the observation parameters.

I performed the spectral fitting in ISIS version 1.6.2-27 [48], which encompasses all of the models available within XSPEC, but with added programmability and parallelization. For each fit, I convolved the model spectrum with the convolution model `rgsxsrc`[2], which convolves the spectral model with an angular structure function defined by a CCD image of the source. In this observation, this results in a degradation of the spectral resolution by $\Delta E/E \sim 0.02$, when using the angular structure file developed for this purpose by Castro et al. [16].

---

[1] SAS is distributed by the *XMM-Newton* Science Operations Center at `http://wmm.esac.esa.int/sas/`

[2] Code developed by Andy Rasmussen of Columbia University

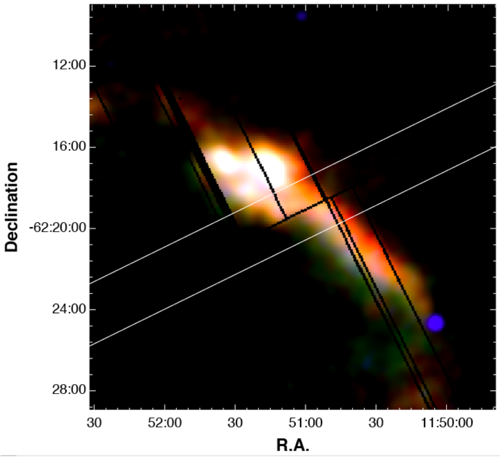

Figure 3-3: An exposure-corrected three-color image of the RGS pointing on the NW shell of G296.1-0.5 created with EPIC PN data smoothed with a Gaussian function of width 12". Red corresponds to emission in the 0.3-0.7 keV band, green to emission in the 0.7-1.0 keV band, and blue to emission in the 1.0-3.0 keV band. The relative intensity levels of the three color images were set to highlight the hard compact source to the lower right of the field and to show the spectral uniformity of the emission from the shell. The white lines indicate the position and direction of the RGS dispersion. (Reprinted from [16].)

3.3 Fit results

In this analysis, I follow the general procedure of a similar charge exchange analysis on the Puppis A BEK by Katsuda et al. [58]. The authors use dispersed data from the *XMM-Newton* RGS to analyze line ratios in X-ray triplets. Compared to emission caused by thermal processes, charge exchange will produce anomalously high forbidden to resonance line ratios as discussed in Section 1.6.1. Katsuda et al. measure the line ratios of the He-like triplets in the dispersed dataset by fitting to the data a Bremmstrahlung model describing a thermal continuum along with several gaussians to describe line emission, then compare the measured line ratio derived from the relative strength of the gaussians to the ratios predicted by a plausible set of thermal plasma models defined by fits of these models to low spectral-resolution data across the remnant by Hwang et al. [51]. I will follow a very similar procedure for the G296.1-0.5 data, using only the OVII triplet, since this is the strongest triplet, and the only one with the statistics to allow for a significant measurement.

I fit the RGS data with a Bremmstrahlung model plus 31 Gaussians, all multiplied by the absorption model `phabs` to account for interstellar absorption. I froze the widths of all of the gaussians to 0.1 eV since the width of the lines is dominated by the width of the dispersed feature. I fixed the locations of the C VI, N VI, N VII, and O VII triplets lines, along with the location of the lines from O VIII based on the identification of these spectral lines by Castro et al. [16], and approximated the locations of all other obvious lines in the spectrum by eye, allowing their centroids to float within 20 eV windows. I set an initial value of n_H to $0.02\times10^{22}\text{cm}^{-2}$, since this is the value derived by the fits in [16], but allowed this value to float. The data with fit ($\chi^2_{reduced} = 1.05$) and residuals from this model is shown in Figure 3-4. I also attempted the fit allowing the location of the O VII triplet to float with the locations of the lines with respect to each other fixed, which did not produce an improved fit. After initial fitting, I ran the ISIS function `conf_loop` to obtain a 68% confidence intervals for the strength of the forbidden and resonance lines of the OVII triplet. This function moves a parameter in small steps, refitting at each step and monitoring the change in χ^2 (restarting the search if a better fit is achieved). A zoomed-in view of the OVII line with the overall fit and the profiles of the fit triplet lines is shown in Figure 3-5.

In order to compare the measured F/R ratio from the data to F/R ratios from plausible thermal models, I produced fake datasets using a variable non-equilibrium ionization (`vnei`) model. I chose this model (as opposed to the `vpshock` model used by Katsuda et al. [58]) because the model was successfully applied to several regions of CCD spectra from the EPIC cameras onboard *XMM-Newton* in the study of G296.1-0.5 by Castro et al. [16]. The results of the fits in this study give a range of plausible thermal models with which to compare the measured line ratio from the data.

In order to obtain the F/R ratio from a particular thermal model, I created a fake dataset using the ISIS function `fakeit`. I assigned the Redistribution Matrix File (RMF) of the actual data, which includes the information usually found in the Ancillary Response File (ARF), and assigned the fake dataset the same exposure as the RGS measurement. I loaded an absorbed `vnei` model convolved with the profile of the filament (to make the best

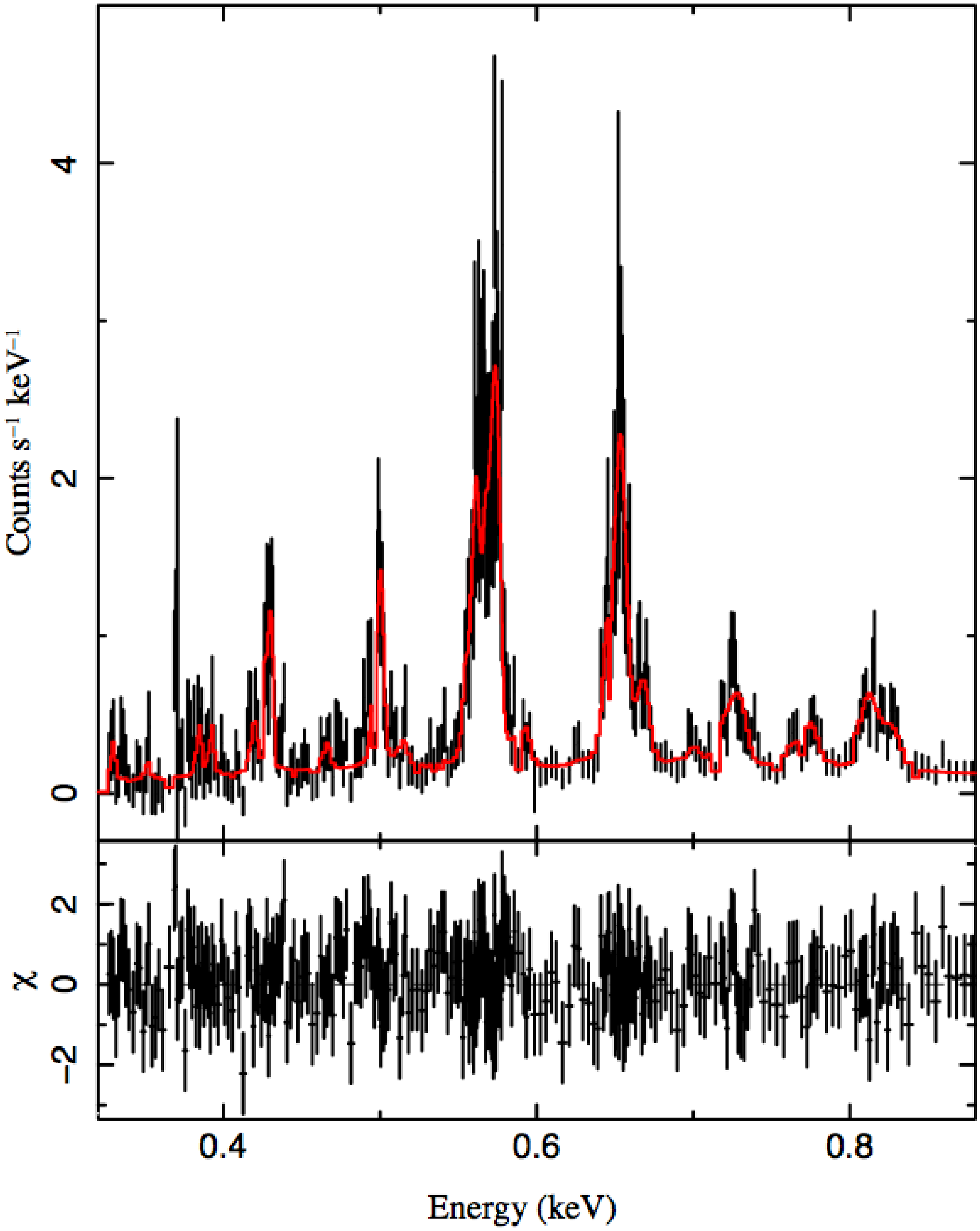

Figure 3-4: The RGS spectrum of the NW filament in G296.1-0.5, with fit of an absorbed Bremmstrahlung plus 31 gaussians overplotted in red. Residuals are shown below.

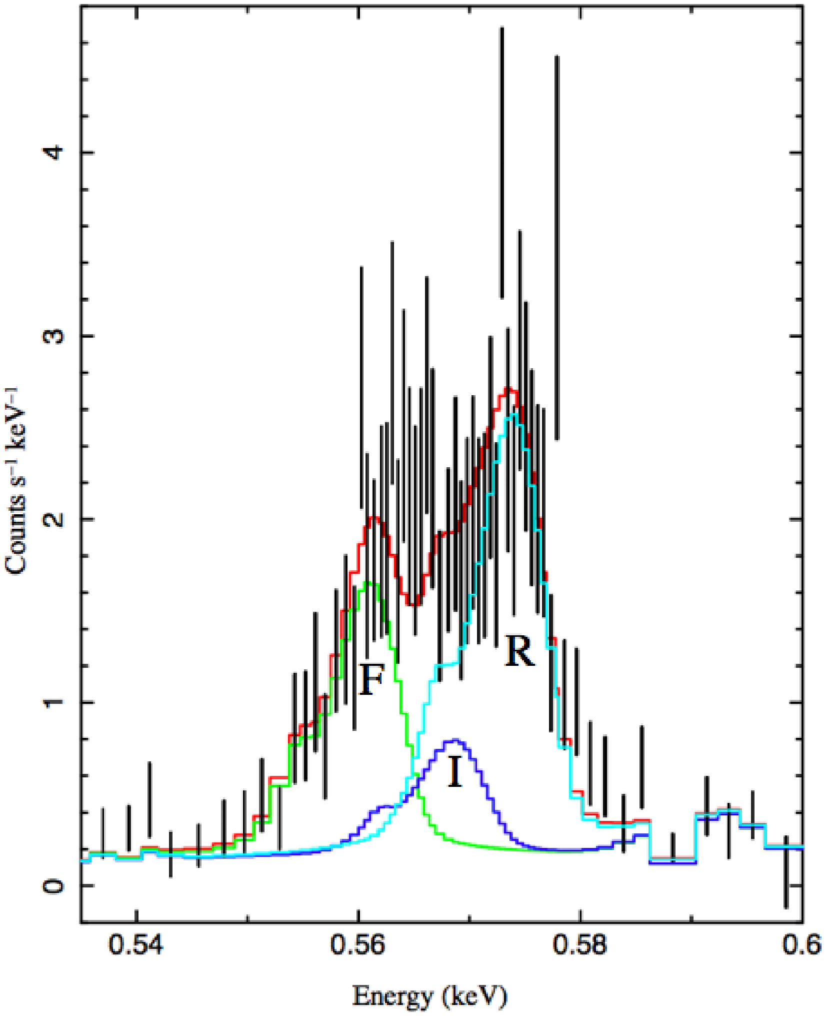

Figure 3-5: A zoomed-in view of the OVII line with the overall model plotted in red, the forbidden line plotted in green, the resonance line plotted in cyan, and the intercombination line plotted in blue.

approximation of what we would measure with the RGS if the loaded model spectrum were incident from the remnant), setting the abundances and hydrogen column density equal to those derived in the `vnei` fit of region a3 in [16] (a long, thin region along the length of the NW filament), and set the temperature and ionization age to values in the plausible ranges (kT=0.55-1.00 keV, $n_e t = 0.11 \times 10^{11} - 0.51 \times 10^{11} \mathrm{s/cm}^3$) taken from the range of values found across the remnant by Castro et al. [16]. Calling `fakeit` creates a fitable dataset that is the closest approximation to what we would measure if the incoming spectrum were described perfectly by the loaded `vnei` model.

Once a fake dataset was created, I loaded the absorbed Bremmstrahlung plus 31 gaussians convolved with the profile of the filament in the dispersion direction used to measure the F/R of the actual data, and used it to measure the F/R of the fake data by the same method. I performed this procedure with models covering the full space of temperature and ionization age defined by the fits in [16] to obtain a range of plausible F/R ratios for thermal models with no charge exchange. The measured F/R for the OVII line in the data was $0.626^{+0.176}_{-0.104}$. The plausible thermal models gave F/R ratios for the O VII line between 0.015-0.35. The data has a higher F/R ratio in the O VII triplet than any of the plausible thermal models by just over 2 sigma. The fit also found a column density of $\sim 4 \times 10^{20} \mathrm{cm}^2$, which is a factor of two higher than that derived by Castro et al. [16], but supports their finding of a relatively low column density, as opposed to the fairly high column density reported by Hwang et al. [50].

Some care is necessary in deriving the one sigma error ranges for the data F/R measurement. The fits give asymmetrical errors for the F and R line fluxes. A common practice in combining measurements linearly, is to use standard error propagation formulas like those derived in Bevington and Robinson [8], propagating the negative and positive errors separately, which not only has no statistical justification, but also produces incorrect results in most cases [3]. In order to obtain more accurate numbers for the uncertainties on the F/R ratio, I ran a simple Monte Carlo simulation, drawing a set of about 1.5 million points from each of the asymmetric distributions defined by the values and uncertainty ranges derived by the fits for the F and R lines, assuming they are gaussian distributed. I then divided the random values in these sampled distributions to get a sample of 1.5 million F/R values. I made a histogram of these values and fit a gaussian to each side of the distribution to find the sigma of the distribution on each side of the measured value. Running this simulation on a symmetric error distribution for F and R reproduced the uncertainties derived using the error propagation formulas in [8], verifying the method.

While charge exchange can produce anomalously high F/R ratios in X-ray triplets, there are several other mechanisms that could also produce this effect as discussed in Section 1.6.1. Katsuda et al. [58] explore several of these in depth, and I follow their analysis to rule out some of these mechanisms. Mechanisms that can result in enhanced F/R ratios with respect to pure thermal models are:

- Resonance line scattering
- Recombinations of H-like ions and electrons
- Inner-shell ionization of Li-like ions
- Charge exchange

First, I fit a `vnei` model to the data, ignoring the O and N line regions so that anomalous triplet ratios would not affect the fit. Then I faked a spectrum with the resulting `vnei` model and fit the continuum plus gaussian model to measure the O VII F and R line fluxes to ascertain whether or not the anomalous F/R ratio was due to an increase in F or a decrement in R from the plasma model that best fits the continuum data from the source. This showed that the data forbidden line flux is larger than the thermal model forbidden line flux *and* the data resonance line flux is lower than the thermal model resonance line flux.

The reduction of the resonance line could be due to a mechanism like resonance line scattering, in which the resonance line is preferentially scattered out of the line of sight. Resonance lines have higher optical depths, so if the optical depth is high enough and the plasma depth long enough, the flux of the resonance line could be reduced enough to skew the F/R ratio away from thermal values [58]. The evaluation of the optical depths involved is beyond the scope of this work, so this mechanism has not been ruled out.

Recombination and inner-shell ionization of Li-like ions can increase the forbidden line flux of a He-like triplet, skewing the F/R ratio higher. Recombining plasmas have been shown to produce shifted ratios like those we have observed [118]. The spectra for a recombining plasma would be much more consistent with a collisional ionization equilibrium model. In order to test whether or not this could be the case here, I fit a `vequil` model to the data and found that it was not able to fit the entire spectrum. The model prefers a very low electron temperature with extremely large abundances to bring up the line strengths at higher energies. When including data in the 1.4-2.5 keV range, the model is unable to find a reasonable fit, ruling out the possibility of a recombining plasma as a cause of the anomalous line ratios.

Inner-shell ionization processes of Li-like ions, in addition to creating enhanced F/R ratios, will also create an enhancement in the forbidden-to-intercombination (F/I) ratio compared to thermal models, because it strengthens the forbidden line flux [80]. I measured the F/I ratios in the data and the plausible thermal models as discussed above and found the F/I ratios to be consistent with several ranges of thermal models. The intercombination line is much smaller than the resonance or forbidden lines and is not individually resolved, so while the ratios are consistent between the data and thermal models, making inner-shell ionization an unlikely cause of our measured F/R ratios, higher resolution data would be very valuable in more definitively ruling out this mechanism. We would also expect strong Li-like ion satellite lines if inner-shell ionization were a significant effect, which high spectral resolution data could resolve if present.

Our measurements show that charge exchange is a viable mechanism for the observed anomalous F/R ratios in the G296.1-0.5 spectrum. While more follow-up and higher resolution data is needed to draw a firm conclusion, this is an indication that charge exchange may indeed be active and contributing significant X-ray emission to the spectrum of the NW X-ray lobe of the SNR G296.1-0.5.

The optical spectroscopy performed in Chapter 2 focused on a filament in the SW region of the remnant. RGS spectra of this region were not available because of the roll angle of the RGS during the *XMM* observation, and because of contamination from a bright flaring source in the region in a subsequent observation. We plan to obtain optical spectra of the promising BDS candidate in the NW corner of the remnant (optical field 3) in a future *Magellan* observation, which will allow for comparison between this X-ray analysis and optical signatures of charge exchange in the same region of the remnant. It would also be valuable to obtain an RGS observation of the SW filament in order to have both optical and X-ray measurements in multiple regions.

3.4 Studying CX Emission with *Micro-X*

The field of X-ray astrophysics has long yearned for a high spectral resolution imaging spectrometer for extended sources. With the demise of *Astro-E* upon launch and the failure of the XRS instrument on *Suzaku* shortly after flight, the field has been close to this threshold for several years. Much of the delay is due to the difficulty of engineering flight systems capable of producing high resolution spectra. In fact, the *Astro-H* satellite, currently scheduled for launch sometime in 2015, has encountered several delays due to the difficulty of creating a robust, low temperature system for spaceflight. While the instrumentation development is difficult for these maturing technologies, the reward is great, providing us with the opportunity to revolutionize the field of X-ray supernova research (along with the studies of other extended sources like galaxy clusters).

The field of X-ray SNR spectral research is currently limited to fitting global plasma models (like the `vnei` model used in this work) to low resolution data and performing line ratio analyses on higher resolution, but still degraded, dispersed data from less extended portions of SNRs. As I discussed in Section 3.3, there is a plethora of physical processes that can explain a departure from global plasma models that are currently the workhorses of the field. These models are approximations of very complex systems, and high-resolution data will almost certainly provide insights far beyond the models' predictions.

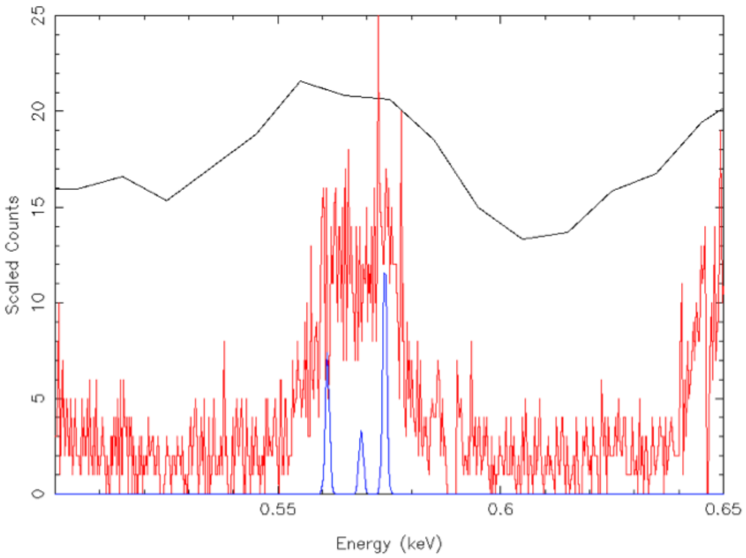

Figure 3-6: The He-like oxygen triplet in the G296.1-0.5 spectrum measured with the EPIC CCD on *XMM* (black) and the RGS on *XMM* (red). The underlying model lines with no continuum component (blue) are plotted with a width of about 1 eV corresponding to thermal broadening in a plasma with temperature 0.62 keV.

While conclusive evidence for charge exchange in supernova remnants has been found in the optical band, as described in Section 1.5, this same conclusive evidence cannot be obtained in the X-ray band until an instrument with high spectral resolution, capable of producing spectra of extended sources, is available. A comparison of measurements with current instruments and an underlying model is shown in Figure 3-6. The analysis in this chapter, [58], [57], and other similar studies provides tantalizing clues to the possible production of X-ray emission due to charge exchange in SNRs. Understanding the specifics of the charge exchange process, the resulting emission, and the significance of charge exchange processes in supernova remnant evolution, will add another piece to the puzzle, unraveling the complex physics in these systems.

In the next two chapters I will describe the design and commissioning of the *Micro-X* sounding rocket payload, featuring an 128-pixel array of transition edge sensor microcalorimeters at the focus of a grazing incidence X-ray mirror. *Micro-X* will target the Bright Eastern Knot in the Puppis A SNR as its first target, which is a prime target for charge exchange measurements. *Micro-X* is designed to provide spectra with a resolution 2-4 eV (see Figure 5-10), and imaging with a PSF of $\sim$ 2.4 arcminutes, opening up a new era in X-ray studies of extended sources.

Chapter 4

The *Micro-X* Telescope: Design and Commissioning

In this chapter I will discuss the details of the design of the *Micro-X* payload and the current state of the commissioning process. To provide some context, I will discuss the *Micro-X* detector array and its needs, then will discuss the subsystems, and how each of them services the detector and/or the observation requirements. Before delving into the details of each subsystem, I will give a big-picture overview of the rocket and our payload.

Micro-X is a sounding rocket payload. The sounding rocket will carry the instrument above the X-ray absorbing atmosphere for an observation of roughly five minutes, before it parachutes back to the ground. After flight, the payload will be recovered, repaired, and flown again. Though limiting observing time, sounding rockets provide a platform to test developing technology within a mission that costs two to three orders of magnitude less than a satellite mission, allowing development of risky new technologies, along with providing the opportunity for development, assembly, and testing to be carried out by a small team of researchers and students, rather than the army of technicians required for a satellite mission. *Micro-X* utilizes an array of transition edge sensor microcalorimeters: a new technology that will make its maiden observation from space on the *Micro-X* mission. As I will describe in this chapter, the detectors must be run at a very low temperature, and much of the challenge

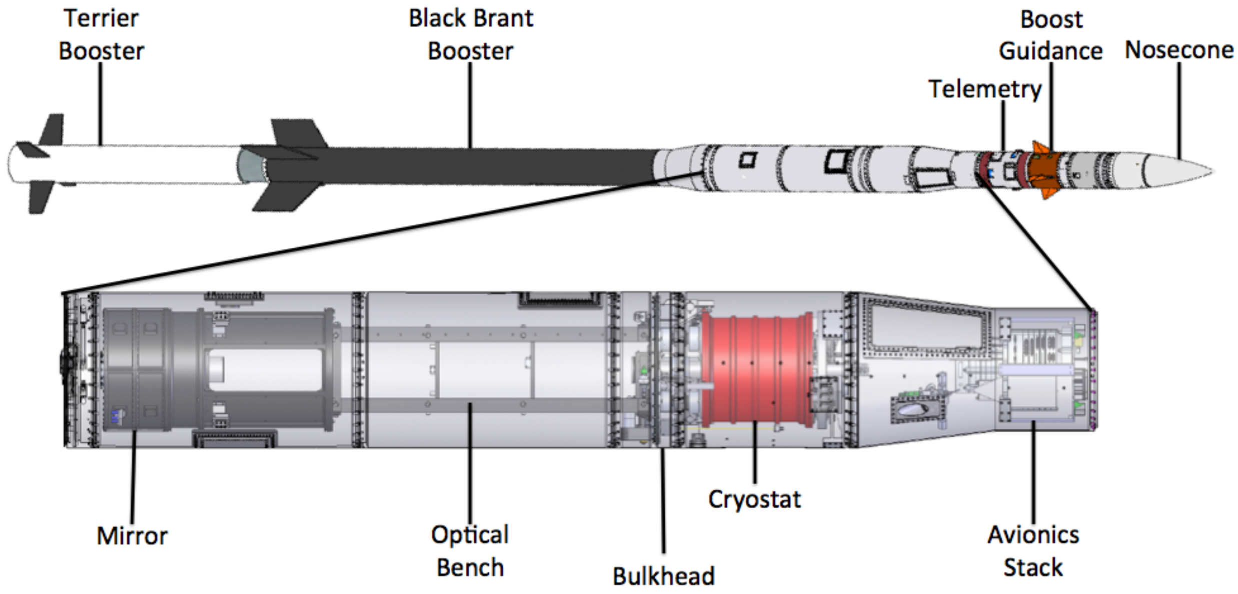

Figure 4-1: A CAD rendering of the entire rocket with inset of the *Micro-X* science instrument. Key systems are labelled.

in the development of the payload is cooling the detectors and maintaining their temperature through the launch and observation.

A diagram of the full rocket and the science instrument is shown in Figure 4-1. The main rocket systems are the boosters: motors that are jettisoned after their respective burns, telemetry: data processing and communication with the ground, boost guidance: steering by adjustment of fins (canards) active in the early stages of flight, and the nosecone containing the parachute. Not pictured are attitude control: fine pointing during observation and the flight termination system: a self-destruct mechanism should the rocket make its way wildly off-course. The rocket systems, developed and supplied by the NASA Sounding Rocket Office Contractor (NSROC), are described in detail in 4.10.

The *Micro-X* team is responsible for the development and testing of the science instrument. The heart of the science instrument is the cryostat. Given the moniker the Lightweight Millikelvin Observatory (LMO), the cryostat is the small red can labelled in Figure 4-1. Most of my work on the payload has been focused on the systems inside the cryostat, especially the refrigeration and vibration isolation aspects. Other important components of the instrument are the mirror, which focuses incoming light, and the optical bench, which holds the mirror and the detectors at the proper separation to ensure good focus. The bulkhead is a vacuum-tight separation between the optical section and the cryostat section. The avionics stack houses the electronics for temperature control, housekeeping, detector control, and data processing, and interfaces to the rocket's telemetry system.

4.1 The Microcalorimeter Array

Micro-X's microcalorimeter array is its distinguishing feature, and it is the specific requirements of these detectors that drive the majority of our design considerations. A microcalorimeter is, at its most basic level, a very sensitive thermometer, able to detect changes in temperature at the microKelvin level. In *Micro-X*, we detect the temperature change of an absorber due to energy deposited by individual incident X-ray photons. The concept of using microcalorimeters as sensitive X-ray detectors in space is not unique to *Micro-X*. The X-ray Quantum Calorimeter *XQC* sounding rocket [71] has used sensitive bolometers to measure the soft X-ray background with high energy resolution and the *Suzaku* XRS instrument was a microcalorimeter array designed for X-ray detection [59]. Unfortunately a design flaw prohibited XRS from functioning on orbit. *Micro-X* distinguishes itself from these previous missions by it's use of a new microcalorimeter technology: the transition edge sensor (TES), which offers increased sensitivity and a path to large arrays, albeit while imposing additional constraints on the system. *Micro-X* is on track to be the first mission to utilize TESs in space.

The best detectors in current regular use for astrophysical X-ray observations are CCDs. These have been used with great success in missions like *Chandra*, and have matured to the point where they exhibit extremely high spatial resolution when utilized with a sophisticated X-ray mirror. However, the energy resolution of these detectors is in the 100-200 eV range in the X-ray band. When an X-ray hits the silicon surface of a CCD, it liberates photoelectrons (an electron requiring 3.7 eV of energy to break free of its atom). The photoelectrons are

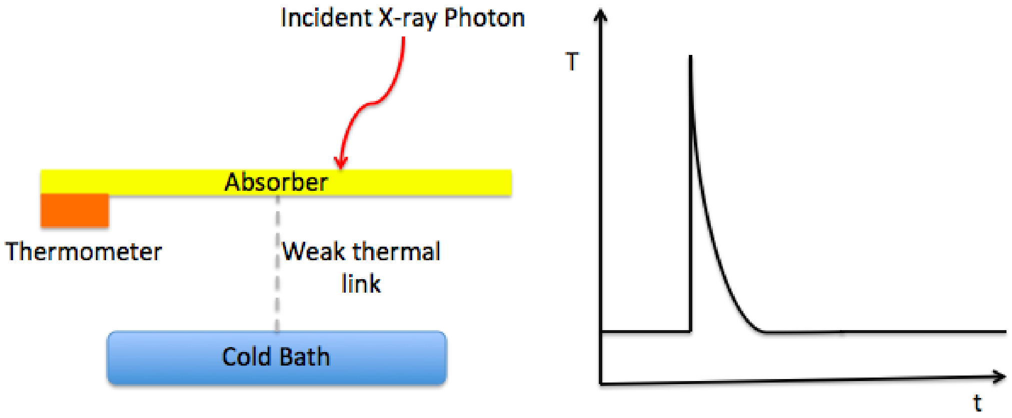

Figure 4-2: A diagram of a microcalorimeter (left). An incident photon heats the absorber, then the heat slowly drains out to the cold bath through a weak thermal link. This temperature response (right) is measured by the thermometer.

then pulled across the surface of the CCD by an electric field and counted. The precision of this process is limited by Poisson uncertainties, since the liberated electrons are a discrete measure of the energy of the incident X-ray photon. Some small fraction of energy from the incident photon is also deposited into the phonon system of the Si.

Microcalorimeters achieve intrinsically higher energy resolution than CCDs. They can exhibit lower than 2 eV FWHM at 6 keV (R=3000), compared to 150 eV FWHM at 6 keV exhibited by the ACIS CCD on *Chandra* (R=40). A microcalorimeter is made up of four components: a stable cold temperature bath, an absorber, a weak thermal link between the cold bath and the absorber, and a thermometer to measure the temperature of the absorber, as shown in the diagram in Figure 4-2.

In *Micro-X* we use transition edge sensors (TESs) as the thermometers for our microcalorimeter system. TES microcalorimeters exhibit better energy resolution than the semiconductor thermistors used in previous space flight systems, by utilizing the unique shape of the temperature vs. resistance curve of superconductors in and around the superconducting transition (shown in Figure 4-3). TESs have been used with great success in several ground-based experiments (SCUBA [47], the Atacama Cosmology Telescope [63],

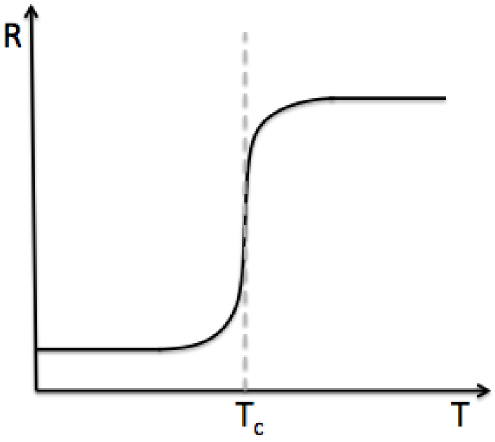

Figure 4-3: The shape of the resistance vs. temperature of a superconductor at its transition.

the South Pole Telescope [73], and CDMS [1], among others). When a superconductor is in its transition between finite resistance and zero resistance, a small change in temperature results in a very large change in resistance, making it one of the most sensitive thermometers available for this application. This small change in resistance can be read out with a system of Superconducting QUantum Interference Device (SQUID) amplifiers, which will be described in Section 5.1.

The *Micro-X* TES array is made up of 128 pixels, arranged as a 12x12 grid with the corners cut out. Only 128 pixels are read out because of the limitations of the wiring for the multiplexing readout, which will be discussed in Section 5.1. Each of the pixels is a 590 μm x 590 μm absorber on a 600 μm pitch, giving a fill fraction of 97%. The array was designed by Megan Eckart and the TES group at Goddard Space Flight Center (GSFC) and is described in detail in [29]. There are several constraints that must be taken into account when designing the TESs. I will discuss each of these considerations and the way in which they have been implemented for the *Micro-X* TES array.

The expected performance of the refrigerator governs the desired transition temperature. As I will discuss, the lower the temperature of the TESs, the better their energy resolution. However, the transition temperature must be high enough that the refrigerator can cool the array below that level with enough remaining cooling power to maintain that temperature during launch and observation. The array is not run at the transition temperature, but is held at a 40-50 mK lower temperature, with a voltage bias used to drive the TES into its transition.

The *Micro-X* TESs are 140 μm by 140 μm Mo/Au proximity-effect bilayers. Through the proximity effect, the transition of the superconducting Mo (with a transition temperature at 920 mK) is tempered by the nearby normal metal (Au with a transition temperature of 0 mK). The transition temperature of the array can be tuned by changing the thickness of the layers. Stripes of ∼350 nm thick Au have been added to the surface of the TES perpendicular to the current flow to partially obstruct current flow across the TES and mitigate the noise on the device[1]. The array currently slated for flight and installed in the *Micro-X* flight dewar[2] has a transition temperature of 120 mK and a resolution of about 4.5 eV, as measured in initial testing at GSFC.

The energy bandpass of the mirror governs the expected energy of incident X-rays[3]. The materials of the absorber should be such that nearly every incident X-ray in the transmission band will be absorbed. The *Micro-X* array is designed to achieve 99% absorption efficiency over the 0.2-3 keV science bandpass with an absorber made of a 3.4 μm thick layer of Au and a 0.6 μm thick layer of Bi. The thicknesses of the Au and Bi are set to be about equal to twice the attenuation length of the X-rays. With its low heat capacity, the Au provides quick thermalization across the absorber while the Bi provides structural stability and additional X-ray stopping power without substantially raising the heat capacity of the entire absorber.

The speed of the multiplexing electronics and the downlink for sending data to the ground during the observation sets a maximum data rate, which defines the desired timescale for pulse decay. The lower the data-rate, the slower the desired pulses, so that the pulse shape can be well-sampled in telemetered and stored data. When setting the decay timescale we must also consider the expected rate of photons, since several photons arriving within

---

[1] The physical process behind this noise mitigation is not theoretically well characterized, but it has been empirically verified.

[2] The term dewar is generally used for a cryogen storage vessel, but is used interchangeably with cryostat and LMO in the lab and throughout this thesis.

[3] In reality the energy bandpass is chosen based on science considerations and both the mirror and the array are tuned to optimize the instrument in that bandpass.

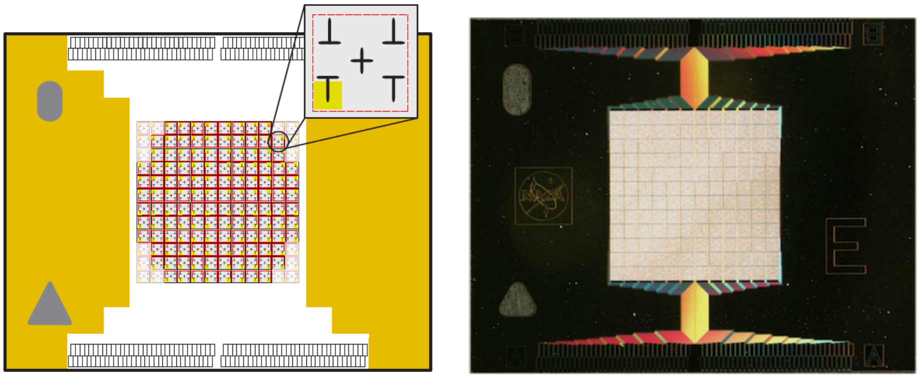

Figure 4-4: A diagram of the detector chip (left) and picture of the same (right). The triangle and oval on the left are insets for the kinematic mount, the signal leads are shown on the top and bottom of the chip, and unwired pixels are grayed out. The inset in the diagram on the left shows the absorber supports in black, the TES in gold, and the perforated boundary of the SiN membrane in red.

a single decay timescale would lead to pileup and resulting degradation in resolution. In *Micro-X* we target 2 ms decay times, which is slower than many similar devices, but can be achieved with a weak thermal link with thermal conductance G less than 100pW/K. In order to understand how the thermal link is formed, it is necessary to understand the assembly of the microcalorimeter elements.

The TES is suspended on a 1 μm thick SiN membrane, which is deposited on a grid of Si laid out along the pixel borders. The absorber is connected to the TES through a T-shaped 'stem' that acts both as a thermal short between the two, and a mechanical support for the absorber. The absorber must remain mechanically separate from the membrane frame and the TES leads, which run along the frame between the pixels and underneath the edges of the absorbers. This is ensured by adding additional T stems between the SiN membrane and the absorber that do not contact the TES. These are shown in the inset in Figure 4-4.

The membrane, TES, T-stems, and absorbers act approximately as a single thermal unit, warming together when the photon strikes. The weak thermal link is made through the edge of the membrane to the main structure of the Si grid. The thermal conduction G from the SiN membrane to the grid boundary scales with the length of the perimeter, which is the boundary for phonon transmission. G is tuned by perforating a square boundary in the

SiN membrane between the TESs and stems, and the Si grid boundary. These perforations slow the process of thermalization by limiting the boundary through which phonons can be transmitted. This perforated boundary is also shown in the inset in Figure 4-4.

The Si grid is part of a larger Si chip that forms the base of the TES array. This is kinematically mounted to the surface of the Front End Assembly (described below) on ball bearings, and is heat sunk to the Front End Assembly (FEA) surface with gold wire bonds. The FEA is attached to a plate, which is connected to the refrigerant thermal bus through a magnesium cold finger. All metal to metal contact surfaces are gold-plated to assure good thermal conductivity between the detector chip and the refrigerant providing the cold bath for the microcalorimeters.

The array fabrication process is finicky, but the GSFC team has a good deal of experience and has produced several flight-worthy arrays with the proper tuning for the *Micro-X* system. The array fabrication process has benefitted greatly from recent great strides in Si microfabrication techniques allowing precise deposition and etching of microscopic layers on Si wafers. We ran an initial non-flight array with a transition temperature of 170 mK in the *Micro-X* dewar several times, and currently have the higher resolution array with a transition temperature of 120 mK, which is slated for use in flight, installed in the payload.

4.1.1 The Front End Assembly

The light-tight box housing the focal plane and the first and second stage readout electronics is called the Front End Assembly (FEA). The FEA is made of lightweight magnesium, gold-plated for fast thermalization and good thermal contact to components inside the FEA and the thermalization path to the refrigerant. The bottom plate holds the TES array chip, the multiplexing (MUX) chips mounted on interface chips that provide the wire routing to the array, thermometers off of which the temperature control is based, and breakout boards for the science chain readout circuit. NK-Series, 85-pin Nanonics connectors have been soldered into printed circuit boards that are wirebonded to the interface chips. Each of the chips on the FEA is kinematically mounted, resting on three tungsten carbide balls and constrained

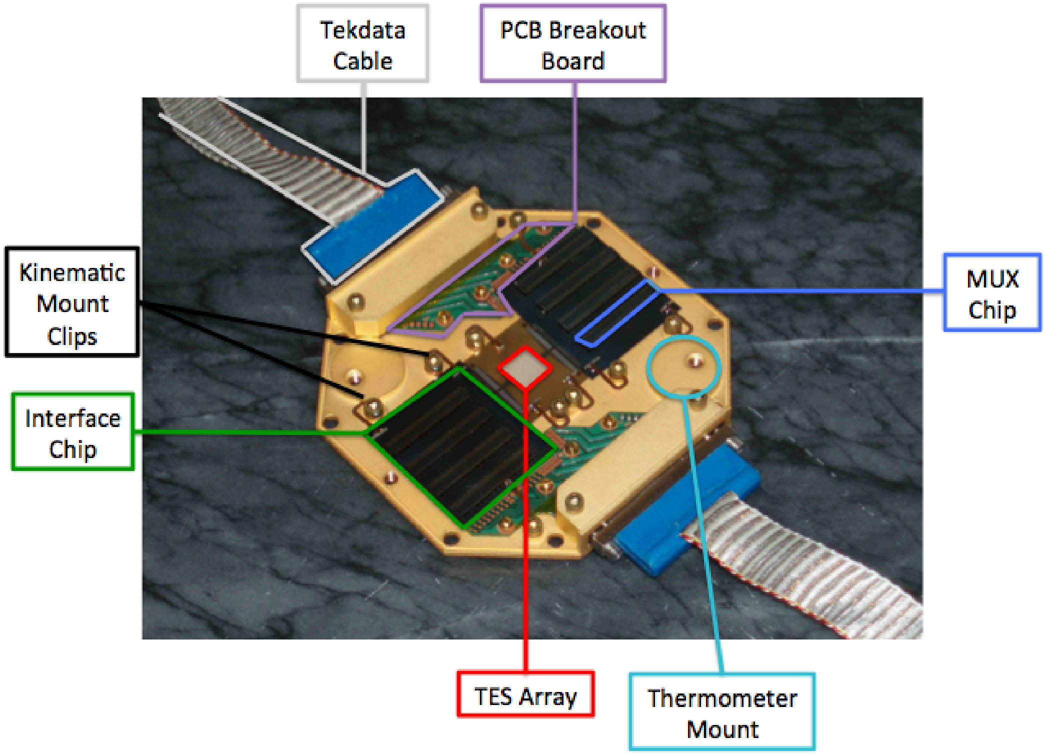

Figure 4-5: A labelled picture of the FEA without the lid. The Germanium Resistance Thermometer (GRT) thermometers are not mounted in this picture.

at six points of contact by flexible clips. A labelled picture of the FEA without its lid is shown in Figure 4-5. John Rutherford assembled the focal plane and oversaw wirebonding by the flight-qualified technicians at GSFC. The bonds were pull-tested to non-destructive forces to ensure they would survive launch, and have survived several rounds of vibration testing.

The FEA lid is also made of gold-plated magnesium. The inside of the lid will be blacked to keep the inside of the FEA box from becoming a resonant cavity for any infrared radiation that is able to enter the box through the connectors. The 50 mK filters mount to the top lid of the FEA. The 85-pin connectors that interface to the FEA are custom-potted into woven Tekdata cables that run to the 2 K readout electronics to read out the science chain signals. One worry is that these cables, which are fairly delicate, will hit the edge of the

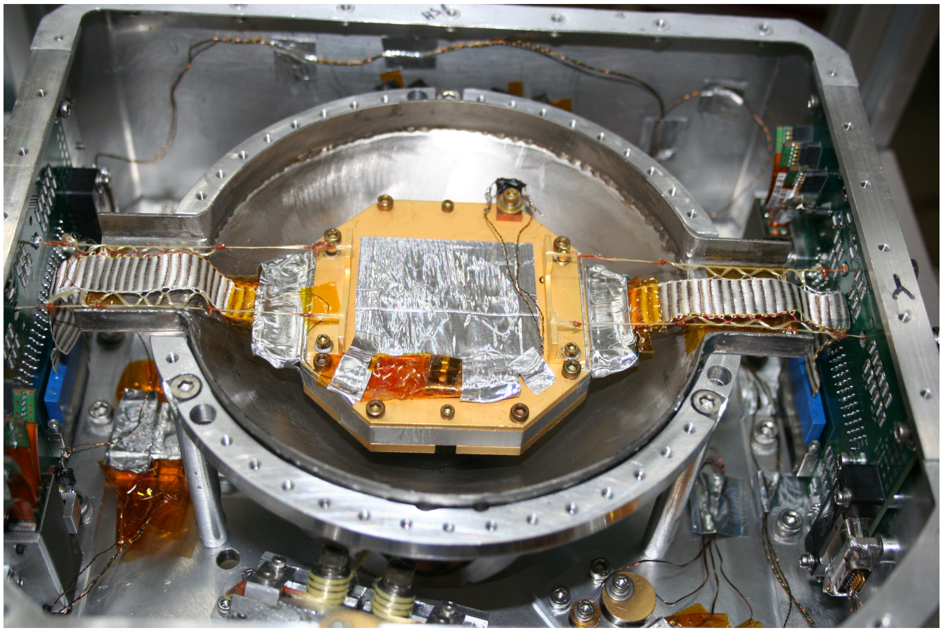

Figure 4-6: A picture of the FEA installed in the insert with the Tekdata cables supported by the kevlar 'tekdata suspension'. In this picture there is a layer of aluminum tape over the aperture instead of a filter. A resistor is attached to the FEA lid and acts as a heater during thermal tests.

magnetic shield (Section 4.4) during vibration, causing damage. To avoid this, a kevlar suspension is put in place to support each Tekdata cable. Two kevlar 'rails' run parallel to the Tekdata cable from their mounts on the top of the FEA lid to the 2 K board mount, where they are tensioned with weak springs. Additional kevlar strings are epoxied to these 'rails' and are woven through the outer edges of the Tekdata cable to keep it suspended at the same elevation as the rails and away from the edges of the magnetic shield. This 'Tekdata suspension' is shown in Figure 4-6. I was responsible for the construction and maintenance of this system, which has proved its viability surviving 13 separate vibration tests with no damage to the Tekdata cables during the August, 2013 vibration campaign at Wallops.

4.1.2 Microcalorimeter Physics

In this section, I follow calculations in [34] regarding microcalorimeter theory. More detailed calculations and a full set of references can be found in that publication.

When an incident photon of energy E_γ is incident on a properly engineered absorber, it deposits nearly all of that energy. If the absorber has heat capacity C, then the temperature change of the absorber due to the energy deposition will be $\Delta T = \frac{E_\gamma}{C}$. Since the absorber is connected to the cold bath via a weak thermal link, the heat will drain into the cold bath and the absorber will slowly return to its original temperature. This will create a heat pulse temperature profile for each photon, with the pulse height corresponding to the energy of the incident photon.

In any physical system there will be power on the absorber from sources other than incident science photons (this includes contributions from both parasitic power sources like radiation loads and Joule heating from the electrothermal feedback used to keep the TES in its transition). I will discuss the details of these power sources shortly, but for now will denote this power as P. The temperature as a function of time will depend on the balance of the incoming power and the power flowing out through the link. We write this balance equation for a system with temperature $T(t)$ and bath temperature T_b, in which an incident photon hit the absorber at time t=0 in Equation 4.1.

$$C\frac{dT(t)}{dt} = P - P_{link}(T(t), T_b) + E_\gamma \delta(t) \tag{4.1}$$

First, we would like to describe the power flowing through the link more completely. In most systems, the power going through the link has the form shown in Equation 4.2, where K is a constant and n is between 2 and 5, depending on the dominant physical mechanism governing the power transfer.

$$P_{link}(T(t), T_b) = K(T(t)^n - T_b^n) \tag{4.2}$$

We define the thermal conductance G to be $\frac{dP_{link}}{dt}$, which gives $G = nKT^{n-1}$ for this situation. To give a functional form to the power P, we must consider the method of electrothermal feedback used to keep the TES in its transition. In this method, the TES is voltage biased (meaning that a constant voltage is applied across the TES). Power from electrothermal feedback (ETF) voltage will be given by $P_{ETF} = V_{bias}^2/R(T)$. When the TES is warmer, it has a higher resistance and P_{ETF} falls, allowing the TES to cool down. When the TES is cooler, it has a lower resistance, increasing P_{ETF} and leading to heating. In this way the application of a constant bias voltage acts to regulate the TES temperature through Joule heating. V_{bias} is set such that the equilibrium point of the TES is somewhere low in the superconducting transition (where the gain is still high but where pulses will not saturate the TES by pushing it up out of the transition). Since we are interested in the dynamic behavior of the TES we will, for now, neglect the parasitic power since it will simply lead to a constant temperature offset of $\Delta T_{parasitic} = P_{parasitic}/G$. We can now rewrite Equation 4.1 in Equation 4.3.

$$C\frac{dT(t)}{dt} = \frac{V^2}{R} - K(T(t)^n - T_b^n) + E_\gamma \delta(t) \tag{4.3}$$

This equation can be solved by Taylor expanding in ΔT, the temperature difference from the quiescent state due to the heat deposition from the incident photon. It is now convenient to define the parameter α describing the sharpness of the superconducting transition in Equation 4.4.

$$\alpha \equiv \frac{T}{R(t)}\frac{\partial R(T)}{\partial T} \tag{4.4}$$

The Taylor expansion and these substitutions give us Equation 4.5.

$$\Delta\dot{T}(t) = -\left(\frac{\alpha V_{bias}^2}{TCR} + \frac{G}{C}\right)\Delta T + \frac{E_\gamma}{C}\delta(t) \tag{4.5}$$

Solving this for ΔT, we get the exponential decay shown in Equation 4.6 where the time constant τ_{eff} is given by Equation 4.7. Remember that we are treating T, the quiescent temperature, and T_b, the cold bath temperature, as constants, and ΔT as the dynamic variable.

$$\Delta T = \frac{E_\gamma}{C} e^{-t/\tau_{eff}} \tag{4.6}$$

$$\tau_{eff} = \frac{C/G}{1 - \frac{\alpha}{n}\left(1 - \frac{T_b^n}{T^n}\right)} \tag{4.7}$$

So we see that the temperature pulse will exhibit a sharp rise in temperature with total height proportional to the photon energy, followed by an exponential decay in temperature with time. An approximation of this pulse shape is shown in Figure 4-2. In most systems T and T_b are known and α and n are determined by fitting pulse data to the functional form above.

The above derivation assumes that the rise in temperature due to the incident photon is instantaneous. In reality, the absorption process is fast, but not instantaneous. I will not quantitatively derive the timescale here, but will provide a qualitative description of the process. When X-rays are incident on Au and Bi, the absorption occurs mostly through the photoelectric effect. Photon absorption could occur through Rayleigh or Compton scattering, however the cross sections for these processes are much lower than that for the photoelectric effect, so in practice they are not important.

The energy from the incident photon is absorbed by a single atom, releasing an energetic electron. This electron travels through the absorber ionizing other atoms with a high cross-section, gathering a ball of energetic electrons around it. As this occurs, the mean energy of these electrons decreases, increasing the probability of phonon production. As phonons are produced, the electron ball size increases even further, as the phonons have higher mean free paths than energetic electrons. As the phonons and electrons travel through the absorber, the mean energy of all of the particles in the absorber will equilibrate to a higher value, achieving thermalization. The gold in the absorber helps to provide this fast thermalization, avoiding position-dependent degradation of the energy resolution [29].

As mentioned previously, pileup on the detector is possible if the rate of incoming photons is such that a photon arrives before the previous pulse has decayed. This degrades energy resolution since a shorter portion of both the initial and the second pulse shapes are available to fit to derive an estimate of the pulse heights. Currently we segregate the events based on the uncertainty in their pulse shapes, so any piled up events would be thrown out. The

SNRs we will observe do not have high enough count rates to cause significant pileup on our detectors, however we have to be careful to throttle the onboard calibration source (described in Section 4.5) to avoid pileup.

Aside from external noise sources, which will be described more thoroughly in Section 5.3.1, there are two contributions to noise on the detectors. The first is Johnson noise on the TES resistance. This is caused by Brownian motion of electrons in the resistor and has a more or less white spectrum in our band of interest. The second source of noise is phonon noise from the connection to the cold bath. This is caused by power fluctuations through the thermal conductance between the TES and the cold bath and leads to thermal fluctuations on the calorimeter. The power fluctuations from these produce a nearly white spectrum across our frequencies of interest. While the noise sources are fairly even across frequencies, the TES's response to these is not. If we neglect the effects of the electrothermal feedback, the system has a natural time constant of $\tau_0 = C/G$, thus any fluctuations with frequencies greater than $2\pi\tau_0$ will be damped by the slow response of the TES.

In [53], the energy resolution for a calorimeter in the limit where $\frac{\alpha P}{TG} >> 1$ is derived to be the expression in Equation 4.8, where k_B is the Boltzmann constant and T is the quiescent temperature of the detector.

$$\Delta E_{FWHM} = 2.355\sqrt{4k_B T^2 C \frac{1}{\alpha}\sqrt{\frac{n}{2}}} \tag{4.8}$$

We can see that the width is directly proportional to the temperature of the detector, so the colder we are able to keep the detectors, the better our resolution will be. I will discuss how this is achieved in the *Micro-X* payload in Section 4.2.

4.2 The Cryostat

The *Micro-X* focal plane must be run at a very low temperature to limit thermal noise. As discussed in Section 4.1.2 the FWHM of the measured energy lines is proportional to the temperature of the detector. Getting the detector (which is itself about the size of a penny) cold and keeping it at that low temperature during launch and observation requires a complex cryogenic system much much larger than the detector itself: the *Micro-X* cryostat. The cryostat is known as the Lightweight Millikelvin Observatory (LMO) and is the heart of the payload. The components of the cryostat each serve one of three purposes: cooling the detectors, isolating the detectors thermally or vibrationally, or carrying signals and power into and out of the dewar.

4.2.1 Refrigeration

There are many types of refrigeration currently in service of low temperature experiments. Each has particular needs and benefits that make it optimal in particular situations. I will give a brief overview of several refrigeration methods, then go into more detail about adiabatic demagnetization, the method utilized to cool and temperature-control the detectors on the *Micro-X* rocket. More detailed descriptions of all of these methods along with an exhaustive collection of references can be found in [79].

Evaporative cooling is important, because it is the first step in cooling for every system involving cryogens, including most systems utilizing adiabatic demagnetization or dilution refrigeration. We use evaporative cooling of a liquid helium bath as the first stage of cooling in *Micro-X*. The heat of evaporation for liquid helium (transitioning from liquid to gas) is about 2.6 $\mathrm{kJ}l^{-1}$ at its normal boiling temperature of 4.2 K. The latent heat of evaporation of liquid nitrogen is about 60 times higher than that of liquid helium at its normal boiling temperature of around 77 K, making it a much more efficient refrigerant than helium and a better choice for use at temperatures above 77 K. It is also more than a factor of 10 less expensive than liquid helium and more readily available.

Temperatures lower than 4.2 K can be achieved by pumping on a liquid helium bath, lowering its pressure and thus lowering the boiling temperature. Most evaporation cryostats only pump on a small fraction of the He bath, as about 40% of the liquid evaporates in the pumping process and often only a small volume of pumped liquid helium is necessary to cool a sample or stage. In 1922 H. Kamerlingh Onnes set the lowest temperature record of his time of 830 mK, by pumping on a bath of mostly ^{4}He with several pumps. It was later found that the rarer and much more expensive isotope of ^{3}He can be pumped down to 0.3 K because ^{3}He has a much larger vapor pressure than ^{4}He at the same temperature. ^{4}He is a superfluid below 2.17 K while ^{3}He does not exhibit superfluidity above 2.5 mK. ^{3}He evaporation cryostats must be closed-cycle because of the expense and rarity of ^{3}He.

Closed cycle refrigeration is becoming increasingly popular as a cryogen-free method of cooling. Avoiding the use of cryogens eliminates frequent cryogen fills and logistical difficulties in acquiring cryogens. In closed cycle refrigerators cooling occurs when a gas (usually He) performs work against internal or external forces. A very popular and commercially available type of closed cycle refrigerator is a **pulse-tube cooler**. This utilizes smooth, periodic and nearly adiabatic pressure variations of the working gas in a 'pulse tube' where a pressure wave is generated by either a high frequency oscillator or low frequency compressor.

This type of cooler can currently achieve 15-20 K as a single-stage and 2 K as a two-stage cooler. The lowest temperature that has been achieved with a pulse-tube cooler is 1.27 K using ^{3}He as a working gas. Closed-cycle refrigerators eliminate the difficulty and expense of working with cryogens, and can be used in space for a much longer time since they will not run out of working gas. They do, however, cause vibration that may cause heating on colder stages attached to the cooler. A pulse-tube cooler will be utilized as the heat sink of an Adiabatic Demagnetization Refrigerator (ADR) in the *Astro-H* satellite currently being developed, with a cryogen tank as a backup in case of failure.

Pomeranchuck cooling is cooling by solidification of ^{3}He. In most materials entropy is higher in a liquid state than in a solid state since solids tend to be more ordered. However, below 0.3 K on the melting curve of ^{3}He, the entropy of the liquid state is less than that in the solid state, so adiabatic solidification leads to cooling. At the end of the 1960's, this method was shown to be able to produce cooling from 50 mK down to 2-3 mK. This requires continuous adiabatic compression and is a one-shot method, having no advantage over continuous dilution refrigeration methods, so it is rarely used in current low-temperature experiments.

Dilution refrigeration is extremely popular in current experiments because it is the only continuous refrigeration method below 0.3 K. Dilution refrigeration relies on the enthalpy of mixing the two quantum liquids ^{3}He and ^{4}He. A sample will cool as its thermal energy is drained in order to move pure ^{3}He delivered by a pump cycle across a phase boundary into a ^{4}He phase. The minimum temperature achieved by this method is 2 mK and dilution refrigerators that can cool to 4 mK are currently commercially available. Current designs are not optimal for spaceflight as they are large, power-hungry, and many utilize gravity, however the *Planck* space mission utilized a dilution refrigerator successfully for several years.

Adiabatic demagnetization of a paramagnetic salt was the first method to break through the temperature limits of evaporative cooling and was the most popular platform for low temperature experiments for many years. It is also the cooling method used in the *Micro-X* payload and the *Astro-H* satellite. In this method a paramagnetic salt with unfilled electron shells is connected to a heat bath (usually a liquid helium bath or pulse-tube cooler). It is magnetized, aligning the electronic magnetic moments. This decreases the entropy resulting in a rise in heat, which is drained into the heat bath by a strong thermal link. Once the salt has thermalized to the heat bath temperature, the heat link is broken and the salt is slowly demagnetized. As it is demagnetized, the entropy increases and the temperature decreases. There are several paramagnetic salts with diverse properties used in various ADR applications. These are described in detail in Wikus et al. [114]. The temperature limits of a particular salt are determined by the interaction between the magnetic fields of neighboring magnetic moments. I will describe this in more detail in Section 4.2.2.

Adiabatic nuclear demagnetization (AND) is a similar process to ADR in paramagnetic salts, but utilizes the nuclear magnetic moments in a material instead of the electronic magnetic moments. Copper is most commonly used as the system of nuclear magnetic moments in this process. Much lower temperatures can be achieved with AND than with a paramagnetic salt ADR because the density of nuclear moments is significantly higher than that of electronic magnetic moments. Also, the ordering temperature in the material due to nuclear dipole to dipole interactions is around 0.1μK and lower, so μK temperatures are regularly achieved with AND. However, to achieve these temperatures requires a very low temperature and very high magnetic field prior to demagnetization (temperatures in the milliKelvin range and magnetic fields of almost 10 T). This is often achieved by using a dilution refrigerator as a heat sink stage. This method is not effective for cooling from 2-4 K down into the mK range, and so is not particularly useful in cooling detectors. Paramagnetic salts and dilution refrigerators are much more effective in this regime.

In any of these methods, heating from outside sources is a large concern. These heat sources can be vibrations from the building or payload in which the system is installed, attached pumps, pulse tubes, or bubbling of cryogens. In any gas-filled tube connecting cold and warm areas thermoacoustic (or Taconis) oscillations may be excited and cause excess heating[4]. Electrical leads running from warmer areas to a cold stage can also transmit excessive heat if not heat sunk properly or if made of improper materials. All of these must be taken into account in system design, and will be discussed in terms of our system in detail in following sections.

4.2.2 Adiabatic Demagnetization

Since *Micro-X* utilizes an ADR to cool the cold stage to its operating temperature and control the temperature during flight, I will go into more detail on this particular process, following the treatment in [114]. The entropy of a magnetic material is the sum of its magnetic entropy, lattice entropy, and the entropy of its conduction electrons. At low temperatures the magnetic entropy dominates and we can neglect the other two contributions. In the materials we are concerned with, the magnetic moments (which determine the magnetic entropy) result from electrons in unfilled shells in transition metals of rare earth ions. These unpaired electrons have total electronic angular momentum J, resulting in 2J+1 possible

---

[4] We often see this effect when pumping on our helium bath

orientations in a disordered state. In this case they contribute $S_m = R\ln(2J+1)$ to the magnetic entropy where R is the ideal gas constant.

When an external magnetic field B_{ext} is applied, the magnetic moments will align with the field, causing the magnetic entropy to decline steeply. If we assume that the magnetic moments are independent and non-interacting (which is not the case in all materials and situations) we can show using statistical mechanics that the magnetic entropy for a paramagnetic material is given by Equation 4.9, where x is defined as $x = \frac{\mu_B g B_{ext}}{2k_B T}$. Here μ_B is the Bohr magneton, g is the Landé g factor and k_B is the Boltzmann constant.

$$\frac{S_m}{R} = x\left(\coth(x) - (2J+1)\coth\left(x(2J+1)\right)\right) + \ln\left(\frac{\sinh(x(2J+1))}{\sinh(x)}\right) \tag{4.9}$$

The Landé g factor for a material with total electronic momentum J, spin angular momentum S, and orbital angular momentum L is given by Equation 4.10.

$$g = 1 + \frac{J(J+1) + S(S+1) - L(L+1)}{2J(J+1)} \tag{4.10}$$

The independence of the magnetic moments is only a good approximation if $k_B T >> \mu_B g B$ (the thermal energy dominates the magnetic energy). If this is not the case and the field b from neighboring moments has to be taken into account (which tends to be the case at low temperatures as the external magnetic field approaches zero), then the moments cannot be approximated as non-interacting. In this case [79] suggests replacing B_{ext} in Equation 4.9 with $B_{eff} = \sqrt{B_{ext}^2 + b^2}$ where b characterizes the magnetic field contribution from neighboring magnetic moments. This substitution illustrates why zero temperature cannot be achieved using an ADR.

The first step of the ADR process is to keep T constant while increasing B (which is practically achieved by applying a magnetic field with a strong thermal link between a 2 K pumped liquid helium bath and the salt). The heat produced by magnetizing the salt is drained into the helium bath. We can see through Equation 4.9, that keeping S constant while lowering B_{ext} will cause a drop in T, which occurs when we lower the magnetic field adiabatically after disconnecting the thermal link between the helium bath and the salt. The implication of Equation 4.9 is that as $B \Rightarrow 0$, $T \Rightarrow 0$, however as mentioned previously, the neighboring moment field b keeps the effective magnetic field from reaching zero so $T = 0$ cannot be achieved through adiabatic demagnetization in physical materials.

The heat that can be absorbed by the salt at the end of the cycle at magnetic field and temperature B_f and T_f is given by Equation 4.11, showing that the higher the field at the base temperature T_f the larger the cooling power of the salt.

$$Q(B_f) = \int_{T_f}^{\infty} T(\partial S/\partial T)_{B_f} dT \tag{4.11}$$

There are many contributing factors to choosing a paramagnetic material. The higher the total angular momentum J and Landé g factor of a material, the greater its cooling power. We also look for a low magnetic ordering temperature. This is the temperature at which a transition occurs and the magnetic moments spontaneously align, leading to a reduction of the magnetic entropy to zero. This temperature is inversely proportional to the distance between magnetic moments to the third power so large inter-ion spaces in a salt lattice are desirable to produce a material with a low ordering temperature. Other desirable features are small magnetic and thermal hysteresis (allowing faster cycle times without losing efficiency), a large electrical resistance (to minimize eddy current heating that can occur during magnetization or vibration while magnetized), and a high thermal conductivity (to minimize the temperature gradients through the salt and increase efficiency). It is difficult to find a material that optimizes all of these considerations, but they can guide our selection of material.

4.2.3 The *Micro-X* ADR

The *Micro-X* ADR is a compact system capable of cooling the detectors to their operating temperature, and controlling that temperature throughout launch and observation. The ADR design is based on the *XQC* payload design [71], with several modifications made to accommodate the TES detectors. These modifications include magnetic shielding, a modified kevlar suspension system to accommodate the magnetic shielding and a heavier suspended

Figure 4-7: A picture of the insert with the suspended mass installed with kevlar strings. The magnet leads run to the high current connectors toward the bottom of the image. The aft side of the insert is on the right side of the image while the forward side, which sits inside the helium can bore is on the left side of the image. The detector box, 2 K thermal shield, magnetic shield, and 2 K electronics are not installed in this image.

mass, and a more spacious interior for ease of assembly. The ADR includes the Ferric Ammonium Alum (FAA) salt pill (Section 4.2.4), the superconducting magnet, the helium can (Section 4.2.8), and the heat switch (Section 4.2.7) mounted on the helium can. The helium can and the rest of the ADR components are surrounded by (and in some cases supported by) layers of thermal and vibrational insulation to keep radiation loads on the detectors low and limit thermal loads on the helium can (Sections 4.2.11 and 4.3).

The salt pill, detectors, magnet, and first stage of thermal shielding are mounted on a removable stage known as the insert (shown in Figure 4-7). The insert mounts inside the cylindrical bore in the helium can, shown in Figure 4-8, attaching with screws on both the forward and aft sides. These screws provide both structural and thermal connections. The helium can is mounted on a series of G10 tubes glued into aluminum rings (described in more detail in Section 4.2.10). Thin aluminum covers are attached around the G10 tubes, cooled by clamps connected to the helium exhaust line, and covered with multi-layer insulation (MLI) for thermal shielding.

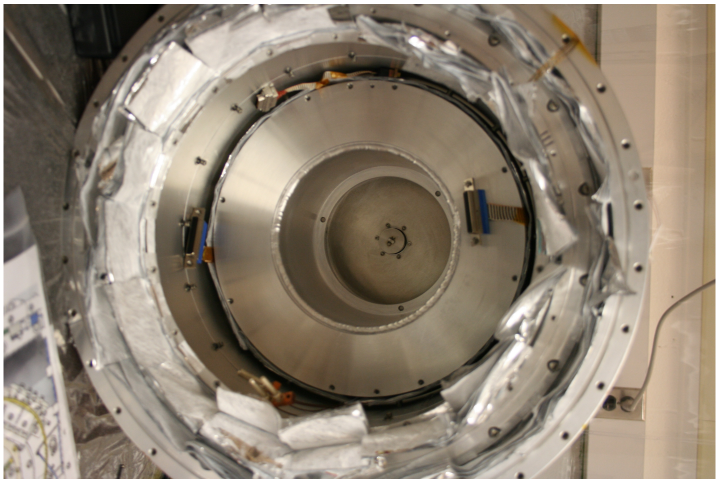

Figure 4-8: A picture of the helium can installed in the cryostat. The insert fits into the center bore of the helium can. There are ten screws on the outer aft surface of the helium can and three on a lip on the forward side of the helium can. This picture was taken with the first iteration of heat switch design when the heat switch was located on the insert. The connectors for the science chain (left and right), housekeeping (top) and the magnet (bottom) can be seen running along the sides of the helium can. These are plugged into connectors on the outside of the insert after it is installed.

The *Micro-X* magnet is a superconducting magnet with a transition temperature around 9 K. The magnet coil is wrapped in woven white insulation, and can be seen in Figure 4-7 between the aluminum plates on either side of the insert. It is made up of a multifilament NbTi/Cu double solenoid, coiled around an aluminum base. The primary coil surrounds the bore in which the salt pill is suspended, while the shorter secondary coil is wider and positioned on the aft side of the salt pill bore (to the right in Figure 4-7). This serves as a 'bucking' coil, producing a magnetic field in the opposite direction of that created by the primary to attempt to null out the large magnetic field on the detector side of the insert. Magnetic shielding will be discussed in detail in Section 4.4.

Both the primary and secondary coils are fed by the same leads (and thus carry the same current). The magnet was designed and optimized using the electromagnetic Finite Element Method (FEM) package in COMSOL, then commissioned from Cryomagnetics, Inc. The maximum current rating of the magnet is around 9.5 A, creating a field of about 4 T. This is more current than the *XQC* magnet, which reaches about 8.2 A, but is still relatively low current compared to most ADR magnets, and does not create unreasonable performance requirements for our power supply or current leads. The inductance of the magnet is 22 H.

One of the main concerns when running a superconducting magnet is quenching. A quench can occur when any part of the magnet rises above it's superconducting transition temperature and becomes normal. This creates massive Joule heating and heats the areas around it causing them to turn normal in a runaway process. The initial temperature rise can be caused by settling of the magnet coil in a new magnet or when running the magnet in a new orientation, Joule heating in joints or nearby resistive elements in the circuit, or eddy currents. When a quench occurs, the stored magnetic energy in the magnet is converted to heat, resulting in boil-off of cryogens. In the laboratory, quenches often cause the insert and helium can temperature to rise from 2 K to 20 K in a matter of seconds with helium still in the helium tank, requiring several minutes to reequilibrate to 2 K. Also, the sudden resistivity of the magnet at high current creates a large voltage spike across the leads. Diodes are included in the magnet housing to help dissipate energy released during a quench.

Several voltage taps are installed at different points along the magnet leads to monitor the voltage across the magnet during operation. We also closely monitor the insert temperature at large currents. A spike in either voltage or insert temperature may be an indication that a quench is imminent. The *Micro-X* magnet has quenched several times during the commissioning process. This occurred several times due to initial 'settling' of the coils upon first use of the magnet and later because of poor heat sinking of the magnet leads or bad solder joints. When quenches have occurred, the voltage spikes and temperature increase have not preceded the quench by more than a matter of seconds, not allowing time for ramp down of the magnet current to prevent the quench, but the recorded data from these signals has been useful in diagnosing the original location of the quench and guiding design changes to alleviate any issues.

4.2.4 Salt Pill

The *Micro-X* salt pill consists of 75 grams of Ferric Ammonium Alum (FAA) salt grown around a gold wire mesh in a cylindrical tube. A mesh of 200 gold wires runs through the center of the salt, with subsets of the wires brazed into the copper buses on either side of the pill. These buses serve as the thermal link between the salt and the heat switch on the forward side and the salt and the detector on the aft side. This two-bus design is somewhat unusual and is utilized in *Micro-X* because of the space and symmetry constraints of the rest of the instrument. The architecture is shown in Figure 4-9. Construction and testing of the salt pill has been one of my major responsibilities during the commissioning of the *Micro-X* payload.

The gold wire mesh is built from 99.99% pure gold wire manufactured and annealed by California Fine Wire. A cage is assembled using 316 stainless steel threaded rods, nuts and mesh (other alloys of stainless steel are susceptible to corrosion when exposed to the salt and/or magnetization by the high magnetic fields used in the refrigeration process [114]). The gold wires are cut to length and glued into the mesh with superglue that is later cleaned out using acetone. Once the wires are installed in the meshes, the extra lengths are bundled in preparation for brazing. Roughly one third of the wires are installed such that they extend past the stainless steel mesh by about one inch on the forward side of the pill. These will be braised into the forward bus and serve as the thermal connection between the salt and the heat switch. The other two thirds of the wires are installed such that they extend past the stainless steel mesh on the aft side. These will be braised into the aft bus and serve as the thermal connection between the salt and the FEA. The completed wire bundle is shown in Figure 4-9.

During the brazing process, the wires are brazed into the oxygen free high thermal conductivity (OFHC) copper buses using Harris safety silver solder 56 (chosen because it maintains its high thermal conductivity at low temperatures). Simultaneously, each bus is brazed into the corresponding stainless steel end cap. This simultaneous process is necessary because the wire-to-bus and bus-to-end cap braze joints are in nearly identical locations. The brazing step was done by the MIT central machine shop on the first two salt pills manufactured at MIT, but in later pills was completed by Scott Porter at NASA GSFC using a similar brazing procedure to that utilized for several successful salt pills manufactured there. Following the brazing step, the entire wire cage, end cap, and bus assembly is cleaned, then gold plated to allow for better thermal contact to the buses and to protect the braze joint and buses from the corrosive salt. The entire cage is annealed to remove any thermal conductivity issues introduced into the gold wire by cold working during construction of the cage. In addition, Stycast 2850 FT is painted over the braze joint on either side to further protect the vulnerable copper bus from the salt. In future pills we will likely use a less viscous type of Stycast so it can be more easily applied using a syringe.

Once the cage is finished, it is welded into the center of a thin 316 stainless steel tube, after which the assembly is leak tested to make sure that there are no pinholes in the weld joints. It must be vacuum tight because contact with air can dehydrate the crystallized salt. Also, pinholes could allow the salt solution to leak out during growing, or under vacuum. Once this step is completed, the salt can be grown. FAA is used because it has a large angular momentum of J=3/2 and reasonably high Landé g factor of g=2 [114]. It is also easily available, and is able to provide the cooling power necessary for the *Micro-X* system with a reasonable volume of the salt (the volume of the enclosure is 51.2 cm^3).

However, FAA has several drawbacks. As previously mentioned, it is extremely corrosive, so steps must be taken to protect the pill enclosure and caution used when handling, as contact with skin can be harmful. It can also dehydrate if exposed to air for extended periods of time. To prevent this, depleted salt solution or deionized water must be kept on top of the existing crystal at all times. Finally, the salt will denature at temperatures above 39°C, so it can be damaged by body heat. During and after growth, the pill must be handled as little as possible to prevent damaging the salt [114]. The salt must also be stored in a cool environment to prevent damage.

The salt is grown layer by layer in the MIT laboratory. The aim of the growing process is to create a single large crystal of salt inside the salt enclosure because crystal boundaries

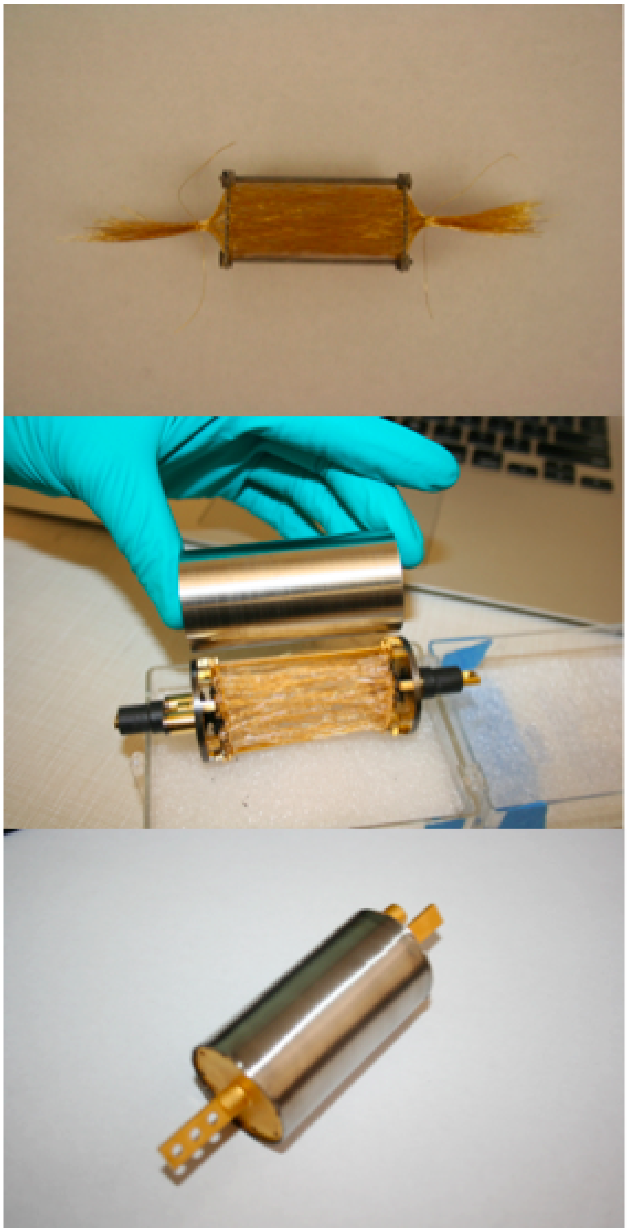

Figure 4-9: Pictures of the inside of the salt pill enclosure in each stage of fabrication. Top: the gold wire bundle containing 200 gold wires, shown with the forward side to the left. Middle: the gold wire bundle with wires brazed into the copper buses and the buses brazed into SS end caps, with the enclosure tube held above it, shown with forward side to the left. Bottom: the completed salt pill enclosure with stainless steel tube welded onto the cage, shown with the forward side up.

and voids between crystals inhibit heat flow and limit the amount of salt that can be grown in the enclosure. In practice this is not possible because the gold wires make it difficult for a single, uninterrupted lattice to form, however the procedure aims to maximize the crystal size (the guideline provided by our GSFC and UW collaborators is a crystal size of at least 5-10 mm, which we believe was achieved in all of our pills). This is done by attempting to eliminate multiple crystal growth sites. If crystals start to grow in multiple locations in the enclosure, then voids are likely to form at the meeting points of the crystals.

Eliminating multiple crystal growth sites is done in two ways. One is to rinse out the enclosure thoroughly each time the solution is changed. This will wash out some of the salt that has grown in the correct locations, but mainly will get rid of any small crystals that have begun to form in other locations, most often on the gold wires. A boroscope can be used to examine the inside of the enclosure after rinsing to ensure no secondary growth sites remain. The second method is to limit the number of crystals existing in the solution as it is added. This is achieved by making sure syringe is the same temperature as the solution (cooling encourages crystallization) and passing the solution through a warm syringe filter as it is being added to the enclosure.

The salt solution is made by combining FAA crystals purchased from Fischer Scientific with a 7% sulfuric acid solution in an even ratio of grams of salt crystals to milliliters of solution, and heating the mixture above 37°C. Since the temperature must be strictly controlled above 37°C and below 39°C we place the beaker with the crystals and sulfuric acid solution into an immersion circulator bath controlled at 39°C. The syringe, syringe filter, and tips are placed in the same immersion bath to regulate their temperatures.

Once the crystals are dissolved, the warm salt solution is added to the salt enclosure, after which the enclosure is attached to a cooling plate, which encourages crystallization. The salt will crystallize out of the solution leaving a layer of spent solution on top of the crystal. This spent solution will protect the crystal from dehydration until more solution can be added. Before a new batch of solution is added, the spent solution is drained and the enclosure rinsed with deionized water. When new, warm solution is added, the first cold surface it encounters should be the cold, existing crystal, which will encourage it to continue crystallizing on that lattice rather than start a new crystallization site elsewhere in the enclosure.

Each round of salt growth produces between 0.2 and 6 grams of salt depending on how much solution is inserted, the time of crystallization, and how much rinsing is required to get rid of extraneous crystals. The entire growth process takes about 2 to 3 weeks and requires constant monitoring. Once the salt has filled the enclosure the remaining spent solution is drained and plugs are welded into the ports on the forward side of the pill with the body of the pill in an ice water bath to prevent the welding heat from damaging the salt. Once this process is finished the pill is ready for testing. Tests determine the base temperature and heat capacity of the salt, the thermal conductance, G, between the salt and the detectors, and the parasitic heat load on the salt when installed in the *Micro-X* system. These tests will be described in more detail in Section 4.2.12.

We have built several salt pills at MIT with varying degrees of success. Our initial salt pill had a base temperature below 45 mK (the lowest calibration of our thermometers) but showed an unacceptably large thermal resistance between the salt and the bus ($\sim$0.1μW/mK conductance compared to the value of $\sim$1μW/mK measured for the *XQC* salt pill). This pill has been used extensively in the *Micro-X* system but cannot be used with detectors with a transition temperature less than 130 mK because it is limited to cooling detectors to a 75 mK base temperature due to the large thermal resistance.

Our second salt pill was manufactured in the same way as the first, but without gold plating step due to concerns that the gold plating might be causing heat conduction problems between the salt and the wires. This pill showed the exact same thermal performance as the first. In addition, because we did not have the gold plating to protect the braze joint, the salt came into contact with the bus, resulting in corrosion.

The third pill was brazed, gold plated, and annealed at GSFC, but was destroyed because of a materials problem. The tube and end caps were made from 304 stainless steel rather than 316. We believe that they were machined with an iron tool, and the inside of the tube

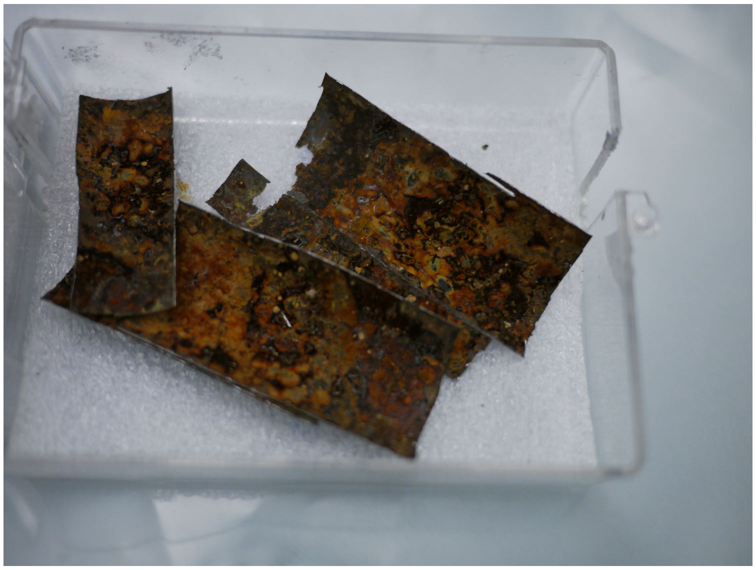

Figure 4-10: The inside of the stainless steel enclosure of the third salt pill after it was cut off of the gold wire cage. We suspect contamination during machining combined with the use of 304 stainless steel rather than 316 stainless steel caused the salt to corrode the tube to the point of mechanical failure.

was contaminated (the oxide was scratched off while machining and a small piece of iron remained on the surface preventing reoxidation). This allowed corrosion of the stainless steel to the point of failure. We were able to cut off the stainless steel tube, but the gold wire cage was too contaminated by rust flakes to salvage. A picture of the corroded stainless steel tube is shown in Figure 4-10.

Our fourth pill was brazed, gold plated, and annealed at GSFC. We ensured that all stainless steel parts were made from certified 316L stainless steel, which has the strongest corrosion resistance of any stainless steel alloy. After machining, the parts were passivated, ensuring reoxidation. We made two of each part and soaked the extra parts in a bath of salt for several weeks to make sure that there would be no corrosion (the corrosion in the third pill occurred within three days). On initial cool down, this pill leaked from the top fill-tube weld joint so it was cut open, rinsed out, regrown, and resealed. Vacuum tests have shown no leakage in the re-grown pill and thermal tests will be completed in the early summer of 2014.

4.2.5 Temperature Control

A stable cold bath temperature is vital to high resolution measurements since changes of detector temperature due to bath temperature change can skew fits of data pulses (we require control to better than 1 μK for best results). We control the temperature of the focal plane using the ADR electronics stack, which contains a PID loop operating off of one of the two thermometers mounted on the FEA. The temperature is modulated by changing the amount of current running through the magnet, and thus the magnetic field on the salt. This same circuit is responsible for bringing the FEA back to operating temperature after any heating experienced during launch.

Figure 4-11 shows the magnet current and temperature for the *XQC* during the course of launch, observation, and reentry. The temperature is regulated for a short time before flight to check that all systems are operating properly, then the electronics are set to hold (keeping the current across the magnet at a constant level). Launch causes just over 3 mK heating, which the ADR electronics cools quickly before observation when put in regulate mode just over one minute after launch. The temperature spikes during reentry because of the vibration from buffeting of the rocket skin by the atmosphere as the payload tumbles towards the earth. Regulation is able to once again hold a steady temperature just before landing while the payload is descending after the parachute has opened.

XQC launches with about 100 mA of current on the magnet and the cold stage at 50 mK, which is near their planned regulation temperature for observation. This leads to the fastest regulation after launch. With *Micro-X*, we will likely launch with the cold stage around 300 mK (about 800 mA on the magnet). This is advantageous because the specific heat of the salt pill is much larger at higher temperatures so the energy from vibration that makes its way to the suspended mass will have less of an effect when the salt is at a higher temperature. Since vibration isolation has been an issue in this payload, this will give us the best opportunity for a successful launch. After launch we will quickly demagnetize to the typical ∼100 mA residual current available at operating temperature.

Micro-X will utilize a spare set of *XQC* ADR electronics, which have been refurbished and

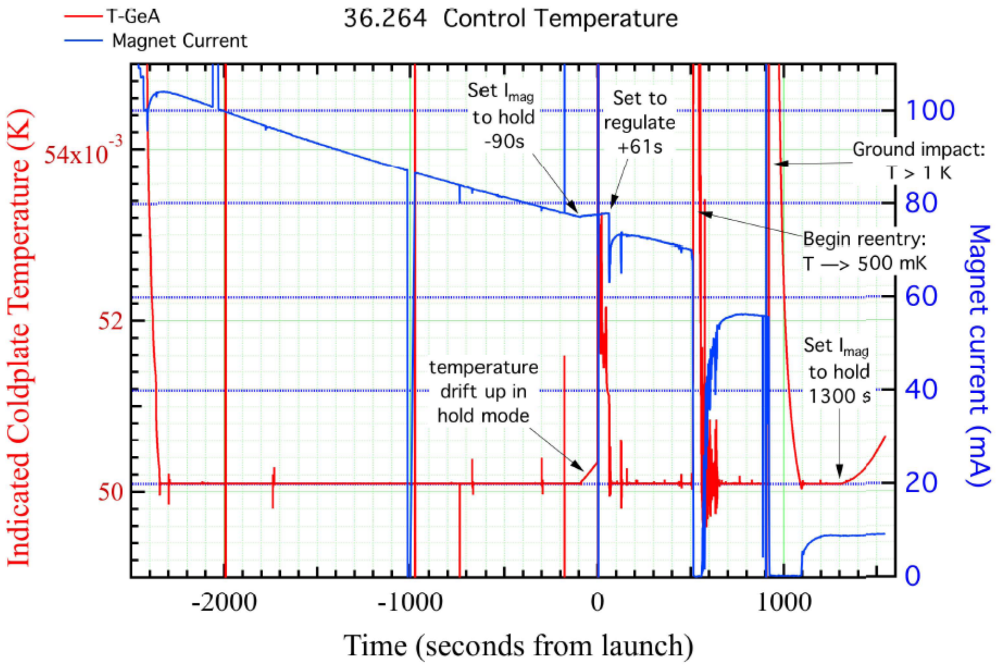

Figure 4-11: Magnet current and temperature recorded during an *XQC* launch demonstrating the temperature control.

modified for our purposes. The housekeeping and telemetry boards have been changed out for boards that better meet the specific needs of the *Micro-X* payload. The ADR electronics housekeeping is responsible for monitoring liquid helium level, insert temperature, magnet voltage, and the touch sensor. The touch sensor has two possible readings, corresponding to whether or not an electrical connection exists between the cold stage and dewar ground, which should only be the case when the heat switch is closed. The main functions of the system are to ramp the superconducting magnet up and down within its full range of field, and to control the focal plane temperature, which is achieves by controlling the voltage across the magnet. Controlling the magnet voltage rather than the more obvious current, takes advantage of the magnet's inductance to filter high frequency power supply noise. The average value of the current will slowly drain as the stored magnetic energy is converted into cooling power. Parasitic resistance from non-ideal joints will also cause a current drain, even with the system set to hold.

The temperature control circuit is shown in Figure 4-12. It operates as a lock-in amplifier, reading the voltage from one of the GRTs in the FEA in response to an oscillating excitation signal with constant amplitude. This oscillating signal is produced at the Sin generator marked (a) in the figure, and is converted to a much smaller oscillating drive signal at the capacitor (b). The resulting voltage drop across the GRT is amplified at (c): part of the preamplifier located on a separate board inside the cryostat vacuum enclosure. A set point resistor (h) determines the temperature at which the ADR electronics will lock. This resistance is set by a tunable pot during testing, then replaced by a permanent resistor for flight. A nulling signal, calculated based on this set point resistance, is summed with the amplified GRT voltage drop at (d), creating an error signal. This error signal is amplified at (e) and (f). This amplified error signal is fed into the PID (g), and becomes an input to the nulling signal used at (d).

The ADR electronics also output the error signal V_{err}. The rms modulation of V_{err} demonstrates the stability of the temperature control. Another control loop is used to compensate for any phase shift between the excitation signal and the voltage signal from the GRT caused by stray wire capacitance. This type of phase mismatch could cause ripples in the error signal when nulling the GRT signal with the set point signal. This loop, called the 'quadrature loop,' operates $\pi/2$ out of phase with the primary loop and uses (i), (j) instead of the primary loop's (e), (f). V_{quad} can be monitored to give information on how well the system is dealing with phase mismatches.

The ADR controller has two temperature settings. For use at higher temperatures, a larger input signal and lower amplifier gain is used, whereas at low temperatures a small input signal and higher amplifier gain is used. This keeps the circuit from causing self-heating at the thermometer with too high a drive current. There are also two settings for the magnet ramping speed, though during temperature control the circuit uses the full range of ramping speeds regardless of this setting.

The PID controller (g) outputs a control voltage across the magnet leads (the magnet return is grounded so it need only drive the supply lead). This output voltage is integrated

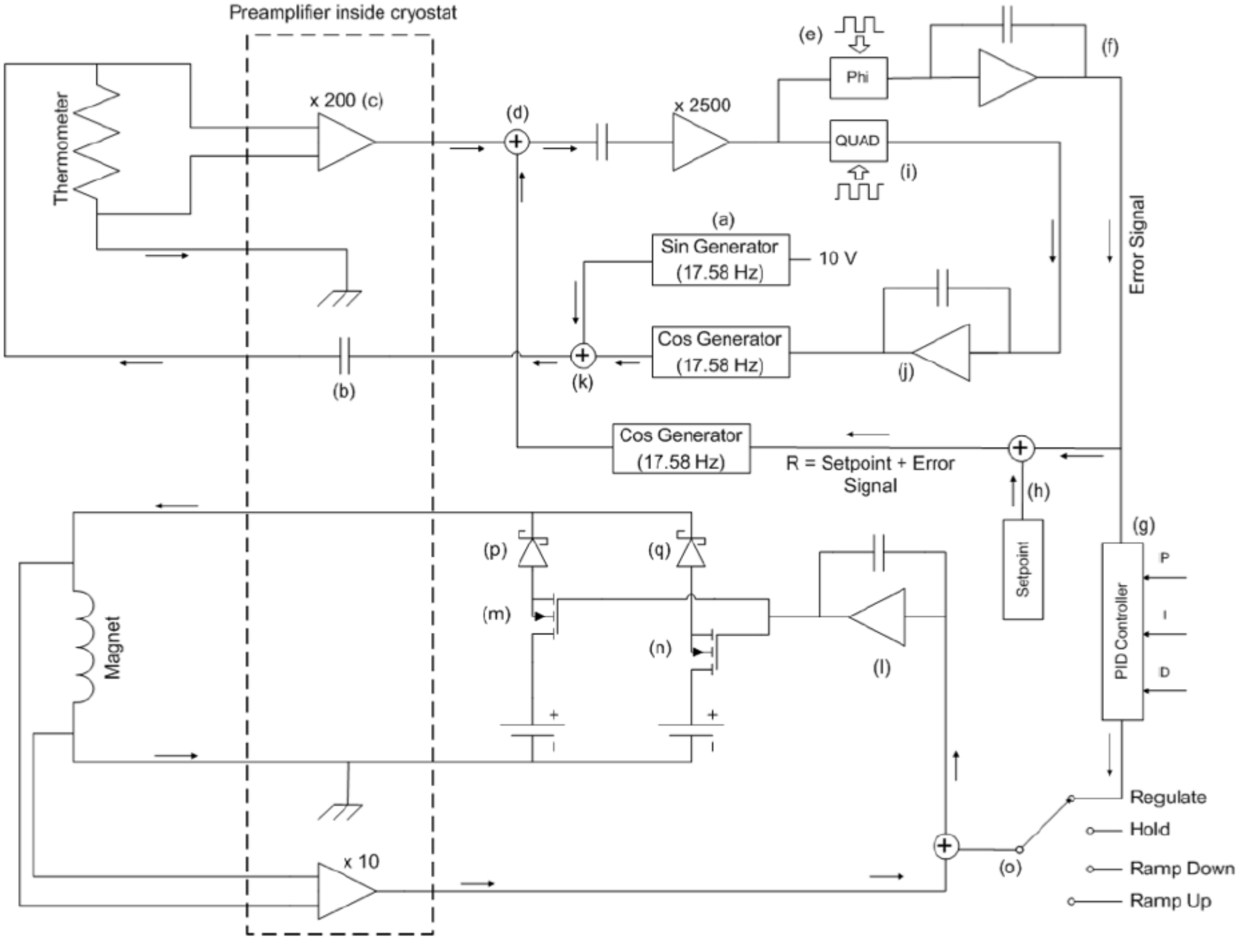

Figure 4-12: A diagram of the temperature control circuit utilized by the ADR electronics, reprinted from [86].

at (l) to control two redundant MOSFET power supplies (m,n). We have found that these must have closely matched characteristics or the system will rail. Since on a superconducting magnet dI/dt is proportional to V, positive voltage across the magnet leads ramps the magnet up (raising temperature) and negative ramps it down (lowering temperature). In the case where commands are sent to hold or ramp up or down rather than temperature control, a constant voltage is input instead of the PID output. The magnet current from the power supplies passes through Schottky diodes (p,q), which evenly distribute the power load between the two supplies at high currents, and isolate them so that a single failure will not affect both supplies.

On *XQC*, this control circuit showed 100 nK (rms) stability over a bandwidth of 1 Hz. At MIT, we have completed initial commissioning of the ADR electronics on our system. We demonstrated functionality of the touch sensor, helium level gauge, insert temperature diode, and magnet voltage tap. We were able to ramp the magnet to 9.4 A: close to it's maximum level of 9.5 A and high enough to achieve our current best base temperature. We broke out one of the two thermometer signals before the ADR preamp and read it out with the Lake Shore bridge. We then compared those results to the readout from the ADR electronics circuit and found good agreement. Temperature control showed an rms stability of about 0.1 mK. We expect this to improve with better PID tuning and improved shielding of signals inside the dewar to prevent crosstalk between the magnet voltage input and the thermometer readout. Much of the work readying the ADR electronics for this test was done by Rick Foster, Phil Oakley, Meredith Danowski, and David Goldfinger. I completed the installation of the preamp inside the dewar, wiring for the thermometer breakout, and monitoring of the non-flight electronics during testing.

4.2.6 Kevlar Suspension

In order to achieve magnetocaloric cooling, the salt pill and detector stage it will cool must be thermally isolated from the helium bath during demagnetization of the salt. This requires that the support structure for this mass (hereafter the suspended mass) must be not only strong but also provide thermal isolation. This is achieved in the *Micro-X* payload using a Kevlar suspension system, made up of seven loops of 8520 denier[5] Kevlar-49 fiber under tension[6]. Six of the Kevlar loops (four on the forward side and two on the aft side) constrain the position of the suspended mass, while the seventh (on the aft side) provides the tensioning force of about 400 N. The tensioning force is chosen to be in the neighborhood of half of the breaking strength of a single loop (1100-1300 N) so that each loop will be as far as possible from both failure modes: breaking and going slack. Kevlar is chosen because of its low thermal conductivity and high tensile strength [23]. The construction and testing of the kevlar suspension has been one of my major responsibilities during my tenure as a graduate student.

The design of the configuration of the suspension as it relates to vibration and heating is described in Section 4.3.4. Here I will discuss the extensive testing and design campaign for the individual loop design. A similar Kevlar suspension system was utilized in the *XQC* payload. However, instead of using loops of Kevlar, a single Kevlar string is glued into an aluminum piece on each side. One aluminum piece is fixed to the suspended mass and the aluminum piece on the other side is fixed to the support structure at 2 K. The problem with this design is the tendency of the glue joints to creep and fail under tension[7]. In the *XQC* payload the creeping is monitored and the suspension replaced when necessary. This would be more difficult in our system since our heavier suspended mass would require more frequent replacement of the suspension.

The *Micro-X* suspension piece design aims to protect the glue joint from creeping and failure by shielding it from the tension seen by the kevlar string using friction. A string is glued into an aluminum piece fixed on the 2 K stage, then wrapped around a spiral piece on the 2 K stage, a roller on the suspended mass, and a mirrored spiral piece on the 2 K stage, beyond which it is glued into a second aluminum piece on the 2 K stage as shown in

---

[5] Denier is a unit inherited from the silk industry. It gives the weight in grams of 9000 meters of fiber. This irksome unit has confounded more than one member of the *Micro-X* team, proving some things truly are harder than rocket science.

[6] Kevlar was provided by the Fiberline corporation

[7] 'Creeping' occurs because the glue never truly achieves a solid state, but is an extremely viscous liquid. Under enough force the string slowly slides through this liquid.

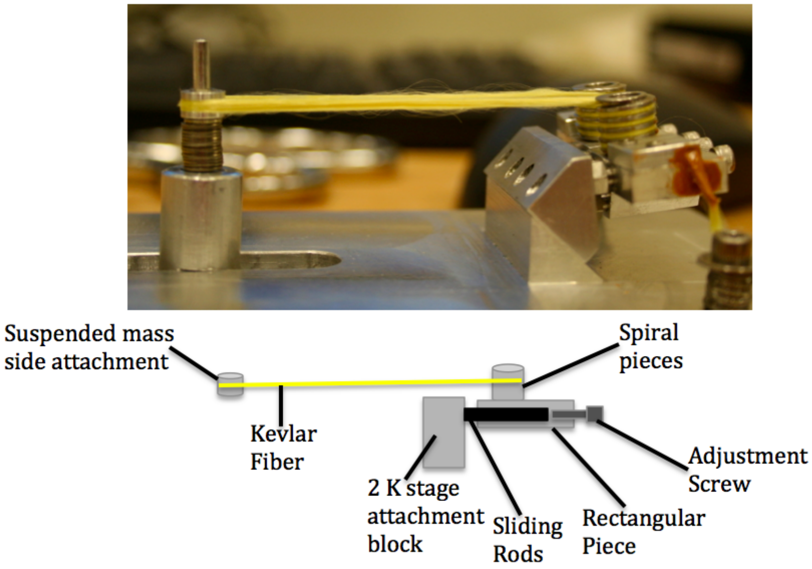

Figure 4-13: Side view of the first version of the kevlar attachment piece design with labelled schematic below. There are glue joints on the rectangular pieces, which slide on the sliding rods. The kevlar makes a loop around the suspended mass attachment piece from two spirals on the rectangular pieces, which are used to frictionally isolate the glue joints from the string tension.

Figure 4-13. The spirals and glue pieces are mounted on rectangular blocks, which slide on rods attached to a base block on the insert surface. The length of the piece can be changed by inserting adjustment screws in the back of the rectangular pieces, pushing them back on the rods. This is necessary to take up any slack in each piece before initial tensioning of the system, which will be discussed later.

In *XQC*, the Young's modulus of each suspension part approaches that of the raw Kevlar fiber 112400 MPa [23]. The modulus is important because the amount that the parts stretch in response to force controls how stiff the suspension system will be, and thus affects the resonance frequency. The lower the Young's modulus of the pieces making up the suspension, the lower the resonance frequency of the suspension. I will discuss this in much more detail in Section 4.3. We tested the Young's modulus of our own pieces by using an Instron 4201 pull test machine shown in Figure 4-14. The roller is fixed to the moving deck of the machine at the top of the figure, while the base of the piece is fixed to the stationary base of the

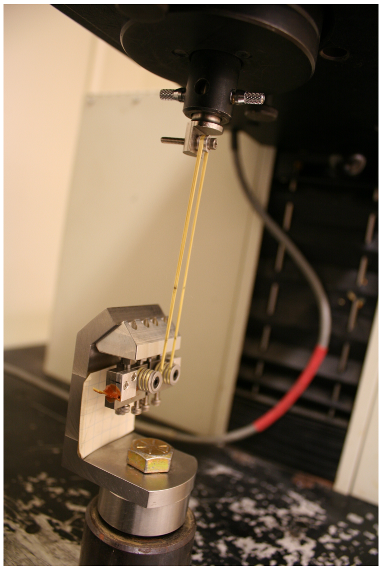

Figure 4-14: A test Kevlar suspension part installed on the Instron 4201. The roller is attached to a piece fixed in the load cell installed in the upper moving deck while the base is fixed to an adapter connected to the stationary base of the machine.

machine. The Instron moves the deck at a constant rate specified by the user, and measures the resultant force on the test piece using a calibrated load cell installed in the moving deck. Displacement and load are recorded using a Labview program. The Instron also senses mechanical failure, stops the deck, and reports the maximum load achieved and load just prior to break. Using this information, along with the known length of the part and cross-sectional area of the string, we can calculate the Young's modulus and breaking load of the part.

When we initially tested an individual suspension loop, we found that the modulus was only 15-20% that of the raw Kevlar. Even more strangely, we saw that the modulus increased when a part was pulled through a load range it had previously experienced (i.e. when pulled to a given load, relaxed, and pulled back to that same load). These problems turned out to be only somewhat related. The latter is caused by the string slipping over the spirals. The parts are strung by hand and only moderate tightness achieved during stringing. When a part is initially tensioned to a given load, the string slides and tightens along the spiral, where it remains due to friction unless further tensioned, or allowed to go completely slack.

This causes more stretching per force on the first pull through a given load range than on subsequent pulls. After the initial pull, subsequent pulls on the initial design gave a modulus near 35-40% of the raw Kevlar modulus. We do not consider this an issue since we expect the kevlar to be pulled tight around the spirals during initial tensioning and vibration.

To diagnose whether the unexpected softness was due to the mount or the kevlar itself, we tested a much longer sample (around 100 mm in length compared to the usual length of about 50 mm). This ensures that a larger fraction of the initial length of the part is kevlar, and thus a larger fraction of the stretching will be due to the kevlar rather than the mount. As expected, the modulus of these pieces was closer to that of that expected for raw kevlar, leading us to the conclusion that the softness was due to bending in the mount pieces.

In order to diagnose the location and magnitude of the bending, we employed photography, which proves much better than the human eye in identifying and quantifying movement. We taped a piece of graph paper behind the pull test sample to serve as a reference both for angles and distances, marked the kevlar with pencil to enable measurement of possible string slippage, then took pictures every 50 N during a pull using a camera mounted on a tripod and triggered by remote. These pictures were then strung into a video using Quicktime to enable us to see where bending was occurring qualitatively. We observed that the bending was occurring between the base block and the rectangular pieces on which the spirals and glue pieces are mounted. The location and direction of this bending is marked in Figure 4-15 To measure the bending quantitatively, we measured the angles of different parts of the assembly on the individual pictures as a function of load. An example of these measurements is shown in Figure 4-15. This bending accounted for some of the softness of the pieces seen in the modulus measurements.

Initial attempts to mitigate this bending included tightening the tolerances between the rods and the rectangular pieces, sandblasting the spiral parts to keep the kevlar from slipping as easily, installing thicker screws through the center of the spiral parts to stabilize them, and replacing the stainless steel rods with titanium. These had slight effects, increasing the

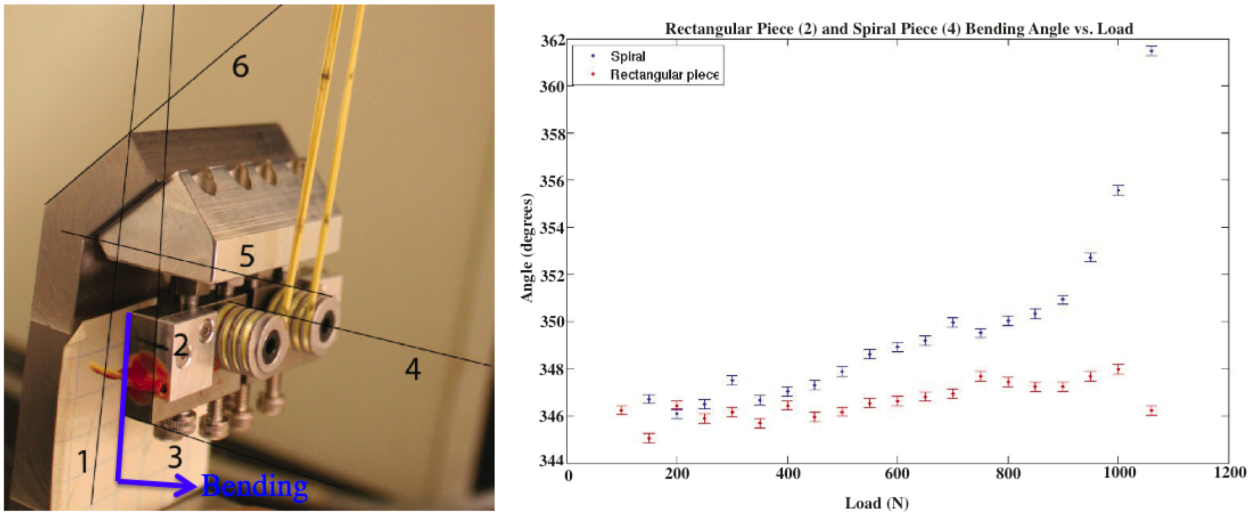

Figure 4-15: A picture of the kevlar suspension pull test setup with angle measurements labelled (left). A graph of the resulting angles on the rectangular piece and spiral as a function of pull load (right). We can see that both of the components bent as load increased. Around 1000 N in this particular measurement, the screw holding the spiral broke, causing that angle to sharply increase and the angle of the rectangular piece to decrease. After this test we replaced the screws holding the spirals with thicker shoulder screws.

modulus to 25-35% on initial pull and around 50% on subsequent pulls; this was better, but not sufficient for our purposes so we decided to undertake a more serious redesign.

Since the main cause of the bending is the torque on the rectangular pieces by the kevlar pulling at the top of the spirals, we decided the best course of action was a redesign of the parts to reinforce them in the direction of this torque. This was achieved by lengthening the base block and adding pieces to secure the top of the spirals on sliding rods in a similar manner to the rectangular pieces on the bottom of the part. In this design, the kevlar passes through a hole in the base block and pulls against the block, moving the torque from the bottom rods to the much more solid insert plate and base block. Figure 4-16 shows this new design and Figure 4-17 shows how the change supports the assembly against the torque applied by the kevlar. While these top pieces make assembly of each kevlar loop much more difficult, the modulus of this piece is 35-45% of the expected modulus of kevlar on initial pull and 55-65% on subsequent pulls, giving a marked improvement over the initial design.

We believe the remaining softness comes from the preferential tensioning of some of the strands of kevlar as the string passes around the radius of the spiral in addition to some remaining bending of the aluminum structure of the base block. In order to rid ourselves of some of the effects of preferential tensioning, we started wrapping the kevlar around the spiral pieces for only a quarter of a turn as opposed to the three and a quarter turns utilized in initial tests. While this leaves the glue joint more vulnerable, we believe the isolation is still sufficient, as we have seen no evidence of creeping, even under a full launch load vibration tests and several weeks of continuous tension.

We did not test this design iteration on the Instron, but performed an *in situ* test with the full suspension by hanging weights on the suspended mass directly opposite a single kevlar piece and measuring the resulting movement. A picture of this setup is shown in Figure 4-18. Using this setup we saw the measured modulus rise from $\sim$65% to $\sim$100% when switching from 3.25 turns around the spirals to 0.25 turns around the spiral. This test is much more difficult to perform and likely leads to higher errors on the modulus measurement, but the measured improvement is significant.

The assembly and tensioning of the suspension system is a tricky process requiring a combination of hand-eye coordination, dexterity, and mother's intuition. First, the suspended mass is secured in the correct orientation and position in the insert bore with a jig consisting of a tripod on the aft side and a set of bumpers that sit between the suspended mass and the bore on the forward side. Each kevlar loop piece must be carefully moved from the jig on which it was constructed (a kevlar piece is shown in its jig in Figure 4-13) to its position on the insert. Ideally, this process is completed by two people, though it is possible for a single person to complete it if necessary. The tensioning piece is constructed with the tensioning springs held back by silver plated screws[8].

Once all the pieces are installed, the goal is to have the kevlar slightly tighter than slack in each loop. This is achieved by adjusting the screws in the back of the rectangular pieces. On the forward side the screws holding in the bumpers can be removed and the exact position of the suspended mass adjusted to the point where all of the bumpers are loose. On the aft side

---

[8] Silver plating is necessary to keep the force of the springs from cold welding the screw to the thread

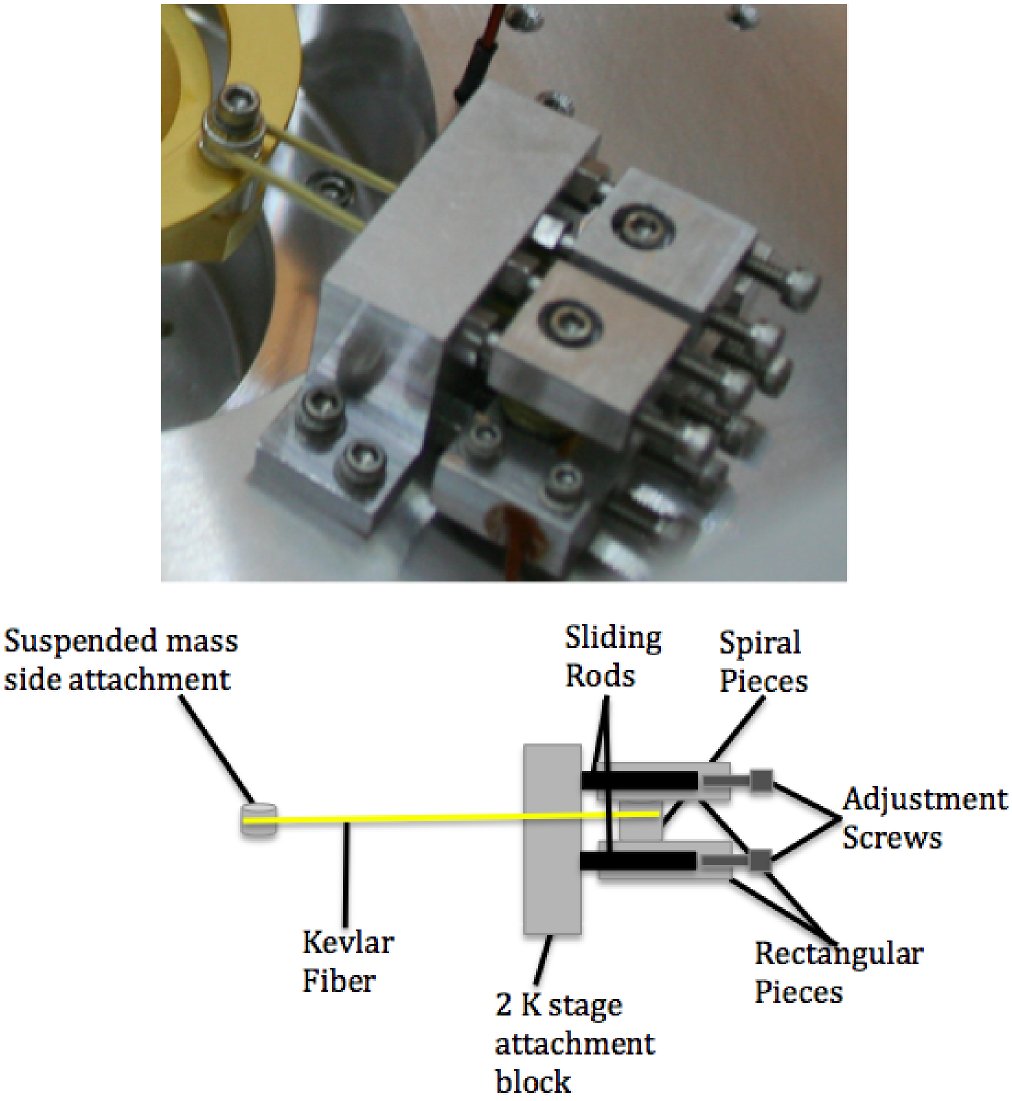

Figure 4-16: The new version of the kevlar attachment piece design with labeled schematic below. There are glue joints on the rectangular pieces, which slide on the sliding rods. The kevlar makes a loop around the suspended mass attachment piece from two spirals on the lower rectangular pieces. The 2K attachment block has been extended upwards, and the top rectangular pieces have been added in order to support the top of the spiral and keep the torque from causing bending in the lower sliding rods.

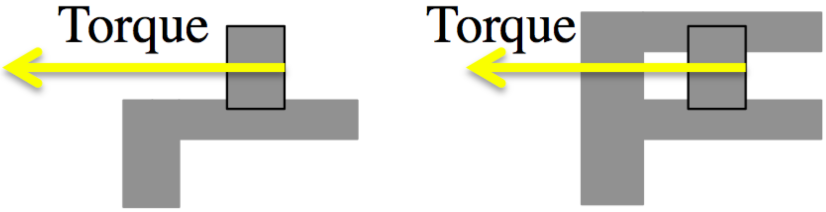

Figure 4-17: The location of the kevlar torque with respect to the mechanical support in the original design (left) and the new design (right).

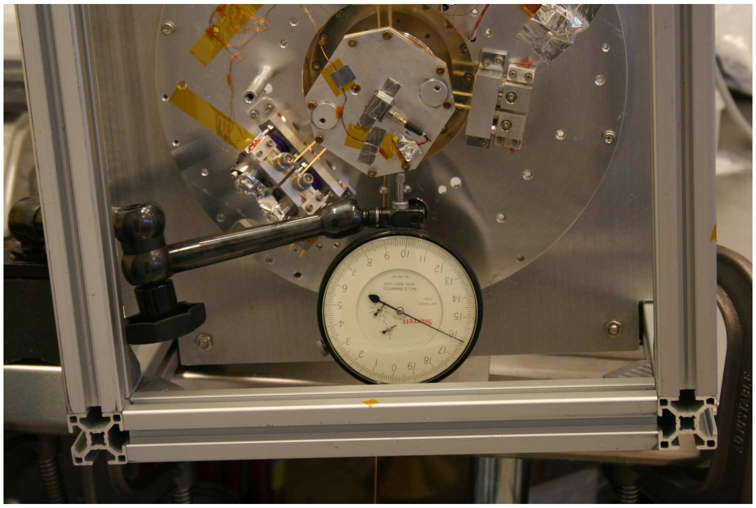

Figure 4-18: A picture of the *in situ* setup designed to test the elasticity modulus of a single kevlar suspension piece with the entire suspension in place. A known weight is hung on the suspended mass (on the bar supporting the octagonal piece that can be seen at the top of the image) using a loop of kevlar and the shift in the position of the suspended mass is measured using the push-dial seen at the bottom of the image.

the screws between the tripod legs and the insert surface can be removed and the position of the suspended mass adjusted to where the screw holes line up with no force exerted on the suspended mass by anything except for the kevlar, then the tripod can be removed from the suspended mass.

Tensioning the suspension is a simple, though stressful, process. The silver-plated screws simply have to be removed from the tensioning pieces to apply the tension. There are guard pieces [9] that must be installed once the screws are out to catch the back parts of the tensioning suspension piece if the kevlar breaks (otherwise they would be turned into bullets by the tension of the spring unopposed by the kevlar string and damage either the 2 K shield if it is installed, or whomever is unfortunate enough to be standing on that side of the insert if it is not). After this step, the system should be allowed to creep[10] for at least 24 hours.

Though the system is fully constrained by the other six suspension parts, the application of the tension causes the string to tighten around the spirals on all the pieces, causing creep in the position of the suspended mass. Since the springs take up the slack caused by this creeping, the suspended mass usually moves toward the tensioning suspension piece by several millimeters in the first twenty four hours after tensioning. After this creep has occurred, the suspension system must be adjusted to bring the suspended mass back into alignment. This is done by adjusting the lengths of the loops using the screws in the back of the rectangular pieces. It is usually best to take the tension off of the system using the silver-plated screws in the back of the tensioning suspension piece while making these adjustments to avoid unnecessarily stressing the threads in the back of the rectangular pieces. It is easiest to check alignment by installing the base of the magnetic shield and ensuring that the suspended mass is centered within the shield rather than reinstalling the tripod and bumper pieces. This process must be iterated until the system does not noticeably creep in a twenty four hour period.

---

[9] Known affectionately as the graduate student guard

[10] In this application 'creeping' does not imply the movement of the kevlar through the glue joint, but simply slow movement.

We went through several iterations of the design of the overall kevlar suspension system from a vibration isolation standpoint. I will describe this process in detail in Section 4.3.4.

4.2.7 Heat Switch

One of the most important parts of the adiabatic demagnetization system is the heat switch, allowing the paramagnetic salt to be connected to the helium bath while it is magnetized and then disconnected (made adiabatic) before and during demagnetization. There are many different approaches to heat switches utilized in various applications. *Micro-X* utilizes a mechanical heat switch made up of a scissor-like apparatus in which two jaws are closed on the bus of the salt pill by actuating a kevlar string attached to the mechanism that runs out to the forward side of the dewar. The jaws are heat sunk to the helium can using copper foil or braid and the heat switch mechanism is attached to the helium can with several screws.

The original heat switch was attached to the insert. The actuating string was connected to a plunger with a T-shaped piece on the end of it, which was mounted inside a light-tight bellows on the forward side of the helium can. Pictures of both sides of this mechanism are shown in Figure 4-19. The T plunger fit into a slit in the heat switch when the insert was installed in the helium can. The insert then had to be rotated by ninety degrees to lock in the plunger part. When actuated, the string would raise a plate attached to the scissor mechanism that slid on four brass poles to keep it parallel to the insert surface, ensuring that the jaws closed on the bus evenly. Unfortunately this design had several flaws. First, the rotation of the insert once in the helium can was difficult to do without snagging the various connectors running along the side of the helium can and insert. More seriously, the heat switch was prone to jamming if the plate was cocked at even a slight angle. This tendency often caused a weak clamp between the heat switch and the salt pill bus leading to very long thermalization times for the salt pill.

These problems led us to redesign the heat switch, using the *XQC* heat switch design as a template. The new mechanism is similar to the old design, but sits on the helium can rather than the insert and has a direct connection between the actuating string and the jaw

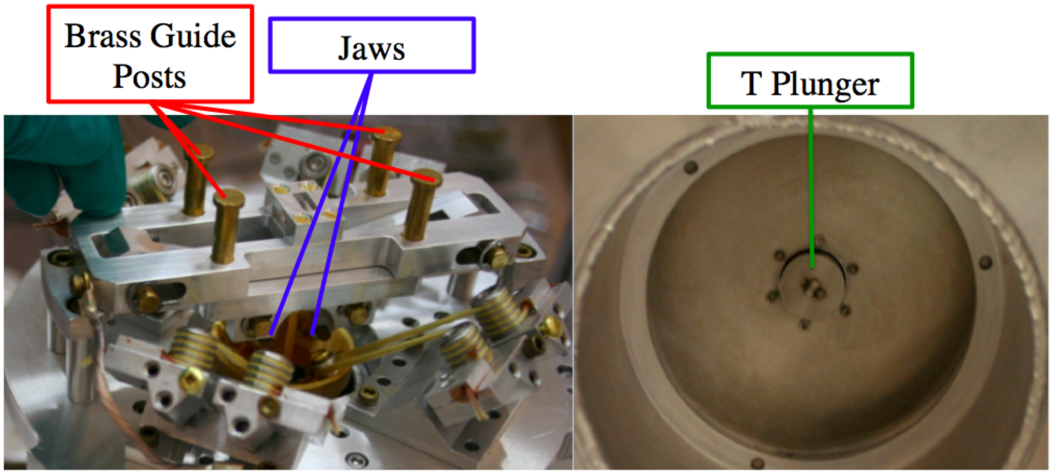

Figure 4-19: The original heat switch installed on the forward side of the insert (left). The mating plunger-bellows assembly installed on the helium can (right). The insert slid into the helium can bore and the slit in the top of the heat switch interfaced with the T piece on the plunger. In this design the insert is rotated ninety degrees to lock the plunger into the heat switch. The plunger is actuated by a kevlar string that runs to the forward side of the dewar, actuating the scissor mechanism and clamping the heat switch jaws around the heat bus.

parts so that the plate and guiding posts are no longer necessary. This raises the danger of bumping the salt pill bus on the heat switch jaws while installing the insert. However, we have mitigated this risk with guide parts that ensure the insert is in the correct position and orientation before getting close enough to the heat switch to risk bumping the bus. This design is much smoother in operation and has exhibited a consistent, strong thermal link between the salt and the helium bath[11]. A picture of this new design is shown in Figure 4-20.

We have had some issues achieving a sufficiently low pre-demagnetization salt pill temperature with this heat switch design. These issues seem to be a result of inadequate heat sinking at several locations. The kevlar string that actuates the heat switch is currently not heat stationed at any point except for at room temperature and at the helium tank[12]. The heat stationing of the heat switch jaws that clamp onto the salt pill bus at 2 K is done

---

[11] The assembly of this new design is much more difficult, but its functionality outweighs its inconvenience.

[12] This was true in the previous design as well, but the kevlar string was not connected directly to the heat switch so it did not affect performance as strongly.

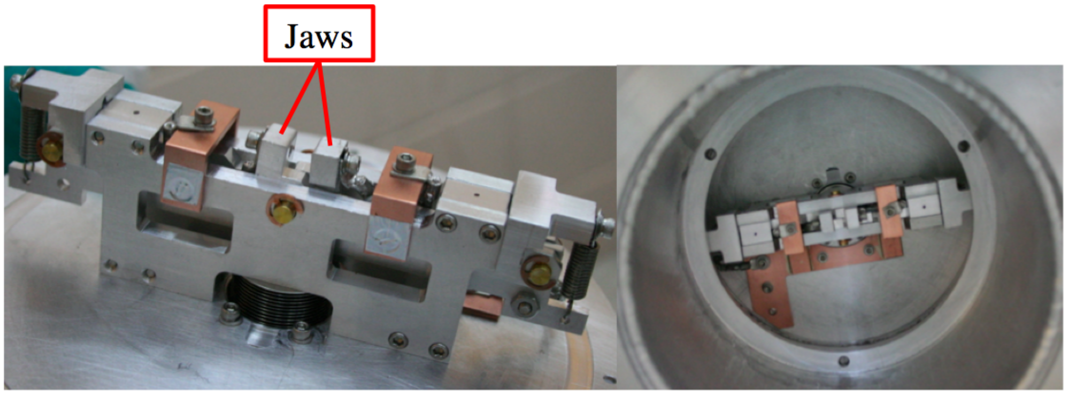

Figure 4-20: A close-up picture of the new heat switch mechanism when not installed on the helium can (left). The new heat switch installed in the helium can bore (right). For this design ‘goal post’ pieces are installed on the forward side of the insert to guide it into place without damaging the salt pill bus. Unlike the previous design iteration, no rotation of the insert is necessary after it has been installed.

through two aluminum-to-aluminum joints, which do not provide sufficient thermal conductivity. We plan to change the joints to gold-plated copper-copper connections, along with heat-stationing the kevlar at the 150 K and 50 K stages by gluing copper braids to the string and attaching them to the thermal shield lids, which we expect to correct these issues.

4.2.8 Liquid Helium Tank

The liquid helium tank serves as the support structure for the insert as well as the sub-2 K heat bath for the ADR. The tank is a welded aluminum annulus supported on the G10 support structure described in Section 4.2.10. The tank holds about 6.5 L of liquid helium, which is pumped on by a rough pump, resulting in a tank temperature between 1.6 and 1.8 K depending on the strength of the pump. Once it is pumped down, about 3 L of liquid helium remains in the tank. The hold time of liquid helium is just under 24 hours at room pressure and around 10.5 hours when the helium bath is pumped down. This necessitates filling the tank twice a day when pumping down for ADR cycles to run the detectors or complete thermal tests. This hold time could be improved, however it is not necessary for our purposes.

Since the payload will be run in a near-horizontal configuration after the optics are integrated and before transportation to the launch rail, we also tested the boil-off rate of the helium bath as a function of angle. We found a decrease in hold time of only 10% between vertical and about 84°, however we see a decrease in hold time by over 60% between vertical and horizontal, so we are designing carts for the payload integrated with the optics that will maintain an angle less than 84° from vertical.

There are two openings into the helium tank: one for the liquid helium level gauge and the other for the fill tube. The fill tube is made up of several sections of bellows welded together, and serves as fill tube, exhaust path for the cryogen boil-off, and pump-port. It is attached to the main body of the helium tank as well as to the outer vacuum jacket of the dewar with indium seals[13]. The flexible bellows serve a dual purpose. First, they allow for changes in spacing between the stages due to thermal contraction during cooling without damage to the line. Second, the structure in the bellows also causes turbulence in the exhaust gas, improving thermal contact between the helium vapor and the metal. This is important because the outer thermal shields are thermally heat-sunk to the fill tube and so rely on this thermal conductance for their cooling.

The base of the fill tube has a porous plug to allow boil-off to escape while preventing liquid helium from sloshing out of the can in the low gravity environment experienced during flight. The porous plug is made up of a sintered stainless steel annulus supplied by the Mott Corporation with 1μm pore size. The hole in the center of the annulus allows for filling and more efficient pumping, but is plugged with a stainless steel rod (affectionately dubbed the porous plug plug or PPP) during flight. This setup has been tested by installing the PPP and flipping the dewar over with a full liquid helium (LHe) tank.

The level gauge is made up of a five inch strip of superconductor with a transition temperature just above 4.2 K. The resistance of the strip is roughly proportional to the un-submerged length of the strip. The level gauge electronics are incorporated into the ADR electronics and drive about a mA through the strip while measuring the resulting

---

[13] Indium seals are made of soft indium rings compressed by pressure, and are used in situations where the seal will be cold and a rubber O-ring might freeze

voltage. This voltage is then mapped to the percentage of the strip that is superconducting (percentage of the tank filled with helium). Both the level gauge and the fill tube are located on the side of the tank that is up when the payload is horizontal. This means that the level gauge is not useful once the payload is sideways. However, since the boil-off rate should be consistent from run to run, level gauge readings will not be essential to operations after initial runs.

When cooling from room temperature, we first use liquid nitrogen to cool the tank from 300 K to 77 K. After allowing time for thermalization (usually overnight) we push out the nitrogen and use liquid helium to cool from 77 K down to 4 K. This is more efficient cost-wise since nitrogen is much less expensive than helium. During this entire process we try to maintain a cooling rate in the range of 1-1.5 K/minute on the insert thermometer. This rate has been empirically determined to be slow enough to prevent thermal contraction from stressing connections in the dewar or fracturing of materials due to thermal shocks. In many larger dewars, including the *Micro-X* lab dewar Gonzo, a liquid nitrogen tank encircles the liquid helium tank to intercept much of the heat load, but since the boil-off rate in LMO is acceptable for our needs and an additional tank would require valuable space and add weight it is impractical for the flight dewar.

4.2.9 Pumping Valve

As described in Section 4.2.8, we need to pump on the helium bath to achieve the ∼1.6 K starting temperature for the ADR. We cannot pump during launch, since attaching a pump to the the payload would be far too complicated and risky, so we need a system to close off the helium pump line before launch, open it again once the atmospheric pressure is low enough that the vacuum of space will provide the vacuum, and close it before reentry. This assembly is the pumping valve: a skin-mounted assembly containing a hermetic valve, a pressure relief (or blowoff) valve, and a pressure gauge. It is connected to the helium fill/pump tube using a flexible bellows encased in a rubber sheet to damp vibration of the bellows during launch. From the pumping valve assembly, a long, flexible, ribbed vacuum

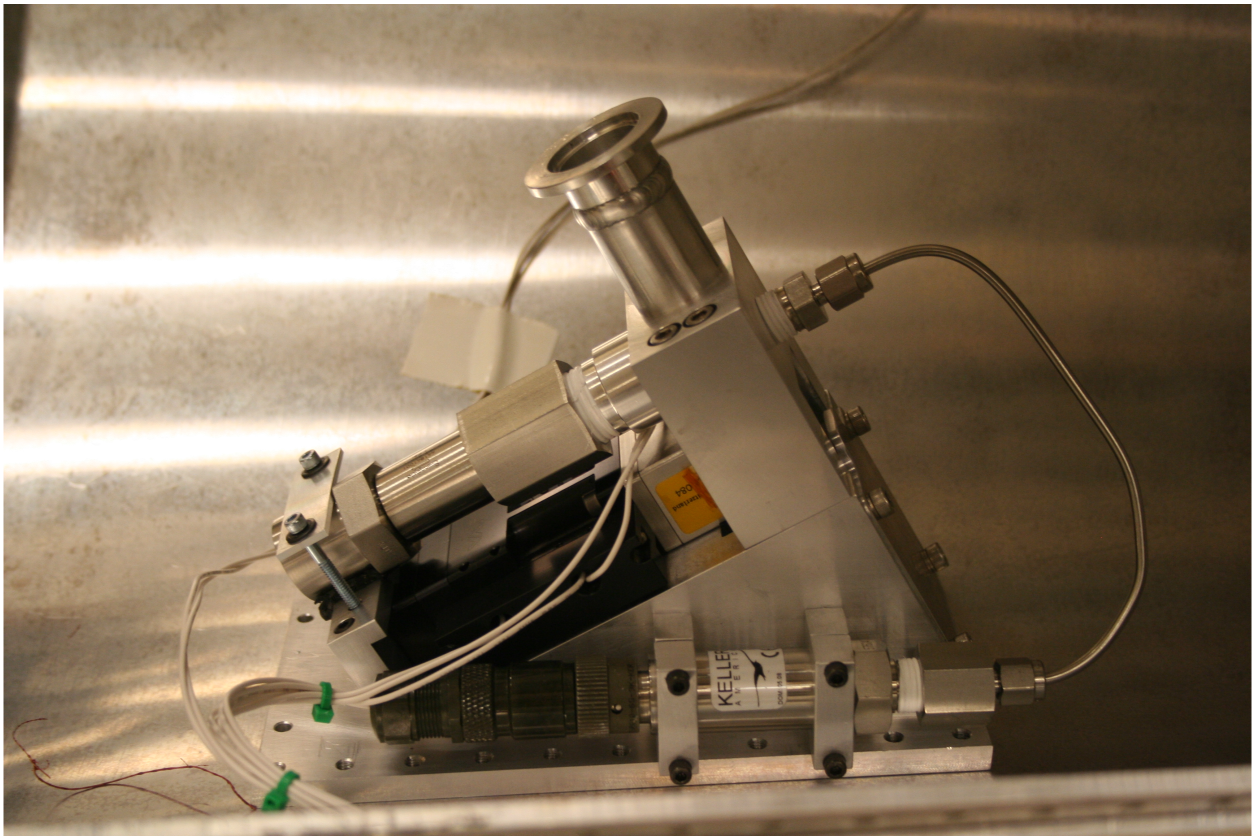

Figure 4-21: The pumping valve installed on the rocket skin, as viewed through an access window on the side of the skin.

hose connects via a slide-in press seal designed to disengage during launch, and runs down the rail to two pumps running in parallel. These are the same pumps utilized by the *XQC* team for pumping on their helium bath.

Just before launch the pumping valve is closed. Pressure from the boiling helium exhaust will build up above the helium bath for about 70 seconds until the payload achieves 100 km in altitude. At this point, the pumping valve opens again, releasing the built-up exhaust and allowing the vacuum of space to pump on the bath through the porous plug. The valve will stay open until the payload falls below 100 km on reentry, at which point it will close and remain closed until recovery. The blowoff valve assures that the exhaust can vent if the pressure in the helium can becomes too high. A picture of the pumping valve assembly is shown in Figure 4-21.

4.2.10 G10 Structure

The helium tank and insert are suspended from a series of cylindrical shells made from a 0.5 mm thick, commercial compound, made of laminated glass and epoxy. Several grades of this material are available commercially. In *Micro-X*, we use G10 glued into grooved aluminum rings using Armstrong A12 epoxy. A helium can suspension of nested G10 shells was originally used with great success in *XQC*, and the concept has been utilized in a similar manner in the *Micro-X* payload. We custom-ordered the shells to specified sizes from Stevens Products.

The G10 shells serve three functions: structural support, thermal isolation, and vibration isolation. The structural support is provided in the thrust (vertical) direction, along which G10 is extremely strong. For this reason the G10 tubes are also sometimes referred to as 'thrust tubes'. While being very strong longitudinally, the G10 is quite weak transversely. For this reason the tubes require extremely careful handling when not installed safely in the cryostat, especially during machining. To ensure that the glue joints between the G10 and the aluminum rings were structurally sound, I performed pull tests using the same Instron setup used on the Kevlar pieces described in Section 4.2.6. I found that the G10 broke before the glue joint and concluded that the glue joint was not a likely failure point.

G10 has excellent thermal properties to function as a thermally isolating structure between the 300 K vacuum can and the 2 K helium tank. Its thermal conductivity in the longitudinal direction decreases with temperature, with a value of 0.85 W/(m K) at 300 K and a value of 0.3 W/(m K) at 50 K. [117]. Figure 4-22 shows the 'Russian doll' configuration of the G10 shells. The outer G10 assembly (described in more detail in its current incarnation in Section 4.3.8) is suspended by its forward-most aluminum ring from the 300 K vacuum jacket of the cryostat. The inner G10 assembly is bolted to the aft-most aluminum ring of the outer G10 assembly on the aft side of the dewar. The outer thermal shield is bolted to the aft-most ring of the inner G10 assembly and clamps on its forward side to the helium pump line as described in Section 4.2.11. This shield typically has an equilibrium temperature $\sim$150 K.

The inner G10 assembly is made up of two separate G10 cylinders with an aluminum ring between them, and aluminum rings on the aft and forward sides of the assembly. The inner forward thermal shield is bolted to the center ring of the inner G10 assembly and also clamps to the helium pump line on the forward side. The inner thermal shield runs ∼50 K. Finally, the helium can is bolted to the forward-most ring of the inner G10 assembly sitting inside the hollow center of the inner G10 assembly. This long, winding thermal path helps to isolate the helium can from the warm temperature of the outer vacuum jacket and increase helium hold time. The science chain, housekeeping, and magnet wires run along the outside of these shields, allowing heat stationing at several locations and a long length of wire between the warm and cold components of the dewar.

The use of the G10 structure as vibration isolation is described in detail in Section 4.3.8. The spring constant of the G10 assemblies sets the resonance frequency of the helium can stage to help damp vibrations coming in to the system through the outer vacuum jacket's attachments to the skin.

4.2.11 Thermal Shielding

Since the detector plane is maintained at its operating temperature by a salt with a limited cooling capacity, the less heat load on the suspended mass, the better. In other words, our goal is to lose as little as possible of the salt's cooling capacity to parasitic heat loads. As mentioned in Section 4.2.8 the heat load on the helium tank determines its hold time (or the amount of time between necessary helium tank fills). For both these reasons, we wish to minimize the heat load on both the suspended mass and the helium tank. This is achieved with several layers of thermal shielding, each thermally isolated from the others.

The outer two layers of thermal shielding[14] are isolated from each other and from the warm outer vacuum jacket by the G10 structures described in 4.2.10. These layers of thermal shielding are shown in Figure 4-22. Two thin, cylindrical welded Al shells attach to the aluminum rings epoxied to the G10 cylinders. These are screwed to circular lids that clamp

---

[14] These are creatively called the inner and outer shields.

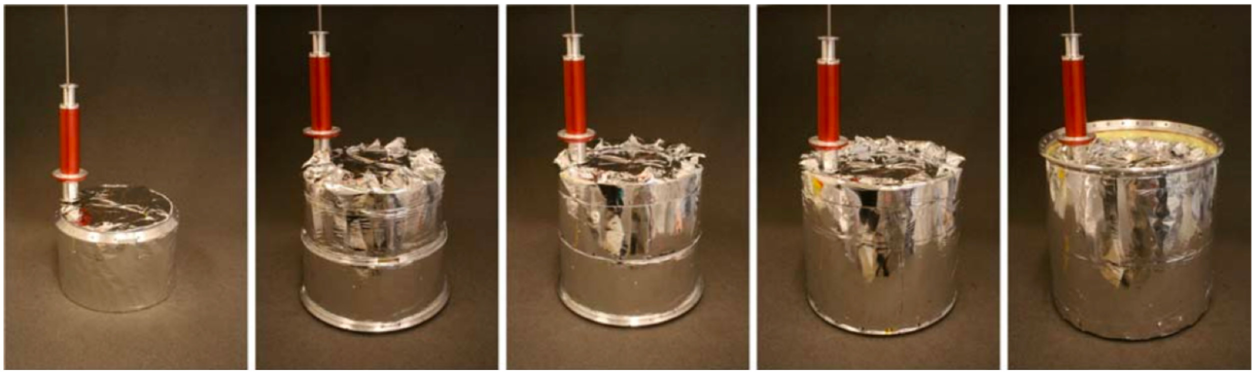

Figure 4-22: The layers of thermal shielding in the *Micro-X* dewar. These are built up like a russian doll, with several nested layers. The layers in this picture are (from left to right): helium can, inner G10 assembly, inner G10 assembly with inner forward shield installed and the outer G10 assembly.

to the helium pump line and are cooled by the cooling capacity of the helium vapor passing through the pump line. These shields operate at approximately 50 K and 150 K. The helium can is screwed to yet another aluminum ring isolated from the others by G10, and the 2 K shield is attached to the aft side of the insert, protecting the 2 K board electronics (including the SQUID arrays), the suspension, and the suspended mass. The FEA structure and lid serves as the thermal shielding for the inner SQUID stages and the detector plane and is thermally isolated from the helium stage by the low thermal conductivity kevlar suspension.

While the G10 structures and the kevlar suspension reduce the heat load from the direct contact of hotter stages, radiative (blackbody) infrared heat is a major concern. There are complete metal enclosures at each stage: 50 mK, 2 K, 50 K, and 150 K. These enclosures offer the best approximation to an infrared light-tight box as possible. Unfortunately, the potting compound used for most of the connectors taking signals through these shields is nearly transparent to infrared radiation. Aluminum tape is used to seal up as many small holes as possible, as well as to try to block light from getting into and around connectors, but it is inevitable that some will get through. In order to minimize the affect this has on the components inside the shield, the 2 K shield will be 'blacked' to reduce the Q of the cavity so that most of this leaked light will be absorbed by the inner walls of the cavity rather than being absorbed by the (often high emissivity) sensitive components inside. Blacking is done with ‘Bock Black’, a compound made of Stycast 2850 FT and lampblack (finely powdered black soot), that is extremely absorbent in the infrared. The thickness of the layer inside the cavity should be dictated by the wavelength of the radiation that may penetrate the cavity. Care is taken to seal any light leaks along the paths of the heat switch actuating string and the filters (Section 4.7) reduce the infrared light leaks along the path of the X-ray light.

The G10 structures and the metal shields at 50 K and 150 K are covered in multi-layer insulation (MLI). Each MLI blanket is made up of 20 layers of thin aluminized mylar separated by coarse netting, creating an uneven surface on each of the layers of mylar designed to trap infrared photons. Each shield is wrapped in two CoolCat 2NW MLI blankets from RUAG Space GmbH, with seams sealed by low emissivity tape from Austrian Aerospace (now RUAG Space GmbH). We originally planned to cover the sides and forward end of the helium can with MLI as well, however, the MLI is not as useful for trapping photons at the temperatures and wavelengths experienced on the helium can, and the MLI encourages stray air molecules to bounce along its surface rather than to adsorbing to it, which causes these molecules to adsorb instead to the 2 K filter on initial cooling . This is undesirable because air molecules can absorb radiation preferentially around nitrogen lines, lowering transmission and changing the calibration of the filters.

4.2.12 Heat Loads

One of the first steps of validating the design of, and workmanship on, our cryogenic system, is to measure the degree of isolation of the various thermal stages by measuring the heat load on each stage. The heat load on the helium bath is calculated using the observed hold time and the latent heat of vaporization of liquid helium. The heat load on the cold stage is slightly more difficult to attain, but is vitally important to measure, since large heat loads on the cold stage can prevent sufficient cooling of the detectors and affect cold stage hold time.

The heat load on the cold stage comes from infrared radiation from the surrounding 2 K materials and conduction from the 2 K stage through the kevlar suspension and science chain

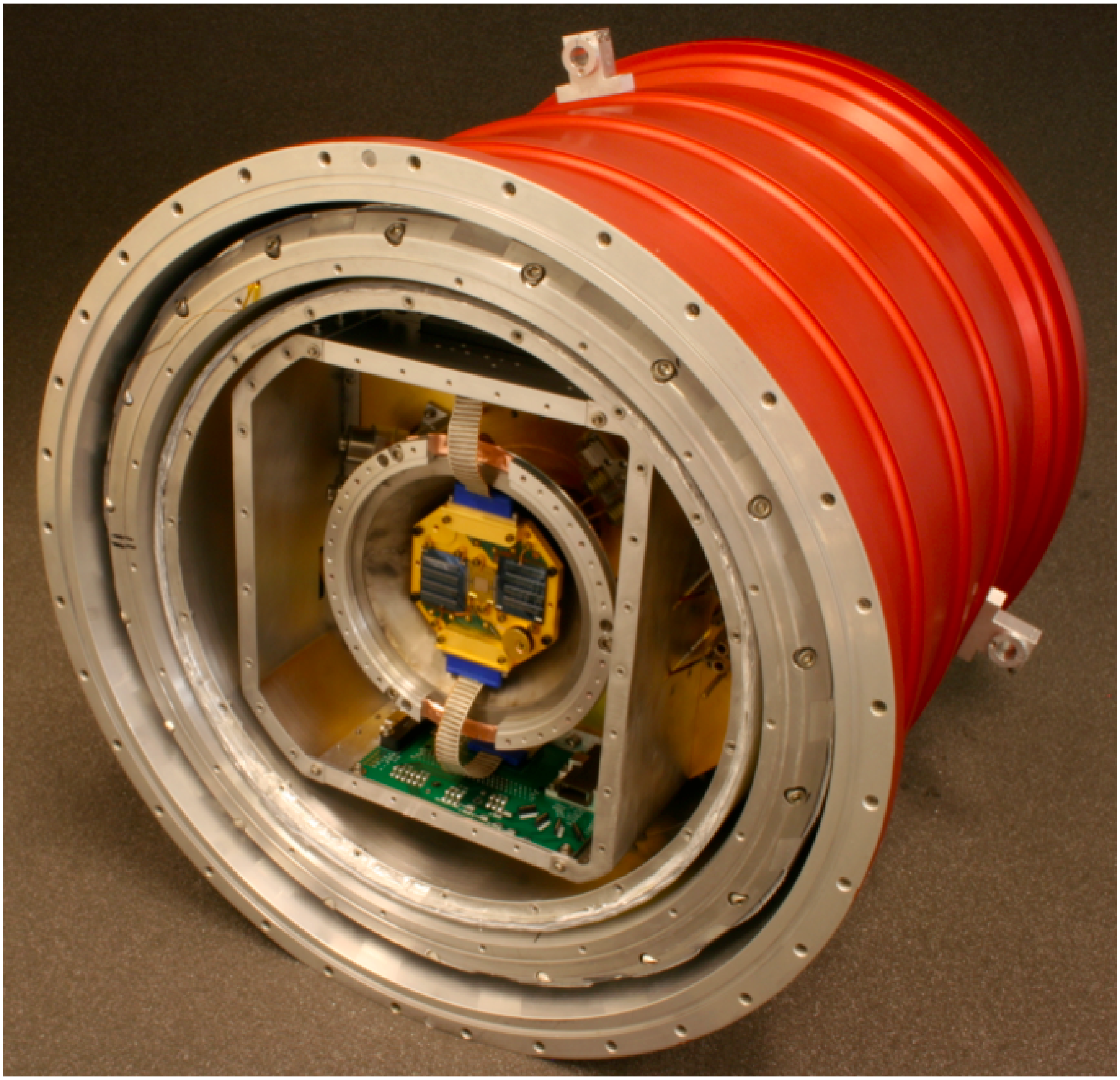

Figure 4-23: A picture of LMO with the aft end lids of all of the thermal shields and the FEA lid removed. The concentric metal rings visible here are the ends of the cylindrical thermal shields. The circuit board visible towards the bottom of the image is one of the 2 K electronics boards.

readout cables. There are two science chain cables, each of which is a ribbon cable, made of aramid fiber woven and twisted around 43 twisted pairs of CuNi-clad NbTi wire with a diameter of 50 μm. At their operating temperatures, the NbTi wires are superconducting and so only conduct heat weakly through phonons, however heat flows through the aramid fibers and the cladding.

In all low-temperature measurements it is important to take care with the setup of thermometers. Most of the thermometers we use measure the temperature of the radiation environment in which they are operating unless covered in copper tape to heat sink the sides to the contact surface and act as a radiation shield. Proper heat stationing of the thermometer wires is also necessary for accurate temperature readings.

The heat load on the FEA can be measured in a fairly straightforward manner. We start at base temperature, after a full ADR cycle, and measure the slope of the heating (which is constant within a small temperature range). Then, we apply a calibrated power through a heater mounted on the FEA lid. We perform this measurement quickly at a temperature close to that during the initial heating slope measurement, so that in a ratio of the two slopes, the specific heat of the cold stage will cancel, yielding a measurement of the parasitic power. We measured the parasitic power on the cold stage to be 3μW in the current setup.

We can determine the amount of this parasitic power due to radiative loading by measuring the steady state temperature difference between the suspended mass and the insert with the heat switch open. In this configuration, the suspended mass sits at a slightly higher temperature than the insert surface because of the radiative load it experiences. Using knowledge of the thermal conduction between the two (G), which can be measured as described below, we can use $\mathrm{P}_{rad} = G\Delta T$ to obtain the radiative load, which we measure to be about 0.3 μW. About 1 μW of the parasitic power comes through the science chain cables while the remaining $\sim$2 μW comes through the kevlar suspension. The 1 μW load of the science chain cables applied directly at the detector plane is problematic. We may need to make an effort to heat-sink these wires to the forward side of the salt bus so that the resultant heat load will be applied at a less sensitive location in the system.

The thermal conductance G can be obtained by applying a calibrated power to the heater on the FEA lid and observing the resulting temperature jump. The definition of conductance, $G = dP/dT$, can be applied in the limit of small temperature differences as a result of a known applied power to obtain $G = P/\Delta T$. This measurement can be made using heaters and thermometers in various locations to obtain the G between the FEA and the salt, the heat switch and the salt bus, the insert and the helium can and between the TES pixels and the FEA surface.

4.2.13 Vacuum Design

All cryogenic systems require some form of vacuum isolation. Gas between cold components and the room temperature outer surfaces of the system will act as a thermal short causing high heat loads on cold stages. The 'vacuum jacket' I have referred to previously is LMO's red, outer, ribbed aluminum cylinder[15], which can be seen in Figure 4-23. Vacuum is held at both ends with O-ring seals. Three ports on the forward plate accommodate 'military'-style hermetic circular connectors (two for the science chains and one for housekeeping). These are sealed with O-rings, as are seals on ports for the heat switch string and the fill tube. The fill-tube bellows is sealed to the outer, red anodized fill tube cover with an indium seal that will not freeze during cryogen transfers.

There is a single port in the aft plate for X-rays to enter the cryostat, which connects to the bulkhead through a flexible vacuum bellows. The bellows allows for the movement of the cryostat on its flexible mounts without breaking the vacuum seal. On the opposite side of the bulkhead, in the evacuated optical section, a gate valve forms a seal between the two sections. This gate valve will be sealed until just before the observation as described in Section 4.2.13. The gate valve is a commercial valve, placed in a custom housing shown in Figure 4-24. It is equipped with a pressure sensor so that it will not open unless the pressure in the optical section is sufficiently low. This condition can be overridden for testing.

Before the system is cooled, we evacuate the dewar using a Pfeiffer HiCube80 turbo

---

[15] While most of the dewar structure was machined at the MIT Central Machine Shop, this was machined at Wallops because of their experience dealing with large cylindrical vessels.

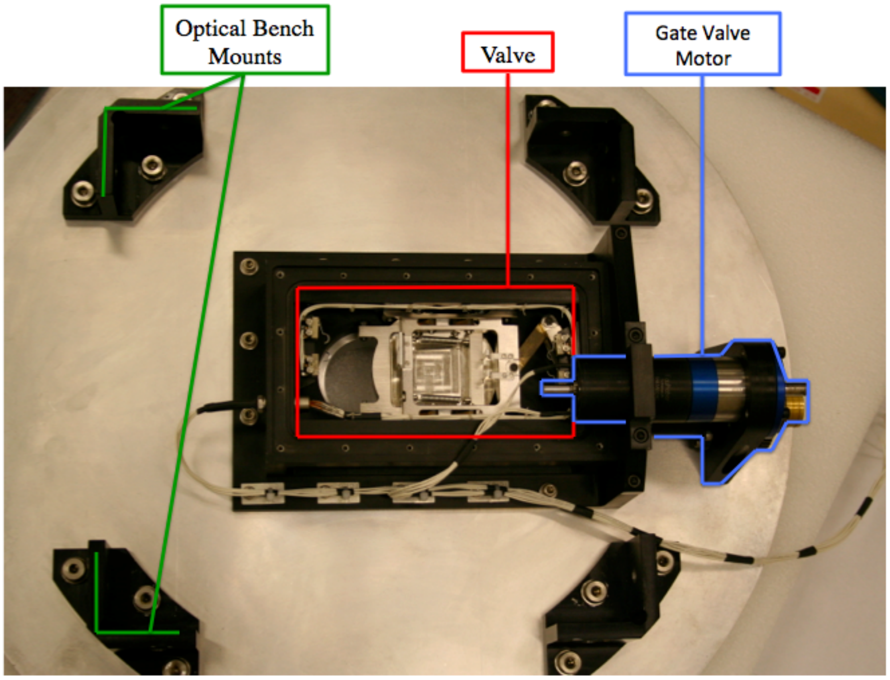

Figure 4-24: A picture of the gate valve with the valve, motor and optical bench mounts labelled. The pressure gauge is located on a lid that fits over the valve not pictured here.

station[16] in parallel with a helium leak checker[17]. Once we have attained a pressure of about 10^{-3} mbar, we perform a helium leak test. At each stage of cooling (liquid nitrogen at 77 K and liquid helium at 4 K), we perform additional leak tests to make sure that no seals have been broken during the cooling process. Once all of the components thermalize at 4 K, we remove the pumps, since cryopumping becomes stronger than the pumps. Cryopumping is a process in which molecules adsorb to cold surfaces, pulling a vacuum in the open space, which provides a vacuum of approximately 10^{-6} mbar in LMO once the entire system has thermalized.

---

[16] This all-in-one system with a dry diaphragm rough pump and an internal turbo pump capable of a displacement of 0.3 ft^3/min is very convenient, though its quirks and small size have earned it the nickname 'Dopey' in the lab.

[17] Leybold vacuum PhoeniXL 300

4.3 Vibration Isolation

The duration of the *Micro-X* sounding rocket flight will be approximately 15 minutes, with the observation lasting about 5 minutes. The ADR must be cycled before flight and the detectors kept cold during launch, as the timeframe makes recycling of the ADR in flight impossible [112]. This requires very effective vibration isolation between the skin and the detector stage to shield the detectors from vibration from the near-white, $\sim$12.7 g_{rms} vibration spectrum of the Terrier Black Brandt rocket launch [98], which has the capacity to cause significant heating.

The vibration isolation system for the *Micro-X* payload has several stages: damping suspension pieces between the skin and the dewar (Section 4.3.2), a system of G10 tubes inside the dewar supporting the helium can (Section 4.3.3), and a kevlar suspension to isolate the detector stage from the liquid helium stage (Section 4.3.4) [112]. These stages are labelled on a schematic of the system in Figure 4-25. Isolating the inner stages from the vibration at the outer stages is achieved by staggering the resonant frequencies of the stages in such a way that the resonant frequencies of the stages increase closer to the detector. This means that the coldest stages are the stiffest, and have resonant frequencies that sit in regions that are damped by each of the warmer stages [113].

In June, 2012, we travelled to Wallops flight facility to submit the payload to launch-level vibration testing. This testing resulted in detector stage heating far above acceptable limits and prompted a testing and redesign phase discussed in the following sections. We returned to Wallops in August, 2013 for further vibration testing. I will also discuss the results of these tests and the redesigns they have prompted. Table 4.1 summarizes the measured resonances of each of the rocket stages for each of the design iterations discussed in this section.

4.3.1 Laboratory vibration setup

Since trips to a vibration table are costly, we created an inexpensive, in-house vibration setup to test design iterations using audio transducers sold commercially as home theater equipment. We experimented with many different setups to test various subsets of the damping

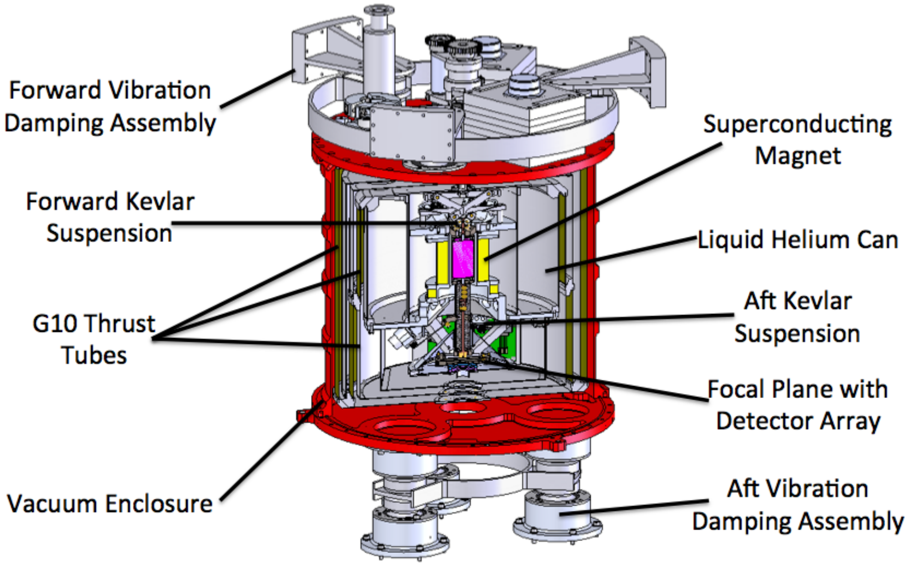

Figure 4-25: A schematic of the Micro-X dewar and dewar suspension. In this schematic the forward side of the dewar is up and the aft side is down. The pieces marked ”damping assembly” connect directly to the rocket skin on the forward side and the bulkhead (which is rigidly connected to the rocket skin) on the aft side.

systems and identify the resonance frequencies at each stage. We used two different transducers for these setups. The first is the Clark Synthesis TST329 Gold Transducer (called the ‘UFO’ in the lab because of it’s shape) and the other is the Crowson Technology EDH-100 (similarly nicknamed ‘Bigfoot’). The UFO is stronger at higher frequencies. It can be mounted on the top of the dewar (exciting the dewar directly rather than through the response of the skin-dewar suspension system) or directly on top of the insert stand-alone jig. The Bigfoot is stronger at lower frequencies and sits on the floor with the test subject on top of it. The Bigfoot is mostly used in a capacity similar to the Wallops vibration table, underneath the skin, with the dewar mounted as for flight, or underneath the insert jig. Pictures of these setups are shown in Figure 4-26. This testing campaign was completed by John Rutherford, Phil Oakley, and myself, with help from Patrick Wikus in data interpretation and redesign considerations, and is described in [43].

In the setup shown in the upper right of Figure 4-26, the transducer mounts to the top plate of the dewar so that we can vibrate the dewar directly. We drive the transducer with a slow sine sweep produced by a dynamic signal analyzer, monitoring either accelerometers mounted on various stages of the dewar at room temperature, or the heating produced by the sweep when the liquid helium and detector stages are at 4 K. We have found that the accelerometer data is often difficult to interpret, so our most reliable results have been obtained monitoring heating as a function of frequency. This method does not take into account the frequency response of the transducer itself, but has been quite reliable in helping us to understand changes between design iterations.

The Bigfoot setup, shown in the lower right of Figure 4-26, has been most useful in analyzing the resonances of the suspension between the skin and the dewar. We sweep the Bigfoot in frequency using the dynamic signal analyzer while monitoring accelerometers on both the skin and the dewar lid, also using the dynamic signal analyzer. Again, this is most useful in diagnosing changes between iterations as the frequency response of the transducer is not taken into account in the data taking. We can also perform the heating test in this setup, but it cannot be performed at 4 K since the Bigfoot does not have the power to excite the dewar enough to cause heating through the dewar suspension damping stage at this temperature. The heating can be seen with the detector stage at 100 mK, but the interpretation of this data is complicated by the fact that the heating frequencies are the result of the entire damping system. The other weakness of the Bigfoot setup is that the Bigfoot can only shake one side of the skin, producing a rocking motion rather than a motion in the thrust or radial axes the way the Wallops shake table would. This can exaggerate the effect of couplings between the horizontal and vertical axes.

While the setup using Bigfoot to shake the skin is best to test the resonances in the skin to dewar suspension system and the UFO setup shaking from the dewar is best to test the resonances of the helium can and their coupling to the resonances of the kevlar suspension system, we would like to test the resonances of the kevlar suspension system without the interference from other suspension stages. In order to accomplish this, we designed testbeds utilizing both the UFO and the Bigfoot to shake the insert outside of the dewar. When the

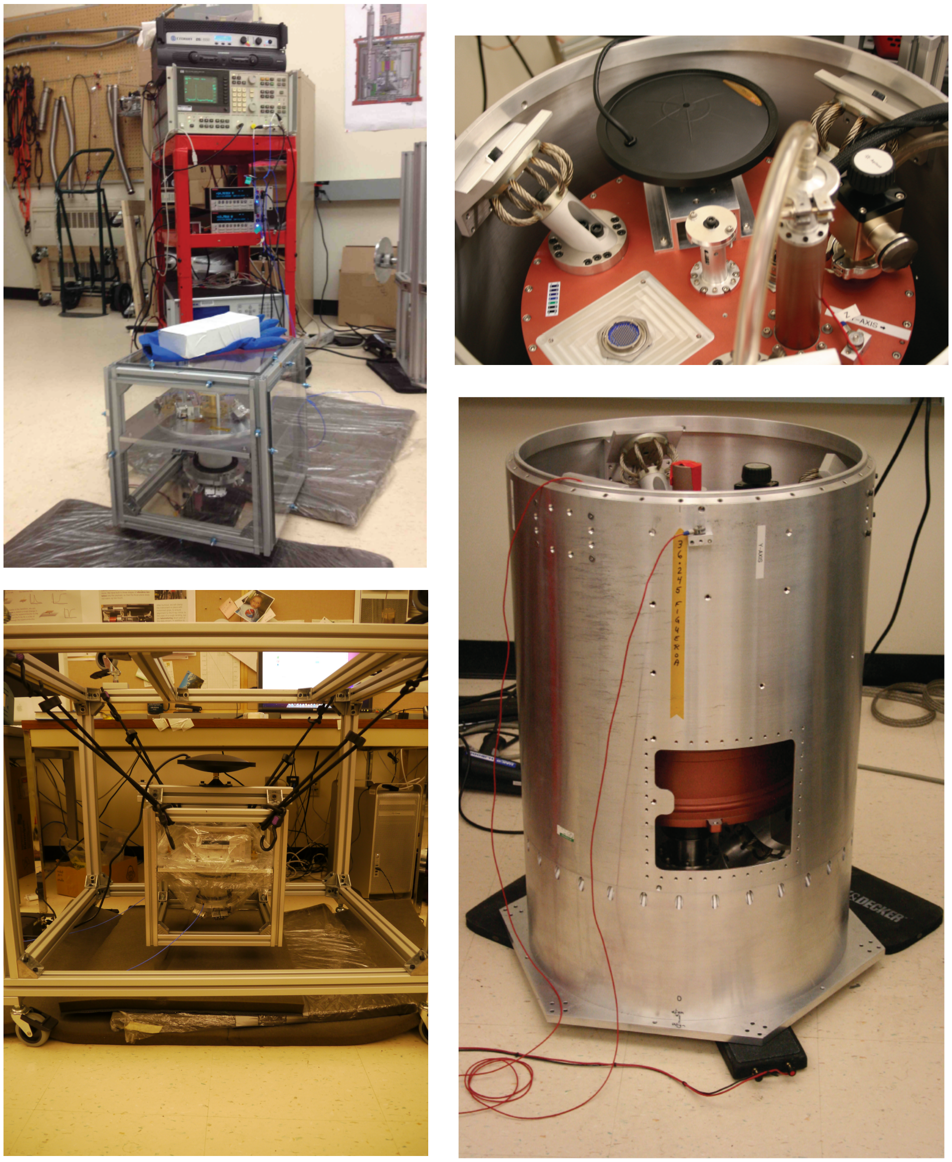

Figure 4-26: Pictures of the four, in-lab vibration setups. The insert setups are shown on the left. In the top left setup the insert cube is sealed with plexiglass plates and weighed down with a lead brick on top of the Bigfoot transducer. Accelerometer signals are read out by a dynamic signal analyzer. In the lower left image the insert cube is suspended by bungees and the UFO transducer is used to excite vibrations. In the upper right setup the UFO is mounted on top of LMO with LMO suspended from the skin. Temperature slopes are used to measure responses to the vibrations excited by the UFO. In the lower right setup the Bigfoot transducer is placed under one side of the skin and used in the same capacity as the Wallops vibration table.

insert is outside of the dewar we store it in a cube constructed of configurable aluminum posts and brackets[18] and an aluminum plate.

In order to use the UFO to excite the insert, we suspended the storage cube by bungie chords, and attached the UFO on an additional bar centered on one axis of the cube. A picture of this setup is shown in the lower left of Figure 4-26. We then performed a sine sweep on the transducer and monitored the response of accelerometers on both the insert surface and the suspended mass using the dynamic signal analyzer. We found data from this setup to be difficult to interpret because the bungie system is excited by the vibration of the UFO.

Hoping for results that would be easier to interpret, we moved to a system shaking the insert cube using the Bigfoot transducer. We closed the cube sides using shatterproof plexiglass, then placed the cube on top of the Bigfoot with a weight on the top of the upper plexiglass plate. A picture of this setup is shown in the upper left of Figure 4-26. Again, in this setup we drove the transducer with a sine sweep and monitored the response of the accelerometers on the insert plate and the suspended mass using the dynamic signal analyzer. To change the axis of the acceleration we simply rotated the cube such that the measurement axis was vertical. I describe the system design changes brought about using these setups in Sections 4.3.4 and 4.3.2, and the results of the Wallops vibration test following our redesign efforts in Section 4.3.6.

In any of these setups we can measure the resonance frequencies using peaks in the response of accelerometers or temperature in response to stimulation in any particular axis, but it is difficult to extract the exact shape of movement associated with a particular resonance from this data. For instance, simulations lead us to expect the lowest frequency resonance of the suspended mass will be a rotational mode, while the next highest resonance frequency is associated with a bowling-pin type rocking motion, and yet a higher frequency resonance is characterized by purely vertical motion. However, the predicted resonance frequencies from the models did not line up with those measured. In order to characterize the motion of the resonances identified in the laboratory vibration testbed, as well as to make a precise mea-

---

[18] 80-20 purchased from Bosch-Roxroth

surement of the resonance frequency of the purely rotational mode, we utilized high speed video (HSV) equipment loaned to us by the MIT Edgerton center.

The HSV camera we used took video at 2900 frames per second, allowing good sampling for the frequencies in the 100-300 Hz range in which we were most interested. We repeated the bigfoot insert cube shakes with suspension design B (discussed in Section 4.3.4), but this time with the camera focused on the corner of the FEA stand-in to record the motion. John Rutherford wrote a routine to track the FEA motion frame-by-frame at resolutions below a single pixel. This analysis showed that a 280 Hz driving force in the z axis coupled strongly into motion in the x- and y-axes, confirming the 'bowling pin'-type motion of the mode, which was predicted at a much higher frequency (near 400 Hz) by the simulations. To confirm that this was the primary resonance frequency of this type of movement, we also filmed the edge of the FEA in response to an impulse in each of the x, y, and rotational directions. The power spectrum of the movement of the FEA during the ringdown showed strong natural frequencies at 100 Hz (rotational) and 280 Hz (translational), confirming our interpretation of the shake data.

4.3.2 Dewar Suspension

The suspension of the dewar from the rocket skin is the lowest frequency vibration damping stage. The initial design of the suspension utilized six rubber dampers from Barry control (three on the aft side and three on the forward side). These dampers were linked together on each side of the dewar with stabilizing rings. One of the best features of these dampers is that they have metal stops, ensuring that the dewar cannot hit into the skin or the bulkhead during launch or landing. This suspension scheme is utilized in *XQC*. In our initial vibration test, the dewar showed a broad resonance in the 40 to 50 Hz range when suspended from the rubber dampers. This is higher than the expected frequency by a factor of ∼1.5. We have not been able to identify the reason for this discrepancy. A picture of the Barry control isolator is shown in Figure 4-27. A lower resonance frequency of this stage would result in a lower excitation level of the helium tank at its resonance frequency around 200 Hz. For this reason we sought to lower this resonance frequency by about a factor of two (this number was found to provide sufficient isolation in the simulation discussed in Section 4.3.5).

In between the initial vibration test in June, 2012 and that in August, 2013 we transitioned to a system of wire rope isolators (WRI) from Isotech, Inc., which showed a resonance around 30 Hz. A picture of a WRI is shown in Figure 4-27. The wire rope isolators are made up of several stainless steel wire braids glued into disks with threaded holes in their centers. These isolators are very strong in compression but are fairly soft in shear and rotation. We have designed the mounting angles of the wire rope isolators in the new suspension to ensure that a subset of the isolators is always in compression, and that none of the isolators are free to rotate. This suspension system has three WRI on the forward side and three on the aft side with no stabilizing rings. They also introduce the disadvantage of not having the hard mechanical stop utilized by the Barry control isolators, however they are more likely to return to their equilibrium positions after displacement than the Barry control isolators.

From a decrease in resonance frequency, a larger displacement follows as a natural consequence. This led us to remove clamping mechanisms that were previously installed to recenter the dewar after launch, as the clearance was not sufficient to avoid collisions between these and the dewar during vibration given the increased displacements due to the WRIs. With the clamping mechanisms removed, we will have to use the laser alignment diodes to track the detailed orientation information of the dewar during flight to get specific pointing information (Section 4.8).

In August, 2013, we used the Wallops vibration table to perform a full launch level sine sweep in the lateral (Y) axis to test the stability of the isolators and assure that there was sufficient clearance between the dewar and the skin to avoid collisions during launch and landing while using the WRI system. These are not typically performed as buckling of the payload can occur[19]. We were able to visually confirm the resonance near 30 Hz and could see movement of the dewar with respect to the skin on the order of several millimeters, but

---

[19] This test was made especially stressful by the Wallops engineers pulling out their personal cameras to tape it in case something YouTube-worthy were to occur.

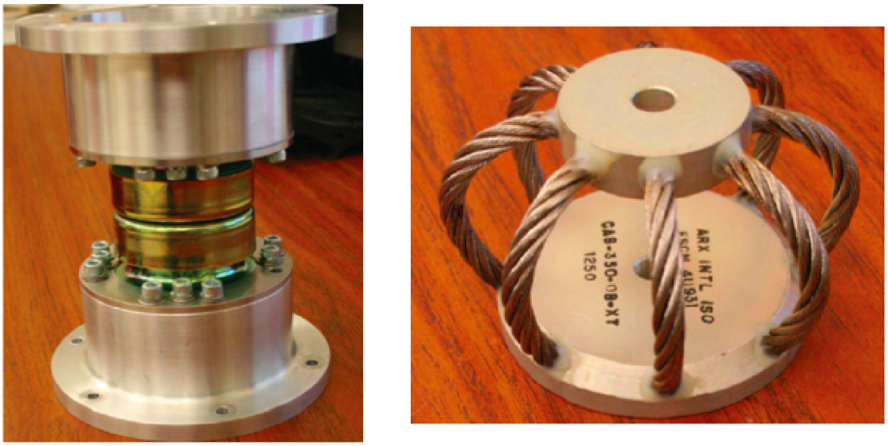

Figure 4-27: Rubber dampers from Barry Control with attachment fixtures (left) and wire rope isolator from Isotech, Inc. (right). The wire rope isolators are shown suspending the cryostat in Figure 4-26 and the Barry control setup is shown in the schematic in Figure 4-25.

also confirmed that the dewar remained several centimeters from the skin, so we do not expect any collisions during launch or landing.

4.3.3 G10 Assembly

The suspension of the helium can (on which the insert and suspended mass are installed) is achieved by attaching the can to aluminum rings glued to shells of G10 as described in Section 4.2.10. G10 is extremely strong in compression and tension, though very weak in shear, and provides very strong support when rolled into cylinders, as in the payload. We performed several 'pull tests' at MIT on pieces of G10 glued into aluminum grooves to determine the strength of both the G10 and the glue joint. These were performed in the same way as the pull tests on the kevlar suspension pieces described in Section 4.2.6. We measured an average breaking strength of just over 1330 N and a typical elasticity modulus of around 11 GPa.

Tests in both the lab setup and on the Wallops vibe table have shown the resonance frequency of this system to be around 200 Hz, which is about a factor of two higher than what we expect from calculations using the pull test results. The *XQC* team does not see a similar shift between expectations and measurements and the cause of the shift in the *Micro-X* payload is still unexplained.

4.3.4 Kevlar Suspension System Redesign

Our most intensive redesign effort to improve vibration isolation has been in the kevlar suspension system for the detector stage. The system is made up of seven kevlar loop attachments: six to constrain the position of the stage and one containing springs for tensioning. See Figure 4-28 for schematics of this system and Figure 4-29 for pictures of the aft side of the system.

At our vibration test in June 2012, we found our initial design (design A in Figure 4-28) exhibited a resonance frequency near 200 Hz, which is significantly lower than was predicted, and very near that of the helium stage. The coupling between these resonances led to a large amplitude vibration of the detector stage, leading to excessive heating. After additional FEM modeling we determined that the orientation angle of the non-tensioning aft strings between the vertical and horizontal axes led to coupling between the axes, and encouraged a bowling-pin-like mode of the detector with a low frequency.

Our first redesign (shown as design B in Figure 4-28) oriented these pieces horizontally (normal to the axis of the rocket) and moved them closer together so that the component of their force opposite the tensioning piece on the aft side was larger, strengthening the suspension in that direction. See Figure 4-28 for schematics illustrating these design changes. Design B exhibited a broad resonance peak around 285 Hz. Despite this, we still saw strong heating around 200 Hz when we excited the dewar using a sine sweep in the lab setup described in Section 4.3.1. We believe this was due to coupling between the helium stage resonance at 200 Hz and the side wing of the broad detector stage resonance at 285 Hz.

These results prompted an additional redesign effort producing the design labelled C in Figure 4-28. Pictures of designs B and C are shown in Figure 4-29. We determined that bending of the screws at the attachment point of the kevlar on the detector stage could both lower the resonance frequency of the entire system and account for some of the broad

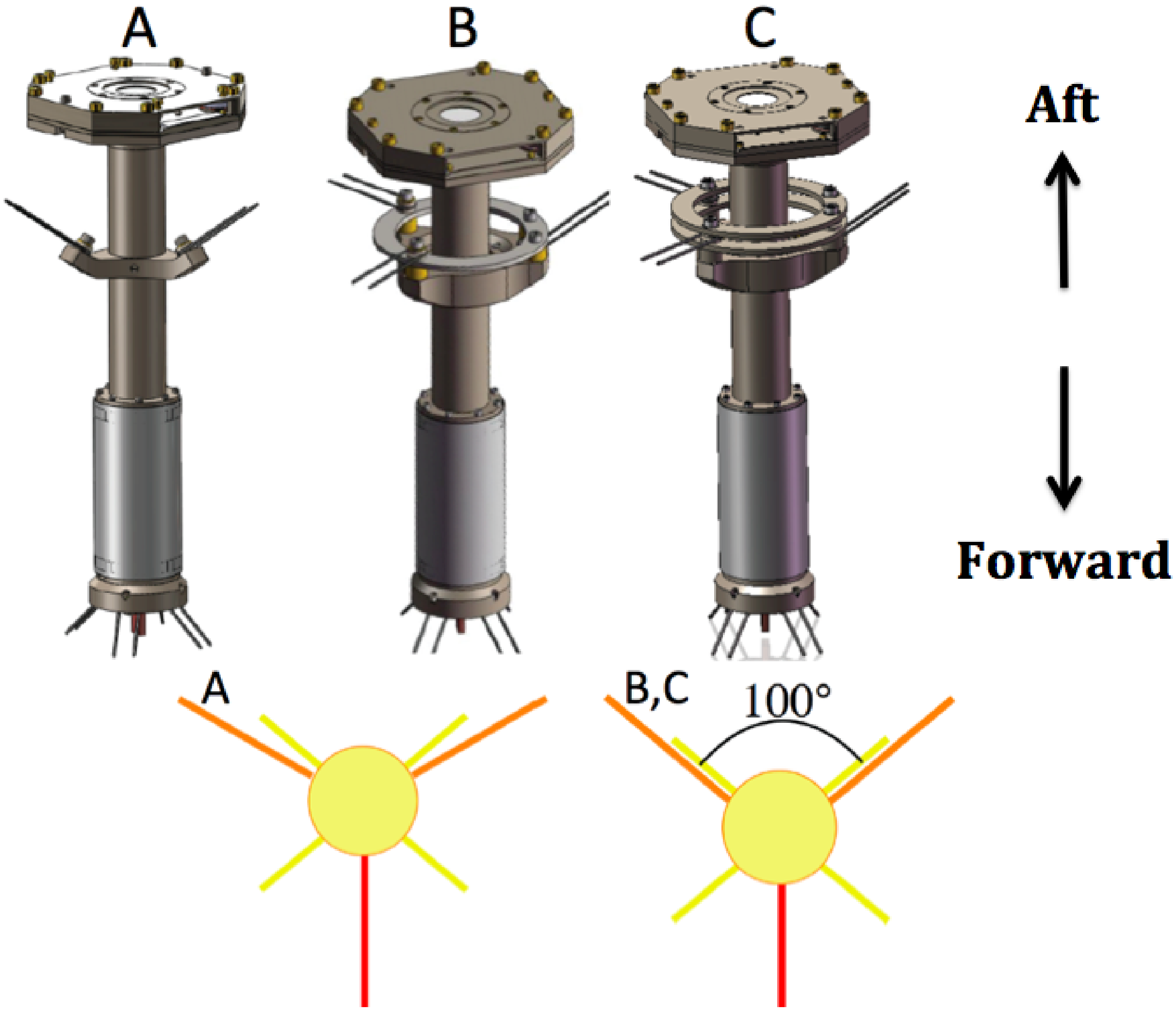

Figure 4-28: Schematics of the suspended mass for the three design iterations of the suspension. Design A was our initial design tested in the June, 2012 vibration test, design B was an intermediate iteration, and design C is our current design that was subjected to a launch-level vibration test in August, 2013. Side views are shown above while top views showing the angular orientation of the strings are shown below, with forward strings shown in yellow, aft non-tensioning strings shown in orange and the tensioning string shown in red. Four of the seven kevlar attachment points are on the forward side of the stage and the remaining three, including the tensioning piece, are on the aft end of the stage.

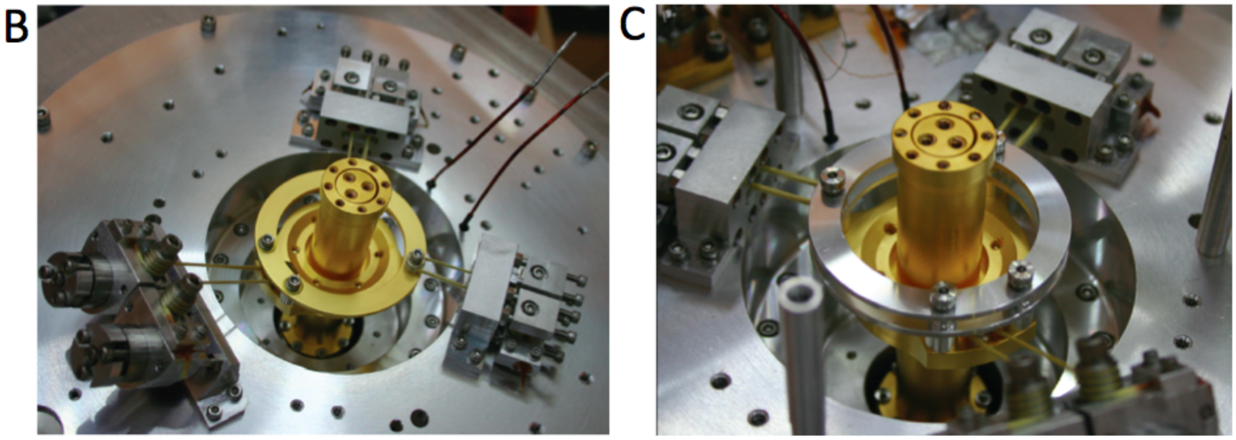

Figure 4-29: Pictures of the aft side of the suspension without the detector box installed for designs B (left) and C (right). Each kevlar attachment consists of a single piece of kevlar glued down on both ends and wrapped around a spiral part at the liquid helium stage and looped around a cylindrical attachment on the detector stage. This can be most clearly seen in these pictures on the tensioning piece (leftmost) in the design B picture.

nature of the resonance we witnessed. To mitigate the bending, we added a stabilizing ring at the top of these screws. In addition, we used thicker kevlar (8520 denier rather than 4650 denier) on the two horizontal strings on the aft side to provide additional strengthening against horizontal motion. Finally, we determined that the spirals, which are designed to provide frictional isolation for the glue joint from the full tension on the kevlar (shown in Figure 4-29) were still sufficiently able to provide this isolation with the string wrapping around them for only a quarter of a turn rather than the three and a quarter turns we were initially using. This helped to stiffen the system because the innermost strands of each string are preferentially engaged as it wraps around a radius, so the less radius around which a string travels, the more strands of kevlar participate in stiffening the system.

These changes led to a shift in resonance frequency from 285 Hz to about 325 Hz, along with a reduction in the width of the resonance peak. When performing tests in our lab system we now see a much smaller heating peak around 200 Hz and a new peak at 325 Hz showing we have effectively decoupled the resonances of the helium tank and the suspended mass. The data from the heating tests of designs B and C is shown in Figure 4-30.

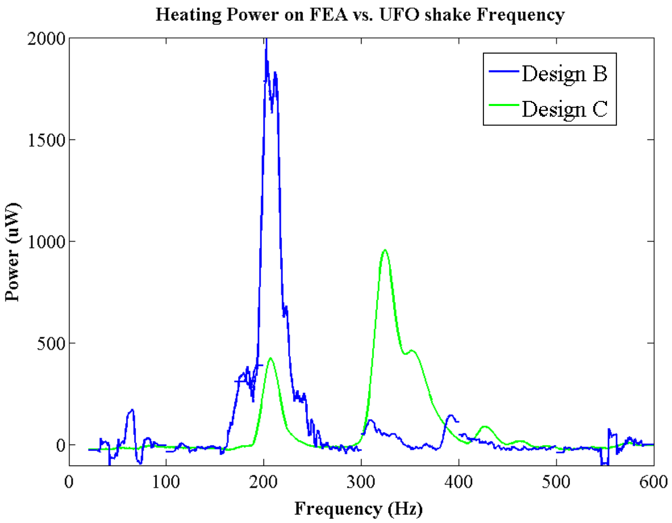

Figure 4-30: Heating results due to vibration of the dewar with the detector stage at 4 K. Results from tests of design B are shown in blue and have a main peak at 200 Hz. Results from tests of design C are shown in green and have a much smaller peak at 200 Hz with a main peak at 325 Hz. We convert temperature slope to power, by measuring the temperature slopes produced by several known applied powers using a heater on the detector stage.

4.3.5 Simple Analytic Modeling

In order to help diagnose our heating problems, Enectali Figueroa wrote a six degree-of-freedom, one-dimensional model in Mathematica to predict the motion of each stage of the cryostat. This 'lumped-mass' model connects the six components of our vibrational system (rocket skin, cryostat, outer G10 assembly, inner G10 assembly, helium tank, and suspended mass) with damped oscillators. One can write the equations of motion for each of these components, which are coupled to each other. These coupled differential equations can be written in matrix form as in Equation 4.12, where **C** is the damping coefficient matrix, **K** is the matrix of spring constants between stages and $\mathbf{F(t)}$ is the vibrational excitation.

$$\mathbb{I}\ddot{\mathbf{X}} + \mathbf{C}\dot{\mathbf{X}} + \mathbf{K}\mathbf{X} = \mathbb{I}\mathbf{F}(\mathbf{t}) \tag{4.12}$$

The damping coefficients determine the strength of dissipation, which also determines the amount of heating generated by relative motion between each stage. In practice, this heating is only measurable at the FEA level: the result of dissipation in the kevlar due to relative motion between the FEA and the insert.

Values for the spring constants in **K** are taken from measurements of materials, but have been tweaked to match vibration measurements in cases where systems (like the G10 tubes) showed resonant frequencies much different than those based on measurements of the individual components.

The results of this model with an input excitation of the expected rocket motor vibration is shown in Figure 4-31. This model was used as a guide to identify departures from expectations in our Wallops measurements, and to establish goals for the frequencies of each of our damping stages to obtain acceptable heating power levels below 2 μW.

4.3.6 August 2013 Vibration Results

In August, 2013 we travelled back to Wallops to test the payload at full launch levels after implementing the changes described in the previous sections. The test showed acceptable heating levels as a result of full launch load vibration tests on both lateral axes (30 mK heating corresponding to an energy input to the suspended mass of 0.0595 J during a full random launch level vibration in the Y axis and 20 mK corresponding to an energy input of 0.024 J heating during a full random launch level vibration in the X axis), and a much reduced, but still unacceptably high heating level (300 mK corresponding to an energy input of 0.558 J) during a full launch load vibration in the thrust (vertical, Z) axis. The input energy values are determined by applying a known power to a heater attached to the lid of the FEA and measuring the time necessary to achieve the temperature change measured in the vibration test. These heating calibrations were done at similar temperature and magnetic field conditions to those in the vibration test to produce the most accurate calibration possible. The X and Y heating levels are different because the Y-axis is oriented along the tensioning suspension piece, in the weakest direction of the suspension, so the mass is more susceptible to vibrations in that axis than in the X-axis.

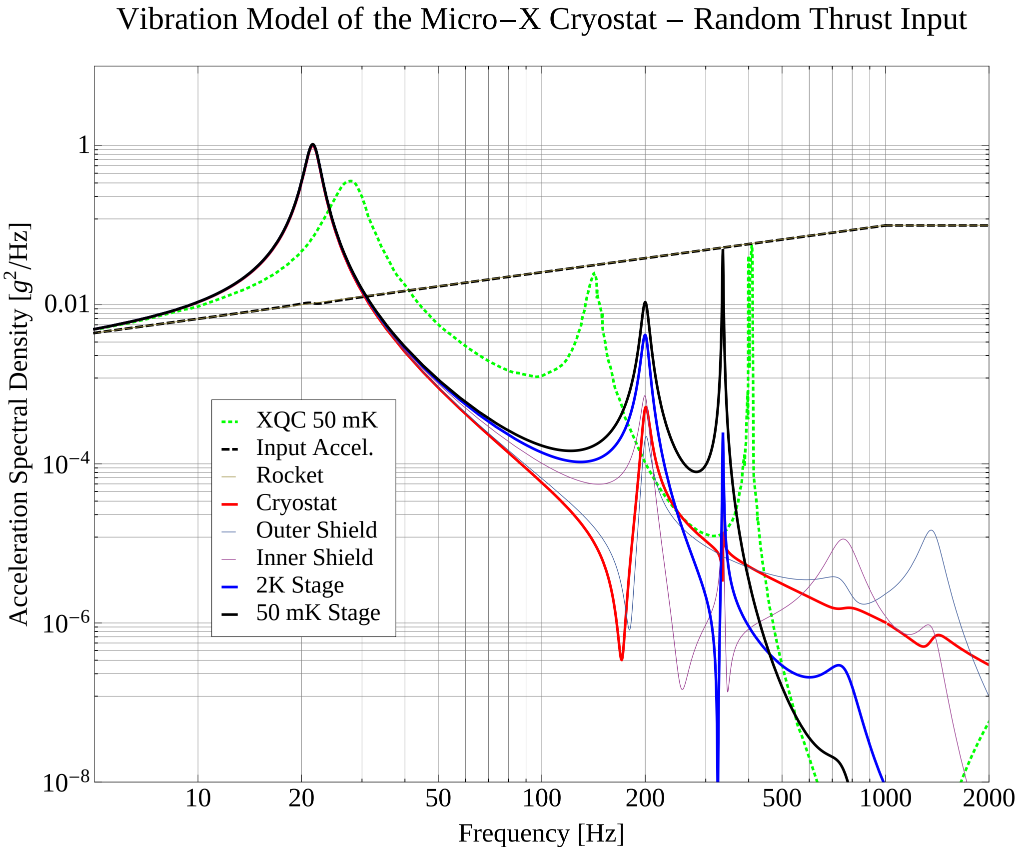

Figure 4-31: Predicted responses of various components in the one-dimensional model to the excitation of the rocket motors. The vibration of the *XQC* system [71] is shown in green. The model correctly predicts the heating *XQC* sees during launch (power level of 0.9 μW) and predicts that with the same k values *Micro-X* would show similar heating, even with our heavier suspended mass. However, the *Micro-X* payload exhibits different k values than *XQC* in almost all damping stages.

We also performed slow, half-g-level sine sweeps in each axis to identify the frequencies at which the heating is strongest, similar to the tests we performed in our lab setup. The results of these tests are shown in Figure 4-32. These tests showed the bulk of the heating occurring at and just above 200 Hz in the Z axis, though we have shown in the lab that the resonance of the suspended mass is no longer near 200 Hz. We have identified the cause of the heating seen in this test as a coupling between a previously unknown resonance in the skin system near 250 Hz and the helium tank resonance around 200 Hz.

4.3.7 Tuned Mass Damper

Prior to the August, 2013 vibration test we designed and fabricated a tuned mass damper (TMD) for use in the Z (thrust) axis. This consists of a mass on a spring system and is mounted on the outer skin of the dewar in order to dissipate energy outside of the dewar by setting up an oscillation of the mass at its resonance frequency. A simulation showed that this would notch out the excitation spectrum of the He tank near the resonance frequency of the TMD, greatly reducing the heating.

The mass is made up of a ring in three parts that sits around the vacuum bellows between LMO and the bulkhead on the aft side, and hangs from a system of metal tabs that act as springs. We designed the TMD to be installed without breaking vacuum on the system. Since the measured helium tank resonance was around 200 Hz and the suspended mass resonance was around 320 Hz, we manufactured springs for resonances at 200 Hz and 300 Hz. Once we performed the vibration test and found that the main heating contribution in the Z axis was near the He tank resonance at 200 Hz, we installed the TMD with the 200 Hz springs. This was a particularly arduous[20] process because of the tight space allowance between the dewar and the bulkhead. A picture of the TMD installed on LMO is shown in Figure 4-33

Unfortunately when we performed a full launch level random vibration in the Z axis with the TMD installed, we measured higher heating than without the TMD (a temperature rise

---

[20] Arduous may be a bit of an understatement, describing a process requiring four people, four hours, multiple raids on Wallops toolboxes, and more than a few bumps and bruises.

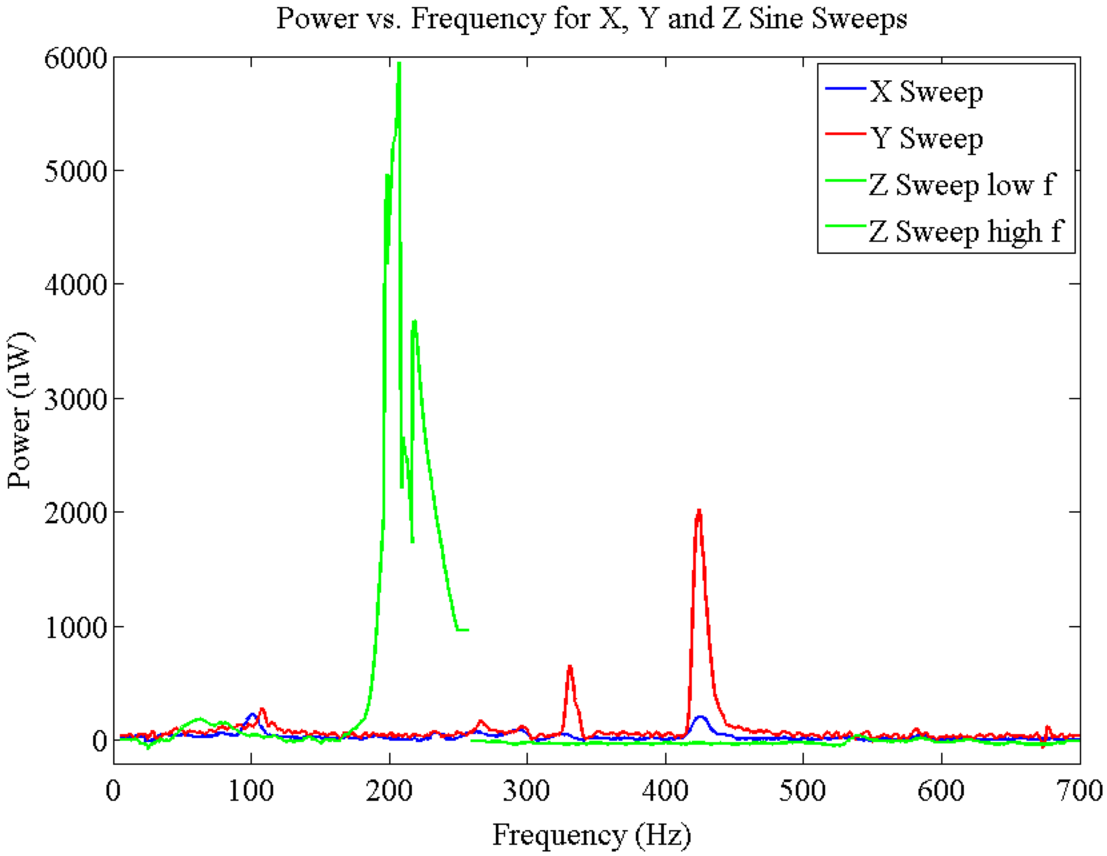

Figure 4-32: Plot of the power vs. frequency during slow, 0.5 g level sine sweeps on the vibration table in each of the three axes. We convert temperature slope to power by measuring the temperature slope produced by applying a known power through a heater on the detector stage. The break between the low f and high f datasets in Z occurs because the table aborted sweeps at 249 Hz due to a strong resonance in the skins. We thus swept the table frequency up from 0-248 Hz and down from 700-250 Hz to bracket the resonance. The Z-axis heating is a factor of ten larger than the heating in the X or Y axes.

Figure 4-33: A picture of the TMD installed on the aft side of the dewar during the Wallops vibration test in August, 2013.

of about 470 mK during the full launch level random vibe test). The reason for this excessive heating was clarified with a slow sine sweep measurement in the Z axis with the TMD in place. The heating spectrum (plotted with the heating spectrum without the TMD in place for comparison) is shown in Figure 4-34. We can see that the TMD was quite effective in notching out the heating spectrum around 200 Hz, however we also see a much broader resonance around and just above 200 Hz and several harmonics at 100 Hz, just above 300 Hz, and just below 600 Hz. The harmonic just above 300 Hz is likely close to the primary suspended mass resonance and the harmonic just below 600 Hz is likely close to the thrust axis resonance of the suspended mass. Due to this performance, the TMD is not a feasible solution to excessive vibrational heating.

4.3.8 G10 Assembly Redesign

As mentioned in Section 4.3.6, the excessive heating appears to be the result of coupling between the 200 Hz resonance of the helium can supported by the G10 assembly and a resonance in the skin assembly around 250 Hz, both in the Z-axis. To correct this, we'd

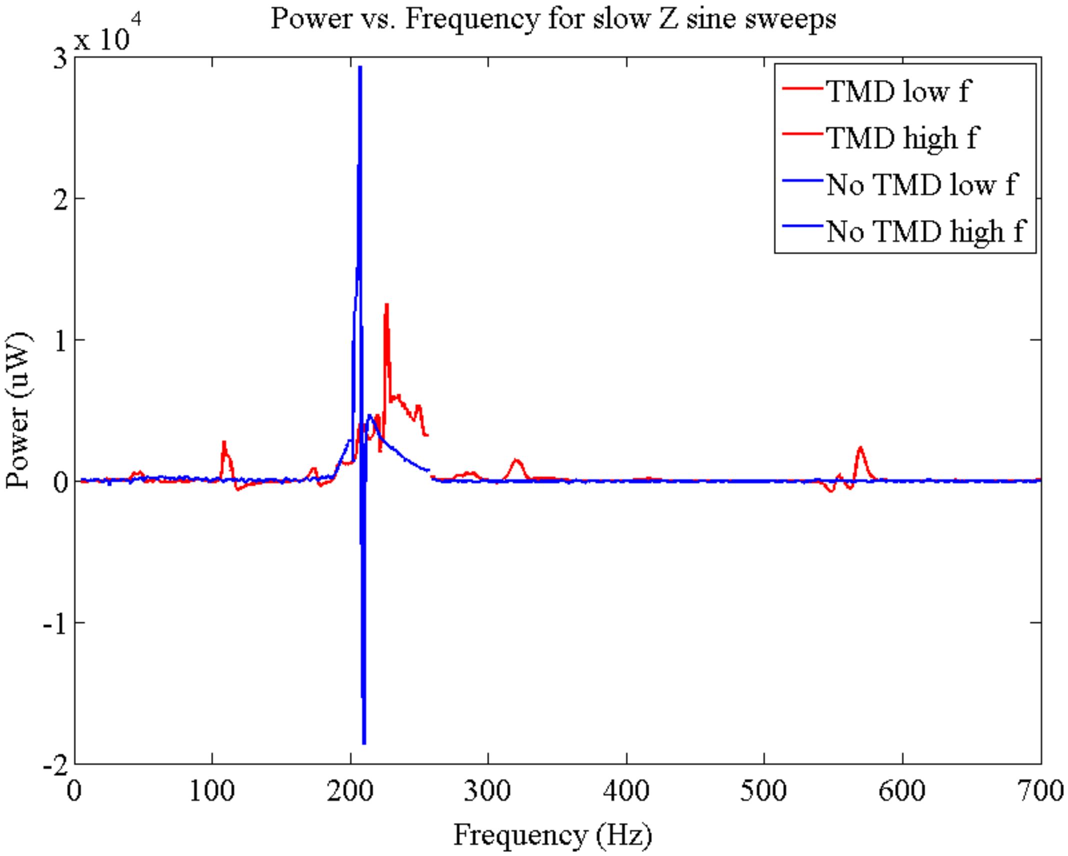

Figure 4-34: Heating spectrum due to a slow sine sweep in the Z axis with the TMD installed with 200 Hz springs. The notching of the heating spectrum at 200 Hz is clear. However, the broadening of the resonance near 200 Hz, along with the additional harmonics near 100, 300 and 600 Hz lead to higher overall heating during the full level random vibration than in the setup without the TMD. The negative power measured just above 200 Hz without the TMD is a result of cooling from the cooling capacity of the salt after passing the heating resonance of the system.

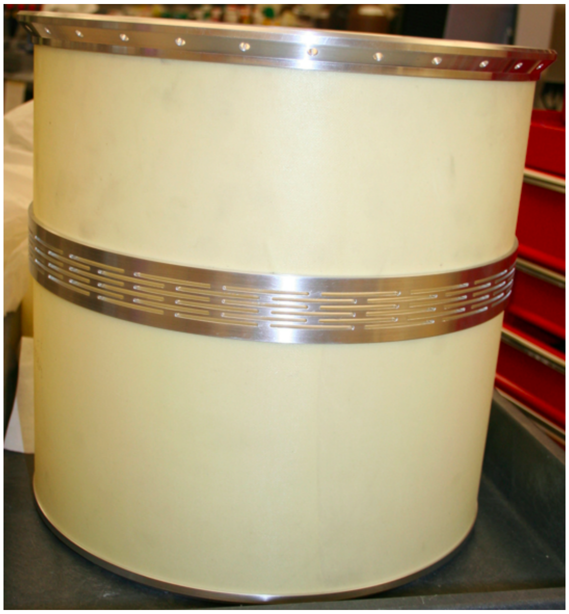

Figure 4-35: The new outer G10 assembly with ‘spring-ring’ replacing a section of the original G10 cylinder. This will be installed and tested on the next trip to Wallops, likely in the fall of 2014.

like to lower the resonance frequency of the helium can stage. This could be achieved with thinner G10, but this is infeasible because of both manufacturing and mechanical concerns.

Instead, we designed an aluminum ring, which will be installed in middle of the outermost G10 cylinder (replacing a section of G10 so as not to change any dimensions). The ring will have a lower spring constant than the G10 due to a pattern of slits cut into the material. A picture of the outer G10 assembly with this ring in place is shown in Figure 4-35. Simulations have shown that this design change should lower the helium can resonance frequency to near 80 Hz, far lower than the 250 Hz resonance in the skins. We are hopeful that this change will sufficiently decouple the resonances to survive launch vibrations without excessive heating. This ring should not affect the X and Y axes significantly. There is some question as to its ability to survive landing but simulations show it should easily survive launch, so it has been deemed an acceptable solution.

Table 4.1: Measured resonance frequencies of each of the stages of the rocket system for each of the design iterations discussed in this section. In June 2012 we had only the cryostat skin section attached, Barry control isolators between the skin and the cryostat, the original G10 suspension system for the helium can, and our original kevlar suspension design. In August 2013 we had both the cryostat and avionics skins attached, used wire rope isolators between the skin and the cryostat, kept the original G10 suspension system for the helium can, and used the redesigned kevlar suspension system. At time of writing, both the cryostat and avionics skins are attached, wire rope isolators are suspending the cryostat from the skins, the G10 support has been modified with a soft 'spring ring', and we are using the August 2013 design for the kevlar suspension system.

Stage	June 2012	August 2013	Current Resonance
Skin System (thrust axis)	Not Measured	249 Hz	249 Hz
Cryostat Vacuum Jacket	50 Hz	30 Hz	30 Hz
Helium Can	200 Hz	200 Hz	80 Hz (Modeled)
Detector Stage	200 Hz	325 Hz	325 Hz

4.4 Magnetic Shielding

While the sensitivity of superconductors in their transition benefits us greatly in detecting the X-ray signal, it also causes the detectors to be very sensitive to environmental factors, especially magnetic fields. Both the TESs and the Superconducting QUantum Interference Detector (SQUID) readout are sensitive to both static and dynamic magnetic fields. The TESs are able to tolerate a static field of about 1 μT. However, they are more sensitive to changing magnetic fields due to the fact that changing magnetic fields cause a flux change in the inductor, inducing current noise on the bias line. It is estimated that the readout can only sustain $\sim 3pT/\sqrt{Hz}$ magnetic field noise.

To address the problem of a dynamic field, including the field from the primary coil, which changes during the cooling cycle and during temperature control, we follow the common practice of enclosing the detector plane in a superconducting cavity. This practice utilizes the Meissner effect in superconductors, in which surface currents arise and expel magnetic fields from the bulk below the transition temperature T_c. This shielding effect is not without limit, as superconductors will become normal above a critical magnetic field. The *Micro-X* magnetic shield is manufactured from niobium, a Type II superconductor. Type I superconductors become normal anywhere above the critical field, whereas Type II superconductors develop magnetic vortices above the critical field and become normal at a higher field. Niobium is a popular choice because it is fairly workable (it can be rolled, milled or welded) and has a relatively high critical temperature of 9.2 K, easily achievable with liquid helium cooling. Lead would be an attractive material as well (it is a Type I superconductor with a T_c of 7.2 K) but niobium is much lighter, so better suited to a rocket payload.

A 'bucking coil' provides an initial, coarse level of magnetic shielding. It is a coil between the primary magnet and the aft (detector) side of the insert, fed by the same set of magnet leads in series with, and wound in the opposite direction of, the primary coil. The bucking coil has a slightly larger radius than the primary coil, so that it partially cancels the field of the primary coil near the detectors without affecting the field in the bore of primary magnet. This coil helps keep the magnetic field in the region of the niobium can from reaching the critical field, as well as aiding the niobium can in shielding the detectors from the primary coil field.

The niobium magnetic shield design has converged from design modeling and prototype testing. Both the original and current designs for the magnetic shield have the same basic shape: an inverted cone with a lid shown on the left in Figure 4-36. The angled sides of the cone accommodate the aft kevlar suspension. There are holes in the tip of the cone shape to accommodate the suspended mass with the salt pill descending into the magnet bore, in the center of the lid to allow X-rays to pass through to the detectors, and on two sides to allow the science chain cables carrying signals to and from the FEA to escape. The long 'snouts' along the wires help to limit the amount of magnetic field that penetrates the can through the openings and were added in the second magnetic shield iteration.

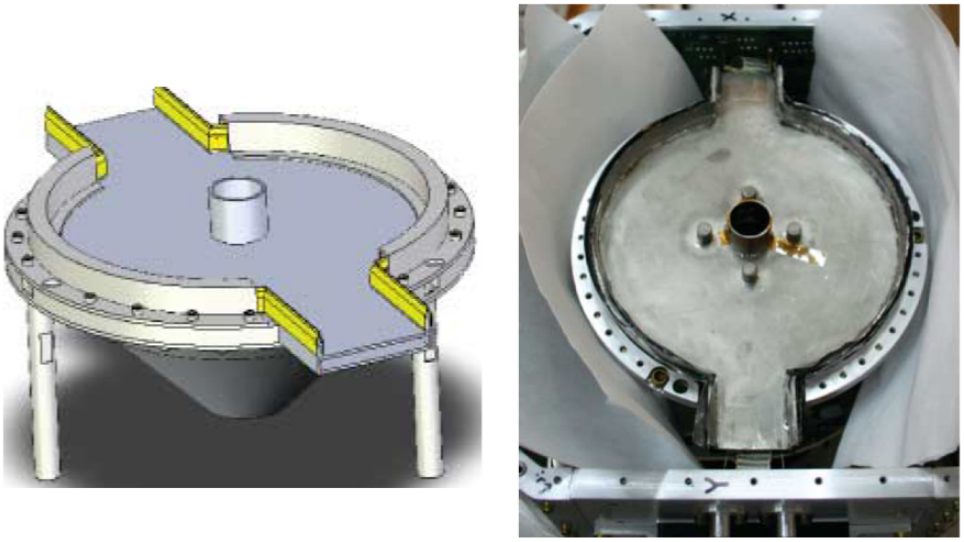

Figure 4-36: A CAD rendering of the magnetic shield with the lead tape ‘zipper’ shown in yellow (left). A picture of the magnetic shield from the top before the lead tape is ‘zipped up’ (right). Both show the latest magnetic shield design.

The original shield was designed using FEM simulations in the COMSOL 2D E&M package with axial symmetry. The lid of the original shield was offset from the cone by about 1 cm for ease of manufacturing and assembly. COMSOL simulations suggested this would be acceptable for the magnetic shielding requirements of the detectors. However, measurements of the attenuation using Hall probes at 4 K gave an attenuation ratio perpendicular to the optical axis three orders of magnitude higher than that predicted by the model. We later discovered that this gapped design was highly susceptible to transverse fields and misalignment that were not modeled when applying the axial symmetry condition. Extending the model to 3D allowed us to better understand the weaknesses of this design.

Our initial design also included a sheet of gold-plated ultra low carbon steel (ULCS), a high permeability material, on the surface of the insert. However, we found that this became permanently magnetized after being exposed to the high fields produced by the magnet, and so removed it.

Using the full 3D modeling in COMSOL, we redesigned the magnetic shield with thin snouts for the science chain cables to escape (rather than the large gap between the can and the lid in the previous iteration). Conversations with our collaborators at GSFC revealed that the best practice for strong magnetic shielding was to create a superconducting path between the can and the lid using a lead tape zipper. John Rutherford developed a method to connect this zipper by roughening the niobium to remove the oxide, wetting it with indium, and soldering on lead tape stripped of its adhesive using Roses alloy, a low temperature solder. The new, zippered design performs significantly better in shielding the TESs from changing magnetic fields. We tested this in the lab by spinning a permanent magnet on a desk chair near the dewar, which produces an oscillating field on the order of 1μT in the region of the detectors. Without the zipper soldered shut, this caused a modulation on the locked SQ1 signal of a few mV, which is a few percent of the pulse height. With the zipper shut we cannot detect a modulation on the locked SQ1 signal. We will be able to test the magnetic shielding more thoroughly when we travel to Goddard to complete detector testing. During the initial design and testing John Rutherford performed the simulations and soldering while I focused on the testing and analysis.

While the niobium shield provides shielding from changing magnetic fields, it cannot shield against the earth's field, since fields present during the superconductor's transition will be 'frozen in' to the cavity of the magnetic shield. This static field (of about 0.5 Gauss in the case of the Earth's field) results in a shift in the transition temperature of the TESs down by several tens of mK, and creates kinks in the response curves of the SQUIDs that make tuning more difficult and degrade the detector resolution. One solution to this problem is the addition of several layers of Metglas (a high permeability material sold in thin metallic sheets) to the inside of the shield to draw this static field away from the detectors. Initial tests suggested this was a promising solution, however a flight-worthy implementation is difficult since the Metglas is susceptible to rusting in humid air and is difficult to secure to the inside of the magnetic shield.

Two possible external solutions are currently under consideration for shielding the detectors from the earth's magnetic field during cooldown. For any solution we would like to be able to use it when the optics have been integrated and we would like to be able to install it on the outside of the payload during cool down and remove it afterwards. In the past, large cylindrical Mumetal ‘buckets’ (custom designed and fabricated by Ammuneal) have been used for magnetic shielding during cool down of similar systems. One of our options is to obtain a long, cylinder (without caps) fabricated by Ammuneal with the appropriate holes for the helium fill line and whatever structure will support the payload. This has the advantage of providing a ready-made, well-characterized magnetic shield. Its downsides are that the shield will be very large, heavy, cumbersome, and expensive.

The other solution, which has been utilized at GSFC, is to make a Metglas ‘blanket’ that could be wrapped around the payload during cooldown. At GSFC they have manufactured a Metglas blanket by taping up to six layers of Metglas on poster paper and laminating it to avoid rusting, resulting in a flexible sheet that can be wrapped around the payload. The Metglas blanket at GSFC has shown very good performance. The benefits of this are that it is fast to manufacture, inexpensive, light, and flexible, and thus easier to handle than the Mumetal shield. On the downside it’s performance is not well characterized, limited to the knowledge that a similar method has yielded good results for the GSFC team, and the permeability of the Metglas may be degraded with working during wrapping and unwrapping of the blanket, so it may have to be replaced. At time of writing, we are currently evaluating both options and will likely try the Metglas blanket and see how the detectors perform before ordering the Mumetal shield.

Most systems at GSFC also utilize a ‘field coil’ inside the magnetic shield to provide the ability to zero any static field that may be trapped in despite the static magnetic shielding. In early testing, we were able to use such a coil taped to the top of the magnetic shield to null out the trapped-in earth’s field. Meredith Danowski is currently developing simulations of a flight-worthy field coil that may be utilized if it is deemed necessary after tests of other shielding options.

4.5 Calibration Source

Turning pulse data into a calibrated energy spectrum is achieved by mapping observed pulse heights to known calibration photon energies. We will perform extensive calibration in the lab and on range using external calibration sources before and after flight, and we will use the pre-flight data to determine optimal device settings, map individual pixel gains, understand the noise characteristics of the array, and diagnose cross-talk issues. However, we cannot solely rely on the pre- and post-flight calibration data. The environment encountered by the array during flight will change rapidly and unpredictably, due to vibrations, possible temperature changes, changing magnetic field, etc. These changing conditions will cause changing pixel responses, necessitating an on-board calibration source to provide persistent lines of known energies.

Optimally, we would have a calibration source as close as possible to the detector to track changes in the array calibration and a second source shining on the detectors through the filter stack to diagnose any changes in filter calibration due to ice buildup or damage. The *XQC* utilizes a source located on the inside of the gate valve providing low energy photons (below the Oxygen K edge) to diagnose ice on the filters. However, this is not feasible in *Micro-X*. The gate valve in *Micro-X* is further away from the detectors than it is in *XQC*. This design decision was made to limit the effect of microphonics from the gate valve motor on the detectors, as well as to protect the O-ring on the gate valve from freezing. To compensate for this additional distance, *Micro-X* would require a far stronger source than those available to us to provide enough calibration flux (the Cm source used by *XQC* is no longer available, and Po sources with the required strength are available only to certain government agencies). For this reason *Micro-X* will not utilize a gate valve source. Fortunately the largest effect of possible ice on transmission through the filters will be below 540 eV, which is outside of our science band.

Micro-X will utilize a small calibration source located on the lid of the magnetic shield about a centimeter from the detector array to provide continuous array calibration photons. This source is made up of an annulus of ^{55}Fe illuminating a co-axial annulus of KCl. Lead

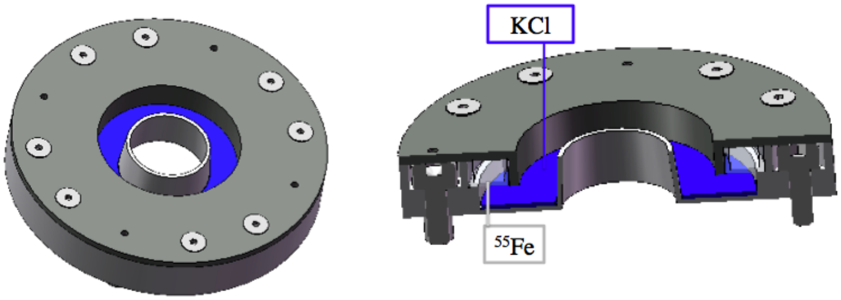

Figure 4-37: A CAD rendering of the calibration source. The cross section (right) shows the locations of the ^{55}Fe and its fluorescent target. Calibration photons escape from the source upwards in these figures.

walls absorb stray X-rays. This design, modeled after [119], is shown in Figure 4-37. Under fluorescence from the just under 6 keV X-rays from the ^{55}Fe, the KCl target produces fluorescent lines at 2.62 keV (Cl Kα), 2.82 keV (CL Kβ), 3.31 keV (K Kα), and 3.59 keV (K Kβ). All of these are close to, but out of, our science band, which makes them ideal energies for calibration. The source is manufactured by mixing a liquid ^{55}Fe compound with epoxy, then pouring the mixture into an annular Polymethyl methacrylate (PMMA) holder to cure. The specific geometry was tuned to produce as uniform an exposure of the focal plane as possible within physical constraints.

The calibration source has not yet been installed in the cryostat, but has been characterized using CCD images in the MIT CCD lab in July, 2011. At the time, the flux from the source was determined to have a strength equivalent to 8.2 photons/pixel/second on the *Micro-X* array with good uniformity. To minimize pileup while assuring enough photons for calibration, we would ideally have a calibration source rate similar to that of the science target. At the time the source was manufactured, we were unsure of the flight schedule, so the source was made hotter than desired for the flight source, keeping in mind that ^{55}Fe has a fairly short half-life of ∼2.7 years, and that the rate can be throttled by placing aluminized mylar films between the source and the detector. However, since the flight has been delayed beyond any timeline we initially anticipated, we will reevaluate the source to ensure we have sufficient photons for calibration in flight.

4.6 Optics

An important goal of the *Micro-X* mission, in addition to high resolution spectroscopy, is imaging of our targets in the X-ray band. Though the imaging capabilities of *Micro-X* will be modest, they will allow us to focus on a particular target and distinguish photons arriving from different regions of the target. When we consider the process of focusing incident photons, mirrors are a natural solution, however X-rays present particular challenges to mirror design not present in lower energy bands. Outside of the context of astronomy, the mention of X-rays usually calls to mind film of a bone, which can be discerned because X-rays penetrate skin (something that optical light is not able to do). In fact, X-rays hitting a target will most often penetrate it and, if the target is thick enough, be absorbed. This presents difficulties when building optics that aim to reflect X-rays off of a mirror, so a different approach is necessary, grazing incidence.

4.6.1 Grazing Incidence Mirrors

Grazing incidence can be understood through the analogy of skipping a rock on a pond. If you were to throw the rock straight down at the surface of the water it would sink, but throwing it at a low angle allows it to skip off the surface. In the case of X-rays reflecting off of a surface at grazing incidence, this occurs because an individual X-ray photon will interact with many more surface electrons at grazing incidence than it would at normal incidence, allowing it to reflect off of the surface. [2] provides a thorough overview of X-ray optics and derives the critical incident angle θ_c below which total external reflection of an X-ray photon off of a surface occurs (provided that the energy of the photon is not too near any absorbing edges of the reflecting material). θ_c is proportional to $\sqrt{Z}/E$ where Z is the atomic number of the reflecting material and E is the photon energy. From this we can see that a high atomic number is desirable for X-ray reflecting surfaces and that the higher the energy of the incoming photon, the shallower the angle required for its total external reflection. Early X-ray optics used materials like beryllium, aluminum, and nickel to reflect photons with

E<1 keV. Current generation X-ray telescopes typically use gold, platinum, or iridium, with grazing angles of 0.5-1° for 0.1<E<10 keV [2].

In 1952, Wolter proved that two reflections at grazing incidence are needed to form an image over a finite field of view (FOV) and proposed three basic optic geometries for which the optical path to the image plane of all rays incident parallel to the optical axis of the telescope would be identical [116]. The application of these geometries to X-ray astronomy was first proposed by Giacconi and Rossi in 1960 [39]. The geometries Wolter proposed are as follows: Type I requires an initial reflection off of the concave surface of a paraboloid and a second reflection off of the concave surface of a hyperboloid; Type II requires an initial reflection of the concave surface of a paraboloid and a second reflection off of the convex surface of a hyperboloid; and Type III requires an initial reflection off of the convex surface of a paraboloid and a second reflection off of the concave surface of an ellipsoid. Type I is most commonly used in X-ray astronomy because it provides the largest aperture to focal length ratio of any of the Wolter designs. A diagram of the beam path of a Type I Wolter optic is shown in Figure 4-38. The effective aperture of a paraboloid reflecting grazing-incidence photons is $2\pi R\alpha l$ where l is the length of the parabolic mirror arc, R is the radius to the focus, and α is the angle of incidence, which is usually quite small. Since this effective aperture size is small at grazing incidence, many sets of mirrors, or 'shells,' with different radii are nested to create a typical X-ray mirror.

There has been a great deal of progress developing real-world X-ray optics since these initial proposals. As with traditional mirrors, the surface of an X-ray reflector must be highly smoothed. A bumpy surface will scatter incident X-rays. Some roughness of the optic is unavoidable on the Angstrom level. Since this cannot be measured precisely, its effect must be treated statistically, which is discussed in detail in [2]. The amount of scattering is proportional to the square of the energy, so imaging will always be worse for higher energy photons.

Real-world reflectors must also have a small coefficient of thermal expansion and a surface constructed from a high-Z metal, as discussed previously. The application of this surface

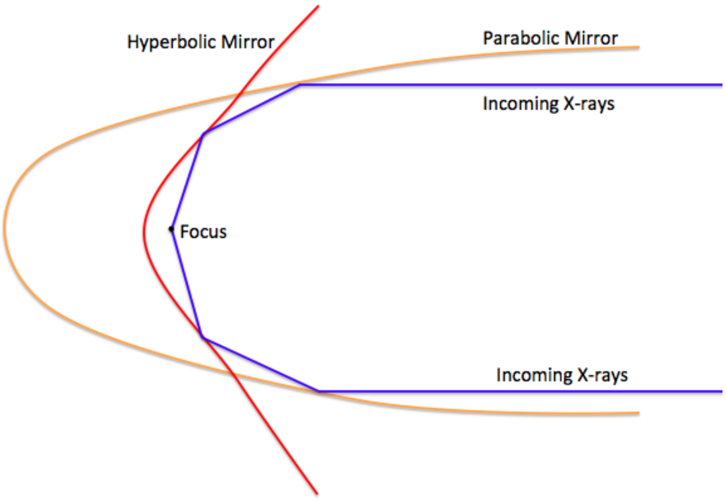

Figure 4-38: A diagram of the Wolter I-type optic. Incoming light (blue) first bounces off the parabolic surface (orange), then bounces off the hyperbolic surface (red) to arrive at the mutual focus of the two surfaces.

metal often requires a binding layer of a material like chromium, which may come into play when a photon penetrates the surface metal because it is incident at too high an angle or its energy is particularly high or near to an absorption edge of the surface metal. Also, molecular contaminants like oxide layers are unavoidable and must be considered in characterizing the reflective surface.

Very high angular resolution mirrors must be very accurately shaped and held rigidly. This requires a thick substrate (mirror shell) with high mass. The required thickness of the shells leads to inefficient utilization of the aperture and fairly low effective area. These type of mirrors have been very successful in missions like *Chandra*, *ROSAT*, and *Einstein*, however they are heavy and expensive to create. Smaller missions are constrained in weight, photon, and financial budget, making these mirrors a poor match to their needs. In the 1970's, Peter Serlemitsos at NASA GSFC pioneered the concept of the thin-foil mirror, which traded off few, thick, expensive shells for many, thin, inexpensive shells, consequently trading off lower angular resolution for higher effective area, lower weight, and lower total cost [90], [78]. Since then, Serlemitsos and his team have been responsible for many of the major breakthroughs in improving these mirrors and have led the fabrication of the majority of these mirrors that have been flown in space.

Thin-foil mirrors replace the paraboloidal and hyperboloidal surfaces by a single conic frustum approximating these shapes. These 'conically approximated' mirrors are much simpler to produce and have only slightly reduced intrinsic imaging. The mirror shells are nested tightly to maximize the on-axis effective area. The conically approximated mirror surfaces are such that many of the nested surfaces describe a segment of the same flat annulus, enabling mass-production of the shells. The design also lends itself to complete optics made up of several distinct angular segments.

Aluminum is the most commonly used substrate for the foils and is most often coated with gold. The epoxy replication method has led to much better smoothness of the gold deposition layer than initial thin-foils attained. Additional key innovations in the development of these optics have been multilayer foils, accurate foil shaping on mandrels, stiffer housings, and precise gang alignment of foils.

4.6.2 The *Micro-X* Optic

The *Micro-X* optic is pieced together from the remnants of previous missions' optics. We initially planned to reuse the mirror from the *Supernova X-ray Spectrometer* (SXS), a sounding rocket mission flown from Woomera, Australia in February 1988 [69]. This mission was the first to fly a conically approximated optic in space. The complete optic remained intact on landing, but the foils were contaminated by sand. Initial attempts to clean them were unsuccessful, so we reused spare foils from the Astro-E2 satellite mission in the *SXS* housing. These foils were re-cut for the size of our optic and installed in the original *SXS* structure. The resulting optic is shown face-on in Figure 4-39 and has 68 concentric foils with diameters of 80-200 mm. The foils themselves are 0.152 mm-thick Al substrates with gold coatings applied using the epoxy replication method, held fixed in the quadrant housings by precisely machined combs.

Figure 4-39: A picture of the *Micro-X* mirror from the aft side (where X-rays enter). The mirror is illuminated from the back with a flashlight, revealing the color of the gold-coated foils.

The GSFC X-ray Optics Lab tuned the focus of each quadrant separately, then staked the foils with epoxy and subjected the quadrants to vibration testing. No image degradation was detected after the vibration test. Each quadrant was calibrated individually on an X-ray beam line, exhibiting an half power diameter (HPD) of 2.4'. Each of our pixels covers approximately 1' square on the sky so the mirror is well-matched to the pixel size. The quadrants were assembled together and focal points aligned to within the same 0.1 mm square area by tuning the mechanical housing. At this point, a permanent mirror was epoxied to the mirror housing aligned perpendicular to the mirror's optical axis. The measured effective area of the optic including the filter (Section 4.7) responses is shown in Figure 4-40.

We will also reuse the optical bench from *SXS*, which holds the optic at the proper distance from the detectors. The focal length of our optic was measured to be 2.1 m. We have made some modifications to the optical bench to allow mating with our bulkhead, and we added a magnetic broom, that sweeps electrons with energies as high as 100 keV out of the optical path. This was designed and implemented by an MIT undergraduate student

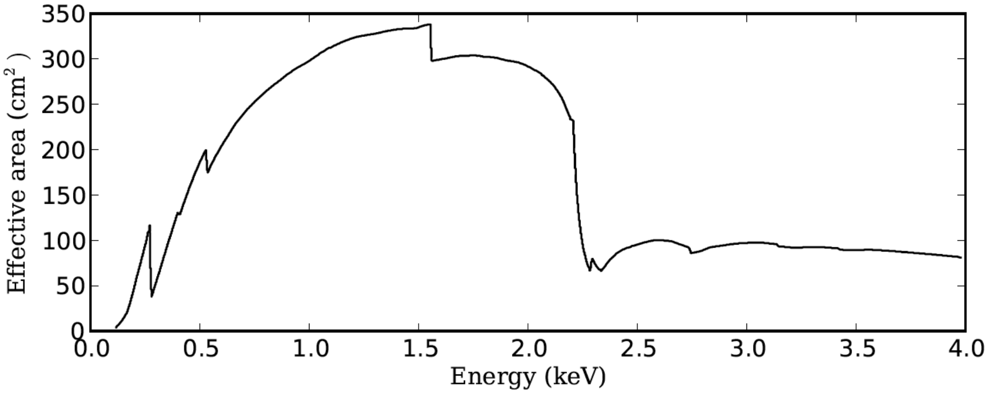

Figure 4-40: A plot of effective area versus energy over the *Micro-X* science band, including the energy-dependent response of the filter stack (reprinted from [86])

using eight NdFeB permanent magnets, based on the design of the magnetic broom on the *Chandra* mission.

Future flight upgrades will include a new mirror currently being designed and fabricated at Marshall Space Flight Center, with predicted 30" resolution, 2.5 m focal length, and about half the effective area of our current optic.

4.6.3 Alignment

The *Micro-X* alignment procedure is detailed internally[21] and implementation is currently underway. As described previously, the focus of our optic was determined with an optical parallel beam source at GSFC. At this time, the focal point was recorded using a digital camera mounted in the bore of the mirror, where the star tracker will eventually sit. The camera was kinematically mounted using three springs compressed by screws and a zoom lens was epoxied to assure the camera can be remounted in the same position.

To align the mirror to the TESs, we will first assemble the entire instrument with an open optical path between the detectors and the mirror (gate valve open and no infrared filters installed). At this point we will reinstall the reference camera in the optic bore and establish the focal point using the pictures we took during optic alignment. We will then

---

[21] Mirror Alignment Procedure RevB.pdf

install shims underneath the mounting of the optical bench until the focal point of the optic is in the center of the array. At this point, we will close the gate valve and mark the focal point on it so that we can check the alignment after we have closed the dewar and pulled a vacuum.

Once the mirror is aligned to the detectors, we must align the star tracker to the mirror [77]. The ST-5000 star tracker, described in more detail in Section 4.10.3, will replace the reference camera before flight and be aligned by NSROC using the permanent mirror installed on the mirror housing during alignment of the optic quadrants at GSFC.

4.7 X-ray Filters

While X-ray light must have an entrance path through the cryostat to the detectors, transmission of light from lower energy bands (namely the optical and infrared) to the detector plane is detrimental due to additional heat load and noise. The infrared emission is largely thermal emission from warmer stages of the cryostat, while the optical emission is primarily astrophysical in origin. We employ a system of five thin filters, one at each thermal stage, to allow nearly total X-ray transmission while blocking a large fraction of the optical and infrared light. There is one filter on each of the outer aft, inner aft, and 2 K shields with two filters on the detector stage. The filters on the three thermal shields are 28 mm in diameter and are suspended on silicon support meshes. The filters on the detector stage are free-standing with 15 mm apertures. Pictures of the filter support mesh and a filter deposited on the mesh are shown in Figure 4-41.

The films are made up of a ∼500 Å layer of polyimide (a strong polymer with good thermal properties) and a ∼250 Å film of aluminum, both deposited by Luxel Inc. The polyimide layer is epoxied to the filter body to prevent it from peeling off. To determine the optimal thicknesses of the filters, I wrote a program to predict the infrared power transmission of the filters as a function of the thickness of each of the layers, and the angle at which the filters are placed with respect to each other. The relative angles of the filters is important because of light reflection. Photons that are not transmitted through a filter are most often

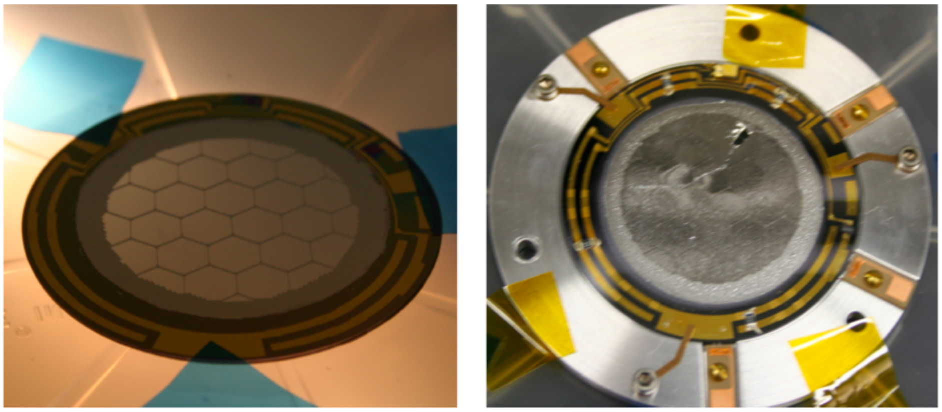

Figure 4-41: The silicon mesh with gold traces around the outside for connections to a heater and thermometer (left). A filter deposited on the mesh and installed on a filter mount (right). There is a tear on this filter so it was used for testing of the initial calibration setup.

reflected (absorption is a small effect). If adjacent filters are parallel to each other, light will continue to bounce between the two, with some fraction transmitting to colder stages with each trip. When the filters are angled with respect to each other the reflected light will bounce off the edge of the filters within a few bounces and be absorbed in the blacked light baffles surrounding the filters. As would be expected, both the X-ray and infrared transmission decrease as the thickness of the filter increases.

These calculations aimed to achieve a design limiting the thermal load on the detector from infrared light transmitted through the filter stack to less than 1% of the expected X-ray power per pixel, or less than ∼10 fW per pixel. Starting from the 300 K stage and moving inwards, I calculated the blackbody radiation produced by the environment and transmitted by the filters, taking geometrical effects into account.

The X-ray transmission through both polyimide and aluminum of various thicknesses can be obtained from `http://henke.lbl.gov/optical_constants/filter2.html`. I was able to obtain acceptable values for both the X-ray transmission and the infrared loading with two 50 mK filters set at an angle with respect to the 2 K filter, with each of the warmer filters set at small angles with respect to each other. In these simulations I took into account the expected formation of an AlO layer of ~50 Å. Taking into account realistic values for the shield temperatures and planned filter thicknesses, the thermal loading is about 5 fW per pixel, an acceptable value. The calculated X-ray transmission through the filter stack is >96%, however measurements from filter calibration give much more accurate values than this.

As with many of our design components, we leaned on the *XQC* filter design, using the same meshes as their payload (in fact, the meshes were constructed by the Wisconsin team). The silicon meshes are made up of a coarse hexagonal grid, with a finer hexagonal grid inside each coarse grid cell. These grids are made using a deep reactive-ion etching process with an implanted SiO_2 layer. Gold leads for heaters are applied around the circumference with an electron beam evaporator. A thermal oxide is grown on the Si to insulate the Si from this gold layer and to round the edges so that no pinpricks will form in the polyimide film near the edges of the mesh. The surface of the filter mesh is aluminized to reflect incident infrared (IR) photons. The detriment to the X-ray transmission due to obscuration by the mesh is about 3%.

The filters are extremely delicate, such that even breathing on them can cause them to break. However, they are robust enough to be installed by hand in the dewar, with care taken not to cause any kind of air flow perpendicular to the filter surface. Pressure differentials must be kept to a minimum during pump down of the dewar (by rule of thumb the larger mesh-supported filters can survive a pressure differential of about 40 Torr and the smaller, mesh-less filters can survive a pressure differential of about 1 Torr), so we will pump down slowly with a needle valve requiring $P/(\frac{dP}{dt}) > 15$ minutes. We must also provide a path for air to escape during pump-down that does not pass through the filters. We initially cut channels in the filter mounts to allow air to flow out around the filters, however our collaborators were concerned that even the airflow this would cause parallel to the filter surfaces could cause damage. Also, these channels create a path for stray light to seep in around the filter. Instead we will add ‘air baffles’ to each of the aft thermal shields to provide air paths further away from the filters.

Residual moisture in the dewar will freeze on the surface of the filters given the opportunity. The oxygen in the H_2O will absorb incoming X-ray photons strongly below the oxygen K-edge at about 540 eV. Heaters on the filters are designed to remove any accumulated ice. The heaters are surface-mount resistors, wired together by gold traces on the Si frame. Tens of volts are applied across the heaters in parallel to sublimate any ice that has built up on them. Diode thermometers are also installed on the filters and read out to ensure that the heating has raised the temperature sufficiently to sublimate any ice formation.

In addition to the heaters, aluminum baffles around the filter create a direction-switching maze to the cold filter surface, making it more difficult for stray water molecules to get to the filters without being adsorbed on another surface first. Filters are also stored in a nitrogen purge-box in the lab to hinder oxide growth that could cause absorption problems similar to an ice layer.

The *XQC* has measured ice formation of up to 2 μm during the early stages of flight. This is a major problem for the mission since the *XQC* science band is mostly below the oxygen K edge. They have since dealt with this problem by heating their outer thermal shields and keeping their heat switch open during their initial nitrogen transfer into the helium tank (cooling it from 300 K to 77 K). This causes any stray water molecules to be adsorbed on the outer surface of the helium tank, where they will remain as long as the surface is kept cold. While ice is not the disaster for *Micro-X* that it poses for *XQC*, since most of our science band is above the oxygen K edge, we will likely follow this procedure to make sure our pre-flight filter calibration remains as accurate as possible.

Initial calibration tests were performed in the MIT CCD laboratory using Manson sources to get a coarse sampling of the transmission curve of the filters. More rigorous calibration (sampled ever 2-20 eV) is beneficial to define the detailed structure around the photoabsorption edges of the K shells of C, N, O, and Al (the main components of the polyimide and aluminum films) and to see how the adhesive affects calibration. John Rutherford performed a full calibration for the entire flight filter stack and three spare filters at the Brookhaven National Synchrotron Light Source. This calibration showed that several of the filter thicknesses were larger than previously thought: up to 20% thicker than spec for the aluminum layer and up to 80 % thicker than spec for the polyimide layer. The full, detailed calibration process and the analysis pipeline is described in [86].

4.8 Position Monitors

As described in Section 4.3, the *Micro-X* cryostat is mounted from the rocket skin on a system of flexible wire rope isolators (WRI). A side effect of this mounting scheme is that the dewar can deflect up to several mm in a gravitational field, depending on its direction. Since we will align the optical axis to the focal plane horizontally in the lab and the observation will be done in microgravity above earth's atmosphere, we expect that the calibrated optical axis and the observation optical axis will be slightly different. There is also the possibility that after the severe vibration during launch the equilibrium position of the dewar may shift, though this risk is lower with the WRI than it would have been with the rubber dampers in the previous design iteration.

For this reason we need a robust measurement of the exact position of the cryostat with respect to the skins during flight, so that the exact image coordinates can be reconstructed after flight. Since Puppis A is large, we do not expect these misalignments to skew our FOV off of the target, but it will be important for analysis to know the precise pointing location. The optics will be rigidly mounted to the rocket skin by the optical bench, so we do not expect any change in mirror position during flight.

The position monitors are four laser diodes mounted on the outside of the cryostat vacuum jacket, read out by photodiodes mounted on the rocket skin. Figure 4-42 shows the locations of the lasers and photodiodes. The photodiodes output voltages corresponding to both the x- and y- positions of the laser beam on their 10 mm x 10 mm detector chips. The University of Florida team designed and manufactured a custom board to power the lasers and photodiodes, and to read out the photodiodes. This board interfaces through RS-422 to report position voltages.

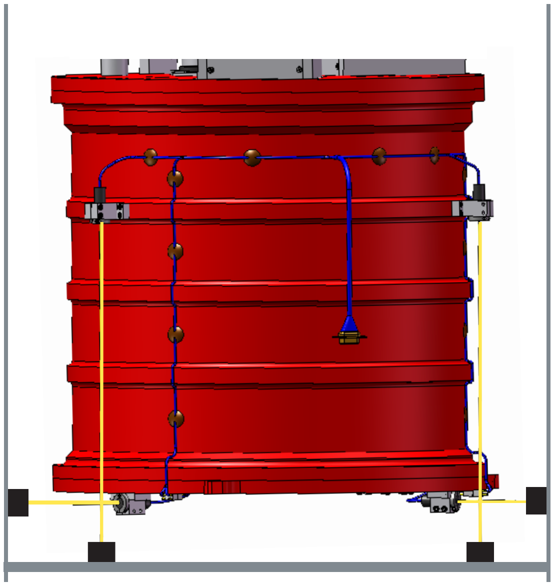

Figure 4-42: A CAD rendering of the dewar with the position monitor lasers and their beams. The black boxes show where the photodiodes are mounted and the gray outline shows the approximate rocket skin/bulkhead location.

Phil Oakley performed the calibration of the diodes by moving the diodes on a fine resolution x/y stage under a fixed flight laser to measure the precise Volts/mm conversion factor for each[22]. The linear conversion factor is different for each axis of each diode, though the values are all near 0.400 V/mm. The precision of the measurement is between 4 and 29 μm depending on the diode and axis. The maximum error introduced by brightness variations of the lasers, which can be powered by anywhere between 3 and 6 V, is about 50 μm. These errors are well within the large pitch of the *Micro-X* pixels.

4.9 Ground Support Equipment

The term Ground Support Equipment (GSE) is used to describe several different systems that allow communication with, and control of, the instrument from the ground. The NSROC

---

[22] `https://wikis.mit.edu/confluence/download/attachments/36996591/Laser_Position_System_Summary.pdf?version=1&modificationDate=1326212364000`

telemetry (TM) team has its own GSE, which receives data from the instrument through telemetry in the air and through the umbilicals on the rail before launch. The *Micro-X* team will connect to the TM GSE to communicate with the instrument while on the rail and during flight.

The science chain readout computers are also considered part of the GSE. The signals coming from the MUX stack pass into TM, which downsamples and reformats the data. In flight this will be the flight encoders and antennae. In the lab we use a telemetry simulator to replace the flight TM. The output of the telemetry (or telemetry simulator) is input to a dedicated server on a Windows machine and sent to a Linux client computer, which displays and stores the multiplexed data for selected pixels using a configurable GUI (`xcal_daq`). The parameters of the biases and feedback signals on the MUX stack, and the preamplifier on the IF stack, are set by a program run on a separate Mac OS computer (`squid_cmd`) to round out the field of operating systems. These machines are currently set up on desks in the lab for a single science chain, but will likely be transferred to moveable racks and a monitor bank when using two science chains and moving towards a flight setup.

Finally, the *Micro-X* team has its own GSE. This GSE acts to provide the commands and power for the instrument while it is on the ground[23], to interact with the housekeeping signals sent from the instrument through the TM during flight, and as a testbed to fill in functionality while flight systems are being developed. On range, our GSE receives housekeeping signals from, and administers commands to, the ADR control electronics through an RS-422 interface, reads out the four laser positions from the position monitor, controls the gate valve position, operates the heat switch motor, closes the pumping valve, and activates backfill of the flyaway line prior to flight. During commissioning, we have added tasks to provide functionality as flight systems are developed. These include the temperature control and helium level gauge in lieu of the ADR electronics and single pixel detector biasing using low noise battery packs in lieu of the flight MUX stacks.

The *Micro-X* GSE was developed and built by John Rutherford. A control computer, power supply, resistance bridge, and other auxiliary instruments are stored in a small, mobile

---

[23] These are provided by the TM system and batteries during flight

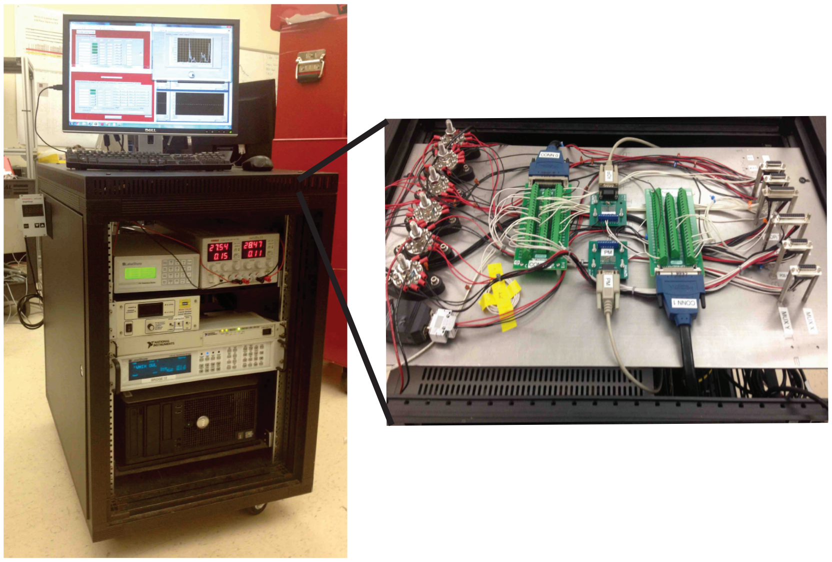

Figure 4-43: Pictures of the *Micro-X* GSE (left) and its breakout deck (right). In this picture, moving from bottom to top, the GSE contains the computer, Lake Shore bridge, GPIB server, LHe level gauge, diode readout, and power supply.

server rack and controlled by a suite of Labview control software. Power and signals are distributed from a covered breakout deck to a bank of connectors that replicates the telemetry interface connectors on the top of the *Micro-X* avionics stack. The *Micro-X* GSE and the breakout deck are shown in Figure 4-43. This system is described in more detail in [86].

4.10 Rocket Systems

The launch vehicle for the *Micro-X* instrument will be supplied by NSROC as a complete system made up of several smaller subsystems. While the parameters for these systems are based on the needs of our payload, they are designed, tested, and controlled by the NSROC teams, completely separate from the science instrument design, testing, and control. The choice of motors is dictated by the weight of our payload and desired elevation and duration of observation. Boost guidance and attitude control keep the rocket on course during initial ascent and control the pointing during observation respectively. Telemetry is configured to allow us to send down as much data as possible during the flight in case the flash cards recording the data on the payload are damaged in the process of landing. Finally, the nosecone houses and deploys the parachute during reentry to keep the payload from crashing to the Earth in free fall. The information in this section was provided in much more detail in the NSROC Sounding Rocket Handbook (SRHB) [98] and discussions with Wallops Flight Facility (WFF) engineers and the *Micro-X* instrument team regarding the specific implementation of these systems for the *Micro-X* payload.

4.10.1 Motors

Micro-X will launch on a two-stage, Terrier-Black Brant IX sounding rocket. This family of motor was developed to carry loads requiring high altitudes and will provide us with around 300 seconds of observing time above 160 km, achieving an apogee of 270 km. The Terrier MK 70 solid state booster fires first, burning for about 6 s before separating from the payload. After this initial separation, the payload will coast for a few seconds before the second stage, the Black Brant, ignites and burns for about 27 seconds. After its burn, the Black Brant stage is jettisoned and the shutter door (colloquially called the 'toilet seat') will open, allowing X-rays to enter the aft end of the science instrument. When assembled before flight the motors are stacked, not bolted, together and are separated from the rest of the payload by springs after their respective burns.

There is enough variation in the motor manufacturing process that science payloads are designed with 3σ low and high values under consideration. At the time of writing there have been several problems with up to 5σ high levels of vibration during launch. These caused so much heating in the most recent flight of the *XQC* payload (in 2013) that the temperature control was not able to achieve stable function at any point during observation. NSROC is currently investigating causes and possible solutions for these issues.

4.10.2 Boost Guidance

All sounding rockets are spun up to 4 Hz on launch to reduce potential deviations from flight trajectory due to vehicle misalignments, and spinning is stopped by the release of a set of weights before observation. Additionally, active boost guidance is utilized for the initial 18 seconds of flight, and can reduce possible impact dispersion by a factor of 5 to 10 from that of a fin-stabilized, unguided rocket. The boost guidance system is an S-19 Boost Guidance System developed by SAAB Ericsson Space. This is an analog system, that detects pitch and yaw angles using a gyro platform, and produces corresponding output signals. After signal processing and roll resolution, these signals are used as servo command signals feeding two pneumatic servos supplied with nitrogen or air from a pressure vessel. Each of these controls a pair of canards (fins), achieving aerodynamic control.

4.10.3 Attitude Control System

After rocket burnout, when the atmosphere becomes thinner, the instrument must be pointed very precisely to keep the target stable in the field of view. Fine pointing of the payload is achieved with small bursts of argon gas from the Attitude Control System (ACS). A control loop operates off of the signal from the ST-5000 star tracker, which is a low bandwidth digital imager, providing error information in 3 axes at a data rate of 10 Hz. Initially, the Lost in Space (LIS) feature determines an attitude solution in 1-5 seconds, typically closer to 1 second. Tracking of up to 32 stars will continue after the initial solution is determined. The ACS microprocessor calculates and delivers gas outputs from two pneumatic valves with separate reserves of Argon, usually held at different pressures.

4.10.4 Telemetry

During the *Micro-X* flight, we will store the entire data stream on onboard flash memory cards located in the MUX stacks for each science chain. However, in the event that these memory cards fail, or the payload is lost or destroyed during reentry and landing, it is safest to telemeter as much data to the ground as possible during flight.

The TM provides the means to format and transmit scientific and housekeeping (HK) data to the ground during flight. It can also provide control signals to the experiment through uplink, provide timing, and power if necessary. The TM section containing three antennae, flight encoders, timers, batteries, and power management electronics, sits in a stage just above the science instrument, and interfaces to a bank of connectors on the top of the *Micro-X* avionics assembly shown in Figure 4-1. The signal assignments and pinouts for these interfacing connectors were defined very early to allow the NSROC team to develop their systems independently of the science instrument development. Initial handshake tests between the GSFC-designed science chain electronics and the NSROC-designed TM electronics have been very successful.

Each of the *Micro-X* science chains produces data at more than 60 Mbits per second, which is much faster than current-generation encoders can handle. We will thus have to downsample our data before it is sent to the ground. Each of the science chains will utilize a 20 Mbit/s, WFF-93 Pulse Code Modulation encoder, while a separate 1.5 Mbit/s encoder will be utilized for the housekeeping signals. Each of these encoders feeds to its own, S-Band (2200-2300 MHz) antenna, producing three completely independent downlinks to the White Sands Missile Range (WSMR) base station during flight.

We will not utilize any uplinks for the first *Micro-X* flight, since all our planned flight events (temperature control, gate valve open and close, etc.) are triggered by timers synched to the launch time. We have considered using an uplink to repoint if initial data suggests we are not well-pointed towards our target, however we do not anticipate having the presence of mind during our first flight to make the possible gains from repointing worth the possible risks that arise from the added complexity.

4.10.5 Nosecone

After the observation, the payload is sent into a tumble as it enters the top layers of the atmosphere to slow it down as much as possible. The nosecone is jettisoned upward after observation, exposing the parachute, which is deployed by the Ogive Recovery System Assembly (ORSA) on an altitude timer about 5 km above the ground. If all goes well, the descent from this point should be relatively smooth, allowing us to obtain post-flight calibration data as the temperature control should still be operational.

4.11 Launch Logistics and Countdown Timeline

The *Micro-X* rocket will be launched from White Sands Missile Range (WSMR) in New Mexico: a Navy-supported facility. The rocket launches hanging from a launch rail at a steep angle, more akin to the launch of a bottle rocket than the more familiar launches of shuttles and larger rockets from launch pads. The *XQC* mission launches from the exact same rail, so the setup of the area and the available systems along with the requirements of the launch personnel nearing launch are well documented.

The integration of the *Micro-X* science instrument with the rest of the payload including telemetry, guidance, and optics will occur 2 weeks to a month before launch. For the first flight, the integration will occur at Wallops Flight Facility (WFF) in Wallops Island, VA, allowing easy access to the payload for the engineers of all systems, most of whom are based at WFF. In subsequent flights, once the payload has been launch-proven, the integration process will be more routine and can be performed at WSMR. Integration allows time for all teams to make sure the disparate systems interface well together and includes final vibration testing to flight-qualify the payload as a whole. Once this process is complete, we will disassemble the payload as little as possible (only what is necessary for shipping purposes) and drive it to WSMR. The subsystems will be reassembled and verified inside the Vehicle Assembly Building (VAB), which is about a mile from the launch rail.

In the last days before launch, several end-to-end tests will check that all of the systems function individually and together to the standards of the mission. The whole launch timeline is run through (minus the motors of course) to make sure all systems will function properly during the flight. These tests are called 'horizontals' as they are performed while the payload is nearly horizontal in the VAB. The final end-to-end test (called 'range vertical') is performed on the launch rail, with the payload raised to its steep launch angle.

In the hours leading up to launch, the *Micro-X* team must prepare the system for launch and data-taking, take final calibration data, and make final checks to make sure all systems are functioning properly leading up to launch. Signals that will not will be read out during the launch and subsequent observation, but will be monitored just prior to flight, are brought out of the payload via umbilical cables that run out of a small door on the rocket skin to a small, blast-proof bunker at the base of the rail. The signals run from the bunker, through an underground fiber-optic link, into the block house, located about 100 m from the launch rail, where the team will be for the duration of the launch. Signals that will be monitored via telemetry during flight are brought out on a separate umbilical by the telemetry team. They link these signals into their GSE, which communicates with the *Micro-X* GSE for the team's communication with the instrument. These umbilicals will be removed before flight, and the telemetry during flight will be through the 20 Mb/s downlinks.

The timeline in the hours just before launch is dictated by the requirements of the payload, worked around the requirements of the rocket systems. For instance, all non-range personnel must clear the pad by T-5 hours. During final arming between approximately T-3.5 hours and T-2 hours no power may be supplied to the payload systems. The launch countdown sequence must be carefully designed to meet all of the needs of both the experiment and rocket systems. The launch timeline is detailed in Table 4.2, which is compiled from a combination of the initial *Micro-X* countdown sequence and the sequence from the 2013 launch of the *XQC* payload.

Launch will be scheduled for solar midnight and will be scheduled for a date meeting the appropriate launch window criteria (namely that there is longer than one hour during the night when the target is more than 10° above the horizon and the moon is either new or far enough from the target to prevent contamination of the data). This allows for some delay in case there is a problem with one of the rocket or science instrument systems, or the winds are too high. After flight, the *Micro-X* team will accompany Navy personnel on a helicopter to retrieve the payload to make sure the cryogens and calibration source do not pose any danger.

Table 4.2: The proposed *Micro-X* launch timeline

Time	Altitude (km)	Event
T –7hr 15min	1.2	LHe transfer
T–6hr 45min	1.2	Begin LHe pumpdown
T–5hr 30min	1.2	Plug in umbilicals
T–5hr	1.2	Power on all systems
T–4hr 50min	1.2	Horizontal checks
T–3hr 35min	1.2	Power off systems, begin arming
T–5820s	1.2	Arming complete, power on systems
T–5700s	1.2	Ramp ADR up
T – 4800s	1.2	HS open; Ramp ADR down, hold
T-3600s	1.2	Vertical checks
T – 2280s	1.2	ADR regulate; calibration data
T – 150s	1.2	pumping valve close
T – 90s	1.2	Possible ADR rampup, ADR hold
T	1.2	Ignition
T + 0.6s	1.2	Rail release
T + 6s	3	Terrier burnout
T + 12s	6	Black Brant ignition
T + 18s	9	S19 canards decouple
T + 45s	45	Black Brant burnout
T + 60s	77	De-spin
T + 68s	92	Nose tip eject

T + 68s	92	PV open
T + 70s	96	Open shutter door
T + 77s	106	ADR regulate
T + 80s	114	Start MUX
T + 111s	160	Open gate valve
T + 111s	160	Start observation
T + 273s	283	Apogee
T + 438s	160	Close gate valve
T + 438s	160	End observation
T + 467s	112	Close pumping valve
T + 478s	92	Close shutter door
T + 619s	5	Parachute deploys
T + 921s	1.2	Impact

Chapter 5

The *Micro-X* Telescope: Data

In Chapter 4, I gave an overview of the payload components, all of which service cooling of the detectors, keeping them cold during flight, and getting science signal to, and read out from, the detectors. In this chapter, I will describe the detector readout, plans for characterization of the detector array, and the work that has been completed up to this point with the *Micro-X* detectors.

A large part of the challenge of commissioning a payload with a novel detector, aside from servicing the unique requirements of the detector, is understanding the detector itself and integrating it into a flight-like system. The *Micro-X* detector has been run in several different configurations on the road to a fully-operational, flight-like system. The detectors were originally run at GSFC, where they were fabricated, as a part of a laboratory system. Since microcalorimeters are the focus of the GSFC group, their lab system is extremely mature, with proper magnetic shielding and a well understood system of readout electronics designed for laboratory use. The detectors were then moved to MIT, where they were installed in the FEA, wire-bonded to the NIST chips, and run in our laboratory cryostat Gonzo, with flight-like cabling inside the dewar and a breakout box at room temperature routing the signals to analog laboratory electronics. Finally, we moved the detectors into LMO, and read them out with the full, end-to-end flight data acquisition system including flight electronics. The array is divided into two sets of pixels, each of which is read out by a completely separate set of science chain electronics. We have tested each science chain individually and have read out several pixels in a single science chain simultaneously but have yet to run both chains at the same time.

Much of our initial testing was completed using a non-flight array with 170 mK T_c. This was convenient because our current salt pill does not have the desired cooling capacity for a lower temperature array, so a detector with a higher transition temperature afforded us more time to run the detector each cycle, and allowed us to push forward the integration of the detectors and flight electronics while still working to improve our salt pill. GSFC has manufactured an array with T_c of 120 mK, which is slated for use as the flight detector. This array has been installed in the FEA and underwent vibration tests at Wallops, but has not been operated as part of the flight system in LMO as of yet. We plan to travel to GSFC with the entire system once we have a reliable salt pill to characterize this array and push the flight system to maturity.

5.1 Detector Readout

The *Micro-X* detector readout consists of several stages of electronics at various temperatures. The readout is based on amplification using Superconducting QUantum Interferance Devices (SQUIDs). SQUIDs are cryogenic devices made up of two parallel Josephson junctions in a superconducting loop [55]. When a SQUID is biased above a critical current level, it becomes resistive, causing a voltage drop to form across it. This voltage drop oscillates with increasing flux, producing a sine-like signal that is nearly linear in between extrema. Typically a feedback loop will be used to 'lock' the SQUID in this region, which I will discuss in more detail later.

As discussed briefly in Section 4.1, the TESs are biased with a constant voltage and the current running through them changes depending upon their resistance, the signal of interest. The change in current through the TES creates a change in flux through the corresponding first stage squid (SQ1), which is flux-coupled to the second stage squid (SQ2). Both the SQ1 and SQ2 are on the 50 mK stage (FEA) within the magnetic shield for the detectors. The signal from the SQ2 runs through woven Tekdata cables[1] to the 2 K boards, which are built into the thermal shield on the insert, where it is further amplified through the SQUID array (SA). The SA is a phase-coupled array of 100 SQUIDs, that acts as a signal amplifier by inductive coupling and can be biased in the same way as an individual SQUID. The signal coming out of the 2 K boards runs out of the cryostat through much longer Tekdata cables to the room temperature electronics.

A requirement for keeping the detector array cold is to limit the number of wires running to the array. Even with a small detector like ours, the number of wires that would be necessary to address each pixel separately would be prohibitive. Therefore, we use time-division multiplexing (TDM). This multiplexing (MUX) is achieved by turning on and reading out a subset of pixels that share a bias line over a short period of time, trading off with other such subsets of pixels. The TDM is a flight version of NIST lab-based systems, which have achieved TDM with 1000 pixel arrays with time constants as low as 0.05 ms [26].

The room temperature electronics for each science chain consist of two electronics stacks: the multiplexing (MUX) stack and the interface (IF) stack. The MUX stack sits on the *Micro-X* avionics deck, and produces address signals for the TESs and constant biases to bias the SQUIDs. The IF stack sits on the top of the cryostat, and acts as a pass-through for these signals. It also contains a preamplifier for the detector and cold electronics signals. The MUX stack records this amplified signal, and uses it as the error signal in a control loop to keep the system in an ideal operating range.

5.1.1 SQUID Readout

Before delving into the details of the SQUID readout circuit, I will give a brief physical picture of the layout of the SQUID system. A labelled picture of the focal plane is shown in Figure 4-5. The detector array containing the TESs is in the center of the focal plane on the FEA. All the SQ1s and FB coils for a single column are etched onto a long, thin

---

[1] These are custom-made of CuNi-clad NbTi twisted pairs, interwoven with kevlar strings.

MUX chip[2]. Each MUX chip has a single SQ2. For each science chain, four MUX chips are epoxied to an interface chip, which routes the signals to a breakout board that connects to the 85-pin science chain connector on the FEA. There is an interface chip with four MUX chips, a breakout board, and an 85 pin connector for each of the science chains. Both the MUX chips and the IF chips were fabricated at NIST and connections between these, the detector chip, and the breakout board are made via wire bonding. The SA are located on the 2 K board. Since they are outside of the magnetic shield for the detector box, they sit inside their own Nb box for magnetic shielding. It is an important distinction to note that detector readout 'rows' and 'columns' are not equivalent to the detector array physical rows and columns, rather reference the rows and columns of the readout electronics. Each science chain (X and Y)[3] has four detector readout columns (A, B, C, D), each of which has 16 rows, adding up to our 128 total pixels.

The SQUID readout uses a series of inductively coupled SQUIDs and coils to amplify the signal from the TES and deliver it to the MUX stack as part of a control loop. A labelled diagram of the detector readout is shown in Figure 5-1. The TES couples to the SQ1 via the SQ1 input coil, effectively translating the change in TES resistance to a change in flux on the SQ1. The SQ1 is flux-coupled to both the SQ2 summing coil and the SQ1 feedback coil. The SQ2 summing coil is in series with the SQ2 input coil, which is flux-coupled to the SQ2. The SQ2 is in series with the SA input coil, which is inductively coupled to the SA. The output of the SA is amplified by the preamplifier card in the IF stack and input to the digital feedback (DFB) card in the MUX stack. The control loop from the MUX stack will take as input the amplified signal from the IF stack, and output a signal to the SQ1 feedback coil to null out the flux change caused by the TES signal.

Tuning the SQUID chain is achieved using two settings for each SQUID stage: the bias voltage and the flux offset. The bias voltage controls the size of the SQUID modulation (the full range of the voltage drop accessible in response to applied flux). Typically this is chosen

---

[2] There are actually 32 SQ1/FB coil pairs etched into each chip, but only the 16 with the most uniform characteristics are wired to the readout chain.

[3] In an example of collaboration efficiency the MIT team denotes the science chains as X and Y, GSFC uses A and B and NIST uses 1 and 2.

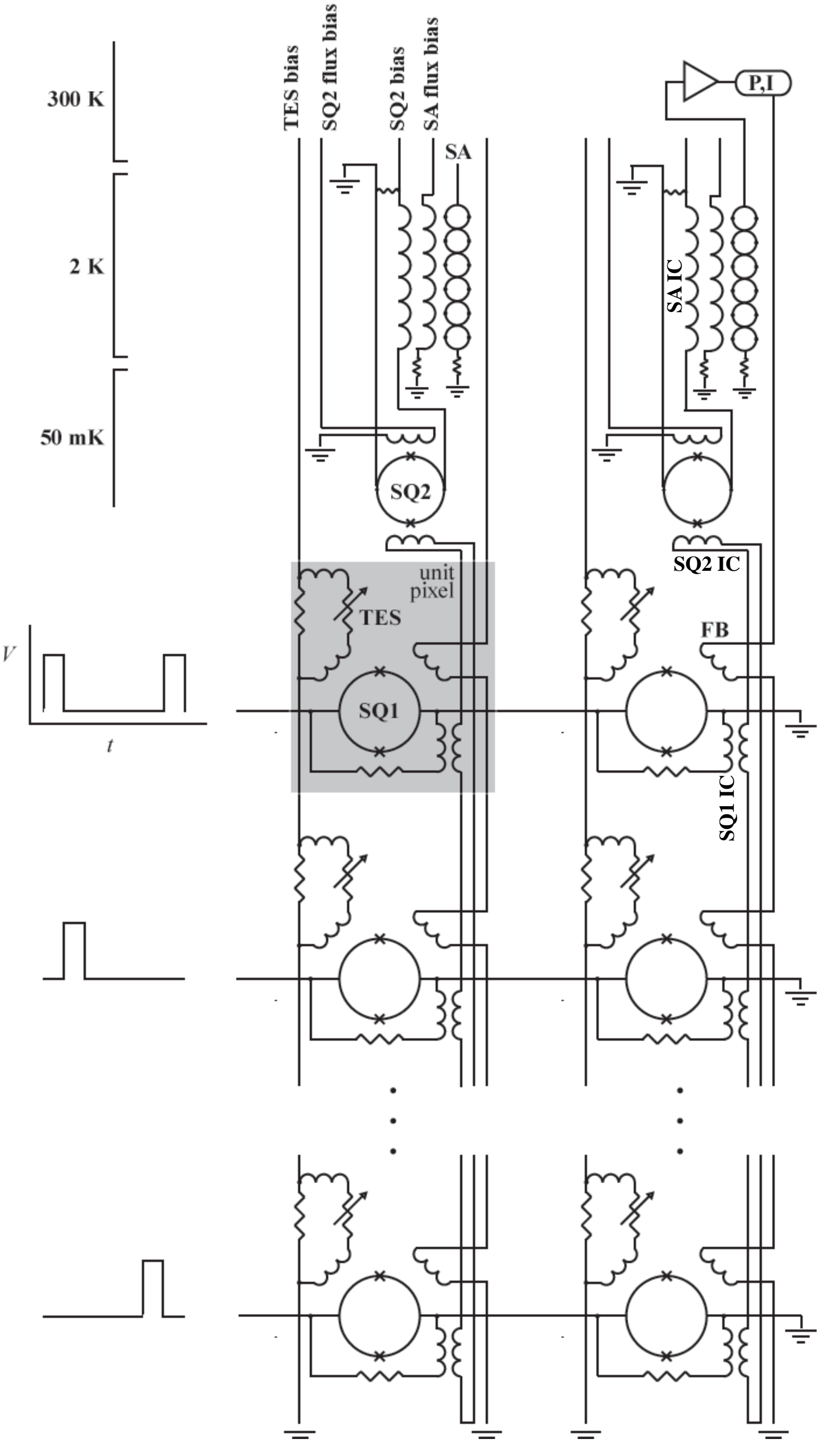

Figure 5-1: A labelled diagram of the science chain readout system. Diagrams of voltage on the left show the pulses applied to the SQ1B lines to turn on and off various rows with time, so that only one SQ1 per column is active at any given time.

to maximize the modulation (which corresponds to maximizing the amplification) The flux offset controls the phase of the modulation. We currently adjust these settings by hand, with the goal of lining up the linear regions of each stage so that the control loop keeps all of the SQUIDs in the linear regime. This is known as ‘flux-locking’. We hope to implement some kind of auto-tuning algorithm before flight since each SQ1 has to be tuned independently and the process is currently fairly lengthy for even a small number of pixels.

5.1.2 Time Division Multiplexing

As mentioned above, multiplexing the row address and the SQ1 FB signals serves to decrease the number of wires running to the detector array. This serves the dual purposes of decreasing the heat load on the detector array and simplifying the wire bundles that have to be routed to the detector array. For each column there need be only one SA, one SQ2, one SQ1FB coil, and one TES bias line. The TES voltage bias for a column is set to a constant value, so all of the TESs are always biased, however we must assure that only one TES signal will be read out at a time by the electronics further up the column. We can achieve this by only biasing one SQ1 at a time, since an unbiased SQ1 will be completely superconducting and so will act as a short and not react to flux changes resulting from TES resistance changes.

A SQ1 is turned on by applying a voltage on the corresponding row address line (SQ1 bias line). The 16 row address lines, each of which biases a row of SQ1s, are shared across all four columns in a science chain, again reducing the total number of wires running to the cold electronics. The rows of SQ1s are addressed sequentially with step functions in bias voltage so that row 0 will be turned on for one clock cycle and will then wait 15 clock cycles to be turned on again. This is time division multiplexing. Other multiplexing methods include frequency-division multiplexing and code-division multiplexing.

5.1.3 Data Stream

I have already discussed the data stream from the standpoint of telemetry in Section 4.10.4, however it is useful to consider the data stream as it is produced by the science chain. We operate two completely independent science chain channels, each of which has its own power distribution cards, MUX stack, IF stack and telemetry stream. Each of these chains produces 66 Mb/s of data. This full data stream is recorded on flash memory by the master control board in the MUX stack while the downsampled data stream is telemetered to the ground. The GSFC team has developed straightforward software to configure the MUX stack as far as bias levels, P and I values for the feedback loop, clock cycle length, settling time after MUX switchover before measurement, etc. Once we have obtained optimized values for each of these in various situations, several global configuration sets will be programmed into the MUX for use on range and during flight.

5.2 Array Characterization and Data Processing

5.2.1 Pulse Data Reduction

The pulse data reduction is achieved using a GSFC-bred suite of automated data reduction routines within the framework of Igor Pro (a commercial software suite). This software takes as input a time stream of triggered pulses (triggering serves to shorten the data files) along with data records without pulses to characterize the noise. A GUI allows the user to select 'good time' regions where data can be extracted, and make noise and pulse height cuts. The output is binned spectra with noise estimates.

The data reduction software uses an optimal filter to analyze the data more quickly and accurately. This method models the time record containing a pulse as a template (obtained by averaging over several pulses) multiplied by a scaling factor, plus a noise template (similarly obtained by averaging over several noise traces in frequency space). This method is optimal for describing data from a detector with a linear detector response and time-independent noise. This is not strictly the case for our detectors, since a TES saturates at high enough energy (that causing a temperature rise so large that the TES rises out of its transition) and because the change in the resistance of the detector with temperature causes a change in both the noise itself (the TES Johnson noise depends on resistance) and the detector's response to noise (the detector noise rolloff depends on the resistance of the detector $\tau = L/R$ [34]). Despite these not-quite-met conditions, this method has been proven very effective for reducing TES data, and analytic calculations can show that the maximum likelihood pulse depends only on the average templates and the constant scale factor [34].

Only one pulse and noise template are calculated for the entire dataset. These are then inverse-Fourier transformed into the time domain, making the method fast to run. This allows fast and simple pixel characterization, as the software allows you to quickly analyze datasets taken under slightly different conditions. We can compare pulses as a function of bias point, TES location on the array, etc. As I will discuss in Section 5.2.2, these functions are necessary for determining the ideal operating parameters for the TESs.

5.2.2 Pixel Characterization

Megan Eckart performed initial characterization of the TESs in the GSFC lab setup. We will likely repeat these characterizations in the flight setup at MIT, both as confirmation of the GSFC measurements, and to verify our own readout and analysis systems. Once the readout chain has been tuned as described in Section 5.1, there are two settings that can be optimized for the detector operation independent of the SQUID chain tuning: the bath temperature and the TES bias voltage. Together these determine the TES's quiescent location in its transition.

The strength of the thermal link to the cold bath (characterized by thermal conductance G) depends on the phonon transmission through the perforated SiN membrane on which the TES is deposited. This phonon transmission depends on the temperature of the membrane, which is determined by the bath temperature. We can measure the G as a function of the bath temperature T_b by measuring the necessary applied power to move the TES halfway into its transition at each bath temperature. The power is applied via the TES bias voltage and G is measured as the slope of this curve. The measurement location of halfway into the transition is chosen such that the measured applied power at the transition temperature will be zero.

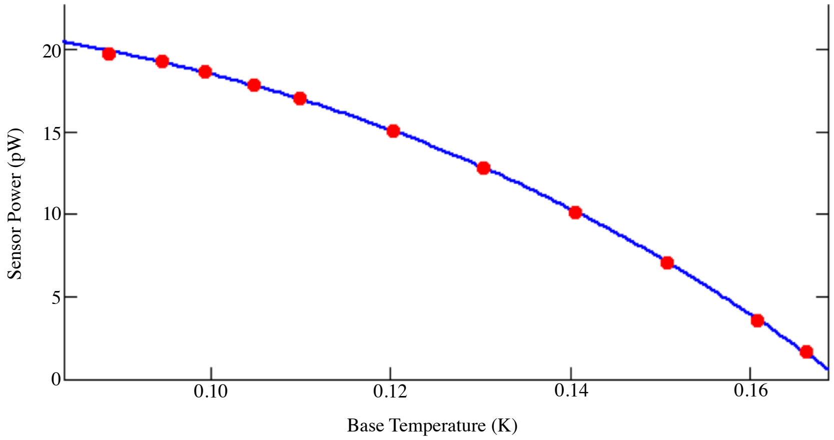

Figure 5-2: Necessary power required to bias the TES halfway into its transition as a function of bath temperature. This measurement was made at GSFC on the 170 mK T_c test array.

The plot of power versus bath temperature for one of the 170 mK T_c pixels is shown in Figure 5-2, and the measured G at T_c was 410 pW/K. Once this measurement is made, the bath temperature can be chosen to produce a G leading to the desired detector time constant.

Just as the characteristics of a superconductor change with applied magnetic field, so too do the characteristics of a superconductor change with the applied bias voltage. The bias voltage can affect the pulse height for a given energy, detector time constant, and noise equivalent power (NEP). The pulse height changes because of the slope of the superconducting transition. As the TES nears the top of the transition the gain decreases, leading to lower pulse heights and, if there is enough temperature change, saturation. Pulse height will generally decrease with bias level. A plot of pulse heights at various bias levels is shown in Figure 5-3. In this and Figure 5-4, the bias levels are reported as the TESs quiescent location in the transition as a percent from 0% at the bottom to 100% at the top. NEP is the equivalent, input-referred power needed to produce a given output noise so lower NEP gives lower noise. Both the time constant and the NEP have U-shaped curves when plotted versus bias level, as shown in Figure 5-4. The change in time constant with temperature can

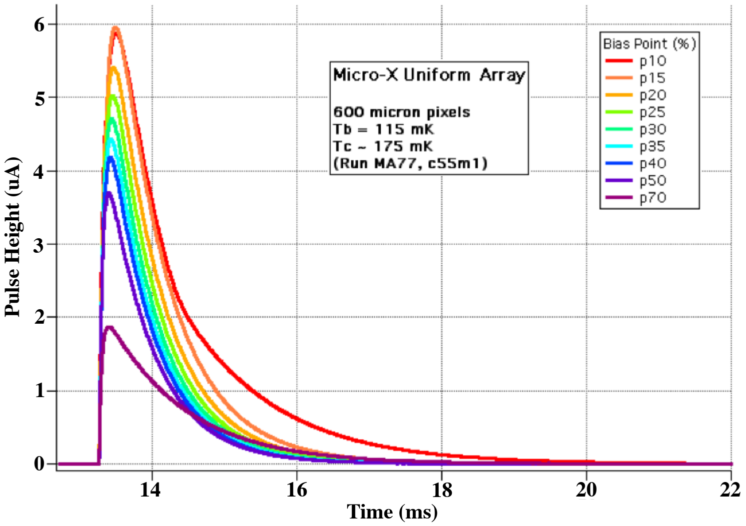

Figure 5-3: Average pulses of a single pixel as a function of bias level from measurements at GSFC. Bias is quoted as percentage of the transition. The higher the bias the lower the pulse height.

also be seen in the pulses shown in Figure 5-3. We will choose the bias that minimizes the NEP as the set point for the TESs. Once T_b and V_{bias} are set, we have a full definition of optimal readout settings and can begin TES calibration.

As discussed in Section 5.1, all the detectors in a particular row share the same TES bias line and all of the TESs share the same cold bath. This makes pixel uniformity very important, as we prefer all of the TESs that share a particular bias line to be optimized at the same bias level and bath temperature.

We were able to make similar measurements to those in Figures 5-3 and 5-4, but were not able to replicate them because we still had not optimized our magnetic shielding and had trapped magnetic field on the detector array. This trapped magnetic field suppressed the transition temperature by almost 70 mK, slowed the timescale of the detector by at least a factor of two, and broadened the transition of the TESs. The GSFC team was able to mimic these effects by applying a field to their detectors during operation.

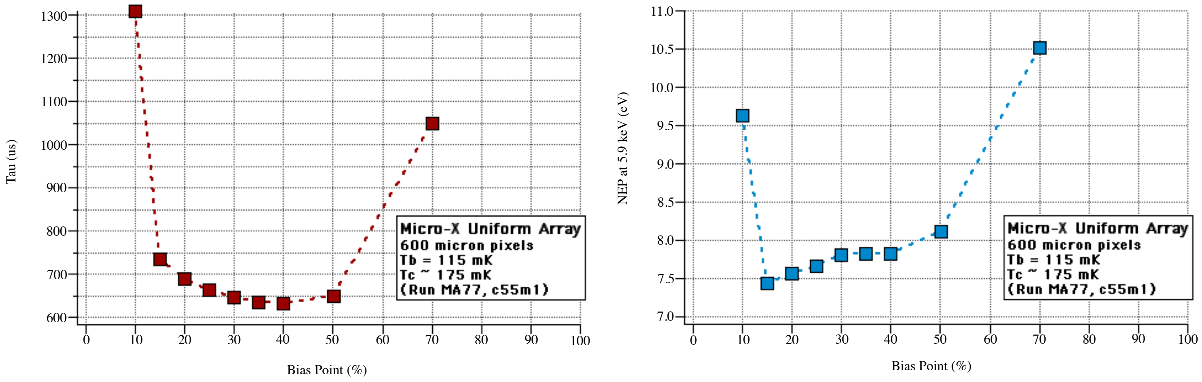

Figure 5-4: Detector time constant τ (left) and NEP (right) as a function of bias. The bias is usually set at the point where NEP is minimized.

5.2.3 Spectra

Once we have optimized the detector and readout chain parameters, we will move on to optimizing grounding and shielding to lower noise and achieve the desired energy resolution. After we have achieved satisfactory resolution we will likely use several different calibration sources to build up a well-sampled energy calibration in and around our science band. During work to lower the noise level, we will use a radioactive ^{55}Fe source as a calibration source. ^{55}Fe decays via electron capture, producing three Mn K lines: Kα_1 at 5.888 keV, Kα_2 at 5.899 keV, and Kβ at 6.490 keV. This is a standard source used for detector characterization of high energy-resolution detectors because of the closely spaced Kα lines.

Figure 5-5 shows the pixel height (determined by the optimal filter) versus time trace for the 170 mK array under illumination by an ^{55}Fe source shined into the dewar through a Be window. For the first ∼hour of this trace, we were using temperature control from the *Micro-X* GSE. We turned it off to allow the detectors to drift afterwards so that we could analyze whether or not the temperature control contributed any noise to the system (it did not). Once a ‘good time’ window is defined, the pulse heights are binned into a histogram and energy calibration applied to create a spectrum, which is shown for both the GSFC and MIT setups in Figure 5-6. While the GSFC setup produced a spectrum with FWHM of 9.5

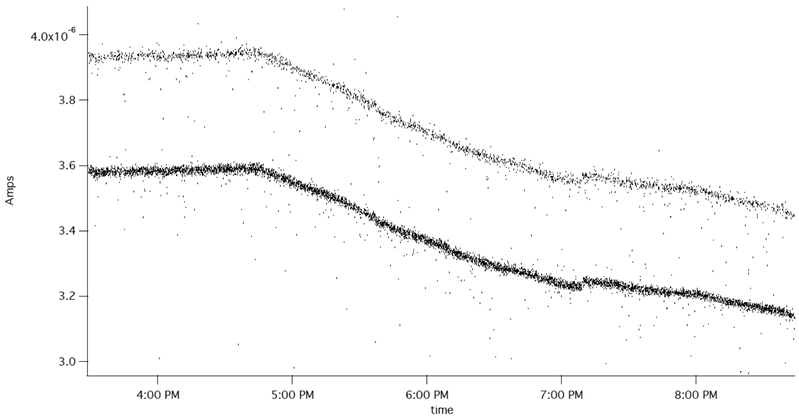

Figure 5-5: The optimal filter-measured pulse height versus time from the ^{55}Fe source. The lower, thicker line is the combination of the Mn Kα_1 and Mn Kα_2 lines while the higher line is the Mn Kβ line. We used temperature control for the first hour of the observation and let the temperature drift afterward. Toward the end of the trace, the system lost lock and relocked at another point.

keV at 6 keV (near the theoretical limit of these detectors), the MIT setup was only able to produce a spectrum with a FWHM of 25 eV at 6 keV because of poor magnetic shielding, unshielded cables, and poorly defined grounding.

We were able to make significant progress with better grounding, magnetic shielding and better cabling, which I will discuss more in the next section. We recorded pulses in a much quieter setup than those used to make the spectrum in Figure 5-6, however we neglected to record noise traces and so were unable to determine their resolution. We plan to begin characterization of the 120 mK array in the summer of 2014 at GSFC. A spectrum of the Mn Kα lines taken with the 120 mK flight array in a laboratory setup at GSFC is shown in Figure 5-7, demonstrating 4.5 eV resolution. Multiplexing using the flight MUX and IF stacks has also been demonstrated. Figure 5-8 shows average pulses acquired simultaneously on seven pixels from the 170 mK array.

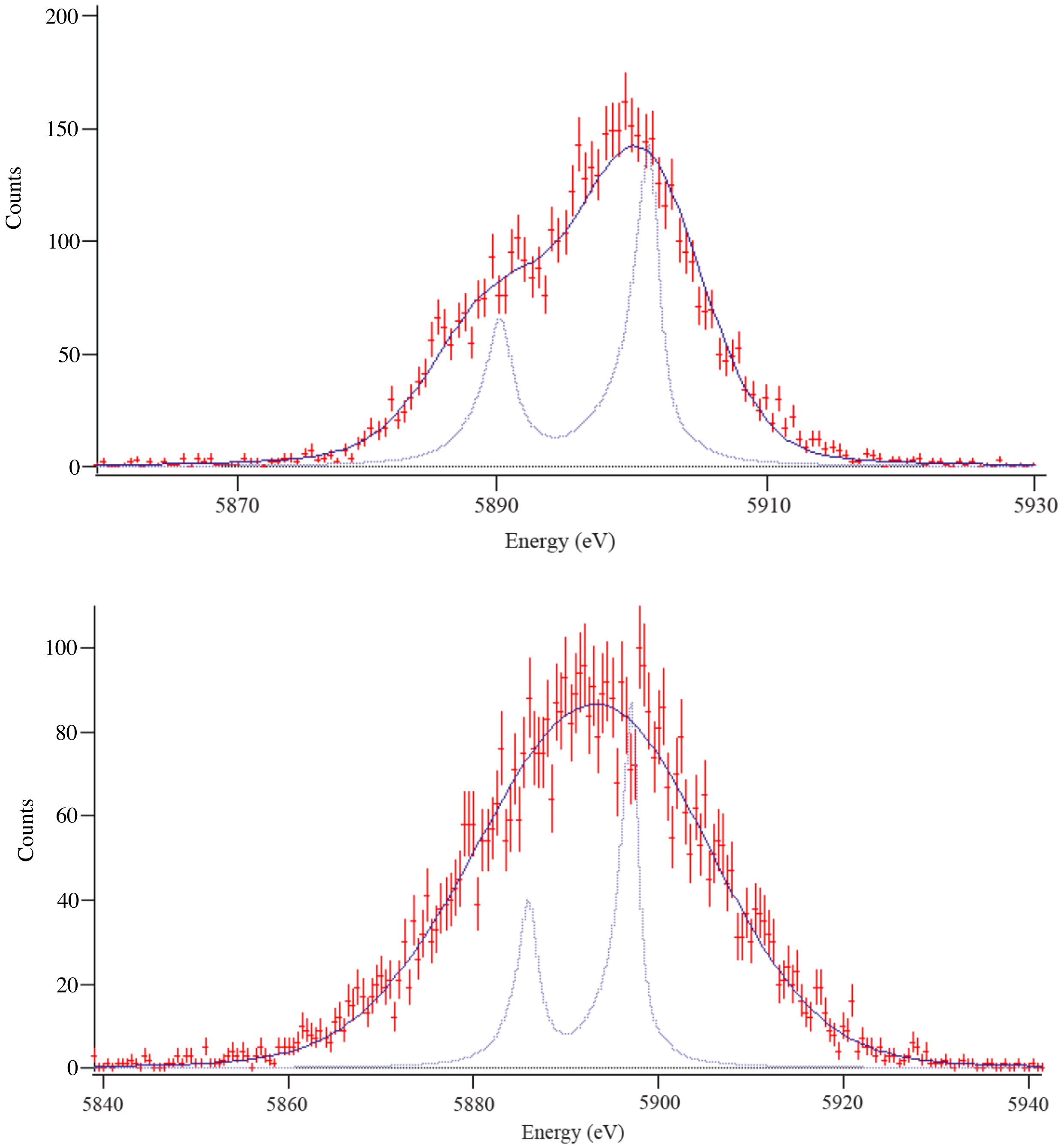

Figure 5-6: Spectra measured at GSFC (top) and MIT (bottom) on the same 170 mK test (non-flight) array. The worse resolution on the MIT spectrum was due to the bad grounding, poor magnetic shielding, and poor radio frequency (RF) shielding in a noisy building.

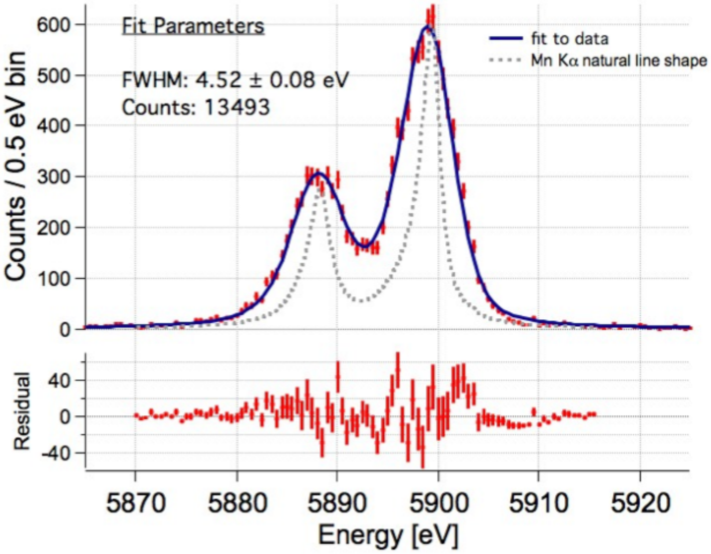

Figure 5-7: The Mn Kα line spectrum measured with the 120 mK flight array in a lab setup at GSFC. A fit to the data gives the detector resolution of 4.5 eV at 6 keV.

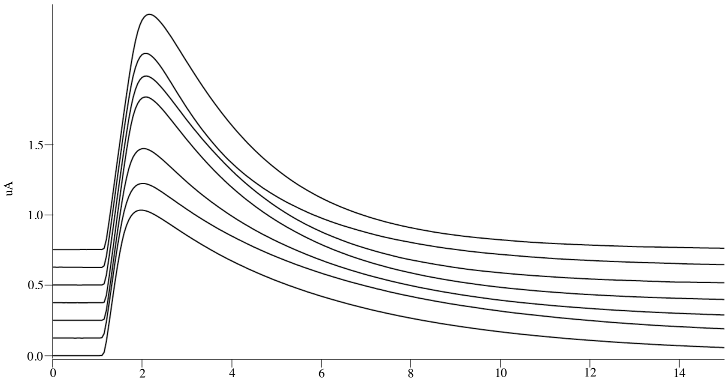

Figure 5-8: Average pulses from seven pixels, run simultaneously using the time-division MUX. The pulses are offset for clarity. The differently shaped pulses on different pixels are likely a result of inhomogeneous magnetic field trapped on the detectors. Ideally the pulse-shape will be the same for all pixels.

5.3 Noise Floor

5.3.1 Analytic Calculations of Science Chain Noise

As a part of efforts to reduce the overall noise on the TESs, I analyzed the contribution to the detector signal from noise on each signal and bias line, or the 'input-referred' noise from each location in the circuit. Comparing the input-referred noise at the TES to the noise level at each location in the circuit gives transfer functions for each location, which can help to identify the circuit inputs that are most vulnerable to allowing a large amount of noise into the TES signal[4]. All of the discussion here will refer to the diagram in Figure 5-1.

To find the input-referred noise at the TES from each noise source in the system, I calculated the contributions from noise sources at the input coils of each stage, then used the mutual inductances of the coils located throughout the system to calculate the final noise at the TES. I calculated the expected noise floor by using the temperatures and resistances of the resistors at each stage to calculate their intrinsic Johnson noise, and plugging in the expected noise from the electronics across the bias and signal lines. This gives the achievable noise level at the TES level if the system suffers no RF pickup noise, no noise on the input above specified values, and no other noise input from extraneous sources. If the input-referred noise from the electronics across the amplifier chain is significantly smaller than the TES noise (the Johnson noise from the resistance of the TES) the electronics noise will not significantly degrade the resolution of the detectors. Our goal is to achieve this state, where the system noise is limited by the TES noise rather than electronics noise.

There are six noise sources that contribute to the noise on the SQUID array (SA) input coil. These are:

1. The intrinsic SA noise
2. Noise from the preamp
3. Johnson noise from the resistor on the SA feedback (FB) input

---

[4] The full analysis can be found at `space.mit.edu/figueroagroup/internal/micro-x/Noise_Analysis/ScienceChainNoise.pdf`

4. Johnson noise from the resistor on the SQ2 Bias (SQ2 B) input
5. Johnson noise from the SQ2 shunt resistor
6. Noise from the SA FB input signal

Assuming that the noise sources are independent and Gaussian we can add them in quadrature to obtain the total noise on the SA IC.

There are five sources of noise on the SQ2 input coil (SQ2 IC). These are:

1. Noise from the SA IC coupling to the SQ2 IC through SQ2
2. The intrinsic flux noise from SQ2
3. Noise from the bias input signal on the SQ2
4. Johnson noise from the resistor on the SQ2 FB
5. Noise from the input signal on the SQ2 FB

Once again the total noise on SQ2 IC will be obtained by adding the noise from each of these components in quadrature:

There are eleven sources of noise on the SQ1 input coil (SQ1 IC). These are:

1. The intrinsic noise on SQ1
2. The noise from the SQ2 input coil coupled to the SQ1 input coil
3. The noise from the signal input on the TES bias
4. The noise from the resistor on the TES bias
5. The Johnson noise from the TES shunt resistor
6. Johnson noise from the resistor on the SQ1 FB
7. Any noise from the DFB loop

8. Johnson noise from the resistor on the SQ1 B
9. Noise from the signal input on the SQ1 B
10. Noise from the shunt resistors on SQ1 from each column in a given row
11. TES noise-Johnson noise over the dynamic resistance of the TES

The total current noise on the SQ1 input coil is then given by these terms added in quadrature.

While these calculations are useful to help us understand the propagation of signals through the system, they have demonstrated only limited success in predicting transfer functions in the system, so most of our work has been focused on using empirical findings to guide changes. Currently the noise from sources external to the system far exceeds the TES noise. The expected Johnson noise from the TESs is 50 pA/$\sqrt{Hz}$ while the measured noise is 300 pA/$\sqrt{Hz}$. This measurement was made on the 170 mK test array through the flight electronics, but not in a 'flight-ready' configuration. Many improvements to this setup can and will be made in the grounding, RF and magnetic shielding, and firmware/tuning procedures before the system will be in a 'flight-ready' configuration. These changes are expected to lead to a large reduction of the noise levels in the system.

5.3.2 Empirical Noise Measurements

Fortunately, the data acquisition software (`xcal_daq`) provides a constantly updating Fourier transform of the noise level. This allows us to make changes to the physical system, like changing the grounding or putting a filter on a particular signal line, and observe the changes in the noise vs. frequency immediately. We can also measure transfer functions using this software by applying white noise at a particular level across a given input line and measuring the response in noise level on the locked SQ1 signal at the TES.

Using the noise acquisition and display capabilities of the `xcal_daq`, along with various attempted grounding schemes, we were able to learn that the return signals for nearly every science chain line running into the dewar needed to be grounded at the vacuum jacket. This is completely different from the lab implementation of the electronics, which are run more or less differentially. We also discovered that the noise was reduced even further when grounding the signals to the vacuum jacket at the top of the interface stack and adding low pass filters to the signal pins. Both of these were achieved using custom flexible connector inserts fit to the various DB connectors at the top of the IF stack, designed to ground return lines to the IF stack case and pass signal lines through miniature RC circuits before passing them into the IF stack. Since grounding on the top of the dewar seemed to be extremely important and sensitive, we also added configurable grounding cards to ground signals inside the IF stack.

The Fourier transform plot of our best achieved noise so far is shown in Figure 5-9. As we can see from the forest of high frequency lines, RF pickup continues to be a difficult problem. We have battled with the ever-present 60 Hz line and its harmonics, and run in a particularly RF noisy building, experiencing problems like the 10 GHz identification signal broadcast by the wireless routers in the room. We were also able to identify a noise issue with the first implementation of the power card, which used noisy, switching DC to DC converters to dole out power to various ports in the MUX stack. We plan to improve this by splitting out the part of the power card using the converters into a separate ‘converter card’ and moving it to a heavily shielded box much further from the rest of the electronics, and routing the signals it produces through a ‘regulator card’ with heavy filtering in the MUX stack.

Our key goal of the integration run at GSFC will be noise reduction and we are hopeful that with the 120 mK array (which has intrinsically higher energy resolution that the 170 mK array), the new filtered flight power supplies, improved magnetic shielding, and a much improved and solid grounding scheme we will be able to achieve the desired resolution for flight.

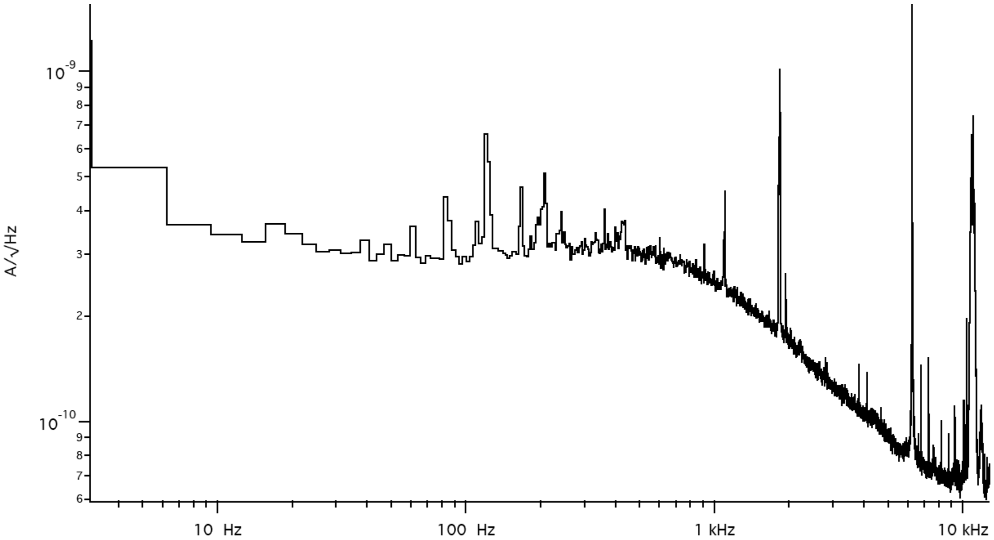

Figure 5-9: An FFT of the best noise currently achieved on the system at MIT. The high-frequency forest of lines is a symptom of RF pickup. The noise level is approximately 5 times worse than that at GSFC.

5.4 Simulated Data

The first flight of the *Micro-X* payload will target the Bright Eastern Knot (BEK) in Puppis A. This is a bright region believed to be the result of the shock running up against a molecular cloud [52]. Aside from being an attractive target because of its brightness, it also presents a wealth of possible science topics. With the *Micro-X* energy resolution, we should be able to easily distinguish lines in triplets (allowing much more precise measurements of possible charge exchange like those described in Chapter 3), diagnose temperature, abundances, velocities, and a host of other plasma parameters with unprecedented sensitivity. The BEK also provides a single knot of material spread across a region of the sky that is extremely well-matched to our FOV.

Puppis A is only available as a target for a specific launch window each year (approximately November through March). We require that it be above the horizon for at least an hour to define the launch window[5]. If we are not ready for launch during the 2014-2015 Puppis A launch window and are prepared for launch significantly before the 2015-2016

---

[5] The location of the moon and Sun are also taken into account as they are extremely strong X-ray sources

launch window opens, we may consider observing our planned second target: the Cassiopeia A SNR, which is available throughout the year. We had planned to observe Cas A with the new, subarcsecond mirror, which would better match its size and complexity. Cas A is much smaller than the BEK, slightly less bright, and has a complicated, knotted structure [85]. Through simulations we have shown that in the brightest pixels we will be able to distinguish Si lines in the brightest areas so we would still be able to get a good deal of interesting science output from a Cas A observation, however we would much prefer the more attractive target of Puppis A for the first flight.

We can simulate the expected data from either of these sources by using previous observations by current instruments. We fit the low resolution CCD data with a `vnei` model, then use those `vnei` best-fit parameters to pass an ideal spectrum produced by the model through the *Micro-X* spectral response. As the `vnei` model is a global plasma model built from somewhat incomplete knowledge of plasma physics, we do not expect this to be an exact match to the incoming photons, however it can serve to give us an idea of what we might see. A simulated spectrum of the BEK seen with *Micro-X* is shown in Figure 5-10. We expect to get roughly 17,000 counts over the 300 second observation. This simulation assumes a 4 eV resolution from the detector. The inset shows that we will easily be able to distinguish the oxygen VII triplet, which will be important for studying charge exchange. As the BEK is a single mass of fairly homogeneous material, the simulations should provide a reasonable approximation of a possible observation. Cas A, on the other hand, has many small knots of material with fairly different properties within a small area on the sky [85]. Given the poor PSF of our current mirror and the large pixels, we will likely see blended spectra from these disparate areas in a single pixel readout, complicating the analysis in that case.

While we have no uplink planned for the first flight, it is an option to employ possible repointing in future flights. John Rutherford simulated a display of incoming counts versus time to determine the feasibility of making a repointing decision quickly and confidently. He showed that a pointing offset could be determined within about 10 seconds for Cas A (a

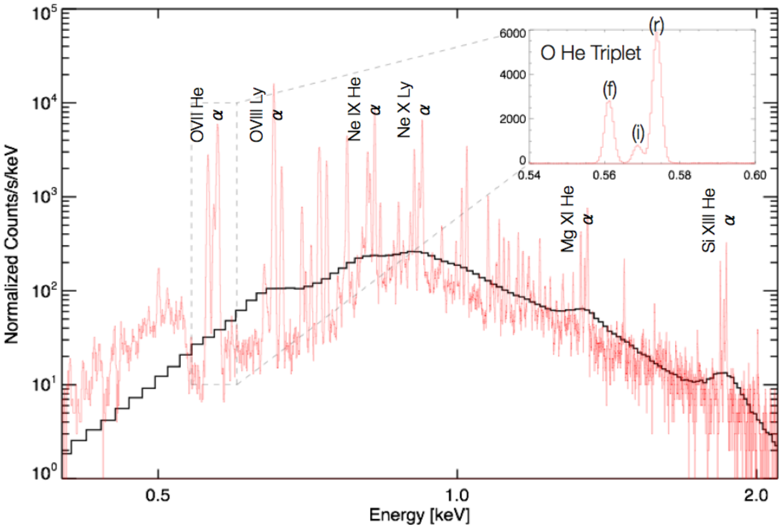

Figure 5-10: A simulated spectrum of the bright eastern knot as seen by *Micro-X* with 4 eV resolution (red) superposed with the best measured spectrum by *Chandra* (black). The inset shows the O VII triplet, the lines of which are completely resolved with the *Micro-X* spectral response.

source much smaller than the FOV). Determining possible pointing offsets in a larger, more diffuse source like Puppis A would take significantly longer [86].

Kosuke Sato developed a software package to produce simulated images based on the *Suzaku* mirror group's work [54]. This software begins with an image of the source from a high spatial resolution instrument, then propagates it through the *Micro-X* optical path. It takes into account vignetting, multiple bounces, occlusion by the solid mirror housing, and the instrument coordinate system.

5.5 Outlook

The *Micro-X* payload has made great strides in the seven years since its funding in 2007. The original launch was planned for early 2011: an aggressive timeline driven by the similarity of the payload to the already-successful *XQC* payload. However, the design and commissioning has been slower than expected, mostly due to the differences between the payloads. Our main time-drains have been our difficulties with the salt pill, trouble with fabrication of the interface chips including diagnosing those issues, slow progress commissioning the flight electronics due to unexpected grounding issues, and most notably the vibration coupling issues we have been battling since our initial vibration tests in June, 2012.

Low temperature instrumentation for spaceflight is a difficult engineering challenge, and similar payloads (like the *Astro-H* payload) have suffered similar issues to our own. *Micro-X* has come from a pen-and-paper concept to a functional detector system and the issues ahead, while formidable, are known, with clear directions to move them to resolution. At the time of writing, we have not set a launch date because of the uncertainty of the timescales involved in solving our current issues. We have identified several key milestones, and flight will be scheduled after these have been achieved. These milestones are: produce a functioning, well characterized salt pill and a heat switch that will allow us to operate the ADR without long time constant delays; solve the vibrational heating problems to a satisfactory level; and achieve a detector noise level less than 10 eV in the laboratory.

TESs will be an important technology moving forward in X-ray instrumentation. *Micro-X* will provide the first step toward a new wave of technology and will be a stepping stone towards a new era of X-ray spectroscopy.

Appendix A

Common Abbreviations and Symbols

ACS	Attitude Control System
ADR	Adiabatic Demagnetization Refrigerator
ARF	Ancillary Response File
BDS	Balmer Dominated Shock
BEK	Bright Eastern Knot
CAD	Computer Aided Design
CCD	Charge Coupled Device
CIE	Collisional Ionization Equilibrium
CR	Cosmic Ray
CX	Charge Exchange
DEC	Declination
DFB	Digital Feedback
ETF	Electro-thermal Feedback
FAA	Ferric Ammonium Alum
FEA	Front End Assembly
FEM	Finite Element Method

FITS	Flexible Image Transport System
FOV	Field Of View
F, R, I	Forbidden, resonance, and intercombination lines
F/R	Forbidden to resonance line ratio
FWHM	Full width at half maximum
G	Thermal Conductance
$\mathcal{G}$	Forbidden plus intercombination to resonance line ratio
GSE	Ground Support Equipment
GRT	Germanium Resistance Thermometer
GSFC	Goddard Space Flight Center
GUI	Graphical User Interface
I/F	Interface
I/O	Input/Output
ISM	InterStellar Medium
IR	Infrared
k	Spring constant
k_B	Boltzmann Constant
LCO	Las Campanas Observatory
LHe	Liquid Helium
LMO	Lightweight Millikelvin Observatory (*Micro-X* flight dewar)
MLI	Multi-layer Insulation
MIT	Massachusetts Institute of Technology
MUX	Multiplexing
N_H	Hydrogen column density
NASA	National Aeronautics and Space Administration
NEI	Non-equilibrium Ionization
NEP	Noise Equivalent Power
NIST	National Institute of Standards and Technology

NSROC	NASA Sounding Rocket Office Contractor
$\mathcal{R}$	forbidden to intercombination line ratio
RA	Right Ascension
RF	Radio Frequency
RGS	Reflection Grating Spectrometer
RMF	Redistribution Matrix File
RSG	Red Supergiant
SA	SQUID Array
S/N	Signal to Noise Ratio
SNR	Supernova Remnant
SQUID	Superconducting QUantum Interference Device
SQ1	First-stage SQUID
SQ2	Second-stage SQUID
SS	Stainless Steel
SXS	Supernova X-ray spectrometer
TES	Transition Edge Sensor
TM	Telemetry System
TMD	Tuned Mass Damper
VAB	Vehicle Assembly Building
`vnei`	Variable (Abundance) Non-equilibrium Ionization
`vpshock`	Variable (Abundance) plane parallel shock
WCS	World Coordinate System
WFF	Wallops Flight Facility
WR	Wolf-Rayet
WSMR	White Sands Missile Range
XQC	X-Ray Quantum Calorimeter

Bibliography

[1] R. Agnese and CDMS Collaboration. Dark Matter Search Results Using the Silicon Detectors of CDMS II. May 2013.

[2] K. Arnaud, R. Smith, and A. Siemiginowska. *Handbook of X-ray Astronomy.* Cambridge Observing Handbooks for Research. Cambridge University Press, 2011. ISBN 9780521883733.

[3] R. Barlow. Asymmetric Statistical Errors. June 2004.

[4] E. Bertin. Automatic Astrometric and Photometric Calibration with SCAMP. In *Astronomical Data Analysis Software and Systems XV*, volume 351 of *ASP Conf. Series*, page 112, 2006.

[5] E. Bertin. SWarp v2.21, User's Guide. *IAP*, 2010.

[6] E. Bertin and S. Arnouts. SExtractor: Software for Source Extraction. *A&A*, 117:393, 1996.

[7] E. Bertin, Y. Mellier, M. Radovich, G. Missonnier, P. Didelon, and B. Morin. The TERAPIX Pipeline. In *Astronomical Data Analysis Software and Systems XI*, volume 281 of *ASP Conf. Series*, page 228, 2002.

[8] P.R. Bevington and D.K. Robinson. *Data Reduction and Error Analysis for the Physical Sciences, Third Edition.* McGraw-Hill Higher Education, 2003. ISBN 0-07-247227-8.

[9] G.F. Bignami, P.A. Caraveo, A. Goldwurm, S. Mereghetti, and G.G.C. Palumbo. *Exosat* and *Einstein* X-ray Observations of the SNR 1E 1149.4-6209 in Crux: A Unified Picture? *ApJ*, 302:606–610, March 1986.

[10] W.P. Blair, K.S. Long, and O. Vancura. A Detailed Optical Study of Kepler's Supernova Remnant. *ApJ*, 366:484–494, 1991.

[11] J.M. Blondin, E.B. Wright, K.J. Borkowski, and S.P. Reynolds. Transition to the Radiative Phase in Supernova Remnants. *ApJ*, 500:342–354, 1998.

[12] J. Brand, L. Blitz, J.G.A. Wouterloot, and F.J. Kerr. The Velocity Field of the Outer Galaxy in the Southern Hemisphere. II. CO Observations of Galactic Nebulae. *Astronomy and Astrophysics Supplement Series*, 68:1–19, February 1987.

[13] S. Broersen, J. Vink, J. Kaastra, and J. Raymond. The High Resolution X-ray Spectrum of SNR 0506-68 Using *XMM-Newton*. *A & A*, 535:A11, 2011. doi: 10.1051/0004-6361:201117390.

[14] G.V. Brown, P. Beiersdorfer, H. Chen, J. Clementson, M. Frankel, M.F. Gu, R.L. Kelley, C.A. Kilbourne, F.S. Porter, D.B. Thorn, and B.J. Wargelin. Studies of X-ray Production Following Charge Exchange Recombination Between Highly Charged Ions and Neutral Atoms and Molecules. In *14th International Conference on the Physics of Highly Charged Ions (HCI 2008)*, volume 163 of *Journal of Physics: Conference Series*, 2009. doi: 10.1088/1742-6596/163/1/012052.

[15] B.W. Carroll and D.A. Ostlie. *An Introduction to Modern Astrophysics, Second Edition*. Pearson Addison Wesley, 2007. ISBN 0-8053-0402-9. URL `www.aw-bc.com/astrophysics`.

[16] D. Castro, P.O. Slane, B.M. Gaensler, J.P. Hughes, and D.J. Patnaude. An XMM-Newton Study of the Bright, Nearby Supernova Remnant G296.1-0.5. *ApJ*, 734:86, 2010. doi: 10.1088/0004-637X/734/2/86.

[17] J.L. Caswell and P.J. Barnes. G296.05-0.50-A Large-Diameter Supernova Remnant. *ApJ*, 271:L55–L58, August 1983.

[18] R.A. Chevalier and J.C. Raymond. Optical Emission from a Fast Shock Wave-The remnants of Tycho's supernova and SN 1006. *ApJ*, 225:L27–L30, October 1978. doi: 10.1086/182785.

[19] R.A. Chevalier and J.C. Raymond. The Optical Emission from a Fast Shock Wave with Application to Supernova Remnants. *ApJ*, 235:186–195, 1980.

[20] D.H. Clark and J.L. Caswell. A study of galactic supernova remnants, based on Molonglo-Parkes observational data. *Monthly Notices of the Royal Astronomical Society*, 174:267–305, 1976.

[21] D.H. Clark, J.L. Caswell, and A.J. Green. New Galactic Supernova Remnants. *Nature*, 246:28–30, November 1973.

[22] D.H. Clark, J.L. Caswell, and A.J. Green. 408 and 5000 MHz Observations of 28 New Galactic Supernova Remnants. *Australian Journal of Physics and Astrophysics Supplements*, 37:1–38, 1975.

[23] DuPont Corporation. *Kevlar Aramid Fiber Technical Guide*. DuPont Corporation. URL `www2.dupont.com/Kevlar/en_US/assets/downloads/KEVLAR_Technical_Guide.pdf`.

[24] R.M. Cutri, M.F. Skrutskie, S. Van Dyk, C.A. Beichman, J.M. Carpenter, T. Chester, L. Cambresy, T. Evans, J. Fowler, J. Gizis, E. Howard, J. Huchra, T. Jarrett, E.L. Kopan, J.D. Kirkpatrick, R.M. Light, H. McCallon, S. Schneider, R. Steining, M. Sykes, M. Weinberg, W.A. Wheaton, S. Wheelock, and N. Zacharias. Explanatory Supplement to the 2MASS All Sky Data Release and Extended Mission Products. 2006. URL `www.ipac.caltech.edu/2mass/releases/allsky/doc/explsup.html`.

[25] J.W. den Herder, A.C. Brinkman, S.M. Kahn, G. Branduardi-Raymont, K. Thomsen, H. Aarts, M. Audard, J.V. Bixler, A.J. den Boggende, J. Cottam, T. Decker, L. Dubbeldam, C. Erd, H. Goulooze, M. Güdel, P. Guttridge, C.J. Hailey, K. Al Janabi, J.S. Kaastra, P.A.J. de Korte, B.J. van Leeuwen, C. Mauche, A.J. McCalden, R. Mewe, A. Naber, F.B. Paerels, J.R. Peterson, A.P. Rasmussen, K. Rees, I. Sakelliou, M. Sako, J. Spodek, M. Stern, T. Tamura, J. Tandy, C.P. de Vries, S. Welch, and A. Zehnder. The Reflection Grating Spectrometer on board XMM-Newton. *A&A*, 365:L7–L17, 2001. doi: 10.1051/0004-6361:20000058.

[26] W.B. Doriese, J.A. Beall, W.D. Duncan, L. Ferreira, G.C. Hilton, K.D. Irwin, C.D. Reintsema, J.N. Ullom, L.R. Vale, and Y. Xu. Progress toward kilo pixel arrays: 3.8 eV micro calorimeter resolution in 8-channel SQUID multiplexer. *Nucl. Phys. A*, 559(2): 808–810, 2006.

[27] A. Dressler and the IMACS team. *The IMACS User Manual*. Carnegie Observatories-Las Campanas Observatory, 2008. URL `http://www.lco.cl/telescopes-information/magellan/instruments/imacs/user-manual/the-imacs-user-manual`.

[28] A. Dressler, B. Bigelow, T. Hare, B. Sutin, I. Thompson, G. Burley, H. Epps, A. Oemler, A. Bagish, C. Birk, K. Clardy, S. Gunnels, D. Kelson, S. Shectman, and D. Osip. The Inamori-Magellan Areal Camera and Spectrograph on Magellan-Baade. *PASP*, 123:901:288–332, 2011. doi: 10.1086/658908.

[29] M.E. Eckart, J.S. Adams, S.R. Bandler, A.D. Brokosky, J.A. Chervenak, A.J. Ewin, F.M. Finkbeiner, R.L. Kelley, C.A. Kilbourne, F.S. Porter, J.E. Sadleir, S.J. Smith, E. Figueroa-Feliciano, and P. Wikus. Large-Absorber TES X-ray Microcalorimeters and the Micro-X Detector Array. *Proceedings of the 13th International Workshop on Low Temperature Detectors*, 1185:699, 2009. doi: 10.1007/s10909-007-9673-6.

[30] R.A. Fesen and H. Itoh. A Two-Dimensional Spectrum of a Nonradiative Shock Filament in the Cygnus Loop. *ApJ*, 295:43–50, 1985.

[31] R.A. Fesen and H. Itoh. A Two-Dimensional Spectrum of a Nonradiative Shock Filament in the Cygnus Loop. *ApJ*, 295:43–50, 1985.

[32] R.A. Fesen, W.P. Blair, and R.P. Kirshner. Optical Emission-Line Properties of Evolved Galactic Supernova Remnants. *ApJ*, 292:29–48, 1985.

[33] R.A. Fesen, R.H. Becker, W.P. Blair, and K.S. Long. High-Velocity, Nonradiative Shock Emission in Kepler's Supernova Remnant. *ApJ*, 338:L13–L16, 1989.

[34] E. Figueroa-Feliciano. Theory and Development of Position-Sensitive Quantum Calorimeters. *PhD thesis, Stanford University*, Published by Goddard Space Flight Center, 2001.

[35] A.H. Gabriel and C. Jordan. Interpretation of solar helium-like ion line intensities. *Monthly Notices of the Royal Astronomical Society*, 145:241, 1969.

[36] J.E. Gaustad, P.R. McCullough, W. Rosing, and D. Van Buren. A Robotic Wide-Angle Hα Survey of the Southern Sky. *Publications of the Astronomical Society of the Pacific*, 113:789:1326–1348, November 2001. doi: 10.1086/323969.

[37] P. Ghavamian, J. Raymond, R.C. Smith, and P. Hartigan. Balmer-Dominated Spectra of Nonradiative Shocks in the Cygnus, RCW 86, and Tycho Supernova Remnants. *ApJ*, 547:995–1009, 2001.

[38] P. Ghavamian, J.M. Laming, and C.E. Rakowski. A Physical Relationship Between Electron-Proton Temperature Equilibration and Mach Number in Fast Collisionless Shocks. *ApJ*, 654:L69–L72, 2007.

[39] R. Giaconni and B. Rossi. A 'Telescope' for Soft X-Ray Astronomy. *Journal of Geophysical Research*, 65:773, 1960.

[40] F. Gök and A. Sezer. Ejecta Detection in the Middle-Aged Galactic Supernova Remnant G296.1-0.5 Observed with *Suzaku*. *Monthly Notices of the Royal Astronomical Society*, 419:1603–1609, 2012. doi: 10.1111/j.1365-2966.2011.19822.x.

[41] A.J. Green, D.A. Frail, W.M. Goss, and R. Otrupcek. Continuation of a Survey of OH (1720 MHz) Maser Emission Towards Supernova Remnants. *ApJ*, 114:5:2058–2067, November 1997.

[42] D.A. Green. Observations of the Western Part of the Cygnus Loop at 408 MHz-The 5C8 Survey. *Monthly Notices of the Royal Astronomical Society*, 209:449, 1984.

[43] S.N.T. Heine, E. Figueroa-Feliciano, J.M. Rutherford, P. Wikus, P. Oakley, F.S. Porter, and D. McCammon. Vibration Isolation Design for the Micro-X Rocket Payload. *Journal of Low Temperature Physics*, 10909:1032, 2014. doi: 10.1007/s10909-013-1032-1.

[44] E.A. Helder, J. Vink, C.G. Bassa, A. Bamba, J.A.M. Bleeker, S. Funk, P. Ghavamian, K.J. van der Heyden, F. Verbunt, and R. Yamazaki. Measuring the Cosmic-Ray Acceleration Efficiency of a Supernova Remnant. *Science*, 325:719, 2009.

[45] K. Heng. Balmer-Dominated Shocks: A Concise Review. *Publications of the Astronomical Society of Australia*, 27:23–44, 2009.

[46] K. Heng. Balmer-Dominated Shocks: A Concise Review. *Publications of the Astronomical Society of Australia*, 27:23–44, 2010. doi: 10.1071/AS09057.

[47] W.S. Holland, E.I. Robson, W.K. Gear, C.R. Cunningham, J.F. Lightfoot, T. Jenness, R.J. Ivison, J.A. Stevens, P.A.R. Ade, M.J. Griffin, W.D. Duncan, J.A. Murphy, and D.A. Naylor. SCUBA: a common-user submillimetre camera operating on the James Clerk Maxwell Telescope. *Monthly Notices of the Royal Astronomical Society*, 303: 659–672, 1998. doi: 10.1046/j.1365-8711.1999.02111.x.

[48] J.C. Houck and L.A. Denicola. ISIS: An Interactive Spectral Interpretation System for High Resolution X-Ray Spectroscopy. In *Astronomical Data Analysis Software and Systems IX*, volume 216 of *A.S.P. Conference Series*, page 591, 2000.

[49] J.B. Hutchings, D. Crampton, and A.P. Cowley. The X-ray Pulsars 2S 1145-619 and 1E 1145.1-6141: Optical Identifications and a Nearby Supernova Remnant. *ApJ*, 86:6: 871–874, June 1981.

[50] U. Hwang and T.H. Markert. An X-ray Study of Five Supernova Remnants in the Carina Spiral Arm. *ApJ*, 431:819–825, August 1994.

[51] U. Hwang, K.A. Flanagan, and R. Petre. Chandra X-Ray Observation of a Mature Cloud-Shock Interaction in the Bright Eastern Knot Region of Puppis A. *ApJ*, 635: 355, 2005. doi: 10.1086/497298.

[52] U. Hwang, K.A. Flanagan, and R. Petre. *Chandra* X-Ray Observation of a Mature Cloud-Shock Interaction in the Bright Eastern Knot Region of Puppis A. *ApJ*, 635: 355–364, May 2005.

[53] K.D. Irwin. An application of electrothermal feedback for high resolution cryogenic particle detection. *Applied Physics Letters*, 66:1998–2000, April 1995.

[54] Y. Ishisaki, Y. Maeda, R. Fujimoto, M. Ozaki, K. Ebisawa, T. Takahashi, Y. Ueda, Y. Ogasaka, A. Ptak, K. Mukai, K. Hamaguchi, M. Hirayama, T. Kotani, H. Kubo, R. Shibata, M. Ebara, A. Furuzawa, R. Iizuka, H. Inoue, H. Mori, S. Okada, Y. Yokoyama, H. Matsumoto, H. Nakajima, H. Yamaguchi, N. Anabuki, N. Tawa, M. Nagai, S. Katsuda, K. Hayashida, A. Bamba, E.D. Miller, K. Sato, and N.Y. Yamasaki. Monte Carlo Simulator and Ancillary Response Generator of Suzaku XRT/XIS System for Spatially Extended Source Analysis. *PASJ*, 59:113–132, January 2007.

[55] R.C. Jaklevic, J. Lambe, A.H. Silver, and J.E. Mercereau. Probable Observation of the Josephson Superconducting Tunneling Effect. *Phys. Rev. Lett.*, 10:230, 1964. doi: 10.1193/PhysRevLett.12.159.

[56] F. Jansen, D. Lumb, B. Altieri, J. Clavel, M. Ehle, C. Erd, C. Gabriel, M. Gauinazzi, P. Gondoin, R. Much, R. Munoz, M. Santos, N. Schartel, D. Texier, and G. Vacanti. XMM-Newton observatory. *A&A*, 365:L1–L6, 2001. doi: 10.1051/0004-6361:20000036.

[57] S. Katsuda, H. Tsunemi, K. Mori, H. Uchida, H. Kosugi, M. Kimura, H. Nakajima, S. Takakura, R. Petre, J.W. Hewitt, and H. Yamaguchi. Possible CX X-ray Emission in the Cygnus Loop Detected with *Suzaku*. *ApJ*, 730:24, March 2011. doi: 10.1088/0004-637X/730/1/24.

[58] S. Katsuda, H. Tsunemi, K. Mori, H. Uchida, R. Petre, S. Yamada, H. Akamatsu, S. Konami, and T. Tamagawa. High-Resolution X-ray Spectroscopy of the Galactic Supernova Remnant Puppis A with *XMM-Newton*/RGS. *ApJ*, 756:49, 2012.

[59] R.L. Kelley, K. Mitsuda, C.A. Allen, P. Arsenovic, M.D. Audley, T. G. Bialas, K.R. Boyce, R.F. Boyle, S.R. Breon, G.V. Brown, J. Cottam, M.J. DiPirro, R. Fujimoto, T. Furusho, K.C. Gendreau, G.G. Gochar, O. Gonzalez, M. Hirabayashi, S.S. Holt, H. Inoue, M. Ishida, Y. Ishisaki, C.S. Jones, R. Keski-Kuha, C.A. Kilbourne, D. McCammon, U. Morita, S.H. Moseley, B. Mott, K. Narasaki, Y. Ogawara, T. Ohashi, N. Ota, J.S. Panek, F.S. Porter, A. Serlemitsos, P.J. Shirron, G.A. Sneiderman, A.E. Szymkowiak, Y. Takei, J.L. Tveekrem, S.M. Volz, M. Yamamoto, and N.Y. Yamasaki. The Suzaku High Resolution X-Ray Spectrometer. *Publ. Astron. Soc. Japan*, 59:S77–S112, January 2007.

[60] R.P. Kirshner and R.A. Chevalier. The Spectrum of Tycho's Supernova Remnant. *A&A*, 67:267–271, 1978.

[61] R.P. Kirshner, P.F. Winkler, and R.A. Chevalier. High-Velocity Emission in Young Supernova Remnants: SN 1006 and SN 1572. *ApJ*, 315:L135–L139, 1987.

[62] S. Komossa, H. Zhou, A. Rau, M. Dopita, A. Gal-Yam, J. Greiner, J. Zuther, M. Salvato, D. Xu, H. Lu, R. Saxton, and M. Ajello. NTT, *Spitzer*, and *Chandra* Spectroscopy of SDSSJ095209.56+214313.3: The Most Luminous Coronal-Line Supernova Ever Observed, or a Stellar Tidal Disruption Event? *ApJ*, 701:105–121, 2009. doi: 10.1088/0004-637X/701/1/105.

[63] A. Kosowsky. The Atacama Cosmology Telescope. *New Astronomy Reviews*, 47:939–943, December 2003. doi: 10.1016/j.newar.2003.09.003.

[64] R. Lallement. On the Contribution of Charge-Exchange Induced X-ray Emission in the ISM and ICM. *A&A*, 422:391–400, 2004. doi: 10.1051/0004-6361:20035625.

[65] C.M. Lisse, K. Dannerl, J. Englhauser, M. Harden, F.E. Marshall, M.J. Mumma, R. Petre, J.P. Pye, M.J. Ricketts, J. Schmitt, J. Trumper, and R.G. West. Discovery of X-ray and Extreme Ultraviolet Emission from Comet C/Hyakutake 1996 B2. *Science*, 274:205–209, 1996. doi: 10.1126/science.274.5285.205.

[66] K.S. Long and W.P. Blair. The Identification of Balmer-Dominated Filaments in RCW 86. *ApJ*, 358:L13–L16, 1990.

[67] A.J. Longmore, D.H. Clark, and P. Murdin. A New Optical Supernova Remnant in Crux. *Monthly Notices of the Royal Astronomical Society*, 181:541–546, 1977.

[68] T.H. Markert, R.C. Lamb, R.C. Hartman, D.R. Thompson, and G.F. Bignami. Two X-ray Supernova Remnants: G296.1-0.7 and 1E 1149.4-6209. *ApJ*, 248:L17–L21, August 1981.

[69] F. Marshall, E. Boldt, S. Holt, R. Kelley, R. Mushotzky, R. Petre, P. Serlemitsos, J. Swank, and A. Szymkowiak. X-ray Spectrometers for Observing SN1987A. *Bulletin of the American Astronomical Society*, 19:735, March 1987.

[70] P. Massey. A User's Guide to CCD Reductions with IRAF. February 2004. URL `iraf.noao.edu/iraf/docs/ccduser3.ps`.

[71] D. McCammon and et. al. . A Sounding Rocket Payload for X-ray Astronomy Employing High-Resolution Microcalorimeters. *Nucl. Instrum. Methods Phys. Res.*,, 370: 266–268, 1996.

[72] G.W. McClure. Electron Transfer in Proton-Hydrogen-Atom Collisions: 2-117 keV*. *Physical Review*, 148:1:47, 1966.

[73] J.J. McMahon, K.A. Aird, B.A. Benson, L.E. Bleem, J. Britton, J.E. Carlstrom, C.L. Chang, H.S. Cho, T. de Haan, T.M. Crawford, A.T. Crites, A. Datesman, M.A. Dobbs, W. Everett, N.W. Halverson, G.P. Holder, W.L. Holzapfel, D. Hrubes, K.D. Irwin, M. Joy, R. Keisler, T.M. Lanting, A.T. Lee, E.M. Leitch, A. Loehr, M. Lueker, J. Mehl, S.S. Meyer, J.J. Mohr, T.E. Montroy, M.D. Niemack, C.C. Ngeow, V. Novosad, S. Padin, T. Plagge, C. Pryke, C. Reichardt, J.E. Ruhl, K.K. Schaffer, L. Shaw, E. Shirokoff, H.G. Spieler, B. Stadler, A.A. Stark, Z. Staniszewski, K. Vanderlinde, J.D. Vieira, G. Wang, R. Williamson, V. Yefremenko, K.W. Yoon, O. Zhan, and A. Zenteno. SPTpol: and instrument for CMB polarization. In *AIP Conference Proceedings*, volume 1185, page 511, July 2009. doi: 10.1063/1.3292391.

[74] E. Michael, R. McCray, R. Chevalier, A.V. Filippenko, P. Lundqvist, P. Challis, B. Sugerman, S. Lawrence, C.S.J. Pun, P. Garnavich, R. Kirshner, A. Crotts, C. Fransson, W. Li, N. Panagia, M. Phillips, B. Schmidt, G. Sonneborn, N. Suntzeff, L. Wang, and J.C. Wheeler. Hubble Space Telescope Observations of High-Velocity Lyα and Hα Emission from Supernova Remnant 1987A: The Structure and Development of the Reverse Shock. *Astronomical Journal*, 593:809–830, 2003. doi: 10.1086/376725.

[75] R. Minkowski. Optical Observations of Nonthermal Galactic Radio Sources. *IAU*, 9: 315, 1959.

[76] K. Morgan, V. Andrianarijaona, I.N. Draganic, X. Defay, M. Fogle, A. Galindo-Uribarri, C.I. Guillen, C.C. Havener, M. Hokin, D. McCammon, D.J. Nader, S.L.

Romano, F. Salces Carcoba, P. Sauter, D. Seely, P.C. Stancil, C.R. Vane, A.K. Vassantachart, and D. Wulf. Charge Exchange X-ray Emission: Astrophysical Observations and Potential Diagnostics. *AIP Conference Proceedings,*, 49:1525, 2013. doi: 10.1063/1.4802288.

[77] J.W. Percival, K.H. Nordsieck, and K.P. Jaehnig. The ST5000: a high precision star tracker and attitude determination system. *Proc. SPIE 7010*, 7010, 2008. doi: 10.1117/12.787917.

[78] R. Petre. Thin shell, segmented X-Ray Mirrors. *X-ray Optics and Instrumentation*, 2010, 2010. doi: 10.1155/2010/412323.

[79] F. Pobell. *Matter and Methods at Low Temperatures, third edition.* Springer, 2007. ISBN 3-540-46356-9.

[80] D. Porquet, J. Dubau, and N. Grosso. He-like Ions as Practical Astrophysical Plasma Diagnostics: From Stellar Coronae to Active Galactic Nuclei. *Space Sci. Rev.*, 157: 103–134, 2010. doi: 10.1007/s11214-010-9731-2.

[81] J.C. Raymond, W.P. Blair, R.A. Fesen, and T.R. Gull. The Structure and Emission Spectrum of a Nonradiative Shock Wave in the Cygnus Loop. *ApJ*, 275:636–644, 1983.

[82] J.C. Raymond, J. Vink, E.A. Helder, and A. De Laat. Effects of Neutral Hydrogen on Cosmic-Ray Precursors in Supernova Remnant Shock Waves. *ApJ Letters*, 731: L14–L19, 2011. doi: 10.1088/2041-8205/731/I/L14.

[83] D. Russeil. Hα Detection of a Clump of Distant HII Regions in the Milky Way. *A & A*, 319:788–795, September 1997.

[84] D. Russiel and Q.A. Parker. First Results from the Combination of the AAO/UKST and Marseille Hα Surveys. *Publications of the Astronomical Society of Australia*, 18: 76–83, 2001.

[85] J. Rutherford, D. Dewey, E. Figueroa-Feliciano, S.N.T. Heine, F.A. Bastien, K. Sato, and C.R. Canizares. A Decade-Baseline Study of the Plasma States of Ejecta Knots in Cassiopeia A. *ApJ*, 769(1):64, May 2013.

[86] J.M. Rutherford. Imaging X-ray Spectroscopy with Micro-X and Chandra. *PhD thesis, Massachusetts Institute of Technology*, 2013. URL `http://hdl.handle.net/1721.1/84183`.

[87] D.R. Schultz, P.S. Krstic, T.G. Lee, and J.C. Raymond. Momentum Transfer and Viscosity from Proton-Hydrogen Collisions Relevant to Shocks and Other Astrophysical Environments. *ApJ*, 678:950–960, 2008.

[88] F. Schweizer and B.M. Lasker. On the Peculiar Spectrum of the Optical Remnant of Supernova A.D. 1006. *ApJ*, 226:167–171, 1978.

[89] H.E. Seraph and M.J. Seaton. Electron Densities in Planetary Nebulae. *Monthly Notices of the Royal Astronomical Society*, 148:367–381, 1970.

[90] P.J. Serlemitsos. Conical Foil X-ray Mirrors-Performance and Projections. *Applied Optics*, 27:1447–1452, 1988. doi: 10.1364/AO.27.001447.

[91] F.D. Seward. *Einstein* Observations of Galactic Supernova Remnants. *ApJ Supplement Series*, 73:781–819, August 1990.

[92] J.M. Shull and C.F. McKee. Theoretical Models of Interstellar Shocks. I. Radiative Transfer and UV Precursors. *ApJ*, 227:131–149, 1979.

[93] P. Slane, D. Castro, E. Helder, and J. Raymond. The Collapse of a Massive Star: Observing SNR G296.1-0.5 with Magellan. *Magellan Proposal*, October 2011.

[94] R. Smith, A. Foster, and N. Brickhouse. Charge Exchange Models for X-ray Spectroscopy with AtomDB v2.0. In *AtomDB Workshop and Work Week 2012*, August 2012.

[95] R.C. Smith. The Discovery of Balmer-Filaments Encircling SNR RCW 86. *Astronomical Journal*, 114:6:2664, 1997.

[96] R.C. Smith, R.P. Kirshner, W.P. Blair, and P.F. Winkler. Six Balmer-Dominated Supernova Remnants. *ApJ*, 375:652–662, 1991.

[97] R.K. Smith, N.S. Brickhouse, D.A. Liedahl, and J.C. Raymond. Collisional Plasma Models with APEC/APED: Emission-Line Diagnostics of Hydrogen-Like and Helium-Like Ions. *ApJ*, 556:L91–L95, 2001.

[98] Suborbital and Special Orbital Projects Directorate. *NASA Sounding Rocket Program Handbook*. NASA Goddard Space Flight Center, 2005. URL `http://sites.wff.nasa.gov/code810/files/SRHB.pdf`.

[99] D. Tody. The *IRAF* Data Reduction and Analysis System. In *Proceedings SPIE Instrumentations in Astronomy VI*, volume 627, page 733, 1986.

[100] D. Tody. IRAF in the Nineties. In *Astronomical Data Analysis Software and Systems II*, volume 52 of *A.S.P. Conference Series*, page 173, 1993.

[101] I.R. Touhy, M.A. Dopita, D.S. Mathewson, K.S. Long, and D.J. Helfand. Optical Identification of Balmer-Dominated Supernova Remnants in the Large Magellanic Cloud. *ApJ*, 261:473–484, 1982.

[102] R.A. Treumann and R. Pottelette. The Outer Heliospheric Radio Emission: Observations and Theory. *International Space Science Institute Scientific Reports*, 5:355–389, 2006.

[103] R.A. Treumann, W.M. Macek, and V. Izmodenov. Heliopause Radio Emission Scenario. *Astronomy and Astrophysics*, 336:L45–L48, 1998.

[104] M. van Adelsberg, K. Heng, R. McCray, and J.C. Raymond. Spatial Structure and Collisionless Electron Heating in Balmer-dominated Shocks. *Astronomical Journal*, 689:1089–1104, 2008. doi: 10.1086/592680.

[105] S. van den Bergh. The Optical Remnant of the Lupus Supernova of 1006. *ApJ*, 208: L17, 1976.

[106] S. van den Bergh. A Systematic Search for Galactic Supernova Remnants. *ApJ Supplement Series*, 38:119–128, October 1978.

[107] K.J. van der Heyden, J.A.M. Bleeker, J.S. Kaastra, and J. Vink. High Resolution Spectroscopy and Emission Line Imaging of DEM L71 with *XMM-Newton*. *A & A*, 406:141–148, 2003. doi: 10.1051/0004-6361:20030658.

[108] P.G. van Dokkum. Cosmic-Ray Rejection by Laplacian Edge Detection. *PASP*, 113: 1420, 2001.

[109] Q.D Wang and J. Liu. Spectroscopic Evidence of Charge Exchange X-ray Emission from Galaxies. *Astron. Nachr.*, 999 No. 88:789–793, April 2012.

[110] B.J. Wargelin, P. Beiersdorfer, and G.V. Brown. EBIT Charge-Exchange Measurements and Astrophysical Applications. *Canadian Journal of Physics*, 86:151, 2008. doi: 10.1139/P07-125.

[111] J.B.Z. Whiteoak and A.J. Green. The MOST Supernova Remnant Catalogue (MSC). *Astronomy and Astrophysics Supplement Series*, 118:329–380, August 1996.

[112] P. Wikus, J. S. Adams, Y. Bagdasarova, S. R. Bandler, W. B. Doriese, E. Figueroa-Feliciano, C. A. Kelley, C. A. Kilbourne, S. W. Leman, D. McCammon, F. S. Porter, J. M. Rutherford, and S. N. Trowbridge. The Adiabatic Demagnetization Refrigerator for the Micro-X Sounding Rocket Telescope. *Advances in Cryogenic Engineering*, 55: 633, 2010. doi: 10.1063/1.3422413.

[113] P. Wikus, J. M. Rutherford, S. N. Trowbridge, D. McCammon, J.S. Adams, S. R. Bandler, R. Das, W. B. Doriese, M.E. Eckart, E. Figueroa-Feliciano, R. Kelley, C.A. Kilbourne, S.W. Leman, F.S. Porter, and K. Sato. The Detector and Readout Systems of the Micro-X High Resolution Microcalorimeter X-Ray Imaging Rocket. In *Proceedings of the ICC*, volume 1185 of *AIP Conference Proceedings*, page 434, 2010. doi: 10.1063/1.3292371.

[114] P. Wikus, E. Canavan, S.N.T. Heine, K. Matsumoto, and T. Numazawa. Magnetocaloric Materials and the Optimization of Cooling Power Density. *Cryogenics*, 2014.

[115] P.F. Winkler, G.W. Clark, T.H. Markert, K. Kalata, H.W. Schnopper, and C.R. Canizares. A survey of X-ray line emission from the supernova remnant Puppis A. *ApJ Letters*, 246:L27–L31, 1981. doi: 10.1086/183546.

[116] H. Wolter. Glancing Incidence Mirror Systems as Imaging Optics for X-Rays. *Ann. Physik*, 10:94, 1952.

[117] A.L. Woodcraft and A. Gray. A Low Temperature Thermal Conductivity Database. In *AIP Conference Proceedings*, volume 1185, page 681, 2009.

[118] H. Yamaguchi, M. Ozawa, K. Koyama, K. Masai, J.S. Hiraga, M. Ozaki, and D. Yonetoku. Discovery of Strong Radiative Recombination Continua from the Supernova Remnant IC 443 with Suzaku. *ApJ*, 705:L6–L9, February 2009. doi: 10.1088/0004-637X/705/1/L6.

[119] C.T. Yap and P.P. Saligan. A Monte Carlo approach to X-ray fluorescence analysis at low energies using an annular 55Fe source. *Nucl. Phys. A*, 251:140–143, 1986. doi: 10.1016/0168-9002(86)91160-5.

[120] J.C. Zarnecki, J.L. Culhane, A. Toor, F.D. Seward, and P.A. Charles. The X-ray Spectrum and Structure of the Puppis A Supernova Remnant. *ApJ Letters*, 219:L17, 1978.